Universidade do Minho
Escola de Engenharia

Nadya Vasileva Dencheva

Development and Investigation of Novel in situ Reinforced Nanocomposites Based on Oriented Polymer Blends

Desenvolvimento e Investigação de Novos Nanocompósitos à Base de Misturas de Polímeros Reforçados in situ

Tese de Doutoramento
Área: Ciência de Materiais

Trabalho efectuado sob a orientação de
Professora Doutora **Maria Jovita Soares de Oliveira**
Professora Doutora Maria Teresa G. Costanzo Nunes

Junho de 2008

ACKNOWLEDGEMENTS

The research work presented in this thesis was performed at the Department of Polymer Engineering, Institute for Polymers and Composites, of the University of Minho, during the period from October 2003 to September 2007. Its completion would not have been possible without the support of many people and institution. Here I take the opportunity to express my gratitude to:

- Prof. Dr. Maria Jovita Oliveira, scientific supervisor of this thesis, for her continuous support, encouragement and guidance throughout the time of my PhD;

- Prof. Dr. Teresa Nunes, co-supervisor, for the fruitful discussions and her practical help related to the solid state NMR measurements and data treatment, not forgetting her kind hospitality during my stay at the Instituto Superior Técnico in Lisbon.

- Prof. Dr. António Sérgio Pouzada for all discussions and helpful suggestions related to the mechanical tests of composite materials.

I am indebted to Prof. Dr. Olga Carneiro for the help rendered in the preparation of the oriented precursors used in this thesis.

My thanks to all of the technical and administrative staff of the Department of Polymer Engineering and to the University of Minho in general for the facilities, equipment and technical aid provided.

I thank to Dr. Mark P. Kearns, molding research manager in Queens University, Belfast, for the impact tests.

I gratefully acknowledge the financial support of *Fundação para a Ciência e Tecnologia,* Portugal through the grants No SFRH/BD/13435/2003 and POCI/CTM/57358/2004. I wish to express my gratitude to the financial support of the Hamburg Synchrotron Laboratory (HASYLAB) at the German Synchrotron Facility (DESY) through grants n° II-01-006 EC and II-04-047 EC, which enabled all X-ray measurements included in this thesis. In particular, I thank Dr. Sérgio Funari, scientist at the A2 Soft Condensed Matter Beamline for his practical help.

I wish to extend my special thanks to Prof. DSc. S. Fakirov, the pioneer of the MFC technology, who supported me in the beginning of my PhD project.

I am grateful for the years I worked in dWare where I learned to be persistent and never to give up in challenging situations.

Finally I would not forget the affection and the undivided support of my family. I specially thank to my parents and my brother, whose love and countenance were very important to me. I thank especially my husband Zlatan not only for supporting me in everything but also for all "hot" debates on MFCs we had during the realization of this work, and my daughter Zlatomira for bringing happiness into my life.

Nadya Dencheva
Guimarães, June 2008

RESUMO

Os compósitos microfibrilares (MFCs) são compósitos polímero-polímero em que, tanto a matrix como os reforços, são obtidos *in-situ* durante o processamento. Utilizando técnicas de processamento convencionais, nomeadamente, extrusão, estiramento a frio e moldação por compressão, foram produzidos MFCs de matriz HDPE, com reforços de poliamidas 6 (PA6) ou 12 (PA12) e Yparex (YP) como compatibilizador. Variou-se a concentração das poliamidas entre 10 e 30 % (em peso) e a do compatibilizador entre 0 e 10 %. De cada composição HDPE/PA/YP foram produzidos compósitos, com geometrias e alinhamentos diferentes da fase reforçadora de poliamida – lâminas unidireccionais (UDP), laminados com lâminas de orientação cruzada (CPC), placas de filamentos com comprimento médio (cerca de 20-30 mm) e orientação aleatória (MRB). A morfologia fibrilar do reforço de PA foi comprovada por SEM, TEM e sincrotrão SAXS e WAXS. O diâmetro dos fibrilos nos MFCs é de 0.5-1.5 μm e o comprimento de 20-120 μm. Estas dimensões dependem da poliamida aplicada (PA6 ou PA12) assim como do conteúdo de YP. Foram realizados ensaios de tracção, flexão e impacto em todos os compósitos. O aumento do módulo de Young atingiu 33% e da resistência à tracção 150%, verificando-se que, quanto maior a concentração de YP, pior o desempenho à tracção. A regra das misturas pode ser utilizada para prever o comportamento à tracção dos MFCs tanto de PA6 como de PA12. Todos os laminados microfibrilares (CPC e MRB) apresentaram melhor comportamento à flexão que o HDPE, tendo o aumento máximo de 180% sido atingido por laminados CPC de PA12. Os compósitos com microfibras de PA12 tiveram melhores propriedades ao impacto que a matriz ou os equivalentes em PA6. A melhoria das energias de impacto no pico e total foram 70 e 135%, respectivamente. A estrutura dos MFCs foi estudada, utilizando ^{13}C NMR de sólidos e técnicas de sincrotrão SAXS e WAXS, e relacionada com o comportamento mecânico Foi investigado o polimorfismo das poliamidas e comprovada a formação de uma camada transcristalina (TCL) na interface fibra-matriz. As lamelas de HDPE na TCL orientam-se epitaxialmente ao longo da fibra de poliamida sendo a orientação das cadeias dos dois materiais coincidente. A espessura da TCL é de 50 a 130 nm, dependendo do tipo de poliamida e do conteúdo de YP. O melhor desempenho mecânico dos MFCs de PA12 está associado a diferenças de geometria e de estrutura da TCL. Os resultados sugerem que a presença da TCL conduz geralmente à deterioração das propriedades mecânicas dos MFCs de HDPE/PA/YP. Foram propostos modelos para interpretar a estrutura dos MFCs de HDPE/PA/YP.

ABSTRACT

The microfibrilar composites (MFCs) are polymer-polymer reinforced composites in which both matrix and reinforcements are obtained *in-situ* during the processing. MFCs based on HDPE as a matrix, polyamides 6 (PA6) or 12 (PA12) - as a reinforcement and Yparex (YP) as a compatibilizer were produced, using conventional processing techniques namely: extrusion, cold drawing and compression molding. The polyamide concentration was varied between 10 and 30 wt.% while that of the compatibilizer was in the range of 0-10 wt.%. Composites with various geometry and alignment of the polyamide phase were produced from each HDPE/PA/YP composition – unidirectional laminae (UDP), cross-ply laminates (CPC), MFCs from middle-length, randomly-oriented bristles (MRB). The fibrilar morphology of the PA reinforcement was proved by SEM, TEM and synchrotron SAXS and WAXS. The diameter of the fibrils in the HDPE/PA/YP MFCs was in the range of 0.5-1.5 μm and the length varied between 20-120 μm. These two characteristics were dependent on the polyamide applied (PA6 or PA12) as well as on the YP content. Tensile, flexural and impact resistance tests were performed with all composites. The improvement of the Young's modulus was up to 33% and of the tensile strength – up to 150%, whereby the bigger the YP concentration, the smaller the enhancement of the tensile properties. The rule of mixtures can be used to predict the tensile behavior of both, PA6 and PA12 UDP MFCs. All microfibrilar laminates (CPC and MRB) showed better flexural behavior than the HDPE, the improvement being the highest in the PA12 CPC laminates (180%). The PA12 fiber reinforcement led to better impact properties, compared to the matrix and to the respective PA6 compositions. The improvement of the peak and the total energies were 70% and 135%, respectively. The structure of the HDPE/PA6/YP and HDPE/PA12/YP MFCs was studied in order to explain their mechanical behavior. Solid state ^{13}C NMR and synchrotron SAXS and WAXS methods were used for this purpose. The PA6 and PA12 polymorphism was investigated and the formation of HDPE trans-crystalline layer (TCL) at the matrix-fiber interface was proved. The HDPE lamellae in the TCL were oriented epitaxially along the polyamide fiber whereby chain directions of HDPE and of the polyamide coincided. The TCL thickness was in the 50-130 nm range and was dependent on the polyamide type and YP content. The better mechanical performance of the PA12 MFCs as compared to the PA6 was related to differences in the structure and geometry of the TCL. A suggestion was made that the presence of TCL generally leads to deterioration of the mechanical properties of the HDPE/PA/YP MFCs. Idealized models for the structure of the HDPE/PA/YP MFCs were proposed.

TABLE OF CONTENTS

LIST OF SYMBOLS AND ABBREVIATIONS

Latin Symbols

C_p , MPa	reduced flexural stiffness (mechanics)
d_{hkl} , Å	interplanar spacing with the respective indexation
E_1 , MPa	Young's modulus in longitudinal direction
E_2 , MPa	Young's modulus in transverse direction
E^* , MPa	complex modulus
l_a , nm	average thickness of the amorphous phase
l_c , nm	average thickness of the crystalline phase
L_B , nm	Bragg long spacing
L_c^m , nm	long spacing from the first minimum of CF
L_c^M	long spacing from the first maximum of CF
T_g , °C	glass-transition temperature
T_m , °C	melting temperature
s, nm^{-1}, $Å^{-1}$	scattering vector, SAXS, WAXS
x_{cl}	crystal fraction within the lamellar stacks

Greek Symbols

ε , mm or %	strain
ϕ , degrees	off-axis test angle (Tsai-Hill equation)
λ (dimensionless)	draw ratio
λ , Å	X-ray radiation wavelength
σ , MPa	stress
$\sigma_{1\max}$, MPa	maximal longitudinal stress (strength)
$\sigma_{2\max}$, MPa	maximal transversal stress (strength)
θ, degrees	scattering angle, WAXS

Abbreviations

A_a , % (WAXS)	integrated area of the amorphous halo
A_c , % (WAXS)	integrated area of a crystalline peak
CCD (image detector)	charge-coupled device

CF	linear correlation function (SAXS)
CI, % (WAXS)	crystallinity index (isotropic samples)
^{13}C NMR	carbon 13 nuclear magnetic resonance
CNT	carbon nanotubes
CPC	cross-ply laminate plates (composite theory)
CP	cross polarization (NMR theory)
1D WAXS	one-dimensional WAXS pattern
2D WAXS	two-dimensional WAXS pattern
DD	draw direction
DD	dipolar decoupling (NMR)
DMTA	dynamic-mechanical thermal analysis
DSC	differential-scanning calorimetry
ECI, % (WAXS)	equatorial crystallinity index (oriented samples)
GF	glass fibers
GS	glass spheres
HBL, Ǻ	hydrogen bond length
HDPE	high density polyethylene
IE, kJ/m^2	impact energy
IM	injection molding
IF	improvement factor (mechanics)
iPP	isotactic polypropylene
ISD, Ǻ	inter-sheet distance
LDPE	low density polyethylene
LLDPE	linear low-density polyethylene
LCP	liquid-crystalline polymer
MAH	maleic anhydride
MAR CCD	the two-dimensional CCD detector of MAR
MAS	Magic Angle Spinning (solid state NMR)
MRB	middle-length randomly distributed bristles

MFC	microfibrilar composite
MWNT	multi-walled nanotubes
NPC	nanostructured polymer composite
NOM	non-oriented mixture
OC	oriented cable
PA6	polyamide 6
PBT	poly(butylene terephthalate)
PA66	polyamide 6,6
PA12	polyamide 12
PC	polycarbonate (based on Bisphenol A)
PEE	poly(ether ester)
PET	poly(ethylene terephthalate)
PLM	polarized light microscopy
PPS	poly(phenylene sulfide)
S, MPa	shear strength (Tsai-Hill)
SAXS	small-angle X-ray scattering
SEM	scanning electron microscopy
SWNT	single-walled nanotubes
TEM	transmission electron microscopy
UDP	unidirectional ply
WAXS	wide-angle X-ray scattering
WP	woven precursor
X, MPa	tensile strength in the fiber direction (Tsai-Hill)
Y, MPa	tensile strength in the transverse direction (Tsai-Hill)
YP	Yparex compatibilizer of DSM

CHAPTER 1

GENERAL INTRODUCTION:
TRANSFORMING POLYMER BLENDS INTO COMPOSITES: A PATHWAY TOWARDS NANOSTRUCTURED MATERIALS

1.1. Introduction

An acceptable composite material for use in engineering applications should satisfy the following three basic requirements [1]:

(i) To consist of at least two physically distinct and mechanically separable materials, which, depending on their properties and amounts used, are called *matrix* and *reinforcing component*;

(ii) There must be a possibility for its preparation by admixing of the above components (sometimes preceded or accompanied by some special treatment so as to achieve optimum properties); and

(iii) The final material is expected to possess several properties being superior to that of the individual components, i.e. some synergistic effect should be present.

The realization of this synergism requires strictly defined and reproducible distribution of the size and dispersity of the reinforcing component within the matrix, as well as a good adhesion and certain compatibility of the separate phases forming the composite [2]. These depend on the presence of chemical and/or physical interactions at their interface. If the said interactions are negligible, because of the inherent immiscibility in polymer blends, mixing normally results in phase-separated and technologically incompatible systems with insufficient mechanical properties. Should either chemical reactions or physical interactions at the interface play a major role, blending may cause better adhesion at the matrix–reinforcing element boundary. This could lead to de desired synergism in the composite properties and even generate materials with unique properties [3].

More than a decade ago a new group of polymer materials was introduced, which became known under the name 'microfibrilar composites' (MFCs). In them, both matrix and reinforcements were obtained *in-situ*, by the transformation of blends of thermoplastic polymers into micro- or nanostructured systems by combination of appropriate mechanical and thermal treatments. Since then, the importance of these novel materials, both for theory and for engineering practice, has increased significantly.

In this first chapter [4], the place of MFCs within the whole variety of polymer-based composites will be outlined. Furthermore, a literature review on the methods of their preparation, the ways of investigating their structure and the relation of the structure and mechanical properties will be presented. In the end, on the basis of this review, the basic scientific goals of this thesis and its structure will be defined.

1.2. Classification of polymer-based composites

With respect to the size of the reinforcing elements, polymer composites can be divided into three basic groups: (i) *macrocomposites*, comprising fibrous or powder-like reinforcing elements with relatively large sizes (most frequently above 0.1mm) of glass, carbon or some special rigid polymers; (ii) *nanocomposites*, where the reinforcement could be either inorganic material (e.g. clay or metal oxide), or structures made out of carbon (e.g. rods, tubes, etc.), with sizes in the nanometer range; and (iii) *molecular composites*, where the reinforcement is built up from single, rigid-rod macromolecules with diameters in the angstrom range.

Examples for conventional macrocomposites are the fiber-reinforced systems consisting of an isotropic matrix made out of a polyolefin, polyamide, polyester, etc., that embeds oriented organic or inorganic fibers of various lengths; the fibers can be of glass, carbon, Kevlar, etc [5–9]. Good examples of nanocomposites are the carbon nanotube (CNT) - reinforced systems. CNTs are considered as a new form of pure carbon that can be visualized as rolled hexagonal carbon networks that are capped by pentagonal carbon rings with diameters in the range 5–10 nm [10]. There are two types of carbon tubes: single-walled nanotubes (SWNTs) and multiwalled nanotubes (MWNTs). Subsequent Young's moduli measurements demonstrated that MWNTs are mechanically much stronger than conventional carbon fibers [11,12] and are extraordinarily flexible when subjected to large strain [13]. In order to employ CNTs, and the nanocomposites thereof, on a commercial basis, it is necessary to control effectively their growth, length, diameter and crystallinity at accessible costs, which is quite a challenging task [10].

Another remarkable form of nanocomposite materials was disclosed in the pioneering work by the Toyota group [14,15]. These materials contain only small amounts of nanosized particles embedded into organic polymer or resin matrix materials thus markedly improving mechanical and wear properties including increased storage modulus, increased tensile and flexural properties and decreased permeability and flammability [16,17]. In general, polymer/layered silicate nanocomposites are of three different types: (i) intercalated nanocomposites, for which insertion of polymer chains into a layered silicate structure occurs in a crystallographically regular fashion, with a repeat distance of a few nanometers, regardless of the polymer-to-clay ratio; (ii) intercalated nanocomposites, for which intercalated and stacked silicate layers flocculate to some extent due to the hydroxylated edge–edge interactions of the silicate layers; and (iii) exfoliated nanocomposites, for which the individual silicate layers are separated in the polymer matrix by average distances that depend only on the clay loading [17]. Lately, clay-reinforced nanocomposites based on natural polymer matrices have been attracting increased attention [18] A short review of the novel trends in polymeric nanocomposites was given very recently by Mark [19].

In all of the macro- and nanocomposites discussed above, both the matrix and the reinforcing phases exist physically before the mixing procedure. The practical importance of these systems in many technical industries is beyond any doubt. Their major shortcoming, however, is their being inherently heterogeneous. The inorganic reinforcing component, as a rule, causes a faster wear of the processing equipment, as well as some problems in recycling [20].

The interest in molecular composites is driven by the experimental fact that significant enhancement of the mechanical properties of the matrix material can be achieved only with high aspect ratio of the reinforcing elements. This ratio improves by increasing the length and/or decreasing the diameter of the reinforcements. Following this reasoning, theoretically, the ultimate reinforcement of the matrix would be reached by single, extended rigid-rod polymer molecules. However, the latter are thermodynamically immiscible with flexible-chain polymers and that is why one never reaches molecular levels of dispersion in such systems. With some approximation, the liquid crystalline polymer (LCP) – containing composites can be considered the closest example of molecular composites. By virtue of their molecular structure and conformation, the LCPs tend to form *in situ*, during processing, very fine fibers having similar or better reinforcing efficiency as compared to that of conventional inorganic fibers [21].

A substantial amount of work has been performed in the area of LCP composites [22–25]. They posses some important advantages over the conventional fiber-reinforced systems: single-step formation, e.g. during the injection molding of the part; improved mechanical integrity of the material; and very good mechanical properties. However, in these composites there is also some immiscibility of the LCPs with the thermoplastics that is difficult to control. In addition, LCP composites are very expensive: e.g. US$26–46 per kilogram as compared to US$1.65 per kilogram for glass fiber composites [26], because processing from the solution of lyotropic LCP complicates the process quite a lot. Last but not least, application of the LCP *in situ* reinforcing approach on a commercial scale requires a very well-defined set of processing conditions. Nevertheless, the anisotropy of the finished article is frequently unavoidably high. Because of all of these reasons, a real breakthrough with LCPs has never occurred [21].

Comparing all of the aforementioned macro-, nano- and molecular composites to the recently developed MFCs described initially in [27–29], one has to recognize the suppressed incompatibility and the possibilities for improved adhesion between the fiber and matrix in the latter systems. Unlike the conventional fibrous or LCP composites, the reinforcing elements in the MFCs are fibrils built of bundles of flexible, organic macromolecules. The latter are produced during processing applying appropriate mechanical and thermal treatment of the blend. These materials were initially designated as microfibrilar composites (MFCs). Since the typical diameters of the microfibrils were found to be within the upper size limit of nanocomposites (i.e. 100–1000 nm) MFCs can also be regarded as nanostructured polymer composites (NPCs). The two abbreviations are often used interchangeably [30] although MFCs/NPCs could hardly be numbered among the typical representatives of the macro- or nanocomposites [31].

With all these ideas in mind, one can consider the MFCs as a special type of *in situ* nanocomposites combining the easier processability of the conventional polymer composites with the nanosized, high aspect ratio LCP and CNT reinforcements (Figure 1.1).

1.3. Preparation of microfibrilar composites

The preparation of MFCs is quite different from that of the conventional composites, insofar as the reinforcing micro- or nanofibrils are created *in situ* during processing, as is the relaxed, isotropic thermoplastic matrix. The MFC technology can, therefore, be contrasted with the electro-spinning methods used to produce nanostructures mainly in the form of non-woven fibers with colloidal length scales, i.e. diameters mostly of tens to hundreds of nanometers {32}.

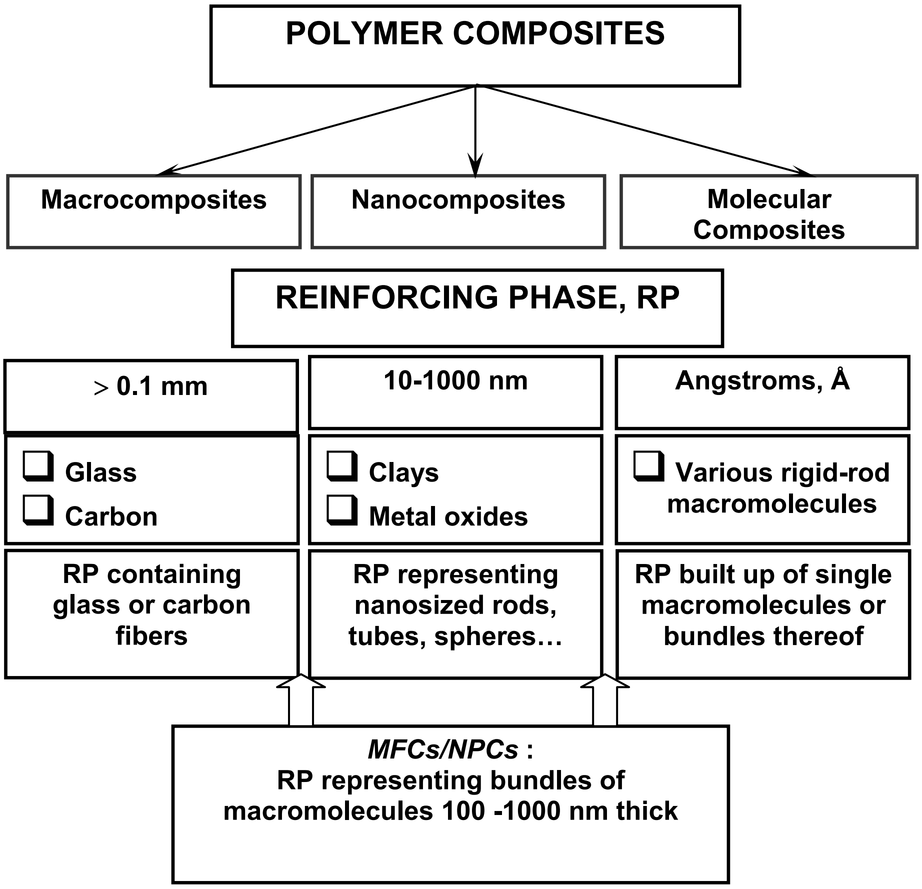

Figure 1.1 Classification of the polymer-based composite materials. In terms of RP size, MFCs/NPCs are closer to the nanocomposites; in terms of the RP morphology, they are closer to the systems with LPC reinforcements.

The preparation of MFCs comprises three basic steps [30,33]. First, *melt-blending* is performed of two or more immiscible polymers with melting temperatures (T_m) differing by 30°C or more. In the polymer blend so formed, the minor phase should always originate from the higher-melting material and the major one from the lower melting component or could even be amorphous. Second, the polymer blend is drawn at temperatures equal or slightly above the glass transition temperatures (T_g) of both components leading to their orientation (i.e. *fibrillation*). Finally, liquefaction of the lower melting component is induced thus causing a nearly complete loss of orientation of the major phase upon its solidification, which, in fact, constitutes the creation of the composite matrix. This stage is called *isotropization*. It is very important that during isotropization the temperature should be kept below T_m of the higher melting and already fibrillated component. In doing so, the oriented crystalline structure of the latter is preserved, thus forming the reinforcing elements of the MFC.

Although MFCs are based on polymer blends, they should not be considered oriented blends. It is the stage of isotropization where the latter are transformed into composite materials. Along with the loss of orientation of the matrix, depending on the chemical functionality of both reinforced and reinforcing components, chemical reactions may also take place resulting in the formation of a copolymeric interface. This interface plays the role of a compatibilizer increasing the adhesion between the matrix and the reinforcing components. If no chemical functionality is present, suppressing of incompatibility between the two materials may be achieved by adding of compatibilizing agents to strengthen the interface. This issue will be discussed in more detail in Section 1.4.3.

In the first studies on MFCs, the composites were prepared on a laboratory scale performing every one of the aforementioned three processing stages separately, one after another. Blending was realized in a laboratory mixer or a single-screw extruder to obtain non-oriented strands that were afterward cold-drawn in a machine for tensile testing, followed by annealing of the oriented strands with fixed ends [27–29,34–37]. Obviously, this discontinuous scheme is difficult to apply in large-scale production. More relevant in this case are the continuous setups developed more recently [21,38–40]. Blending of the components and extruding the initial strands could be performed in a twin-screw extruder coupled with one or more drawing devices as shown in Fig. 1.2 [38]

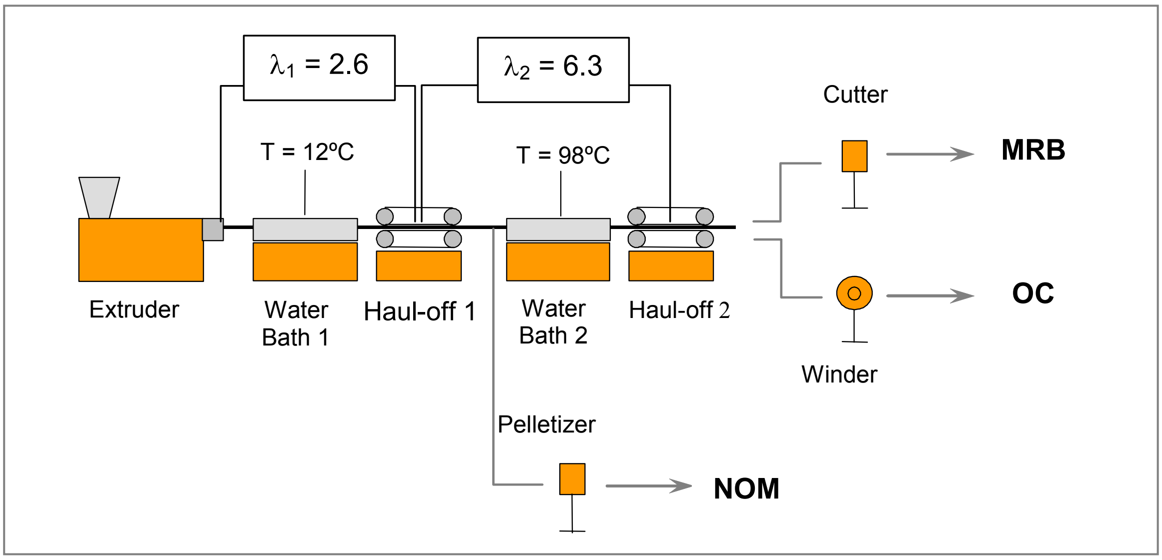

Figure 1.2 Schematic representation of the extrusion line used in [38] for preparation of MFC precursors:. λ = draw ratio.

After the extrusion blending–drawing stage, one obtains the polymer blend at the exit of the second haul-off device in the form of oriented, continuous cables (OC) (Fig. 1.2). To perform the matrix isotropization stage, these strands are further processed by compression molding at temperatures above T_m of the matrix and below T_m of the reinforcing fibrils, whereby the former melts assuming the form of the mold and embedding the bundles of oriented fibrils whose orientation and length may be varied.

As seen from Fig. 1.3, the continuous OC can be compression molded in the form of non-woven or woven fabrics (A, B) imparting different geometry of the fibrilar reinforcement (laminate plates 1 and 2). If OC are cut the resulting middle-length randomly oriented bristles (MRB), after compression molding, can produce an MFC whose matrix is reinforced by bundles of short, randomly oriented fibrils (plate 3). By compression molding of non-oriented granules (NOM) obtained by pelletizing the strand going out after the first haul-off (D), the control samples of a conventional, non-structured polymer blend are produced (plate 4), in which both matrix and reinforcement components are isotropic.

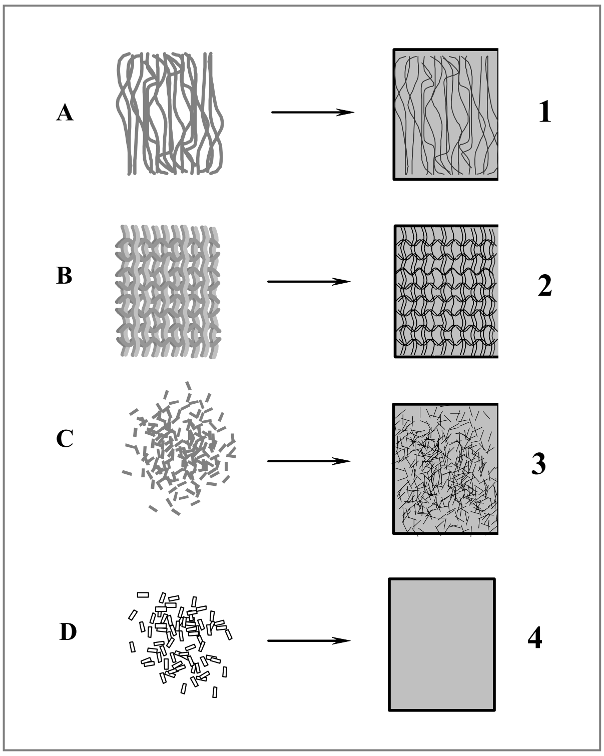

Figure 1.3 Various oriented precursors (A–D) obtained in the extruder line and the respective laminate plates (1–4) obtained after compression molding.: A - arrays of OC with parallel orientation (non-woven fabric), OC being obtained after the second haul-off unit; B - one or several sheets of interweaved OC (woven fabric); C – middle-length randomly oriented bristles (MRB) obtained after cutting of OC; D - granulated non-oriented strands obtained after the first haul-off (NOM). Plate 4 contains both matrix and reinforcing components in isotropic state and represents the control sample. The expected orientation of the bundles of reinforcing fibrils in MFCs 1–3 are shown by thin black lines [According to Ref.4].

Analyzing the examples in Figure 1.3, it can be concluded that the only method for isotropization of precursors A and B should be the compression molding (CM), while with the MRB precursor (C), one can use other molding techniques. This alternative of preparation and processing of in-situ composites was communicated for the first time by Monticciolo et al [41] and applied later on by Pesneau et al [42] and by Evstatiev et al [43] using different polymer blends. After the fibrillation of the respective blend by drawing, the oriented strands are cooled down to freeze the morphology and chopped to pellets. The latter are reprocessed by second extrusion or by injection molding (IM) at a temperature below the T_m of the dispersed fibrilar phase.

A modified method for preparation of *in situ* MFCs has been reported based on consecutive slit or rod extrusion, hot stretching and quenching [20,44–50] used to process thermoplastic polymer blends, mostly polyolefins and poly(ethylene terephthalate) (PET). It is noteworthy that the basic principle of melt extrusion, stretching and a final processing at a temperature below T_m of the reinforcing component reported for the first time by Fakirov and co-workers earlier [27] was maintained unchanged.

1.4. Structure and morphology of MFCs

1.4.1. Orientation of the matrix and reinforcement as revealed by X-ray analysis

The changes occurring in both matrix and reinforcing components during MFC preparation may be followed using different methods, of which most frequently X-ray scattering and electron microscopy are used. Figure 1.4 demonstrates the alterations in the synchrotron wide-angle X-ray scattering (WAXS) patterns reflecting the crystalline structure and orientation during the drawing/annealing cycles in two PET/polyamide 6 (PA6) blends.

The first pattern (Fig. 1.4 (a)) shows the as-drawn PET/PA6 = 50:50 blend. As expected, this pattern is oriented; however, the individual crystalline reflections of both components are not clearly resolved, most probably due to insufficient crystallinity. If the latter is increased by annealing (Fig. 1.4 (b), pattern obtained after 1 h at 200°C), the two equatorial reflections of the oriented PA6 become clearly distinguishable from the less intense point-like reflections of PET. Both components of this blend are oriented along the vertical axis of the pattern. Figure 1.4 (c) shows a pattern of the oriented blend obtained at 245°C, *i.e.* above T_m of PA6 and below T_m of PET. One can see that the point-like reflections close to the equator of the PET component have become stronger and maintain their orientation, whereas the two arcs of PA6 transform into an amorphous halo indicating the melting of the matrix material. The pattern in Fig. 1.4 (d) is of the PET/PA6 blend at 30°C after being kept for 1 h at 245°C. The matrix material has crystallized, losing its orientation almost completely, judging from the appearance of two Debye rings related to PA6. Figure 1.4(c) and (d) visualize the matrix isotropization stage and can be used for evaluation of the orientation of the components. Increasing the amount of PET to 70% (Fig. 1.4 (e)) reveals better the fact that annealing at 245°C isotropizes the PA6 matrix only and does not affect the orientation of the PET fibrils. Should the annealing temperature be set higher than T_m of PET (Fig. 4(f), 30°C after 10 min at 280°C the reinforcing component melts also and loses its orientation.

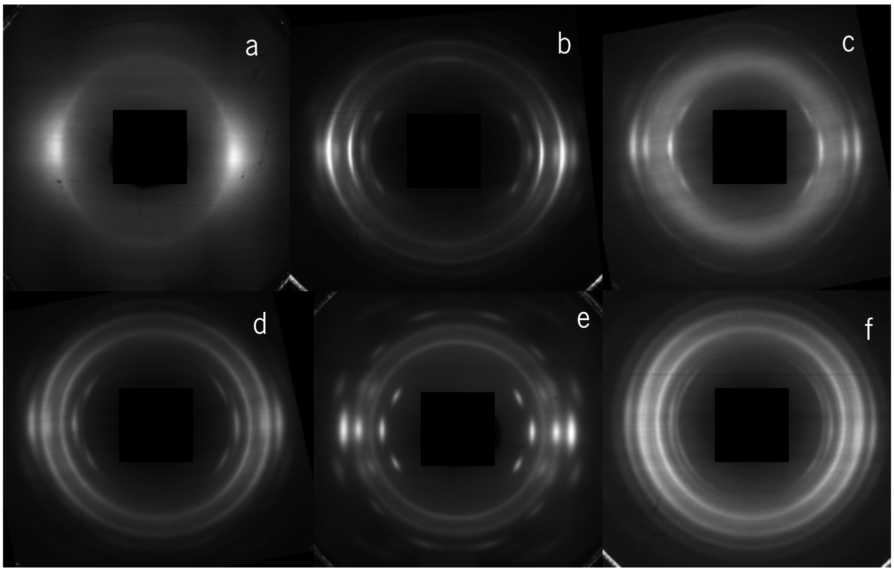

Figure 1.4 Synchrotron WAXS patterns of PET/PA6 blends at different stages of MFC preparation: (a) as-drawn blend, PET/PA6 = 50:50 (mol), pattern obtained at 30° C; (b) sample in (a) annealed for 1 h at 200°C; (c) sample in (b) at 245°C (isotropization); (d) sample in (c) cooled to 30°C; (e) heat treatment same as for (d), PET/PA6 = 70:30 (mol); (f) oriented blend (c) after heating for 30 min at 280°C, pattern obtained at 30°C. Patterns obtained at the Soft Condensed Matter beamline A2, HASYLAB-DESY, Hamburg. Conditions: sample-to-detector distance = 90 mm; detector, two-dimensional image plate perforated in the center; λ = 0.15nm. [4].

Similar WAXS patterns have been obtained by various authors with the same PET/PA6 system [27–29] and also with other MFCs of the same type, *e.g.* PET/PA66 [33], a matrix of a polyether/ester (PEE) reinforced with PET microfibrils [33], and a PET-reinforced matrix of PA12 [35,51]. In an earlier paper, Fakirov *et al.* presents an in-depth X-ray study of the orientation in various MFCs, including PET/PA6, PET/PA12, PET/PEE and poly(butylene terephthalate) (PBT)/PEE [52].

An interesting phenomenon registered during matrix isotropization in the PET/PA12 blends was some reorientation of the PA12 material accompanied by transcrystallization. Apparently, the highly oriented PET microfibrils are not only effective nuclei for transcrystallization of the matrix but are also able to cause a drastic reorientation of the matrix chains making them perpendicular to the PET orientation direction [35].

Orientation in MFCs can also be studied by small-angle X-ray scattering (SAXS) (Fig. 1.5) [53]. All patterns were obtained at the Soft Condensed Matter beamline A2, HASYLAB - DESY, Hamburg, under the following conditions: sample-to-detector distance = 2800 mm; detector, MAR CCD; λ = 0.15 nm, room temperature.

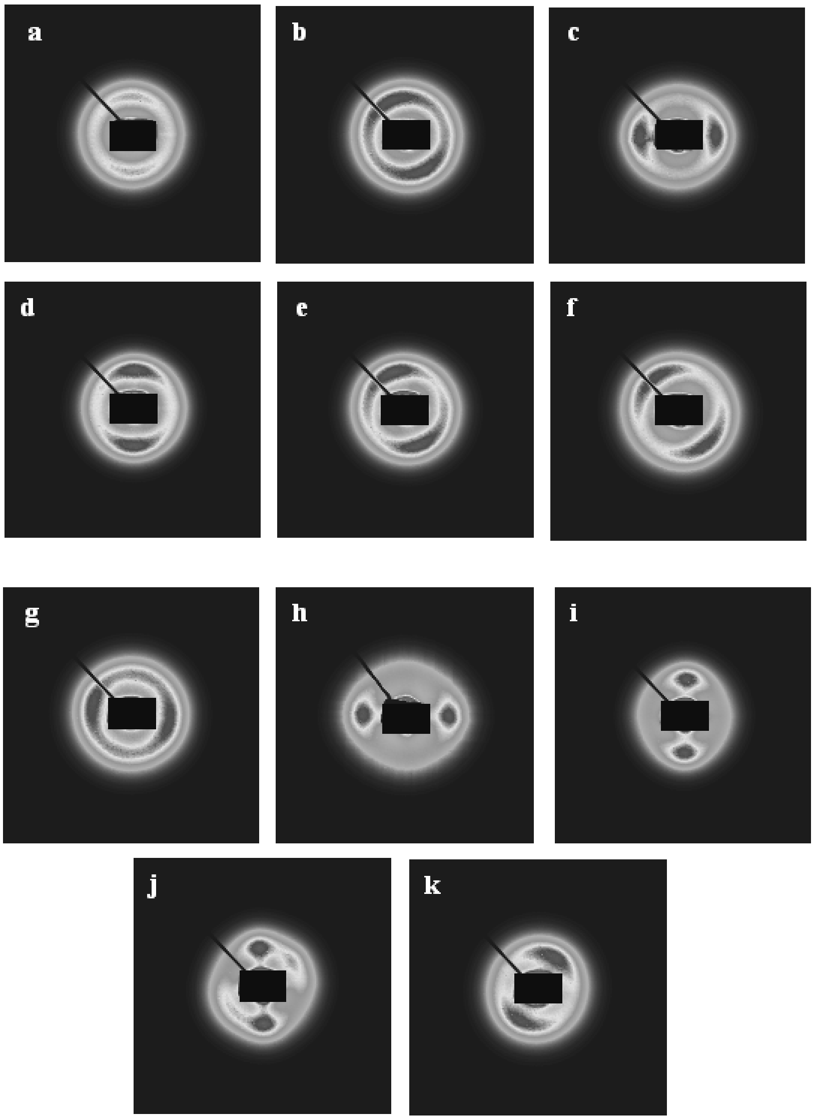

Figure 1.5 Two-dimensional SAXS patterns of film-shaped MFCs from HDPE-PA12 blends: (a) compression molded HDPE strand; (b–f) no compatibilizer; (g–k) with compatibilizer obtained by compression molding from different precursors (see also the designations in Fig. 1.2). Laminate plate 4 (b and g); laminate plate 1, fibril axes horizontal (c and h); laminate plate 1, fibril axes vertical (d and i); laminate plate 2 (e and j); laminate plate 3 (f and k) [53]

From Fig. 1.5 one may see the SAXS patterns of some HDPE/PA12 composites with different expected orientations of the PA12 reinforcing fibrils, e.g. patterns in Figs 1.5 (c)–(f), (h)–(k). The patterns contain some oriented arc- or point-like spots related to the scattering of the PA12 reinforcing elements, and circular or oval distribution of the scattered intensity attributable to the isotropic high density polyethylene (HDPE) matrix thus allowing for the evaluation of the orientation.

Analogously, in a previous SAXS study on drawn, non-compatibilized HDPE/PET blends [54], analyzing the corresponding oriented two-dimensional SAXS patterns enabled the conclusion to be drawn that the matrix and reinforcing components respond independently to the external stress.

1.4.2. Morphology of the matrix and reinforcement components as revealed by microscopy

The first extensive Scanning Electron Microscopy (SEM) investigation of PET/PA6- based MFCs and their precursors performed by Evstatiev *et al* [55] undoubtedly showed the fibrilar structure of the PET reinforcements preserved after the PA6 matrix isotropization. Since then, electron microscopy has been used to visualize the orientation and morphology of the matrix and reinforcing components in almost every report on MFCs. It is worth noting some more recent studies on MFCs comprising low-density polyethylene (LDPE) and PET as matrix and reinforcement, respectively [39,56]. Several microscopic techniques were used, *e.g.* SEM, polarized light microscopy (PLM) and transmission electron microscopy (TEM). Thus, by SEM it was demonstrated that the isotropic LDPE matrix embedded PET microfibrils with random orientation. PLM and TEM of thin slices showed the orientation in the machine direction. The latter method revealed also the formation of transcrystalline layers of LDPE on the oriented PET microfibrils. Similar investigations were performed by Li *et al.* [45] by means of SEM and AFM. As seen from Fig. 1.6, the authors visualized the transcrystalline morphology of PET/isotactic poly-propylene (iPP) MFCs. On this basis, a shish-kebab model was proposed. Microfibrils containing blends of polycarbonate (PC) and HDPE were also produced and characterized by SEM thus proving the presence of PC fibrils in the polyolefin matrix [57].

The SEM results shown in Fig. 1.7 demonstrate the morphology changes along the extruder line in Fig. 1.2, i.e. during the melt blending and fibrillation stages of a HDPE/PA12 blend (80:20 wt%) [38]. Comparing Fig. 1.7 (a) with the sample obtained immediately after the die and 1.7 (b) (sample taken at the first haul-off unit) evidences a decrease in size of the polyamide droplets, the reduction in their diameters being about 50%. This effect can be attributed to some axial orientation of the blend components starting right after the die end by the action of the first haul-off unit. Figure 1.7 (c) shows an oriented strand of the same blend in which the HDPE matrix material was selectively extracted. This sample was collected after the second drawing stage, the draw ratio λ between the two haul-off units being close to 7. It contains bundles of long polyamide fibrils with an average diameter of *ca* 200 nm embedded in the selectively removed HDPE matrix, proving the formation of the PA12 reinforcing elements in the stage of cold drawing.

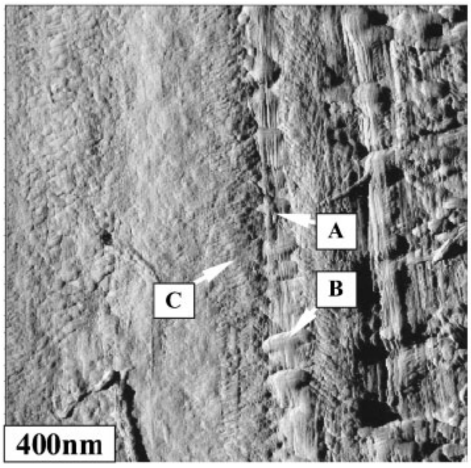

Figure 1.6 AFM phase image of the cryogenic cut surfaces of an as-stretched microfibrilar PET/iPP (15/85 by weight) MFC showing the transcrystalline layers and the shish-kebab structure: A, the shish of iPP; B, the kebab of iPP induced by iPP shish; C, the kebab of iPP induced by PET microfibrils [45].

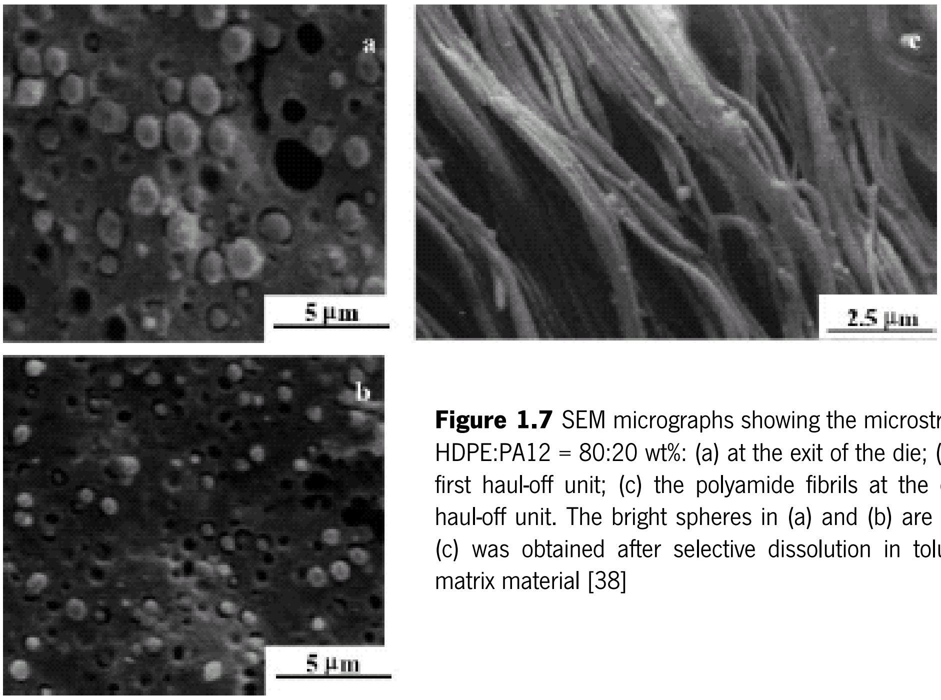

Figure 1.7 SEM micrographs showing the microstructure of the blend HDPE:PA12 = 80:20 wt%: (a) at the exit of the die; (b) at the exit of the first haul-off unit; (c) the polyamide fibrils at the end of the second haul-off unit. The bright spheres in (a) and (b) are the PA12 droplets; (c) was obtained after selective dissolution in toluene of the HDPE matrix material [38]

Some PLM and SEM images of the corresponding HDPE/PA12 MFC films obtained after compression molding of longitudinally placed oriented strands (Fig. 1.2, A and 1) are presented in Fig. 1.8. As seen from the PLM micrograph in Fig. 1.8 (a) taken at 130°C, the PA12 fibrils are crystalline (bright) at this temperature and are concentrated in the middle ('core') zone. They remain oriented in the longitudinal direction, while in the 'shell', *i.e.* closer to the sample surface, there seem to be a higher concentration of the matrix (HDPE) material being molten at this temperature. The SEM images in Fig 1.8 (b) –(d) give more details of the morphology of the core and shell zones. The images in Fig 1.8 (b) and (c) evidence the longitudinal alignment of the PA12 fibrils in the core, as suggested by the PLM image. At the same time, the shell zone is characterized by a more disordered distribution of thicker fibrils (Fig. 1.8 (d)). Furthermore, as seen from the comparison between the non-compatibilized and compatibilized MFCs (images in Fig 1.8 (b) and (c), respectively), in the first case the fibrils are poorly linked to the HDPE matrix while in the second the reinforcing elements are tightly embedded within the matrix.

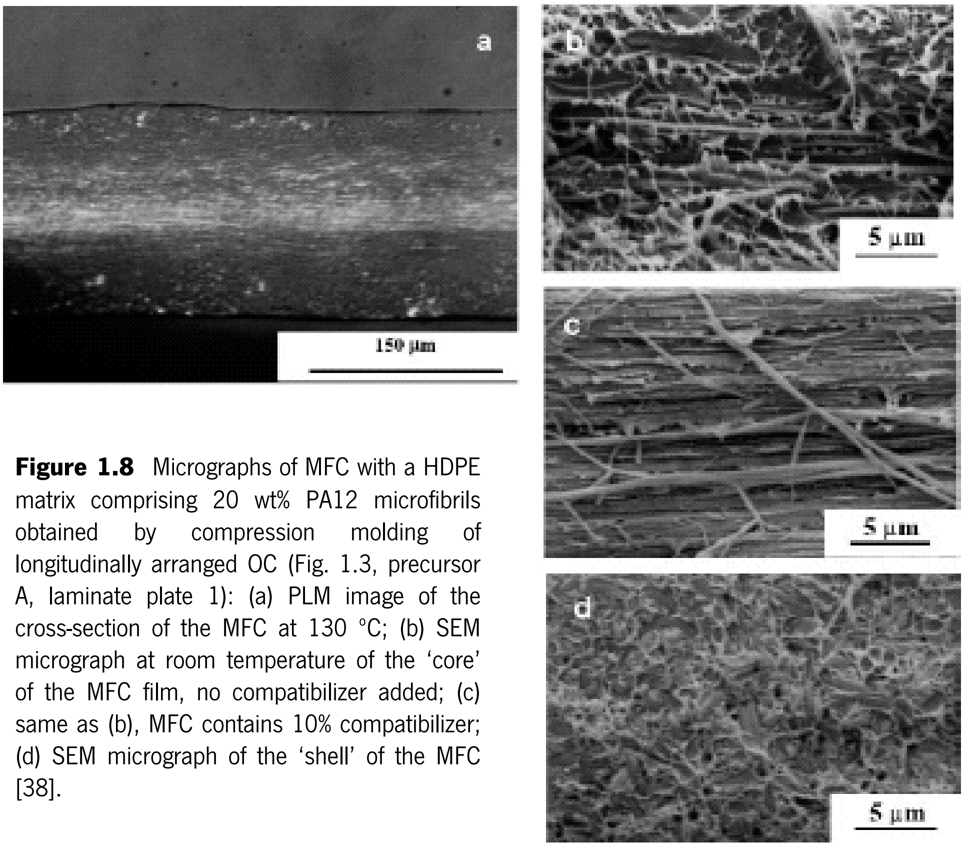

Figure 1.8 Micrographs of MFC with a HDPE matrix comprising 20 wt% PA12 microfibrils obtained by compression molding of longitudinally arranged OC (Fig. 1.3, precursor A, laminate plate 1): (a) PLM image of the cross-section of the MFC at 130 °C; (b) SEM micrograph at room temperature of the 'core' of the MFC film, no compatibilizer added; (c) same as (b), MFC contains 10% compatibilizer; (d) SEM micrograph of the 'shell' of the MFC [38].

SEM micrographs very similar to 1.7 (c) and 1.8 (c) were obtained by Boyaud et al with various MFC-like systems reinforced by PBT fibers [58, 59].

1.4.3 Strengthening the matrix–reinforcing fibrils interface

There are two basic ways to manipulate the adhesion at the phase boundary in MFCs: by chemical interactions or through the formation of transcrystalline layers, which can be considered a physical interaction. We already mentioned some cases of transcrystalline morphology in various types of MFCs that were registered in the absence [39,45] or in the presence [36] of chemical bonding between the matrix and reinforcing components. Basically, when the chemical structure allows it, physical and chemical interactions between the matrix and fibrils may occur at the same time.

As briefly mentioned above, adhesion between the two components of the MFCs are expected to play an important role in their mechanical properties. Polymer blends are, as a rule, thermodynamically immiscible, i.e. inhomogeneous down to molecular level and therefore inclined to phase-separate. Nevertheless, most polymer blends may have some practical compatibility between the components, obtainable by chemical reactions between the latter or by introduction of a third component, called a compatibilizer [2].

MFCs prepared from a mixture of condensation polymers, e.g. PET/PA, PET/PC, PET/PEE, etc., are capable of self-compatibilization due to the so-called *interchange reactions* occurring between functional groups belonging to the matrix and reinforcements at their interface [60]. As a result, block copolymers are formed extending across the interface thus linking the two MFC components chemically. In-depth studies on the interchange reactions in various blends of polycondensates and on the structure of the resulting copolymers have been performed, e.g. in PET/PA6 [61] and PET/PC [62] blends, as well as in some other MFC precursors based on polycaprolactone/poly(2,2-dimethyltrimethylene carbonate) blends with possible medical applications [63]. More details about the chemical interactions in a great variety of blends of polycondensates, can be found in the reference literature [64,65]. In summary, the concrete nature of the interchange reactions depend on the chemical composition of the matrix and reinforcing materials and can occur as a polyesterification, polyamidation or ester–ester interchange requiring the typical conditions and catalysts for these specific reactions.

In polyolefin-containing MFCs, the matrix does not possess the necessary chemical functionality so as to be bonded chemically to the polyester or polyamide reinforcing component; therefore introduction of a compatibilizer is required. In the specific case of HDPE/PA12 MFCs, a good compatibilization effect was obtained with a HDPE–maleic anhydride (MAH) copolymer commercially available from DSM under the trade name Yparex [38].

The mechanism of reaction between the MA units of Yparex and the PA component was elucidated earlier by van Duin et al [66] and Thomas et al [67]. A schematic representation of the compatibilization reactions at the HDPE/PA12 interface is shown in Fig. 1.9.

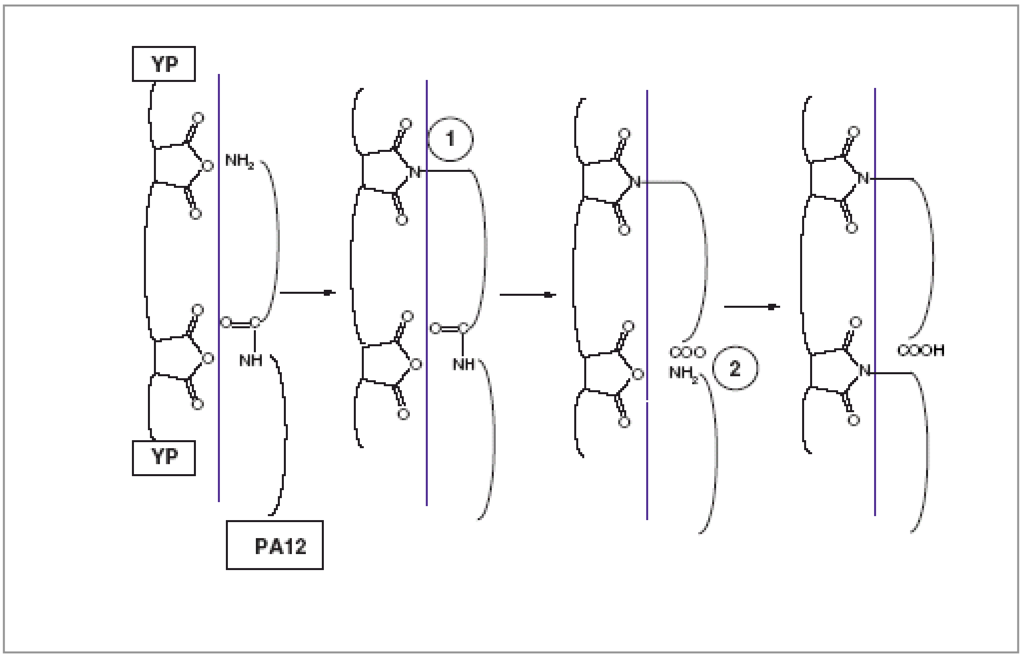

Figure 1.9 Graft copolymer formation between PA12 and YP according to [66]: 1, imide linkage across the interface; 2, chain scission in the PA molecule

The coupling between the PA and MAH copolymer occurs via an imide linkage (1) and is accompanied by PA degradation by main-chain scission (2). The copolymers so formed – PA12 branches grafted on a stem of Yparex – act like an anchor joining the HDPE and PA domains. It is noteworthy that the said chemical interactions are basically realized during the blend mixing. During the fibrillation step, in the compatibilized HDPE/PA blend, the two components deform simultaneously because of their being chemically linked. This results in a lack of defects at the phase boundary (Fig. 1.8 (c)). In the absence of compatibilizer, the two materials deform independently due to their different mechanical properties, which damages the matrix close to the interface by the formation of voids and cracks, being transferred to the final MFC.

Filippi *et al.* [68] described another compatibilizer for polyolefin/polyamide blends based on ethylene–acrylic acid copolymers. In the case of polyester-containing blends, again MA-containing compatibilizers similar to Yparex could be applied, as well as some ethylene–glycidyl methacrylate copolymers [69]. There, the compatibilization principle remains the same, although the concrete chemistry is not clarified in such detail.

Concluding the discussion on the structure- properties relationship in MFCs and in their precursors, one has to mention some additional analytical methods used for their investigation that are related to the mechanical properties. Dynamic mechanical thermal analysis (DMTA) was employed for PET/PA6 composites focusing mainly on the changes in the amorphous phase [70]. This method enables one to distinguish the effects of self-compatibilization of the blend during the various stages of MFC preparation. Interestingly enough, drawing of the PET/PA6 blend induces some measurable compatibilization effect. Annealing below 220°C results in reorganization of the PET and PA6 homopolymers within distinct phases, thus revealing the inherent immiscibility of this blend. Only prolonged heat treatment above this temperature results in compatibilization at the interface. DMTA investigations of a LDPE/PET system [43] by three-point bending in the −20 to +100°C range demonstrated that the MFCs displayed complex modulus E^* values more than 10 times higher than those of neat LDPE. In addition, the E^* values obtained in dynamical mode were quite close to the values of the Young's modulus E measured in static conditions demonstrating in a fine way the reinforcing effect of the microfibrils in MFCs.

Microhardness measurements are an additional possibility for monitoring the structure development in PET/PA6 blends during their transformation into MFC. [71,72] The results obtained showed a linear correlation of the elastic modulus anisotropy and the microindentation hardness anisotropy in all oriented samples studied. Moreover, the indentation modulus values in the blends followed the parallel additivity model of the individual components. The use of the additivity law led to the determination of the modulus of the PET microfibrils within the MFC, otherwise inaccessible from direct measurements.

1.5. Mechanical properties of MFCs

Because of the high aspect ratio of the crystalline and oriented microfibrilar reinforcement, and in view of the various possibilities to strengthen the matrix–fibril interface, the mechanical properties of MFCs are expected to be superior as compared to those of the corresponding neat matrix material. Most frequently, the following mechanical parameters are studied: the Young's modulus, E, the tensile strength, σ, and the ultimate strain ε [30]. Sometimes, the flexural properties (i.e. flexural modulus, strength and deflection) are also considered [40]. Comparison is frequently made between the said mechanical characteristics of various MFCs, on the one hand, and of the neat matrix material (sometimes reinforced by glass spheres (GS) or glass fibers (GF)), on the other.

1.5.1 Mechanical properties of MFCs capable of self-compatibilization

MFCs based on self-compatibilizing mixtures of PA6 (matrix) and PET, PBT or PA66 as reinforcement component, taken in various weight ratios, show a drastic increase of σ and E values after drawing of the extrudate. The values reach those of the reinforcing component, e.g. PET, PBT or PA66, when in the drawn state [30,73]. Subsequent isotropization by CM or IM results in either a slight (for E) or strong (for σ) decrease. However, the properties of the MFC are still undoubtedly better than those of the neat matrix and about the same or slightly better than those of the GF-reinforced polyamide (PA6 + 30% GF). The values of the MFCs are by 30–40% higher than the rule-of-mixture values calculated from the properties of the individual components, e.g. isotropic PA6 and drawn PET [74]. This indicates a mechanical property profile with a clear synergistic effect.

It is important to note that the mechanical properties of PET/PA6 composites are highly dependent on the way the isotropization was achieved: by IM or CM. Table 1 compares the tensile moduli and the tensile strengths of various PET/PA6 MFCs obtained by these two techniques as compared with those of the pure or reinforced PA6 matrix [21].

Table 1.1 Static mechanical properties of MFCs and neat materials [21]

Sample	**Injection molding**		**Compression molding**	
Composition (by weight)	***E*** (GPa)	***σ*** (MPa)	***E*** (GPa)	***σ*** (MPa)
PA6, 100 %	1.2	40	1.0	30
70% PA6 + 30% GF	5.1	71	4.4	60
MFC PET/PA6 = 30:70%	3.2	60	-	-
MFC PET/PA6 = 50:50%	3.6	62	4.15[a] ; 4.8[b]	63[a]; 110[b]

Notes: a) Cross-ply from three laminate layers, one being perpendicular to the other two;
b) From three parallel laminate layers.

Apparently, in both IM and CM cases, the MFCs show a major improvement of the mechanical performance as compared to that of the pure PA6 matrix. Depending on the mode of oriented blend isotropization, the values of the MFCs could be comparable to or even higher than those of the GF-reinforced matrix. The notable differences in the E and σ values for IM and CM methods are apparently related to the different morphology of the PET/PA6 MFCs. The CM approach allows one, in contrast to IM, to stay accurately within the necessary processing temperature window so as to preserve during the isotropization stage the microfibrilar morphology of PET [21]

1.5.2 Mechanical properties of MFCs incapable of self-compatibilization

There is no doubt that the IM technique is more versatile in terms of large-scale industrial application. One of the possible ways to broaden the processing temperature window of injection is to select matrix and reinforcing materials with larger differences in T_m . Among the best candidates for such materials are polyesters (mostly recycled PET originating from the packaging industry) and polyamides, on the one hand, and large-scale commodity polyolefins, also recycled or virgin, on the other.

The MFCs obtained from PET/LDPE blends by IM showed impressive mechanical properties. The elastic modulus was reportedly several times higher than that of LDPE and about three times higher than that of LDPE reinforced with GF, approaching the values of LDPE + 30% GF. The tensile strength was at least two times higher than that of the neat matrix material; the impact strength of the PET/LDPE MFC is 50% higher [39].

Other interesting MFC materials can be produced from PET/PP oriented blends with various PET contents by means of IM or CM [40]. In this study the authors also evaluated the role of the compatibilizer. Thus, the flexural modulus (FM) and the flexural strength (FS) of the IM samples are 50% better than those of the neat PP without expressing any clear effect of the amount of compatibilizer in the blend (Table 2). This was different from the CM samples transforming polymer blends into composites in which both FM and FS increase with an increase of the compatibilizer content. It is noteworthy that the impact energy of the MFC specimens obtained by CM is slightly higher than that of the glass-fiber-reinforced PP and 3–4 times higher than that of the neat PP. From the data in Table 2 it becomes clear that also for the PET/PP MFCs the CM approach results in better mechanics as compared to IM.

The tribological properties of polycondensate/polyolefin-based MFCs were also studied [75]. The authors concluded that the wear rates of MFCs isotropized by IM are from two to three times higher than those of CM ones. The explanation was related to the orientation of the reinforcements: very good in the CM-processed MFCs and almost random in the IM ones.

Table 2 Static mechanical properties of MFCs and neat materials [40]

Sample composition (by weight)	Injection molding			Compression molding		
	FM (GPa)	FS (MPa)	IE (kJ/m^{-2})	FM (GPa)	FS (MPa)	IE (kJ/m^{-2})
PP, 100 %	1.2	38	2.7	1.2	40	2.4
PP + GF = 70:30	3.6	100	7.2	3.3	96	7.5
MFC PET/PP/EGM = 40:60:0	2.0	42	1.5	3.0	90	7.8
MFC PET/PP/EGM = 40:57:3	1.8	55	2.8	4.0	102	8.0
MFC PET/PP/EGM = 40:51:9	1.5	46	2.2	4.2	110	6.2

Notes: FM = flexural modulus; FS = flexural strength; IE = impact energy; EGM = ethylene–co-glycidyl methacrylate compatibilizer..

These results were obtained by means of a flat-on-ring configuration. The pin-on-disc test was found to be unsuitable for the compression molded MFCs. Moreover, PA66 was found to lead to higher wear resistance in comparison to PET in MFCs with the same matrix material.

The study of Li *et al.* [76] demonstrates the influence of the hot stretch ratio on the essential work of fracture W_e, i.e. that component of the total work of fracture, W_f, that is a function of the stressed area. The authors found out that in a HDPE/PET MFC with a fixed weight composition of 85:15, the maximum of W_e appears at a hot stretch ratio of 25 after which it drops slightly.

CM specimens produced from the same HDPE/PET MFC system in a weight composition of 1:1 with various amounts of compatibilizer were studied by Fasce *et al.* [77]. The authors observed significant improvement of the mechanical properties, particularly the elongation at break and the fracture toughness when fibrillation of PET in the HDPE matrix was achieved under appropriate extrusion conditions, the optimum amount of the compatibilizer being 7%. It should be noted here that the mechanical properties profile is clearly worse than in the case of the LDPE/PET MFC system. Most probably the reason could be related to the absence of a stage of strong uniaxial orientation of the blend by cold or hot drawing and therefore a low aspect ratio of the reinforcements.

In an attempt to explain better the mechanical properties of MFCs and to enable their theoretical prediction, Fuchs *et al.* [78] tested the extent of the validity of the Tsai–Hill equation applied to MFCs, in which the reinforcing elements represent microfibrils with diameters around 1 μm and aspect ratios of approximately 100. The commonly used Tsai–Hill equation has the following form:

$$\sigma_x = \left[\frac{\cos^2\phi(\cos^2\phi - \sin^2\phi)}{X^2} + \frac{\sin^4\phi}{Y^2} + \frac{\cos^2\phi\sin^2\phi}{S^2} \right]^{-\frac{1}{2}} \tag{1.1}$$

wherein σ_x is the tensile strength at a given angle ϕ; X and Y are the tensile strengths in the fiber and transverse directions, respectively, S is the shear strength and ϕ is the off-axis test angle. Compression-molded plates of PP/PET MFC were prepared and their structures were established by WAXS and SEM analyses. The tensile tests of cut specimens at various angles with respect to the uniaxially aligned microfibrils showed the degree of agreement with the predictions of Eq (1). The measured values were slightly higher than the calculated ones and this finding was explained by the higher aspect ratios of microfibrils, their more homogenous distribution and, most importantly, by the better matrix–reinforcement adhesion in the case of MFCs as compared to the common composites. The fracture mechanism as determined from the SEM observations of the fracture surfaces was also discussed and a good agreement with the mechanical behavior was found.

In the future the MFC technology will, most probably, be extended to some high-performance special plastics. One of them is poly(phenylene sulfide) (PPS) that has already been used as the reinforcing component in PP/PPS-based MFCs, both materials being recycled [79]. Evstatiev *et al.* used PPS as a matrix, which was reinforced by a LCP in the presence of a compatibilizer [80] thus opening the way for new group of hybrid composite materials. Another example of hybrids with a fibrillar microstructure of the reinforcing component are the MFCs based on a PET-reinforced HDPE matrix filled with carbon black thus producing materials potentially useful as new conductive polymer composites [81,82].

A further development of the MFC concept is the loading of microfibrils by carbon nanotubes. In such a way a double reinforcing effect is realized: reinforcement of the reinforcing material. In addition, one obtains electroconductive materials with good shielding properties. Isolation of microfibrils via selective dissolution of the matrix component offers the potential for their biomedical applications as scaffolds for regenerative medicine or in controlled drug delivery or as nanofilter materials [83].

1.6. Research goals and structure of the thesis

From the literature survey it can be inferred that, in general, the MFC technology combines the strong points of conventional fibrous composites, the LCP and nanoclay - reinforced polymer systems, avoiding some of their most important limitations. Hence, the MFCs are materials with controlled heterogeneity obtainable by conventional processing techniques such as extrusion, compression molding or injection molding, with no agglomeration of the reinforcing phase.

Among the numerous polymers that are reportedly used for matrices of MFC, the high density polyethylene (HDPE) deserves special attention because it is a polymer of major production scale and importance, with very good mechanical properties and relatively low melting temperature. Therefore, it is very suitable as matrix material in the MFC technology. A number of studies are dedicated to MFCs based on HDPE matrices, most frequently reinforced by PET. The reinforcing effect of polyamides in HDPE-containing MFCs was insufficiently investigated. At the time this work started, there were only few studies reporting of HDPE/PA12 MFCs and no reports on HDPE/PA6 MFCs. Having in mind that PA6 and PA12 are materials with excellent mechanical properties, semicrystalline, with relatively high melting temperatures and capable of chemical interactions with HDPE in the presence of suitable compatibilizers, it was decided to work in the field of MFCs based on HDPE matrix reinforced by PA12 or PA6, using as compatibilizer a commercial polymer of maleic anhydride grafted polyethylene (Yparex, of DSM).

The research program passed through the following stages.

- Preliminary study of the structure and mechanical properties of oriented PA12 and PA6 under different processing and annealing conditions;
- Preparation of highly oriented precursors from HDPE/PA/Yparex blends by extrusion, varying the type of PA and composition of the blend;
- Preparation of MFCs with an isotropic matrix by compression molding varying the length and alignment of the oriented precursors;

- Characterization of the mechanical behavior of the MFCs for studying the influence of the blend composition, fibril geometry and alignment on the properties;
- Study of the morphology and structure of the MFCs for establishing the composition-structure-properties relationship.

With all these ideas in mind, the structure of this thesis can be summarized as follows:

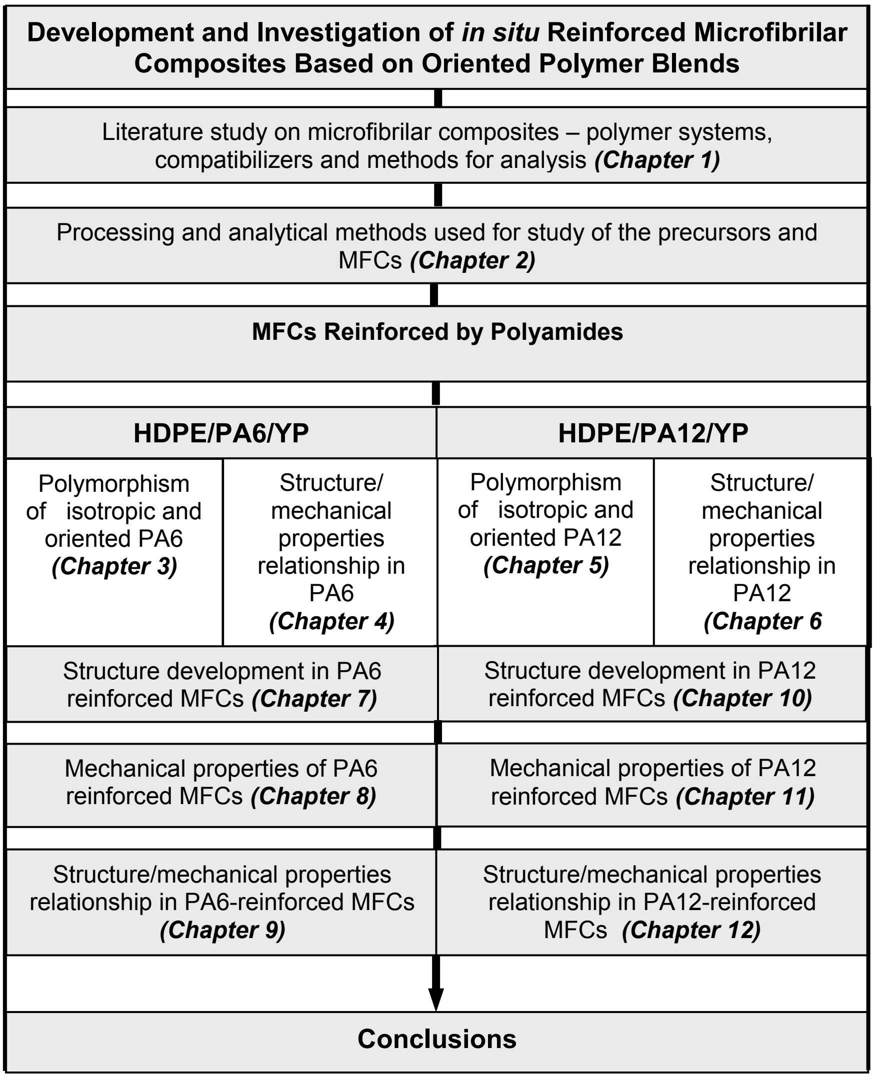

Figure 1.10 The structure of this thesis

1.7. References

1. Hull D, Introduction to Composite Materials, Cambridge University Press, Cambridge, p. 3 (1987).
2. Utracki LA, Polymer Alloys and Blends, Hanser Publishers, Munich, Vienna, New York, p. 43 (1989).
3. Paul DR and Bucknall CB, Polymer Blends, J. Wiley and Sons, Inc., New York, pp.502-537 (2000).
4. Denchev Z, and Dencheva N, *Polym Int*, published online April 3, 2007, DOI 10.1002/pi.2283
5. Hassan A, Yahya R, Yahya AH, Tahir ARM and Hornsby PR, *J Reinf Plast Comp* 23:969 (2004).
6. Vina V, Castrillo MA, Arguelles A. and Vina I, *Polym Comp* 23:619 (2002).
7. Pradas MM, Schaber G, Ribelles JLG and Colomer FR, *Macromolecules* 30:3612 (1997).
8. Sugun BS and Rao RMVGK, *J Reinf Plast Comp* 23:1583 (2004).
9. Jang BZ, *Comp Sci Techn* 44:333 (1992).
10. Terrones M, *Annu Rev Mater Res* 33:419 (2003).
11. Treacy M, Ebbesen TW and Gibson JM, *Nature* 381:678 (1996).
12. Wong EW, Sheehan PE and Lieber CM, *Science* 277:1971 (1997).
13. Falvo MR, Clary GJ, Taylor II RM, Chi V, Brooks FP Jr, et al. *Nature* 389:582 (1997)
14. Usuki A, Kojima Y, Kawasumi M, Okada A, Fukushima Y, Kurauchi T, et al. *J Mater Res* 8:1179 (1993).
15. Yano K, Usuki A, Okada A, Kurauchi T, Kamigaito O. *J Polym Sci Part A: Polym Chem* 31:2493 (1993).
16. Giannelis EP, *Appl Organomet Chem* 12:675 (1998).
17. Ray SS, Okamoto M, *Prog Polym Sci* 28:1539 (2003).
18. Yua L, Deana K, Lib L, *Prog Polym Sci* 31:576 (2006)
19. Mark J, Some Novel Polymeric Composites, *Acc Chem Res* (2006), published on Web 10/16/2006 (DOI: 10.1021/ar040062k).

20. Li ZM, Yang W, Li LB, Xie BH, Huang R and Yang MB, *J Polym Sci Part B: Polym Phys* 42:374 (2004).

21. Evstatiev M, Fakirov S, Bechtold G and Friedrich K, *Adv Polym Techn* 19: 249 (2000).

22. Chakraborty S, Sahoo NG, Jana GK, and Das CK, *J Appl Polym Sci* 93:711 (2004).

23. Tjong SC, *Mat Sci Eng Rep* 41:1 (2003).

24. Song CH and Isayev AI, *Polymer* 42:2611 (2001).

25. Handlos AA and Baird DG, *Int Polym Proc*11:82 (1996).

26. Baird DG and McLeod MA, Liquid crystalline polymer blends, in: *Polymer Blends, Vol. 2 Performance*, ed by Paul DR and Bucknall CB, J. Wiley and Sons, Inc., New York, p. 429-454 (2000).

27. Evstatiev M and Fakirov S, *Polymer* 33:877 (1992).

28. Fakirov S, Evstatiev M and Schultz JM, *Polymer* 34, 4669 (1993).

29. Fakirov S, Evstatiev M and Petrovich S, *Macromolecules* 26:5219 (1993).

30. Fakirov S, Evstatiev M and Friedrich K, Nanostructured Polymer Composites from Polymer Blends: Morphology and Mechanical Properties, in: *Handbook of Thermoplastic Polyesters*, ed by Fakirov S, Wiley-VCH, Weinheim, pp. 1093-1132 (2002).

31. Newnham RE and Giniewicz JR, Non-mechanical Properties of Composites, in: *Comprehensive Composite Materials, Vol. 1. Fiber Reinforcements and General Theory of Composites*, ed by Kelly A and Zweben C, Elsevier, Amsterdam, pp. 431-463 (2000).

32. Burger C, Hsiao BS, and Chu B, *Annu Rev Mater Res* 36:333–68 (2006).

33. Fakirov S, Evstatiev M and Friedrich K, From Polymer Blends to Microfibirllar Reinforced Composites, in: *Polymer Blends, Vol. 11, Formation and Preparation,* ed by Paul DR, Bucknall CB, J. Wiley and Sons, Inc., New York, p. 455-476 (2000).

34. Apostolov AA, Evstatiev M, Fakirov S, Kloczkowski A and Mark JE, *J Appl Polym Sci* 59:1667 (1996).

35. Evstatiev M, Schulz JM, Georgiev G, Petrovich S, Fakirov S and Friedrich K, *J Appl Polym Sci.* 67:723 (1998).

36. Sapoundjieva D, Denchev Z, Evstatiev M, Fakirov S, Stribeck N and Stamm M, *J Mater Sci* 34:3063 (1999).
37. Fakirov S and Evstatiev M, *Adv Mat* 6:395 (1994).
38. Denchev Z, Oliveira MJ and Carneiro OS, *J Macromol Sci – Phys*, B43:143 (2004).
39. Fakirov S, Kamo H, Estatiev M and Friedrich K. *J Macromol Sci – Phys* B43:775 (2004).
40. Friedrich K, Evstatiev M, Fakirov S, Evstatiev O, Ishii M Harras M, *Comp Sci Techn* 65:107 (2005).
41. Monticciolo A, Cassagnau P, Michel A, *Polym Eng Sci* 38:1882 (1998).
42. Pesneau I, Ait-Kadi A, Bousmina M, Cassagnau P, Michel A, *ANTEC 99, New York*, May 2-6 1999; 2661.
43. Evstatiev M, Fakirov S, Krasteva B, Friedrich K, Covas JA and Cunha AM, 2002, *Polym Eng Sci* 42:826 (2002).
44. Li ZM, Li LB, Shen KZ, Yang MB and Huang R, *Polymer* 46:5358 (2005).
45. Li ZM, Li BL, Shen KZ, Yang W, Huang R and Yang MB, *Macromol Rapid Commun* 25:553 (2004).
46. Li A, Lu ZY, Shen KZ, Li LB and Yang MB, *J. Macromol. Sci. – Phys* B44:203 (2005).
47. Wan HQ, Ji X, *J Mater Sci* 39:6839 (2004).
48. Li ZM, Li LB, Shen KZ, Yang MB, Huang R, *J Polym Sci Part B: Polym Phys* 42:4095 (2004).
49. Lin XD, Jia D, Leung FKP and Cheung WL, *J Appl Polym Sci* 93:1989 (2004).
50. Taepaiboon P, Junkasem J, Dangtungee R, Amornsakchai T, Supaphol P, *J. Appl Polym Sci*, 102:1173 (2006).
51. Sarkissova M, Harrats C, Groeninckx G and Tomas S, *Composites Part A: Appl Sci and Manuf* 35:489 (2004).
52. Fakirov S, Stribeck N, Apostolov AA., Denchev Z, Krasteva B, Evstatiev M and Friedrich K. *J. Macromol Sci – Phys* B40:935 (2001).
53. Denchev Z, Oliveira MJ, Mano JF, Viana JC, and Funari SS, *J Macromol Sci – Phys* B43:163 (2004).

54. Fakirov S, Samokovlijski O, Stribeck N, Apostolov AA, Denchev Z, Sapoundjieva D, Evstatiev M, Meyer A and Stamm M, *Macromolecules* 34:3314 (2001).

55. Evstatiev M, Nikolov N and Fakirov S, *Polymer* 37:4455 (1996).

56. Friedrich K, Ueda E, Kamo H, Evstatiev M, Krasteva B and Fakirov S, *J Mater Sci* 37: 4299 (2002).

57. Xu HS, Li ZM, Yang SY, Pan JL, Yang W and Yang MB, *Polymer Eng Sci* 45:1231 (2005).

58. Boyaud MF, Ait-Kadi A, Bousmina M, Michel A, Cassagnau P, *Polymer* 42:6515 (2001).

59. Boyaud MF, Cassagnau P, Michel A, Bousmina M, Ait-Kadi A, *Polym Eng Sci* 41 :684 (2001)

60. Denchev Z, Evstatiev M, Fakirov S, Friedrich K and Pollio M, *Adv Comp Mater* 7:313 (1998).

61. Denchev Z, Kricheldorf HR, Fakirov S, *Macromol Chem Phys* 202:574 (2001).

62. Denchev Z, DuChesne A, Stamm M and Fakirov S, *J Appl Polym Sci* 68:429 (1998).

63. Denchev Z, Bojkova A, DuChesne A, Höcker H, Keul H and Fakirov S, *Macromol Chem Phys* 199:2153 (1998).

64. Kricheldorf HR and Denchev Z, Chemistry of Transreactions in Condensation polymers - kinetics, mechanisms and peculiarities, in: *Transreactions in condensation polymers*, ed by S. Fakirov, Wiley-VCH, Weinheim, pp. 1-78 (1999).

65. Denchev Z, Chemical Interactions in Blends of Condensation Polymers Involving Polyesters, in: *Handbook of Thermoplastic Polyesters: PET, PBT, PEN - Homopolymers, Copolymers, Blends and Composites*, ed by Fakirov S, Wiley-VCH, Weinheim, 757-808 (2002).

66. van Duin M, Aussems M and Borggreve RGM, *J Polym Sci Part A: Polym Chem* 26:179 (1999).

67. Thomas S and Groeninckx G, *Polymer* 40:5799 (1999).

68. Filippi S, Chiomo V, Polacco J, Paci M, Minkova MI and Magagnini P, *Macromol Chem Phys* 203:1512 (2002).

69. Loyens W and Groeninckx G, *Macromol Chem Phys* 203:1702 (2002).

70. Serhatkulu T, Erman B, Bahar I, Fakirov S, Evstatiev M and Sapoundjieva D, *Polymer* 36:2371 (1995).

71. Krumova M, Fakirov S, Baltá-Calleja FJ and Evstatiev M, *J Mater Sci* 33:2857 (1998).

72. Krumova M, Flores A, Baltá-Calleja FJ and Fakirov S, *Colloid Polym Sci* 280:591 (2002).

73. Fakirov S, Evstatiev M and Friedrich K, Microfibrillar Reinforced Composites from Polymer Blends, in: *Polymerwerkstoffe 1998: Verarbeiterung, Anwendung, Recycling*, ed by Radusch HJ and Vogel J, Martin-Luther-Universität, Halle-Wittenberg, Halle/Saale, p. 123 (1998).

74. Evstatiev M, Fakirov S and Friedrich K, Microfibrilar Reinforced Composites – Another Approach to Polymer Blends Processing, in: *Structure Development During Polymer Processing*, ed by Cunha AM and Fakirov S, Kluwer Academic Publisher, Dordrecht, Boston, London, p. 311-325 (2000).

75. Evstatiev O, Oster F, Friedrich K and Fakirov S, *Int J Polym Mater* 53:1071 (2004).

76. Li ZM, Xie BH, Huang R, Fang XP and Yang MB, *Polym Eng Sci* 44:2165 (2004).

77. Fasce L, Seltzer R, Frontini P, Rodriguez-Pita VJ, Pacheco EBAV and Dias ML, *Polym Eng Sci* 45:354 (2005).

78. Fuchs C, Bhattacharyya D and Fakirov S, *Comp Sci Tech* 66:3161-71 (2006).

79. Quan H, Zhong G, Li ZM, Yang MB, Xie BH and Yang SY, *Polym Eng Sci* 45: 1303 (2005).

80. Evstatiev O, Evstatiev M, Fakirov S and Friedrich, *Plast Rubber Comp* 33:353 (2004).

81. Xu XB, Li ZM, Yang, MB, Juang S and Huang R, *Carbon* 43:1479 (2005).

82. Xu XB, Li ZM, Yu, RZ, Lu A, Yang MB and Huang R, *Macromol Sci Eng*. 289:568 (2004).

83. Fakirov S and Bhattacharya D, Nanofibrillar, microfibrillar and microplates reinforced composites – new advanced materials from polymer blends for technical, commodity and medical applications. 21st Annual meeting of the Polymer Processing Society (PPS-21), June 19-23, 2005, Leipzig, Germany.

CHAPTER 2

EXPERIMENTAL PART

The chapter begins with a description of the preparation of the MFCs and the equipment used to the purpose. This is followed by the description of all samples prepared and of every raw material studied. In addition, some general information is given about the methods of sample characterization employed – namely SAXS and WAXS from synchrotron, solid-state ^{13}C NMR, SEM and mechanical tests, the latter including tensile test, impact test and 3-point support flexural test. Where necessary, the data treatment procedures are explained.

2.1. Preparation of nanostructured polymer composites

2.1.1 Preparation of MFC precursors

The scheme in Fig. 2.1 gives a general idea of the preparation of MFCs, which was already described in Section 1.3. In the first stage, the two starting homopolymers – Polymer 1 (PA6 or PA12), which produce the reinforcing phase and Polymer 2 (in this work - HDPE), from which the matrix originates – are homogenized by melt-mixing in the presence or absence of compatibilizer. Then, the polymer blend is fibrillated by cold drawing, thus creating the oriented and crystalline reinforcing fibrils. Stages 3 and 4 are related to the formation of the composite matrix, achieved by selective melting of the major blend component (Polymer 2) and its controlled crystallization.

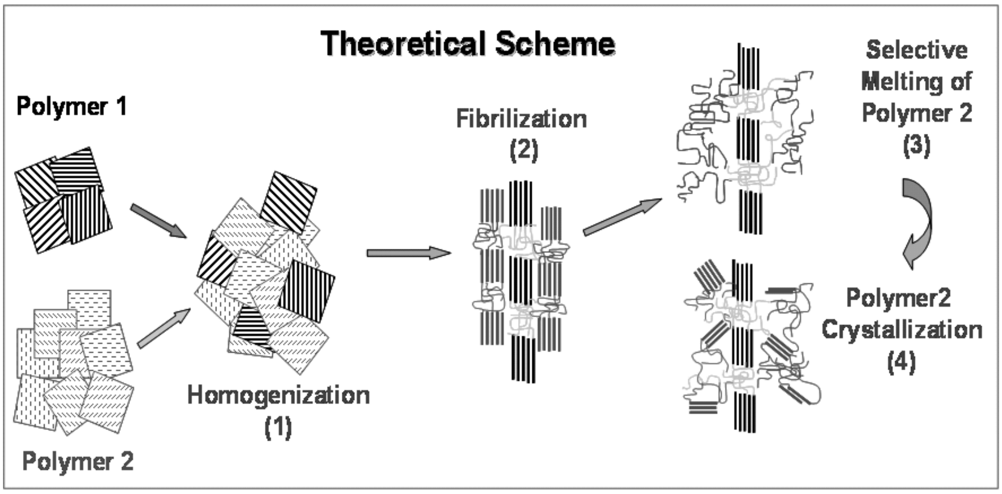

Figure 2.1 Basic stages in MFC preparation. Polymer 1 = PA6 or PA12; Polymer 2 = HDPE

The real extruder line used in this thesis included a specially designed stretching system including two water baths, three haul-off devices, a hot air oven and a multi-axes winder. All these devices were positioned downstream in an extruder line as indicated in Fig. 2.2.

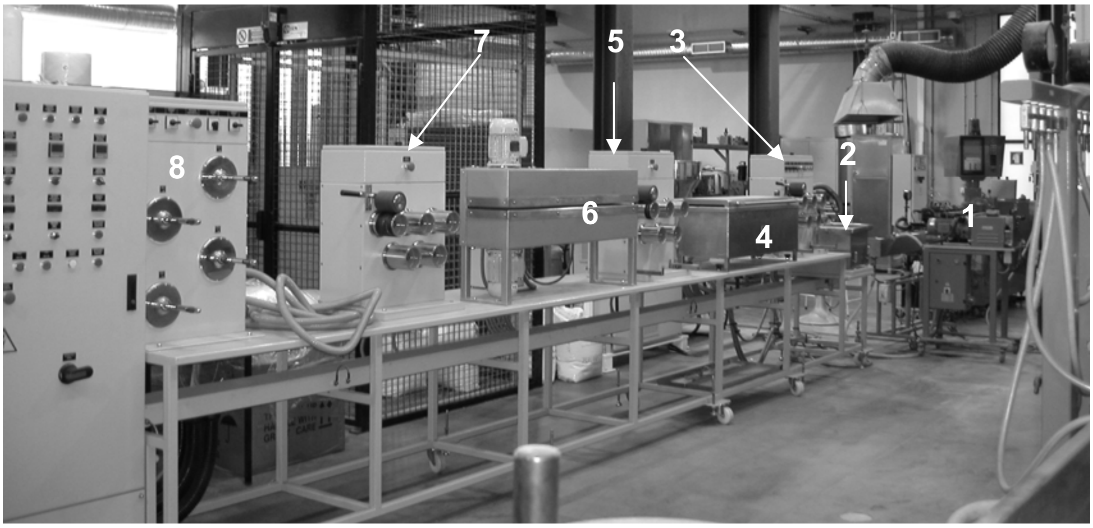

Figure 2.2 The specially designed stretching system used for the MFC precursors preparation: 1 – laboratory extruder; 2 - first water bath; 3 – first haul-off rolls; 4 – second water bath; 5 – middle haul-off rolls; 6 – hot air oven; 7 – final haul-off rolls; 8 – multi-axes winder

The initial blend components were melt-mixed in a laboratory modular Leistritz LSM 30.34 intermeshing co-rotating twin-screw extruder. Its screws rotated at 100 rpm, with a flow rate of the premixed granulated components of 1.5 kg/h, as defined by a K-Tron Soder twin screw compact gravimetric feeder. The latter was used with all HDPE-PA blends where all the components, including he compatibilizers, are supplied as granules. The set temperatures along the extruder were different for each particular mixture varying in the 210-260°C range. Figure 2.3 and Table 2.1 describe in detail the screw geometry. With all blends a pelletizing die with two circular holes of 2 mm in diameter was used.

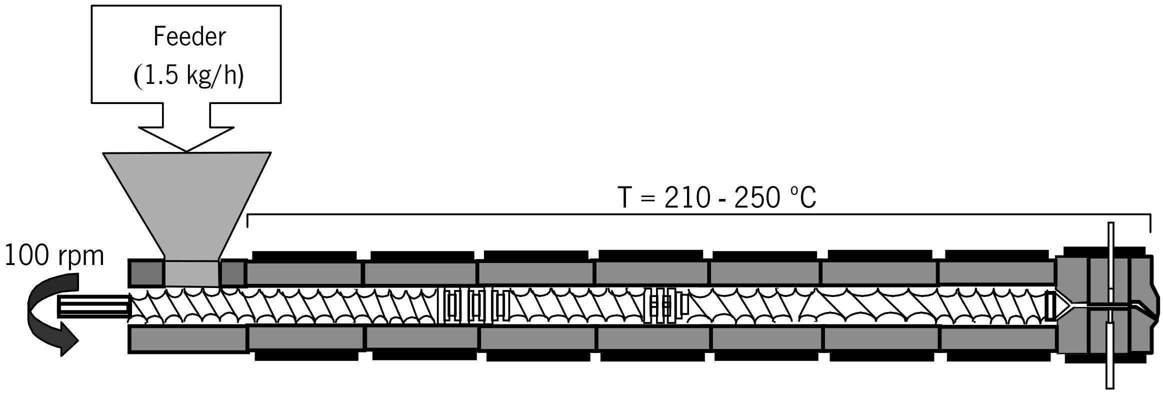

Figure 2.3 - Extruder layout and main operating conditions used to produce the MFC precursors. Reprinted from ref. [1]

Table 2.1 Screw geometry (from the hopper to the die) [1]

Description	Element code *
Transport elements	45/120 + 30/120 + 30/30 + 20/60
Kneading block	12/-60º
Transport elements	30/120
Knitting block	4/90º + 3/-60º
Transport elements	45/60 + 30/60
Left element	30/30
Transport elements	60/120 + 30/60 + 20/60

*Transport elements – pitch (mm)/length (mm); kneading blocks – number of discs/ staggering angle.

The typical procedure of MFC precursors' preparation is the following. The corresponding amounts of granulates of the matrix and reinforcing materials are dried at 90°C for several hours, premixed and fed by the gravimetric feeder to the extruder hopper. The resulting extrudate is cooled in the first water bath to 12°C. Meanwhile, the first haul-off unit applies a slight drawing in order to stabilize the line velocity and the extrudate cross-section. Further drawing is performed in the second and third haul-off units, after heating the extruded strand in the second water bath to 97-99°C. The total draw ratio was of *ca.* 16 causing the diameters of the strands to decrease from 2 mm to *ca* 0.6–0.9 mm.

As presented in Figure 2.4, after the extrusion blending and drawing stages, one obtains the polymer blend at the exit of the last haul-off device in the form of oriented, infinite cables (OC) (Fig. 2.4 (a)). The latter could be used, after proper cutting, in the form of unidirectionally arranged bundles, (Fig. 2.4 (b)) or MRBs (Fig. 2.4 (c)). For the sake of comparison, non-oriented granules of each blend were also obtained by pelletizing of extrudate obtained after the first haul-off (NOM) (Fig. 2.4, (d)).

2.1.2 Preparation of the final MFCs

Once prepared, the above precursors are subjected to selective melting and isotropization of the matrix material (stage 3) and its controlled crystallization (stage 4). These two processes are carried out in a hot press (SATIM, France) at a fixed temperature of 160ªC and a pressure of 20 bar and a cooling rate of ca. 10°C/min.

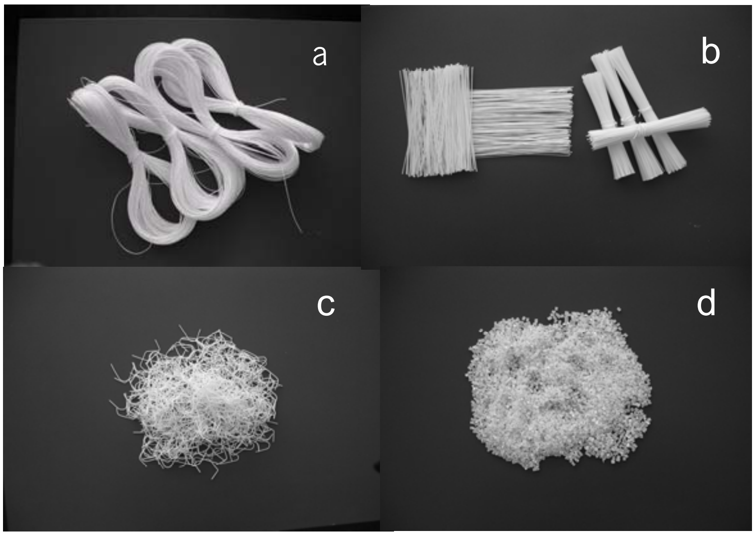

Figure 2.4 Various MFC precursors obtained after the homogenization and cold drawing stages; (a) OC, oriented cable; (b) bundles of cut parallel bristles; (c) MRB, middle-length randomly oriented bristles; (d) NOM, granules obtained by palletizing the extrudate before the first haul-off

Figure 2.5 shows the rectangular laminate plates 155 x 200 mm with a thickness of 1.4–1.8 mm that were obtained from all the precursors with various geometry and orientation of the reinforcing fibrils (Fig. 1.3). In the same press, smaller laminate plates (59 x 119 mm) were also prepared with all MFCs. The bigger plates were used predominantly for cutting of test specimens for the impact resistance and the three-point flexural tests, while the smaller ones were used to prepare specimens for the tensile tests, as well as for structural and morphological characterization.

Figure 2.5 Visual aspect of the final MFC laminates

Table 2.2 summarizes the blend compositions, the MFC type and the extrusion temperatures for all MFCs prepared in this work.

Table 2.2 Composition of the MFC precursors, extrusion temperatures and composite types prepared and studied in this thesis

HDPE/PA6/YP*	**HDPE/PA12/YP**
90/10/0	90/10/0
80/20/0	80/20/0
70/20/10	70/20/10
75/20/5	75/20/5
77.5/20/2.5	77.5/20/2.5
65/30/5	65/30/5
Extrusion Temperature, ºC	
250ºC	210ºC
Composite Type	
UDP, CPC, MRB, NOM	UDP, CPC, MRB, NOM

Notes: *All percentages are by weight. UDP = unidirectional ply; CPC = cross-ply cable; MRB = middle-length, randomly arranged bristles; NOM = non-oriented mixture; YP = Yparex (DSM);

The term “unidirectional ply”, UDP signifies an MFC lamina obtained by hot pressing of parallel bundles of cut OC, whose lengths coincide with the length of the rectangular plate. The term “cross-ply cables”, CPC denotes MFC laminate obtained by hot-pressing of at least two mutually perpendicular arrays of OC bundles, trying to maintain the same density of the reinforcing elements along the two dimensions of the final MFC laminate plate.

2.2. Materials

Table 2.3 contains the most important data of the neat polymers and compatibilizers used in this thesis available from their data sheets.

Table 2.3 Neat polymers and compatibilizers used in this thesis

Polymer type (Abbreviation in text)	**Trade name (Manufacturer)**	**Characteristics**
High density polyethylene (HDPE)	VS4531 (Borealis)	Density: 0.94 g/cm^3 Melt flow index: 0.6 g /10 min (2.16 kg/190ºC) Complex viscosity: 8.10^5 poise Melting point: 133ºC (DSC)
Polyamide 6, medium – viscosity, general purpose grade, (PA6)	Durethan B30 S (Lanxees)	Density: 1.14 g/cm^3 Melt flow rate: - 110 cm^3/10 min Viscosity: - medium Melting point: 220ºC (DSC)
Polyamide 12, high viscosity grade (PA12)	Grilamid L 25 (EMS GRIVORI)	Density: 1.01 g/ cm^3 M_w = 60.000 M_n = 31.000 Melting point: 178ºC (DSC)
Polyethylene-co-maleic anhydride (MAH) random copolymer (compatibilizer) (YP compatibilizer)	Yparex 8102 (DSM)	% Bound MA: 0.5 –1.0 Melt flow index: 2.3 g /10 min (2.16 kg/190ºC) M_w = 120.000 M_n = 15.000 Melting point: 125 ºC

The chemical structure of the Yparex (YP) as given by the manufacturer is the following:

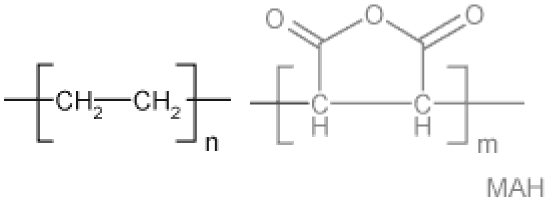

Before extrusion of the precursors, the two polyamides were dried at 90-100ªC for several hours in order to remove any adsorbed humidity. The latter could lead to bubble formation in both precursors and final MFCs resulting in inferior mechanical properties. The HDPE neat polymer and the YP compatibilizer were used as received, due to the hydrophobic character of these materials. Before the CM stage, the granulated polymer blend precursors were dried again at 90°C. The OC precursors, before drying at the same conditions, were winded on special frames so as to produce the straight bristles shown in Fig.2.4. The dry precursors were compression molded immediately.

2.3. Analytical Methods for Sample Characterization

2.3.1. X-ray scattering techniques

All WAXS and SAXS patterns in this thesis were registered at different times at the Soft Condensed Matter Beamline (A2) of HASYLAB, Hamburg, Germany using synchrotron radiation with a wavelength fixed to 0.15 nm. Two basic setups were used. The first one allowed for consecutive two dimensional (2D) SAXS and 1D WAXS measurements. The sample-to-detector distance for SAXS was set in the range of 2700-2800 mm, the diffraction patterns being registered by means of a MAR CCD 2D detector with exposure times of 30 – 60 sec. The 1D WAXS profiles were registered by a linear scintillation detector positioned at a distance of 240 mm in respect to the sample holder. In the second setup for 2D WAXS, the linear detector was removed and the MAR CCD detector was positioned at 90 mm from the sample. Figure 2.6 represents schematically these two setups.

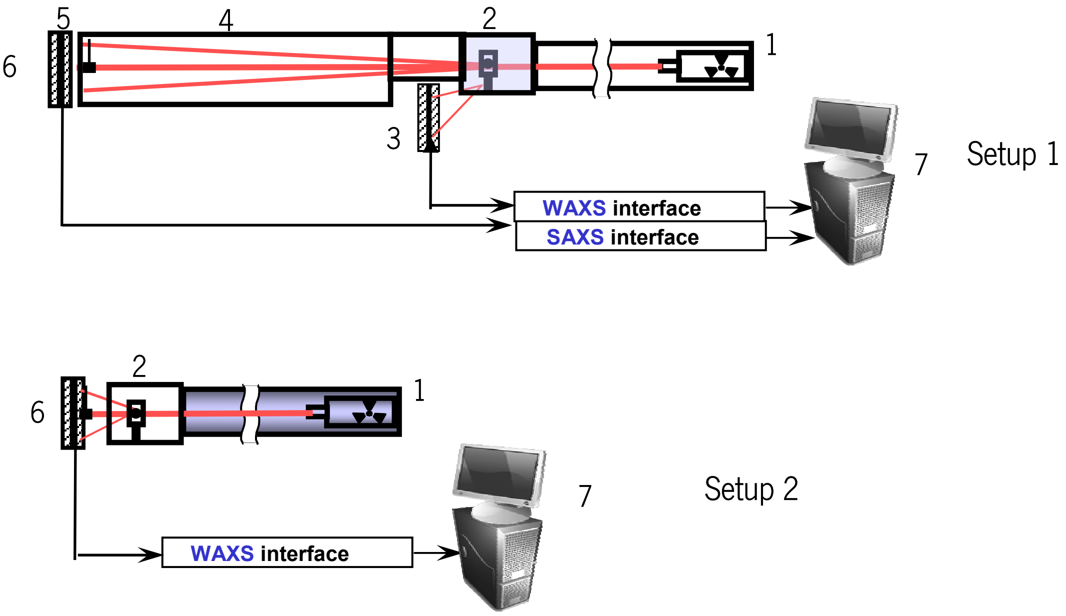

Figure 2.6 Setup 1 – simultaneous 2D SAXS + 1D WAXS; Setup 2 – 2D WAXS. 1 – X-ray source (bending magnet, synchrotron ring); 2 - Sample chamber with heating/cooling device and sample holder; 3 – 1D scintillation detector; 4 – evacuated SAXS optical path; 5 – beamstop; 6 – MARCCD 2D detector; 7 – Computer for image display and data storage (UNIX) (A2 Beamline, HASYLAB at DESY)

The pure polymers, the precursors and the different MFCs were studied as granules, OC and/or plates with various thicknesses. The samples were heated in the respective temperature ranges taking patterns at certain temperatures employing a typical heating rate of 20°C/min. A specially designed sample holder was used allowing for a controlled heating/cooling of the sample in the 25-300°C range. An IMAGO multi-channel process and program controller of JUMO GmbH & Co. KG was used to regulate the sample temperature in heating or cooling at various rates. The difference between the read-out and real temperature of the sample was found to be 3-4°C at a heating or cooling rate of 20°C/min.

To process the 2D WAXS and SAXS images, two software packages were used: the *X-ray* version 1.0 (Copyright© 1996 by Université Mons Hainaut, Belgium) and *Polar* version 2.7.3 (Copyright© 1997-2008 by Stonybrook Technology and Applied research, Inc, USA). Corrections for background scattering, irradiated volume and beam intensity were performed for each image. The 2D SAXS patterns were integrated in the range of $\boldsymbol{s}$ values between 0 and 0.15 nm^{-1}, $\boldsymbol{s}$ being the scattering vector, whose modulus is defined as $s = (s_{12}^2 + s_3^2)^{0.5} = (2/\lambda)\sin\theta$. The *s*-axis was calibrated using a standard rattail tendon sample.

Bragg long spacings L_B were calculated as the inverse value of $s_{\max}$:

$$L_B = \frac{1}{s_{\max}} \tag{2.1}$$

using the Lorentz corrected SAXS profile after subtraction of the contribution of the liquid scattering. L_B represents the sum of the average thickness of the crystal lamellae, l_c and of the interlamellar amorphous regions, l_a .

Apparently, equation 2.1 cannot be used for determination of l_c and l_a . To do that, the approach of Kortleve and Vonk [2] elaborated for the case of isotropic polymers was employed. The Fourier transform of the Lorentz corrected SAXS profile was calculated, namely the linear correlation function $\gamma_{1,r}$ (CF) as:

$$\frac{\gamma_{1,r}}{Q} = \frac{\int_0^\infty (I - I_b) q^2 \cos(qr) \exp(\sigma^2 q^2) \mathrm{d}q}{\int_0^\infty (I - I_b) q^2 \mathrm{d}q} \tag{2.2}$$

Here, $q = 2\pi.s$. I_b is that contribution to the total scattering arising from density fluctuations (liquid scattering), and σ is a term, related to the thickness of the crystal/amorphous interface. Q is the so-called scattering invariant that can be determined by integrating the SAXS profile over all scattering angles, *i.e.*:

$$Q = \int_0^\infty (I - I_b) q^2 \mathrm{d}q \tag{2.3}$$

The advantage of the CF method in contrast to Bragg's law is that, in addition to the long period L the values for l_c and l_a and the degree of crystallinity within the lamellar stacks (x_{cl}) (also called linear crystallinity) can be obtained [3,4].

The 1D SAXS curves in this study were processed by the SASDAP software (Copyright$^{©}$ 1995 by R. Verma, A. Biswas and B. Hsiao, DuPont Experimental Station, Wilmington, DE, USA). In addition to the L_B value, SASDAP calculates for each sample two additional estimates for the long spacing – from the position of the first maximum of CF (denoted as L_c^M) and from twice the position of the first minimum of CF L_c^m . To calculate the values of l_a and l_c on the basis of CF, the procedure described in ref [5] based on the following equation was used:

$$\frac{B}{L_c^M} = x_1(1 - x_1) \tag{2.4}$$

where B is the position of the first intercept of CF with the *r*-axis. From the two solutions $x_{1,2}$ of the above quadratic equation, the one with the higher value is ascribed to the larger fraction of the two phases found within the lamellar stacks. For example, in highly crystalline samples, x_2 would correspond to the crystal fraction within the lamellar stacks (denoted as x_{cl}) and $1-x_{cl}$ would, then, represent the amorphous fraction within the stack.

Once the assignment of x_{cl} is made for each particular case, one may calculate the l_c and l_a from the values of *L* employing the following equations:

$$l_c = x_{cl} L \quad \text{and} \quad l_a = (1 - x_{cl}) L \tag{2.5}$$

where *L,* as indicated in [5], may take the values of L_c^m *,* or L_c^M .

The 1D WAXS curves were processed by OTOKO software (Copyright$^{©}$ by M. Koch, HASYLAB, Hamburg). Their scattering angle axis was calibrated using the angular position of the reflections of a standard crystalline PET sample. The 1D WAXS curves were also corrected for background scattering, irradiated volume and beam intensity. The **s**-range covered in the WAXS measurements was from 0.3 to 4.8 nm^{-1}. 1D WAXS curves were sometimes produced by slicing the 2D WAXS patterns obtained in setup 2.

All WAXS curves were processed with commercial peak-fitting software. In the case of isotropic samples, the total degree of crystallinity (or, crystallinity index, CI) was calculated as a relation of the areas of all crystalline peaks and the total area underneath the WAXS curve:

$$CI = \frac{\sum A_c}{\sum (A_c + A_a)} \tag{2.6}$$

There, A_c is the integrated area underneath the respective crystalline peaks and A_a is the integrated area of the amorphous halo.

In oriented samples, e.g. the PA6 and PA12 OCs, the intensity of the meridional point-like reflections cannot be determined from the 1D WAXS curves, which represent an equatorial cut of the WAXS pattern. In this case, ΣA_c in Eq.2.6 will measure the scattering intensity along the equator only, *i.e.* one can define it as “equatorial crystallinity index” (ECI).

The 1D WAXS patterns in pure PA samples were used also to determine the interplanar spacings d_{h00} and d_{00l} using the Bragg’s law:

$$2d_{hkl} \sin\theta_{hkl} = \lambda \tag{2.7}$$

Here, λ = 1.5 Å is the X-ray wavelength and θ is the half of the 2θ position of the center of the respective crystalline peak. The d-spacing of the (*0k0)* crystalline planes was determined by slicing the meridional point-like reflections of the 2D WAXS patterns of oriented PA samples.

2.3.2. ^{13}C solid state NMR

Solid state NMR measurements were performed in a Bruker MSL300P spectrometer operating at 75.47 MHz for the observation of ^{13}C resonances, using Magic-Angle Spinning (MAS), high-power ^{1}H Dipolar Decoupling (DD), and ^{1}H -^{13}C Cross-Polarization (CP) combined techniques. The ^{1}H -^{13}C CP contact time was 1 ms giving a good discrimination of the protonated signals. The maximum inter-radio frequency pulse sequence delay was 3.0 s at a spinning rate of 3.4 kHz. The B_1 Radio Frequency field intensity was 55 kHz and the number of scans varied between 1000 and 2000. Glycine signals were employed as external references for determination of the chemical shifts with an accuracy of 0.2 ppm. The temperature of the probe head was set to 20 ± 1°C.

2.3.3. SEM

To analyze the morphology of the MFCs and of their precursors, SEM of freeze-fractured specimens was used. For every blend, specimens were collected for morphological analysis typically at three different locations of the extruder line: at the extrusion die, after the first and after the second haul-off units. The final MFCs obtained after compression molding were also analyzed. All samples were sputter-coated with gold and observed in a Leica S360 SEM at magnifications of x 2.0k, x 5.0k and x 7.5k. Most of the specimens studied were capable of cryogenic fracture with liquid nitrogen and were observed by SEM as fractured. The OCs obtained after the second draw unit, as well as some non-oriented precursors (as it will be specified further) were observed with the same technique after selective extraction of the polyethylene matrix with hot toluene for 5 h.

Due to the low resolution of light microscopy and the dense voiding caused by the microtomy on the PE component which was misleading for the observation of the reinforcing phase, this technique was not used in the present thesis.

2.3.4. Mechanical tests

The tensile tests were performed in an Instron model 4505 tensile test machine. The tests were carried out at 23±2°C with a standard load cell of 1 kN at constant crosshead speed of 50 mm/min. The tensile test specimens were cut out from the small compression-molded plates (UDP) with a gauge length and width of 25 mm and 4 mm, respectively. The sample thickness varied in the 1.1 – 1.5 mm range. At least 5 specimens of each sample were studied to calculate the average and the standard deviation values. The nominal stress was determined as a ratio of the tensile force and the initial cross section of the sample. The nominal strain was determined as a ratio of the sample gauge length at any time during drawing and that prior to drawing. The Young's modulus values E were extracted from the respective stress-strain curves at 1% strain (secant modulus).

For each UDP MFC sample, two Young's moduli were obtained – longitudinal (E_1) and transverse (E_2). To this purpose, test specimens were cut parallel and perpendicular to the fibre direction. The theoretical micromechanics suggests [6], that the E_1 modulus of the UDP is related to the properties of matrix E_p and fibres E_f and the volume fraction of fibres V_f by the rule of mixtures:

$$E_1 = V_f E_f + E_p (1 - V_f) \approx V_f E_f \tag{2.8}$$

where $E_p << E_f$ Thus, the greater the volume fraction of the fibres, the higher the longitudinal modulus, E_1.

The transverse modulus E_2 however, does not follow the rule of the mixtures. Correlation between the experimental results and simple theoretical equations such as

$$\frac{1}{E_2} = \frac{V_f}{E_f} + \frac{1 - V_f}{E_p} \tag{2.9}$$

are not usually very accurate. It is perhaps simplest to regard E_2 as having a similar value to that of the matrix [6]. Summarizing, it was an objective of the tensile mechanical tests to obtain the experimental values for E_1 and E_2 and to compare them against the theoretical ones, trying to extract some information about the physical and chemical interactions between the matrix and the reinforcing phases.

In the fibre direction (L) of a void-free unidirectional lamina, the theory suggests that the tensile strength of the ply (except for low fibre volume fractions) is given approximately by:

$$\sigma_{1\max} = \sigma_{f\max}.V_f \tag{2.10}$$

where $\sigma_{f\max}$ is the strength of the fibre.

In transversal direction it is assumed that:

$$\sigma_{2\max} = 0.33.\sigma_{p\max}. \tag{2.11}$$

where $\sigma_{p\max}$ is the strength of the matrix.

Flexural tests were performed in a three-point support designed according to Nunes *et al.* shown in Figure 2.7 [7].

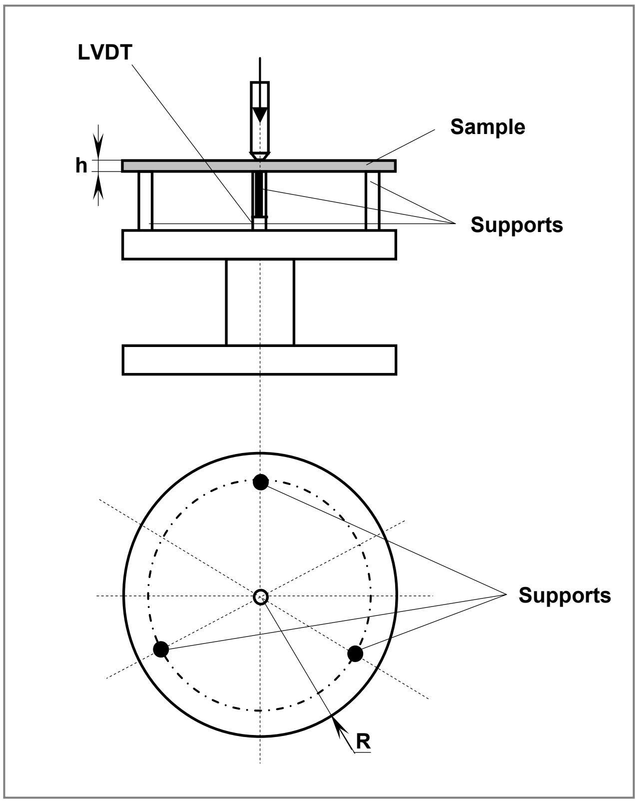

Figure 2.7 Schematic diagram of the three-point support flexural test [7] h – sample thickness, LVDT - Linear Variable Differential Transformer displacement transducer, R = 46.75 mm

The above support was mounted in the same Instron machine working in compression mode. The rectangular samples studied (77 mm x 99 mm) were cut out from the MFC-CP plates and placed upon the support. A constant load of 1 kN was applied at the centre of the sample with a crosshead speed of 5 mm/min. From the force-displacement curves obtained, the slope S_p was determined, which was used afterwards to calculate the reduced flexural stiffness, C_p given by:

$$C_R = \frac{3}{2\pi h^3} R^2 S_p \tag{2.12}$$

Here, h is the sample thickness varying in the 1.4 – 1.8 mm range and R = 46.75 mm is the radius of the circumference on which the three supports are resting. Eight samples of each MFC CPC were tested. Similar measurements were performed with the neat matrix polymer HDPE and the improvement factor, IF was calculated as:

$$IF = \frac{C_R^{Comp}}{C_R^{Matrix}} \tag{2.13}$$

Impact tests were carried out using a CEAST Fractovis instrumented falling weight impact tester at the Queens University, Polymer Processing Research Centre (Belfast, UK). The dart was 3.63 kg, and this was loaded with a mass of 10 kg. Impact samples were machined from the compression molded plates into squares measuring 60 x 60 mm. Eight impact samples of each material were impact tested at -40°C, with cooling being achieved by a mixture of liquid nitrogen and petroleum ether. The samples were impacted from a height of 1 m, and the speed of the dart at impact was approximately 4.4 m/s.

The information that was obtained from the test was the force experienced by the sample as a function of time that, assuming a constant impact speed, is calculated into displacement. From the force *versus* displacement graph, the peak force, peak energy and total energy were determined. The peak force is the force corresponding to the highest point on the impact curve, while the peak and the total energies are the areas under the curve between the origin and the initiation or the end of the fracture, respectively. In each test, the thickness of the impacted sample is also measured and the value for peak and total energy divided by this to give the energy (peak or total) absorbed per millimetre thickness. The latter are considered in the text as peak and total strengths, respectively [8].

2.4. References

1. Oliveira MJ, Carneiro OS, Denchev Z, Machado AV, and Covas JA, *Nanostructured composites of polyethylene/polyamide blends – microstructure and mechanical behavior,* Proceed. Polymer Processing and Structure (PPS 18), Guimarães, Portugal, (2002) (full text on CD).
2. Kortleve G, and Vonk CG, *Kolloid-Z* 225:124 (1968)
3. Strobl GR, Schneider M, *J Polym Sci* 18:1343 (1980)
4. Verma R, Marand H, and Hsiao B, *Macromolecules* 29:7767 (1996)
5. Santa Cruz C, Stribeck N, Zachmann HG, and Baltá-Calleja FJ, *Macromolecules* 24:5980 (1991).
6. Powel PC, *Engineering with Fiber-Polymer Laminates, Chapman & Hall*, p. 23, 1994.
7. Nunes JP, Pouzada, AS, Bernardo CA, *Polym Testing* 21:27 (2002).
8. Pick LT, Harkin-Jones, E, *Polym Eng Sci* 43:905 (2004)

CHAPTER 3

POLYAMIDE 6 – STRUCTURE INVESTIGATIONS IN ORIENTED AND ISOTROPIC SAMPLES

As shown in the literature survey in Chapter 1, in order to optimize the mechanical properties of the MFCs, an in-depth understanding is needed on the structure evolution in the reinforcing phase taking place during the homogenization, orientation and isotropization stages. The present chapter discloses the structural changes caused by heating of polyamide PA6 samples with different thermal and mechanical histories in the 30–240°C range. WAXS and SAXS of synchrotron radiation, as well as solid-state ^{13}C NMR measurements were performed. The NMR spectra show that in both isotropic and oriented samples there is a co-existence of α and γ-PA6 crystalline forms. Deconvolution of the WAXS patterns was performed to follow the temperature dependence of the unit cell parameters of the α and γ forms and also of the equatorial and the total CIs, evaluating the contributions of the two crystalline phases. Estimates for the long spacing and for the average thicknesses of the crystalline l_c and amorphous l_a phases within the lamellae are calculated as a function of the heat treatment employing analysis of the linear correlation function calculated from the SAXS patterns.

The X-ray results allowed the conclusion that upon heat treatment up to 160–200°C, intensive transitions between the PA6 crystalline forms take place, whereby the content of the initial major crystalline phase decreases and that of the initial minor one increases reaching almost 1:1. Close to 200°C a general trend toward increasing the content of the α form is registered. The influence of annealing and quenching after melting on the PA6 crystalline structure was also studied.

3.1. Introduction

There exist a number of studies on the structure development of isotropic and oriented PA6 samples at various processing conditions. It is well known that PA6 is a semicrystalline polymer characterized by two basic crystalline modifications designated as α and γ phases. The α-phase is monoclinic, whereas the γ-phase is considered by some authors to have pseudo-orthorhombic [1,2] or pseudo-hexagonal lattice [3]. The α-crystalline form is organized as anti-parallel polymer chains wherein the amide groups and the CH_2 units lay within the same plane. H-bond formation occurs between adjacent anti-parallel chains, thus forming sheets of H-bonded chains. This structure with antiparallel polymer chains can be formed in the presence of chain folding [4]. The γ-crystalline form of PA6 is built up of parallel polymer chains. To enable H-bond formation in this case, the amide linkages should twist by approximately 60° out of the plane of the molecular sheets, which explains the slightly smaller unit cell [3] and the inferior hydrogen bonding [4] in the γ-crystal as compared to those in the α form. Figure 3.0 illustrates the stacking of the sheets and the juxtaposition of the macromolecular chains within each sheet in the case of the α and γ PA6 polymorphs.

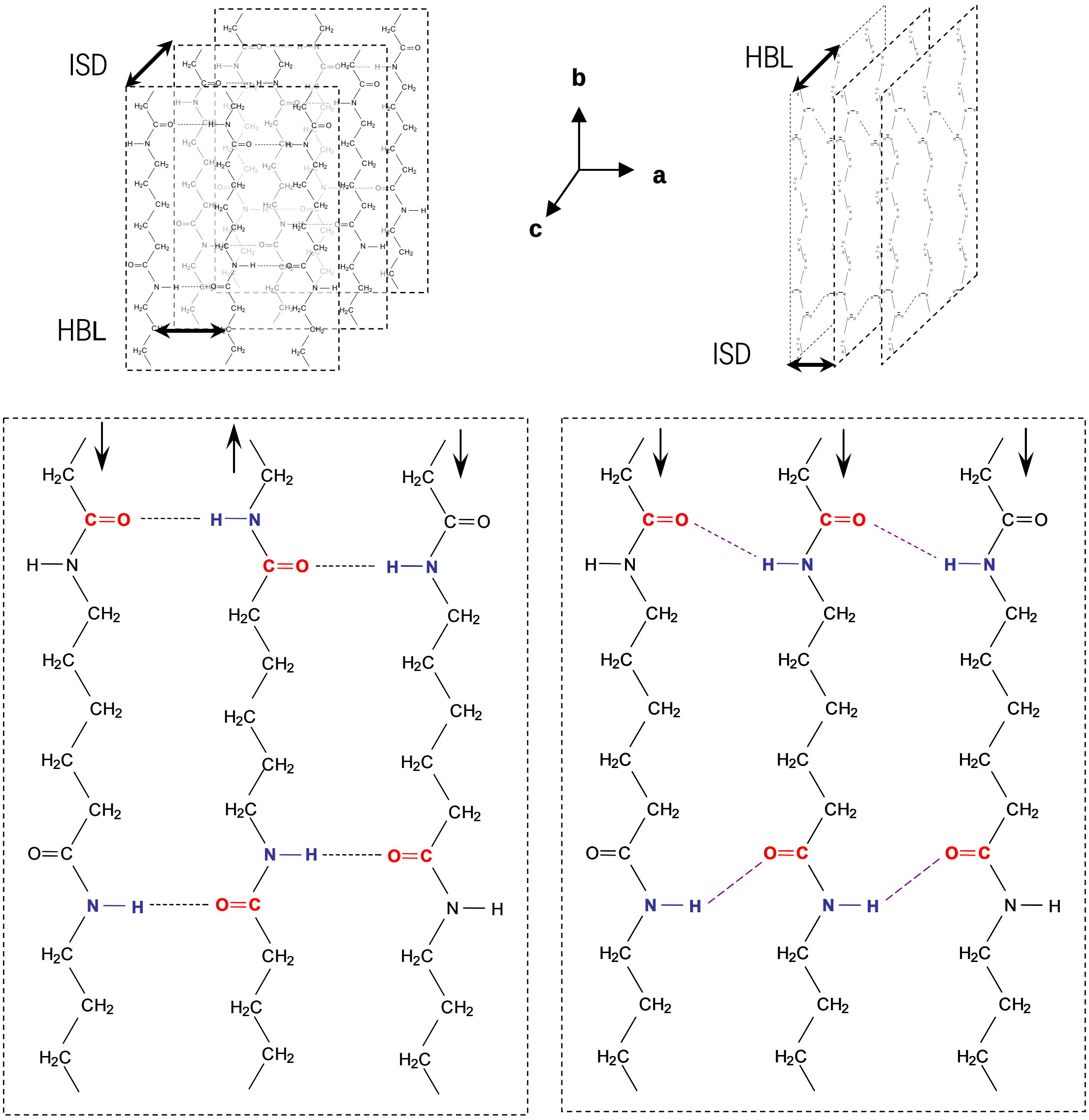

PA6 – α form: anti-parallel chains

PA6 –γ form: parallel chains

Figure 3.0 Schematic presentation of the α and γ crystalline sheets stacking and of the juxtaposition of the H-bonds in each sheet. HBL = hydrogen bond length; ISD – inter-sheet distance.

The two crystalline forms of PA6 normally co-exist. Which one of them is predominant will depend, as repeatedly reported, on the sample preparation conditions: temperature of crystallization, external stress applied, presences of moisture or of certain additives [3]. Several investigations [5,6] showed that crystallization of PA6 for extended periods below 130°C leads solely to formation of γ-crystallites, whereas annealing above 190°C produces only the α form. Temperatures in between these limits result in a mixture of the two forms, with higher fractions of α form being produced at higher temperatures. The disappearance of the γ form close to 190°C in PA6 is commonly referred to as "Brill transition" [7-11]. It is accepted that rapid cooling and low temperature crystallization promotes the γ form in PA6, whereas higher crystallization temperatures or slow cooling results in α-crystalline modification [8,12–14].

Application of external stress can also result in phase transitions in PA6. As shown by Murthy et al. [15-17] by means of SAXS and WAXS in a pre-drawn, relaxed PA6 fiber, a α - to γ- crystal transition possibly occurs through a metastable intermediate crystalline phase. On the contrary, the results of Samon et al. [4] were more consistent with a γ - to - α transition. These authors performed synchrotron SAXS and WAXS studies cold-drawing a PA6 fiber while irradiating.

Rhee and White [18] studied biaxially oriented PA6 films and disclosed a third PA6 phase -β or pleated α-phase. According to these authors, this phase is not very stable and is easily transformed into the more stable α or γ forms, whereas the γ-crystal cannot be transformed into other forms.

It may be concluded that there is still some debate on the structure of PA6 samples prepared under different processing conditions including heat treatment and deformation. It is not quite clear what changes occur in the PA6 microstructure upon orientation by cold drawing and subsequent annealing. As mentioned above, in the HDPE-PA6 microfibrilar composite the polyamide is the reinforcing phase. Therefore, it is important to study the structure development of PA6 under the concrete conditions of HDPE/PA6 composite formation.

3.2. Experimental details

Four different PA6 samples were investigated, all of them being prepared using the material indicated in Table 2.3. The first sample designated as "PA6 granules" comprises as-supplied granules with no initial mechanical or heat treatment. The second sample designated as *'PA6 film'* was obtained by compression molding of dry PA6 granules for 5 min at 250°C followed by cooling at a rate of 20 deg/min to room temperature. The third sample was taken from the oriented cables, OC, prepared in the extruder line shown in Fig. 2.1 at a set temperature of 250°C. (For more details see Section 2.1.1).

Some oriented PA6 cables were annealed with free ends at 120, 160 or 200°C in a Mettler FP 82 hot stage and designated as *'annealed OC'*, which was the fourth PA6 sample investigated. Each annealing temperature was reached at heating rates of 10deg/min. After a 30 min annealing at the respective temperature the sample was cooled with free ends until returning to room temperature at the same rate.

WAXS and SAXS studies were performed while heating the samples designated as PA6 granules, film and oriented cable. WAXS (1D or 2D) and 2D SAXS images were obtained at temperatures in the 30–240°C range, reaching the desired temperatures at a heating rate of 20deg/min. Before taking patterns, the samples were kept at the said temperatures for 30 s. The PA6 granules and the PA6 film were afterwards molten at 240°C and quenched at a cooling rate of approximately 200 deg/min back to 30°C where the final X-ray measurement was performed.

In the case of PA6 oriented cable, two quenching processes were performed: the first after 200°C (i.e. before melting), and the second one — after 240°C, i.e. upon melting and isotropization of the sample. The X-ray patterns of the PA6 annealed oriented cables were obtained at 30°C and at the respective temperature of annealing.

3.3. Results

3.3.1. Solid state NMR

CP-DD/MAS ^{13}C NMR spectra of PA6 granules, film, oriented cable and oriented cable annealed at 200°C were obtained and analyzed. The full-range spectra of all PA6 samples are of the type represented in Fig. 3.1(a). The multiple peaks observed in the 20–50 ppm range belong to the aliphatic carbon atoms. The resonance lines centered close to 173 ppm originate from the carbonyl C-atoms. Each full-range spectrum contains also two spinning side bands, which are due to the larger chemical shift anisotropy of the carbonyl groups. Fig.3.1, (b)–(e) show the extended aliphatic carbon regions of the four samples. The data for the chemical shifts are summarized in Table 3.1. The same table contains also the chemical shifts of the carbon atoms of α and γ-crystalline forms of PA6 as given in Ref. [19].

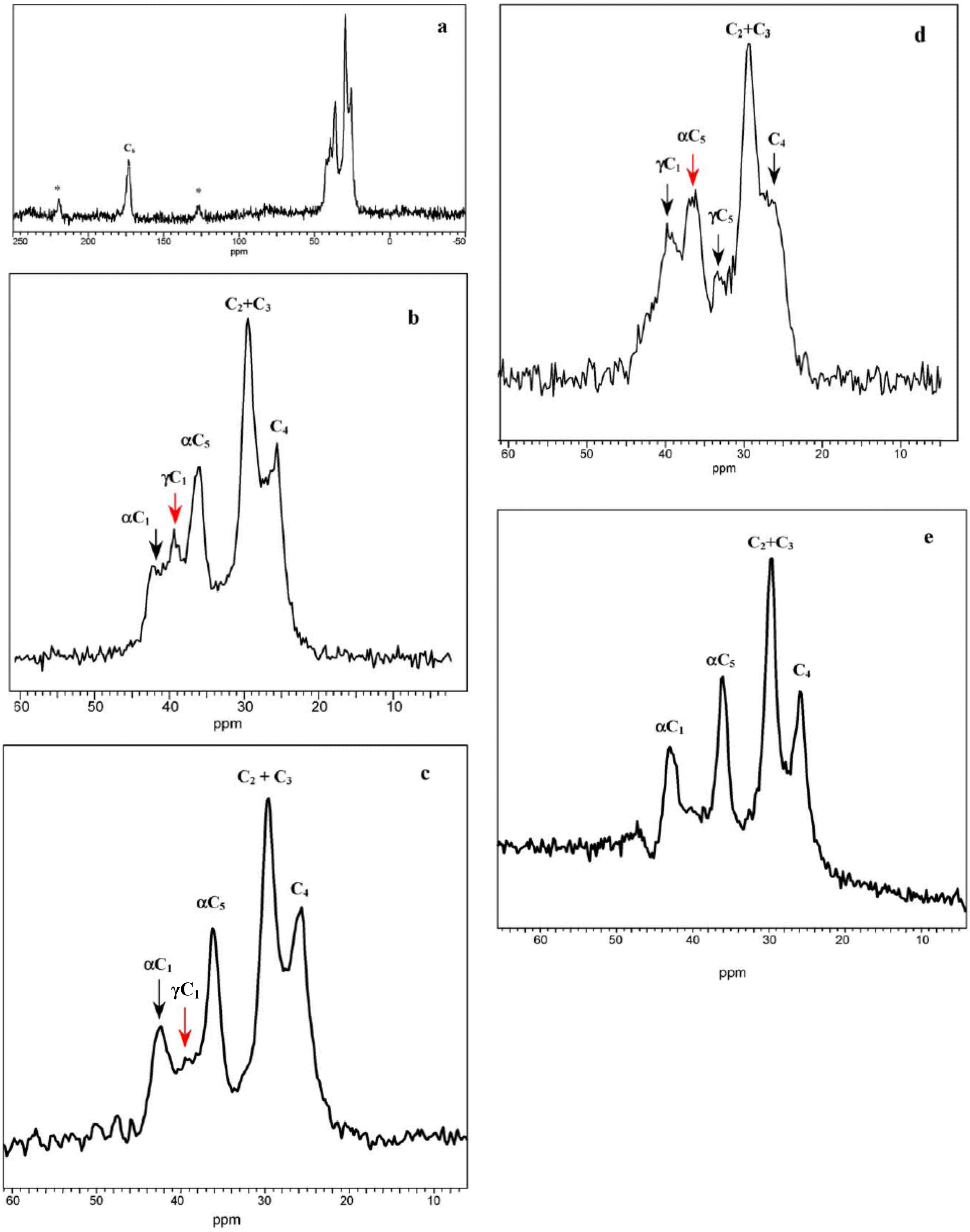

Figure 3.1 ^{13}C CP-MAS NMR spectra of PA6 samples at 20°C. (a) PA6 granules, full range. Asterisks denote spinning sidebands; (b) PA6 granules, magnification of the aliphatic carbons region; (c) PA6 film; (d) PA6 oriented cable; (e) PA6 oriented cable after 30 min annealing at 200°C.Reprinted from Ref. 20.

Table 3.1 Chemical shifts (ppm) registered for the carbons in the ^{13}C solid state NMR spectra of PA6 granules, PA6 film, PA6 oriented cable and PA6 oriented cable annealed for 30 min at 200 °C [20]

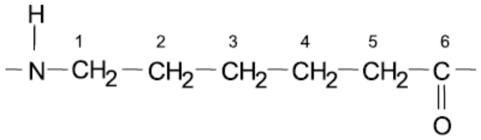

$$-N(H)-\overset{1}{C}H_2-\overset{2}{C}H_2-\overset{3}{C}H_2-\overset{4}{C}H_2-\overset{5}{C}H_2-\overset{6}{C}(=O)-$$

Sample	Chemical shifts of carbons (ppm)				
	C_1	C_2+C_3	C_4	C_5	C_6
α-PA6[a]	42.6	30.0	26.0	36.4	173.4
γ-PA6[a]	39.9	29.8	26.4	33.6	173.4
PA6 granules	42.2; 39.4	29.5	25.6	35.9	173.4
PA6 film	42.3	29.4	25.7	36.3	173.0
PA6 oriented cable	39.8	29.2	26.0	33.3; 36.5	172.5
PA6 or. ann. cable at 200ºC	42.9	29.6	25.9	36.1	172.8

Note: All the spectra are taken at room temperature. Literature data of α and γ-PA6 are given for comparison.
[a] According to Ref. [19].

Comparing the solid state NMR data of α and γ-crystalline forms of PA6 (Table 3.1), one may conclude that the chemical shifts of $\alpha(C_2+C_3)$, αC_4, and αC_6 almost coincide with those of the corresponding γ PA6 carbons. At the same time, the C_1 and C_5 chemical shifts of the α form show a difference of almost 3 ppm as compared to those of the γ form. Most probably, this effect is due to the different geometry and orientation of the H-bonds realized between the amide groups in α and γ PA6. Hence, the C_1 and C_5 resonance lines of PA6 samples can be used to make a distinction between the two crystalline forms.

Having in mind the chemical shifts data of pure α and γ forms of PA6, the peaks at 42.2, 29.5, 25.6, 35.9 and 173.4 ppm (Table 3.1) observed in the spectrum of the PA6 granules should be assigned to the αC_1, (C_2+C_3), C_4, αC_5 and C_6 chemical shifts respectively. The resonance registered at 39.4 ppm found in the same sample (Fig. 3.1(b)) belongs to a γC_1 carbon. No peak for the γC_5 resonance was observed in this spectrum.

In the PA6 film (Table 3.1), all the resonances observed correspond to the carbon atoms of the α form PA6. As seen from Fig. 3.1 c), there is also a low-intensity shoulder centered between 39 and 40 ppm that can be attributed to the γC_1 carbon.

In the PA6 oriented cable (Table 3.1, Fig. 3.1 (d)) the bands at 39.8, 29.2, 26.0, 33.3 and 172.5 ppm are attributable to the γC_1, (C_2+C_3), C_4, γC_5 and C_6 chemical shifts, respectively. In this sample, there is an additional peak at 36.5 ppm that corresponds to the C_5 chemical shift of α PA6 but at the same time the αC_1 resonance line is missing. The spectrum of the PA6 oriented cable previously annealed for 30 min at 200°C (Fig. 3.1 (e), Table 3.1) shows clear carbon resonance lines of PA6 in α form. Similarly to spectrum of the PA6 film, in the 39–40 ppm range there is a very weak γC_1 signal.

Summarizing the solid state NMR data, it can be concluded that the four PA6 samples do not represent pure α- or γ PA6 crystalline modifications but are mixtures of the two forms whose content depends on the previous treatment.

3.3.2. SAXS measurements

Selected 2D SAXS patterns are shown in Fig. 3.2 (a)–(e). The images obtained with the PA6 granules or with the isotropic PA6 film were similar to the patterns in Fig. 3.2 (a) and (e). The oriented PA6 samples showed different SAXS patterns depending on their thermal history. The as-drawn cable heated in the 30–160°C range while irradiated showed patterns similar to Fig. 3.2 (b) presenting spots whose intensity increased with temperature. Close to the Brill transition (195–200°C), two-point diagrams similar to Fig. 3.2 (c) were registered. Prolonged annealing at 200°C followed by slow cooling to 30°C gives rise to a different crystalline structure and perfection, as seen from Fig. 3.2 (d). Heating up to 240°C led to a complete loss of orientation in the PA6 cables, which was visualized by SAXS patterns of circular symmetry (Fig. 3.2 (e)).

Fig. 3.3 displays the set of CFs calculated for PA6 granules heated in-beam at 120, 160 and 200°C (curves 1–3, respectively), as well as at 30°C after melting the granules (curve 4). The structural data extracted by correlation function analysis from all the four PA6 samples as a function of temperature are presented in Table 3.2. It should be noted that in the raw SAXS profiles of PA6 granules at 30 and 90°C, the s_{max} values were so high that calculation of the corrected L_B values was only possible. No estimates for B, L_c^m and L_c^M and x_{cL} are presented for the oriented PA6 samples, either. To obtain correct and comparable data in this case, more sophisticated calculation procedures are needed, such as the Chord Distribution Function (CDF) [21].

It can be seen from Table 3.2 that increasing the temperature results in a general increase of the initial L_B values. The latter are dependent on the sample orientation and pre-treatment and are the largest in the case of PA6 film. Fast cooling results in some depression of the long spacing estimates, as well as of the x_{cl} values.

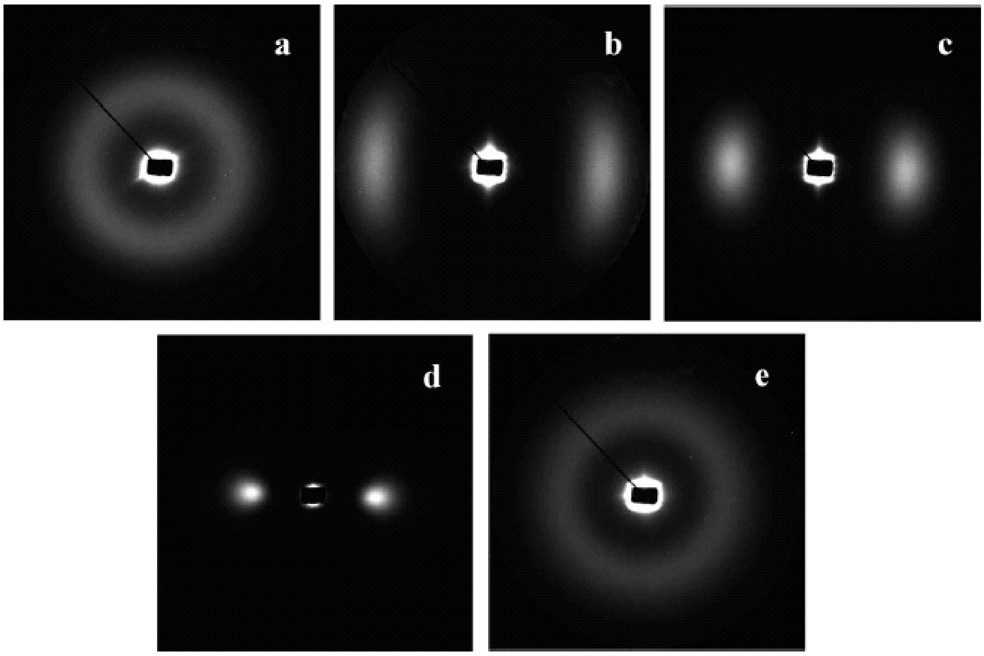

Figure 3.2 Selected 2D SAXS patterns of PA6: (a) PA6 granules at 160°C; (b) oriented PA6 cable heated in beam at 160°C; (c) oriented PA6 cable heated in beam at 200°C; (d) oriented cable annealed for 30 min at 200°C, image taken at 30°C; (e) sample (c) after isotropization at 240°C, image taken at 30°C. Note: the draw direction in oriented samples is horizontal. (Reprinted from Ref. [20])

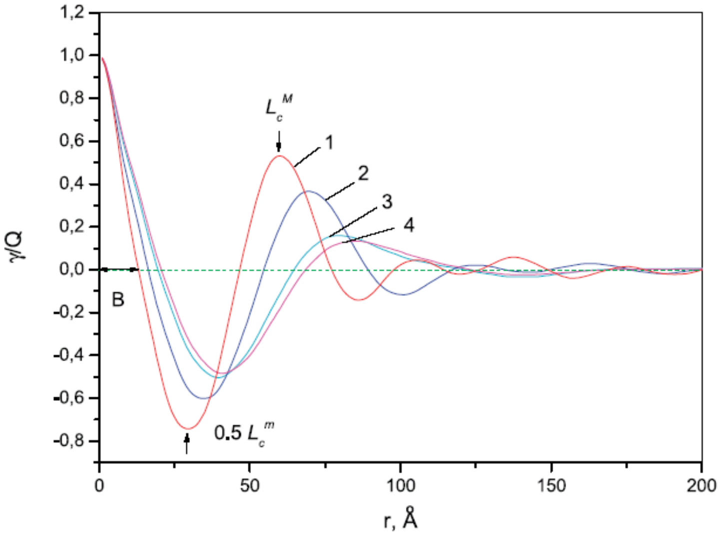

Figure 3.3 Linear correlation function curves calculated from the SAXS patterns of PA6 granules obtained at: 1–120°C; 2–160°C; 3–200°C; 4–30°C after melting at 240°C. Note: The arrows indicate the positions of B, L_c^M and L_c^m parameters for curve 1.

Table 3.2 Structural parameters extracted by analysis of the SAXS profiles of PA6 samples with various mechanical and thermal pre-history [20]

Measurement at (°C)	L_B Å	L_c^M Å	L_c^m Å	l_c Å	l_a Å	x_{cL} Å
PA6 granules (in-beam heating)						
30	52	–[b]	–	–	–	–
90	58	–[b]	–	–	–	–
120	61	60	60	41	19	0.677
160	72	70	70	44	26	0.622
200	94	86	82	51	35	0.589
30 after 240	89	79	78	43	36	0.542
PA6 film (in-beam heating)						
30	82	80	80	51	29	0.634
90	82	80	80	51	29	0.640
120	82	80	80	50	30	0.621
160	85	82	80	50	32	0.636
200	99	92	90	63	29	0.680
215	137	134	114	91	43	0.680
30 after 240	90	84	84	50	34	0.600
PA6 OC (in-beam heating)[c]						
30	57	–	–	–	–	–
120	61	–	–	–	–	–
160	64	–	–	–	–	–
200	85	–	–	–	–	–
30 after 240	87	78	78	47	31	0.608
PA6 OC (hot-stage annealing)[c]						
120	59	–	–	–	–	–
160	62	–	–	–	–	–
200	109	–	–	–	–	–

[a] Calculated after Lorentz correction of the raw SAXS pattern and subtraction of liquid scattering;

[b] Calculation of the linear CF impossible due to large $s_{\max}$ values

[c] Correct values for l_c, l_a and x_{cl} in oriented samples cannot be calculated from the linear CF, see the text.

3.3.3. WAXS measurements

Selected representative examples of 2D WAXS patterns of isotropic and oriented PA6 samples are displayed in Fig. 3.4. The draw direction DD (i.e. the fiber axis) in all oriented images is vertical. The PA6 granules (Fig. 3.4 (a)–(c)) show 2D patterns of circular symmetry with a clear change from one (samples at 30 and 200°C) to two Debye rings (30°C after heating to 240°C and fast cooling), indicative of changes in the crystalline structure. The patterns of the oriented PA6 samples (Fig. 3.4 (d)–(f)) contain equatorial reflections (arcs) being perpendicular to DD, as well as meridional point-like reflections parallel to DD. There is a visible variation in the intensity distribution, form and number of equatorial reflections as the temperature of the measurement changes, which variation has to be related with structural alterations in the crystalline phase. The difference in intensity of the two meridional reflections in the oriented patterns should be attributed to a slight tilt of the sample holder.

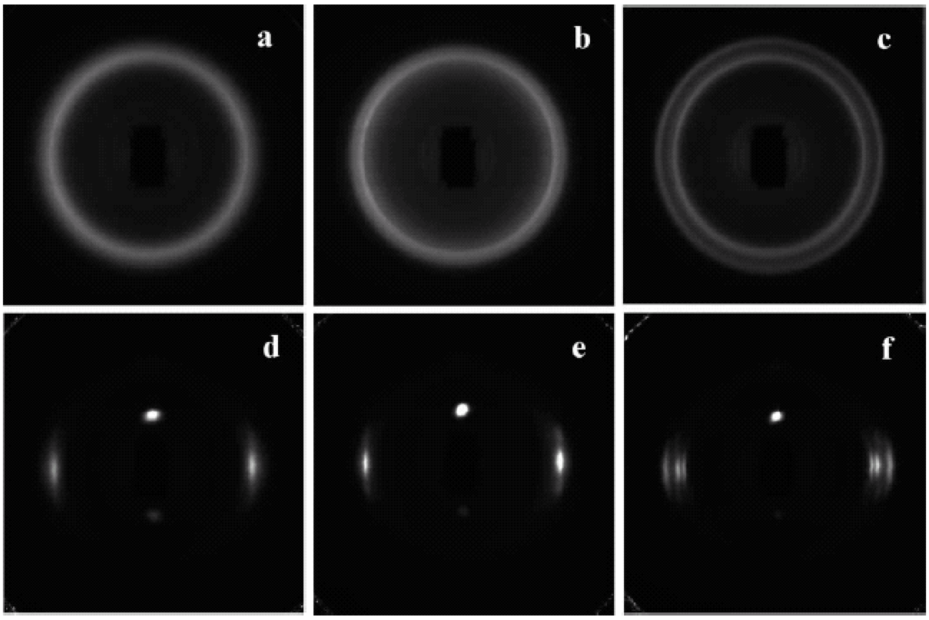

Figure 3.4 Selected 2D WAXS patterns of PA6 samples: (a) PA6 starting granules at 30°C; (b) granules at 200°C; (c) granules at 30°C after melting at 240°C; (d) as-drawn oriented cable at 30°C; (e) oriented cable at 200°C; (f) oriented cable at 30°C after 200°C. Note: the draw direction in the oriented samples is vertical (Reprinted from [20]).

To quantify the content of α and γ-crystalline forms, 1D WAXS patterns were obtained and deconvoluted. Some of the fitted 1D WAXS curves are represented in Fig. 3.5. As suggested by many authors, a monoclinic unit cell lattice was assumed for the α-PA6 form characterized by two peaks corresponding to α[200] and α[002/202] crystalline planes with 2θ being between 19 and 20° and 23 and 24°, respectively. For the γ-crystalline form, non-hexagonal unit cell was initially supposed for all samples, as suggested in Ref. [4], i.e. fits with two Gaussian peaks corresponding to γ[001] and γ[200] crystalline planes were performed with 2θ being between 21 and 22°. These two suppositions for the α and γ - type crystalline lattice led to excellent fits with fitting coefficients $r^2 = 0.999$. However, in the case of PA6 film irradiated at 30°C (Fig. 3. 5(b)) as well as for all samples quenched after melting, the fit was made with two Gaussians for the α form and one for the γ form. Any attempt to introduce a second Gaussian for the γ form led to fitting coefficients inferior to 0.98. This is a sign that a hexagonal γ-lattice is most probably formed in the last cases.

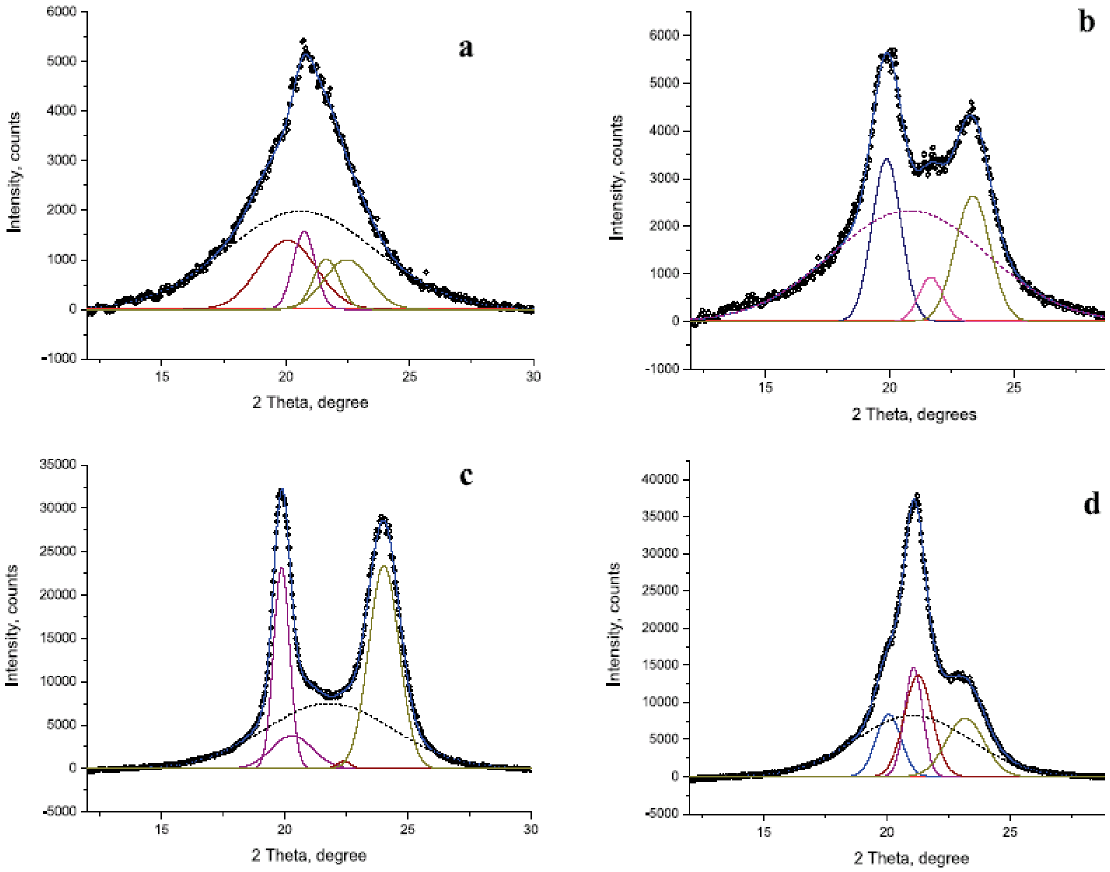

Figure 3.5 Selected 1D WAXS patterns of isotropic and oriented PA6 samples and their deconvolution: (a) PA6 starting granules at 30°C; (b) PA6 film at 30°C;(c) PA6 oriented cable annealed at 200°C, pattern obtained at 30°C; (d) PA6 oriented cable after heating at 200°C and quenching to 30°C, pattern obtained at 30°C. **Note:** crystalline peaks are given by solid lines, the amorphous halo—by dashed lines

Table 3.3 Temperature dependence of CI_{total}, α and γCIs in PA6 granules heated in the X-ray beam at a heating rate of 20deg/min [20]

Heat treatment (ºC)	α_{200}, (%)	$\alpha_{002}/\alpha_{202}$ (%)	αCI (%)	γ_{001} (%)	γ_{200} (%)	γCI (%)	CI_{Total} (%)
30	16.5	9.5	26.0	7.2	5.5	12.7	38.7
120	20.4	3.5	23.7	7.1	7.4	14.5	38.2
160	10.7	8.6	19.3	7.2	12.0	19.2	38.5
200	4.2	19.8	24.0	5.5	6.2	11.7	35.7
30 after 240	17.1	16.2	33.3	–	3.1	3.1	36.4

(CI = αCI + γCI). **Note:** Images are taken 30 s after reaching the respective temperature.

Table 3.4 Temperature dependence of CI_{total}, α and γCIs in PA6 film heated in the X-ray beam at a heating rate of 20deg/min [20]

Heat treatment (ºC)	α_{200} **(%)**	$\alpha_{002}/\alpha_{202}$ **(%)**	**αCI (%)**	γ_{001} **(%)**	γ_{200}, **(%)**	**γCI (%)**	CI_{Total} **(%)**
30	17.1	16.0	33.1	–	3.9	3.9	37.0
90	11.6	19.9	31.5	10.1	1.7	11.8	43.3
120	12.9	11.8	24.7	12.3	8.8	21.1	45.8
160	17.9	7.2	25.1	7.8	9.7	17.5	42.6
195	12.6	5.6	18.2	7.8	10.1	17.9	36.1
200	10.0	9.1	19.1	5.9	12.1	18.0	37.1
215	9.7	15.3	25.0	2.0	6.5	8.5	33.5
30 after 240	19.5	17.3	36.8	–	3.8	3.8	40.6

(CI = αCI + γCI). **Note:** Images are taken 30 s after reaching the respective temperature.

Table 3.5 Temperature dependence of CI_{total}, α and γCIs in PA6 oriented cable heated in the X-ray beam at a heating rate of 20deg/min [20]

Heat treatment (ºC)	α_{200} **(%)**	$\alpha_{002}/\alpha_{202}$ **(%)**	**αECI (%)**	γ_{001}, **(%)**	γ_{200} **(%)**	**γECI (%)**	ECI_{Total} **(%)**
30	8.1	9.8	17.9	12.3	18.1	30.4	48.3
120	8.6	10.2	18.8	16.4	12.0	28.4	47.2
160	12.9	11.6	24.5	9.7	13.7	23.4	47.9
200	18.3	19.1	37.4	8.4	8.8	17.2	54.6
30 after 200	11.1	14.0	25.1	28.1	2.6	30.7	55.8
30 after 240	21.5	15.8	37.3	–	0.7	0.7	38.0

(ECI = αECI + γECI). **Note**: Images are taken 30 s after reaching the respective temperature.

Tables 3.3 – 3.5 contain the changes in α and γ form content, CI and ECI of the three PA6 samples as a function of temperature. Their unit cell edges a, b (in oriented PA6 samples only) and c were also calculated and presented in Table 3.6. These data will be discussed in the next section.

Table 3.6 Unit cell parameters of the **α** and **γ**-crystalline forms in PA6 granules, PA6 film and PA6 oriented cable as a function of temperature. The b-edge direction coincides with the chain axis [20]

Temperature (ºC)	**PA6 granules**				**PA6 film**				**PA6 oriented cable**				
	d_{200} a_α Å	**d_{002}/ d_{202} c_α, Å**	**d_{200} a_γ Å**	**d_{001} c_γ Å**	**d_{200} a_α, Å**	**d_{002}/ d_{202} c_α Å**	**d_{200} a_γ Å**	**d_{001} c_γ Å**	**d_{200} a_α A**	**d_{002}/ d_{202} c_α Å**	**d_{200} a_γ Å**	**d_{001} c_γ Å**	**d_{020} b_γ Å**
30	8.61	7.70	7.99	4.17	8.69	7.42	7.98*	3.99*	8.68	7.76	8.15	4.15	14.92
120	8.53	7.63	8.03	4.18	8.87	7.70	7.90	4.20	8.68	7.86	8.19	4.18	14.80
160	8.84	7.78	8.14	4.20	8.67	7.82	8.06	4.19	8.64	8.04	8.27	4.20	14.92
195	–	–	–	–	8.89	7.87	8.16	4.19	–	–	–	–	–
200	9.22	7.96	8.39	4.32	9.01	7.92	8.28	4.19	8.60	8.15	8.27	4.21	14.92
215	–	–	–	–	9.17	7.95	8.42	4.35	–	–	–	–	–
30 after 200	–	–	–	–	–	–	–	–	8.61	7.47	7.85	3.93	15.44
30 after 240	8.54	7.47	7.99^a	4.0^a	8.65	7.41	7.94^a	3.97^a	8.52	7.57	7.96^a	3.98*	–

[a] Hexagonal form

3.4. Discussion

The four PA6 samples with different thermal and mechanical pre-histories were prepared and characterized under various temperature conditions so as to model the structural changes of the polyamide reinforcing phase during the consecutive stages of MFC preparation. They include melt-mixing at 240–250°C, quenching and cold drawing of the blend, selective melting of the matrix phase in the 150–200°C range, and cooling back to room temperature. For the sake of clarity, the data sets for each particular PA6 sample will be discussed separately.

3.4.1. PA6 granules

As seen from the solid state NMR traces (Table 3.1), there is a co-existence of α and γ-PA6 forms. However, the CP-DD/MAS technique does not permit ultimate conclusions about the exact ratio between the two crystalline forms. Nevertheless, based on the fact that the shape of the NMR spectrum (Fig. 3.1 (a) and (b)) is more like the one of the pure α PA6 form [46] and considering the presence of clear resonance line only for the γC_1 and not for the γC_5, it may be supposed that this sample is predominantly in α-crystalline form with lower content of γ PA6.

A confirmation of the above supposition comes from Table 3.3, which shows WAXS data about the concentration of α-, γ-crystalline forms and the total CI as a function of temperature. In the PA6 granules at 30°C with a CI value of 39%, there is more α than γ type crystallinity, their relation being close to 2:1. This is in agreement with the NMR data evidencing that PA6 granules are predominantly in α form. It may also be seen from Table 3.3 that a transition from α to γ form occurs between 120 and 160°C, the two crystalline forms showing almost identical concentrations at 160°C. Between 160 and 200°C, however, the trend reverses, i.e. the transition becomes from γ to α PA6 form.

The long spacing estimates L_B, L_c^M and L_c^m grow as the temperature increases in the 30–200°C range, whereas the linear crystallinity x_{cL} decreases (Table 3.2). This results in a stronger enlargement of l_a as compared to that of l_c. Since the CI remains almost constant, it may be concluded that no additional crystallization or melting process takes place throughout the entire temperature interval. The said changes in l_a, l_c and long spacing estimates can therefore be related to the phase-to-phase transitions, as well as to possible thermal expansion.

The data from Table 3.6 show that the unit cell edges of both α and γ form PA6 granules generally grow with the temperature. The increase of the d-spacings is different. The strongest growth is registered with the d-spacings of α[200] and γ[001], with 7 and 4%, respectively. These two d-spacings roughly correspond to the inter-planar spacing along the H-bonds direction in α and γ PA6, respectively. On the other hand, the smallest increased is shown by the d-spacings of α([002]/[202]) and γ[200] planes, which characterize the direction of the van der Waals forces in the two forms. The observed increase in the unit cell edges is in accordance to the supposed thermal expansion. Clearly then, decreasing the temperature will be expected to diminish the unite cell edges and the l_c estimates, which was really observed when the sample was quenched to 30°C after melting (Table 3.6, Table 3. 2).

As seen from Eq. 2.5, additional decrease in l_c will also results from the decline in the linear crystallinity x_{cL} within the stack, which is a fact during quenching (Table 3.2). At the same time, l_a remains similar to that at 200°C. In other words, quenching results in 'freezing' of the amorphous phase thickness, whereas the crystalline phase undergoes several changes. First of all, there occurs a volume contraction due to the reduced temperature. Second, formation of crystallites predominantly in α form takes place, with the ratio between the α and γ-PA6 forms reaching 10:1 (Table 3.3). This finding is contrary to some previous reports [8,12–14] stating that rapid cooling favors the formation of γ-crystallites. Third, the remaining γ form suffers modification. During the heating in the entire 30–200°C range this crystalline form is non-hexagonal, as it can be seen from Table 3.3, supposedly with monoclinic lattice as previously described by some authors [18], or with orthorhombic one, which is the minimum requirement to generate two reflections. Quenching after melting, however, changes the γ-PA6 lattice into hexagonal, i.e. it shows only one reflection with 2θ at about 20–21°. Similar changes in the lattice type of PA6 γ-phase upon cooling were reported previously [22].

3.4.2. PA6 film

Based on the NMR data (Table 3.1, Fig. 3.1 (c)), it can be considered that the PA6 film contains predominantly the α-crystalline modification with some minor admixtures of γ form. Analyzing 1D WAXS traces by deconvolution confirms that, in fact, the α form content in the initial film at 30°C is about ten times larger than that of the γ form (Table 3.4).As seen from Fig. 3.5 (b), the latter is characterized by a hexagonal lattice of its unit cell.

Increasing the temperature provokes phase-to-phase transitions, as seen from the data in Table 3.5. Similarly to the PA6 granules, initially a transition from α to γ-crystalline form takes place, which trend reverses at about 200°C. Another observation is that the CI in PA6 film varies in the whole temperature interval. It grows until 120°C and decreases between 120 and 215°C, thus indicating that an additional crystallization or melting most probably occurs along with the phase-to-phase transition.

Table 3.2 shows the long spacings estimates L_B , L_c^M and L_c^m as a function of the temperature. The PA6 film at 30°C displays a long spacing that is notably larger than that in the PA6 granules. This fact may be explained with the way the PA6 film was prepared including compression molding of granules at 250°C followed by a relatively rapid cooling to room temperature, which can be considered as non-isothermal crystallization. As previously observed, annealing of PA6 always results in a growth of its long spacing values [23].

Increasing the temperature up to 160°C does not cause changes in L_B , L_c^M and L_c^m . Since at the same time CI increases, one may suppose that this effect is related with the formation of new crystallites and not with thickening of the existing lamellae. Above 160°C, however, long spacings, as well as l_c land l_a start to grow, this trend being better expressed in the 200–215°C range. Having in mind that the content of the α form increases whereas that of the γ form decreases which is accompanied by a CI reduction (Table 3.4), it may be concluded that in this temperature range the γ to α phase transition mentioned above is accompanied by melting of some crystallites mainly of γ type.

All unit cell edges of α and γ-crystalline lattice of PA6 film grow when the temperature increases from 30 to 215°C (Table 3.6). Here, the strongest expansion is along the van der Waals forces direction in α form and the H-bond direction in γ form, corresponding to the d-spacings of α[002]/[[202] and γ[001], respectively. As it may be seen from Table 3.6, these changes in the unit cell are reversible. Quenching to 30°C after melting restores the initial dimensions of the unit cell. Just like in the case of the granules, this rapid cooling leads to the formation of PA6 mainly in α crystalline modification (Table 3.4). The small amounts of the remaining γ crystallites are with hexagonal unit cell, i.e. a structure similar to the initial PA6 film is formed. Again, the x_{cL} value after quenching is the lowest (Table 3.2).

3.4.3. PA6 oriented cable

PA6 oriented cable also represents a mixture of α and γ-crystalline modifications. Contrary to the previously studied two isotropic samples, the cable shows the presence predominantly of γ form. The CP-DD/MAS ^{13}C NMR analysis of this sample (Fig. 3.1 (d), Table 3.1) shows clear peaks for γC_1 and γC_5 with lower content of the α form (αC_5 resonance only). Having in mind that the oriented sample was prepared from isotropic granules mostly in α form, one can conclude that melting of PA6 followed by cold drawing favored the formation of γ form. The NMR spectra of PA6 cable shows also that the resonance line of the carbonyl C-atom (C_6) appears in slightly stronger fields (below 173.0 ppm) than the one of the non-oriented samples (Table 3.1). Most probably, upon cold drawing of PA6, a conformation with more electron-shielded carbonyl atom is realized, which can be the consequence of a closer packing of the PA6 macromolecules.

Deconvolution of the respective 1D WAXS curves confirms that in the initial oriented PA6 cable at 30°C there is more γ than α crystalline phase, their relation being 1.7:1.0, respectively (Table 3.5). The starting ECI at 30°C in this sample is 48%, i.e. with about 10% higher than the CIs of the two isotropic PA6 samples at the same temperature. Actually, the difference is even larger, because the intensity of the meridional γ(020) reflection is not taken into consideration in the ECI calculation. Most probably, the higher crystallinity in the PA6 cable should be attributed to its strong orientation (DR>10) obtained by cold drawing.

Increasing the temperature above 120°C results in a transition from γ to α PA6 crystalline modification. At 160°C the two forms reach almost equal concentrations (about 24%). In view of the fact that in the 120–160°C range both ECI and L_B values remain almost constant (Table 3.5, Table 3.2), one can suppose that there is no additional melting or crystallization in this temperature range. Above 160°C, the γ to α-transition continues and at 200°C the relation becomes 2:1, now in favor of the α form. At the same time, ECI increases from 48 to 55%. This means that additional crystallization of amorphous material into α-crystallites takes place in the temperature range between 160 and 200°C, which was not the case with the two isotropic PA6 samples. This augmentation of ECI is accompanied by a growth of L_B by approximately 20 Å in the 160–200°C range. It was not possible to determine the discrete contribution of l_c and l_a to the said growth of the L_B at high temperatures. In samples with fiber symmetry (i.e. a two-dimensional system), correct structural parameters cannot be extracted by calculating and analyzing the linear CF or the Ruland's interface distribution functions, which are valid in non-oriented (one-dimensional) systems. That is the reason that Table 3.2 contains only Bragg's long spacings for the PA6 oriented cable. Nevertheless, having in mind that the ECI grows, it can be supposed that the L_B increase should be attributed to thickening of the crystalline lamellae, i.e. to a growth of l_c mainly. Contrary to the thermal expansion, the said thickening should not be reversible when cooling down. As seen from Table 3.2, PA6 cable after quenching displays even larger L_B value, as compared to that at 200°C, which corroborates the above supposition.

Table 3.6 contains data about α and γ form unit cell edges in PA6 cable as a function of temperature. The b-edges of the γ form lattice in this sample were obtained from the diffraction peak of γ(020) plane in the 2D WAXS patterns as described in Chapter 2.3.1. One can see that the b-edge of the γ form remains unchanged until 200°C indicating that there is not lattice expansion in the direction of the polymer chains. The biggest growth here (ca. 5%) is of the interplanar distance along the direction of the van der Waals forces in α form. At the same time, there is no increase of the α-edge of the α form, which even slightly decreases at 200°C. The rest of the d-spacings grow by less than 1%, which is one more fact indicating that in PA6 oriented cable the increase in L_B cannot be explained mainly with thermal expansion, as in the cases of the two isotropic samples.

It was interesting to follow the structural changes in the PA6 cable upon quenching to 30°C before and after melting. As expected, quenching before reaching the melting point does not upset the orientation of the sample (Fig. 3.4 (f)). It leads to the formation of a mixture of α and γ forms with a slight excess of the latter (1.00:1.22), whereby the γ form lattice continues non-hexagonal as in the starting PA6 cable at 30°C. However, if the quenching is performed after melting at 240°C, the sample looses its orientation and the PA6 crystalline phase transforms almost quantitatively into α modification. There are only traces of γ form (less than 1%), which is with hexagonal lattice (Tables 3.5). As seen from Table 3.6, quenching of PA6 cable leads to smaller a and c edges for the two crystalline forms, which means smaller distances between the macromolecules in the plane of the sheet, as well as shorter inter-sheet distances. This would mean that quenching is related to the formation of smaller crystallites of both types with closer packing between the macromolecules.

Interestingly enough, quenching of the PA6 cable before melting leads to a b-edge of the γ form being with 3.5 % higher than the starting value (Table 3.6). In this case the γ modification seems to contain more stretched macromolecules.

3.4.4. Annealed PA6 cable

Fig. 3.6 (a)–(c) displays the changes in ECI and the comparison between the amounts of the two crystalline forms in PA6 cables before any heat treatment, at a certain temperature (120, 160 or 200°C) and after 30 min annealing at 120, 160 or 200°C. In the last case, the X-ray measurements were taken at 30°C after slow cooling. It can be deduced from Fig. 3.6 (a) that at 120°C ECI, α and γ-crystallinities are similar to those of the initial sample, the concentration of the γ-phase being 30% and that of α-18%. After 30 min annealing at this temperature, followed by slow cooling a slight growth of 7–8% of the α form is observed leading to the same increase in ECI. This increase is rather to be attributed to crystallization of amorphous material during the slow cooling to 30°C and not to a phase-to- phase transition since the percentage of the γ-crystallites remains constant.

At 160°C (Fig. 3.6 (b)), the α-crystallinity grows, which is accompanied by a decrease of the γ form concentration, with ECI remaining constant. Evidently, at this temperature there starts already the α to γ-phase transition, not accompanied by additional crystallization. WAXS traces at 30°C after annealing at 160°C, however, show an increase in both α-crystallinity and ECI, whereas the concentration of the γ-PA6 form remains almost unchanged as compared to that at 160°C. Hence, it may be concluded that crystallization has only occurred during the slow cooling to 30°C.

Increasing the annealing temperature of the PA6 cable to 200°C (Fig. 3.6 (c)) results in energetic transformation of γ into α-crystallites. Additional crystallization process takes also place at 200°C. Obviously, these two processes continue during the slow cooling since the measurement at 30°C reveals almost three times less γ-PA6 form as compared to its initial concentration.

Summarizing about the two polymorphic forms, annealing of oriented PA6 cable with an initial ratio of γ/α = 1.8:1.0 leads to an increase of the α-type crystallinity. Up to 120°C, this growth is due to crystallization of amorphous material into α-PA6 form, which takes place only during the cooling. In the

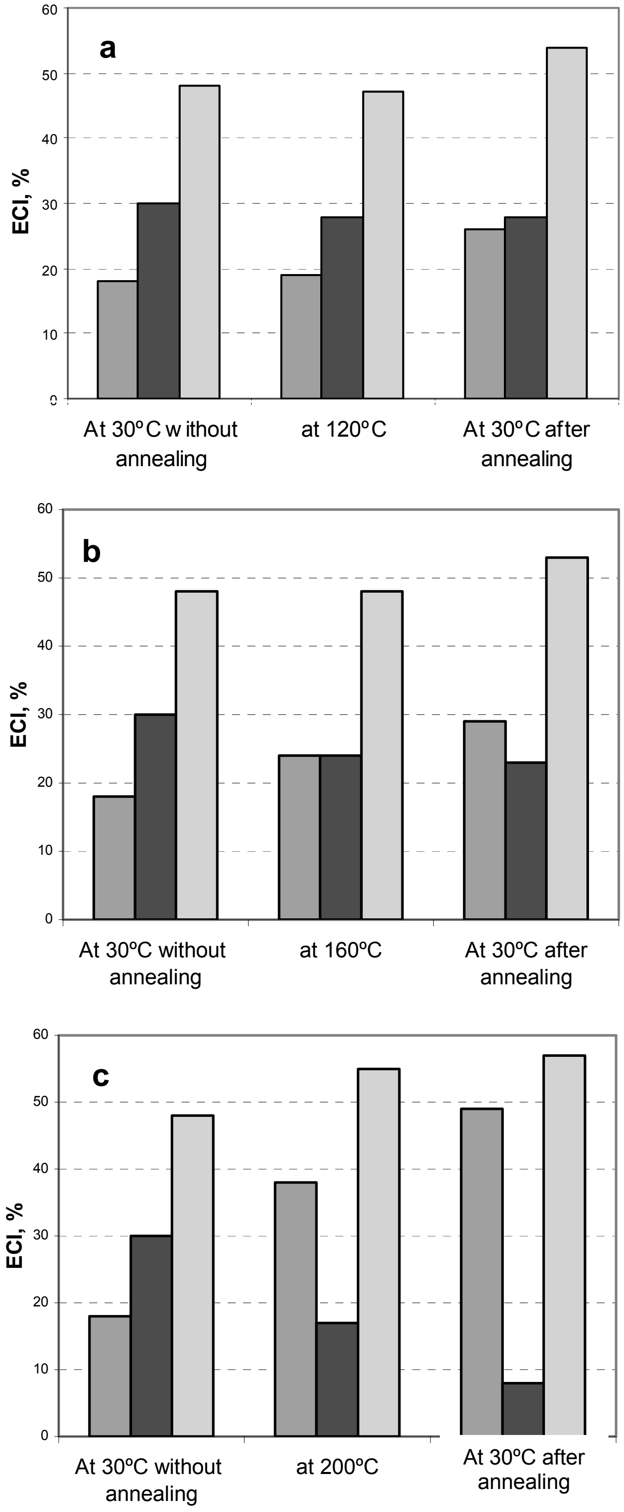

Figure 3.6 ECI and its α and γ-components in PA6 oriented cable as a function of the annealing temperature: (a) 120°C; (b) 160°C; (c) 200°C. ▨ α form concentration; ■ γ form concentration; □ ECI.

temperature range from 160 to 200°C, two processes contribute to the growth of α form: (i) crystallization of amorphous material forming α-crystals and (ii) a γ to α - form transition, the latter being better expressed above 160°C.

Figure 3.7 depicts the temperature dependence of L_B for PA6 cable annealed at various temperatures. Evidently, heating for 30 min at 120, 160 and 200°C results in a clear increase of the long spacing, whereby the higher the temperature of annealing, the larger the increase. Upon cooling from the respective temperature to 30°C, the trend is the same. This increase of L_B can be ascribed to the above-mentioned γ to α - transition, i.e. from morphology with extended parallel PA6 macromolecules (characteristic to the γ form) to morphologies with folded chains with anti-parallel orientation of the segments, typical of the α form of PA6.

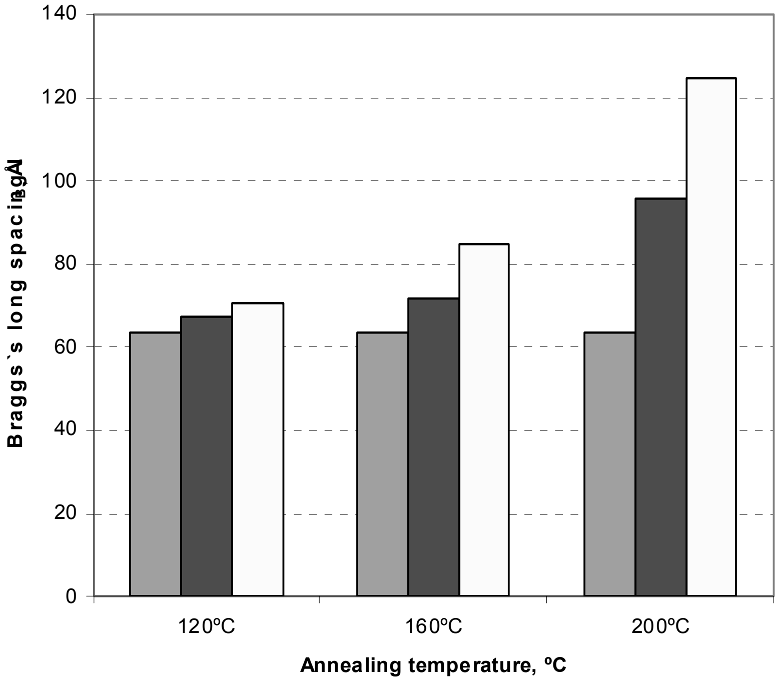

Figure 3.7 Bragg's long spacing L_B in PA6 cable as a function of annealing temperature:
▨ at 30°C, initial cable before annealing;; ■ in the corresponding temperature; ☐ at 30°C after 30 min annealing at the corresponding temperature.

Fig. 3.8 reveals the influence of annealing temperature on the d_{hkl} spacings of α and γ form crystalline planes in samples of differently annealed PA6 oriented cable irradiated at 30°C. It may be concluded that annealing at 120 and 160°C does not lead to well-expressed changes in the d_{hkl}-spacings, except for the b-axis of the γform (the $[\gamma_{020}]$ plane), which grows with almost 9% even after annealing at 120°C. The other unit cell edges suffer noticeable alteration (between 3 and 6%) only after treatment at 200°C.

These changes are different for the particular crystalline planes of the two forms. The d-spacings of the plane of H-bonded sheets, which are [002/202] for the α and [200] for the γ form show a trend towards decrease, whereas the d-spacings of the plane of van der Waals forces between the sheets of the two crystalline forms (α[200] and γ[001] planes) tend to increase. Hence, annealing at 200°C with a subsequent cooling to 30°C leads to the formation of PA6 crystallites, in which the distance between the macromolecules within the sheet is larger and the inter-sheet distance is shorter than in the sample without annealing or in those annealed at lower temperatures.

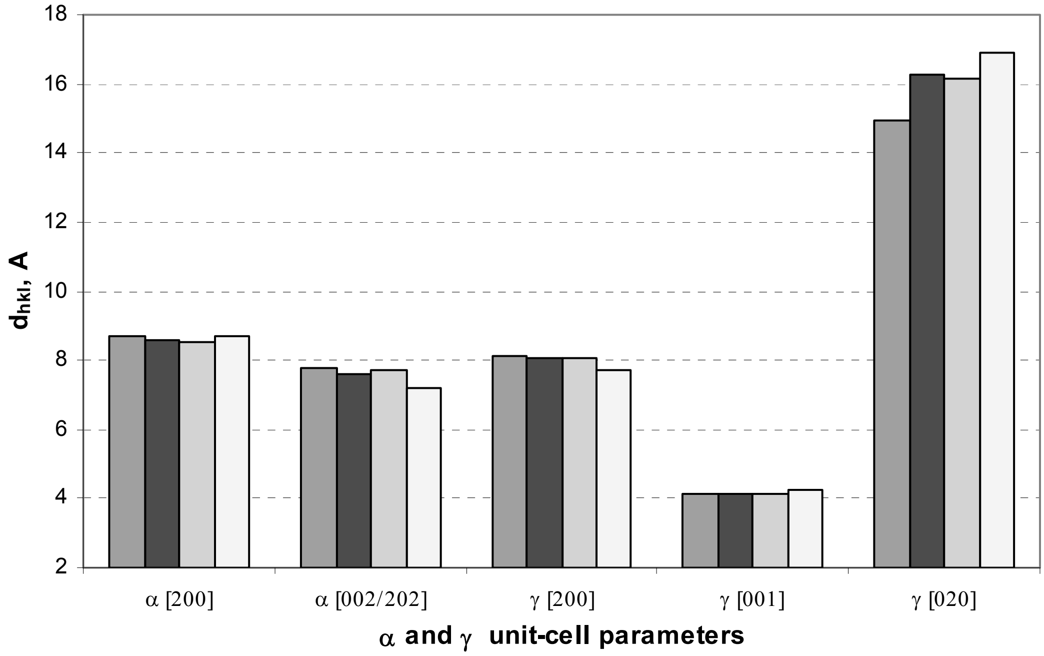

Figure 3.8 Changes in α and γ form unit cell parameters as a function of annealing temperature of oriented PA6 cable: ▨ no annealing; ■ after annealing at 120°C; ▧ after annealing at 160°C; □ after annealing at 200°C. All measurements are taken at 30°C.

3.5. Conclusions

1. Solid state ^{13}C NMR and WAXS studies revealed that in all four samples, irrespective of their mechanical and thermal histories, there is a co-existence of α and γ crystalline modifications of PA6. The α form always demonstrates a monoclinic lattice with two crystalline reflections, whereas the type of the γ form lattice depends on the thermal conditions at which it was created and can be hexagonal (with one) or non-hexagonal (with two reflections).

2. Heating of PA6 above 120°C always results in phase-to-phase transitions. These depend not only on the temperature (as repeatedly reported before), but also on the relative concentrations of the α and γ-crystalline forms in the starting sample. Between 120 and 160°C, a transition from the major to the minor crystalline phase takes place (for isotropic samples it is α to γ, and for the oriented cable from γ to α form) until reaching almost the same concentrations of the two forms. In the 160– 200°C range and especially close to the Brill temperature, γ to α-transition always occurs, irrespective of all other factors.

3. Heating above 120°C is related to L_B increase (in isotropic samples, owing to a growth of both l_c and l_a), as well as to changes in the unit cell parameters of the two crystalline forms, being the strongest at the highest temperature.

4. Quenching after melting always leads to PA6 crystallites predominantly in α form, whereby the small amounts of remaining γ form is with hexagonal lattice. Generally, the size of the resulting crystallites is smaller with decreased linear crystallinity x_{cl}.

5. Annealing of oriented PA6 cable at 120, 160 and 200°C always results in an increase of the α form content, even if the temperature is relatively low. This process is accompanied by a growth of L_B. Below the Brill transition, annealing does not change significantly the unit cell sizes of the two crystalline forms.

3.6. References

1. Varlot LK, Reynaud E, Kloppfer MH, Vigier G, and Varlet J*, J Polym Sci, Part B: Polymer Physics* 39:1360–1370 (2001).

2. Lin L, and Argon AS. *Macromolecules* 25:4011–4024 (1992).

3. Fornes TD,and Paul DR. *Polymer* 44:3945–3961 (2003).

4. Samon JM, Schultz JM, and Hsiao BS, *Polymer* 41:2169–2182 (2000).

5. Gurato G, Fichera A, Grandi FZ, Zannetti R, and Canal P, *Makromol Chem* 175:953–975 (1974).

6. Kyotani M, and Mitsuhashi S, *J Polym Sci Part A-2* 10:1497–508 (1972).

7. Brill RZ, *Phys. Chem.* B53:61–74 (1943).

8. Murthy NS, Aharoni SM, and Szollosi AB, *J Polym Sci Polym Phys Ed.* 23:2549–2565 (1985).

9. Murthy NS, Curran SA, Aharoni SM, and Minor H, *Macromolecules* 24:3215–3220 (1991).

10. Ramesh C, and Gowd EB, *Macromolecules* 34:3308–3313 (1991).

11. Lincoln DM, Vaia RA, Wang ZG, Hsiao BS, and Krishnamoorti R, *Polymer* 42:9975–9985 (2001).

12. Salem DR, Moore RAF, and Weigmann HD, *J Polym Sci, Part B: Polym Phys* 25:567–589 (1987).

13. Campoy I, Gomez MA, and Marco C, Polymer 39:6279–6288 (1998).

14. Okada A, Kawasumi M, Tajima I, Kurauchi T, and Kamigaito O, *J Appl Polym Sci* 37:1363–1371 (1989).

15. Murthy NS. *Polym Comm* 32:301-305 (1991).

16. Murthy NS, Bray RG, Correale ST, and Moore RAF, *Polymer* 36:3863-3873 (1995).

17. Murthy NS, Bednarczyk C, Moore RAF, and Grubb DT, *J Polym Sci Polym Phys* 34:821-835 (1996).

18. Rhee S, and White JL, *Polymer* 43:5903–5914 (2002).

19. Weeding TL, Veeman WS, Gaur HA, Huysmans WGB. *Macromolecules* 21:2028-2032 (1988).

20. Dencheva N, Nunes T, Oliveira MJ, Denchev Z, *Polymer* 46:887-901 (2005).

21. Stribeck N, Fakirov S, Apostolov, AA, Denchev Z, Gehrke R, *Macromol Chem Phys* 204:1000-1013 (2003).

22. Penel-Pierron L, Depecker C, Séguéla R, Lefebvre J-M, *J Polym Sci Polymer Phys* 39:484–495 (2001).

23. Alexander LE, *X-Ray Diffraction Methods in Polymer Science.* Huntington, New York: Robert E. Krieger Publishing Company, p. 342, 1979.

CHAPTER 4

RELATIONSHIP BETWEEN CRYSTALLINE STRUCTURE AND MECHANICAL BEHAVIOR IN ISOTROPIC AND ORIENTED POLYAMIDE 6

This chapter reports on the study carried out to investigate the relationship between the crystalline structure and the mechanics of differently processed PA6 samples. Their processing included thermal and mechanical treatments similar to those used in the MFC preparation. Thus, PA6 isotropic films and OC were prepared by compression molding or by consecutive extrusion and cold drawing. These samples were isothermally annealed in the 120–200°C range and then subjected to tensile tests at room temperature. Synchrotron WAXS and SAXS patterns were obtained before and after mechanical failure. These data were related with the mechanical properties of the respective PA6 samples.

The annealing of isotropic PA6 resulted in an increase in the modulus E and yield stress, σ_y, values, which was attributed to the observed proportional reduction of the d-spacings of the ISD in both the α PA6 and γ PA6 polymorphs. Analysis of the WAXS and SAXS patterns of isotropic PA6 after break allowed the supposition of structural changes in the amorphous phase, with these being better pronounced with increasing annealing temperature; this made the samples less ductile. In oriented PA6 samples, annealing resulted in a drastic increase in the E and σ_y values accompanied by a phase transition from γ PA6 to α PA6 and a well-pronounced reduction in the inter-sheet distances of both polymorphs. The stretching of the oriented samples led to an additional γ-to-α transition, whose extent was also related to structural changes in the amorphous phase.

4.1. Introduction

Of all the *n*-polyamides currently known and manufactured on an industrial scale, PA6 has achieved the widest commercial use and is the best studied. The processing of PA6 may be divided into three broad categories: melt spinning, extrusion, and injection molding. The end products are various types of yarns, films, sheets, rods, tubes, coatings of electric conduits, and so on [1]. As pointed out in Chapter 1, a recent application of PA6 is as reinforcing component in MFC.

All of these processing techniques comprise controlled heat and/or mechanical treatments that have important impact on the PA6 crystalline structure and, hence, on its mechanical properties. Although there are a large number of studies relating the structure or the properties of PA6 to the conditions of its orientation and annealing, relatively few works have been published so far on the relationship between the mechanical properties and crystalline structure. Galeski *et al* [2] studied the mechanisms of deformation of PA6 in uniaxial extension by means of X-ray scattering, microscopy, and calorimetric techniques. The stretching of PA6 reportedly led to the orientation of the α and γ crystals with macromolecular chains parallel to DD. It was also demonstrated that the α phase experienced a larger amount of breakdown between the planes determined by the hydrogen bonds compared to the γ phase. In plane-strain compression mode, Gasleski *et al* [3] also observed a shear-induced α – to – γ transition, which created small amounts of γ polymorph in the originally all-α-form crystalline phase. The latter underwent extensive deterioration by a chain-slip mechanism along the (002) planes containing the hydrogen bonds.

More recently, Lin and Argon [4] performed extensive structural and mechanical investigations on plastic deformation in PA6 by means of X-ray scattering and SEM. Quasi-single crystal PA6 samples were prepared by plain-strain compression at an elevated temperature in a channel die. Investigation of the crystallographic slip processes confirmed the conclusion that in the more stable α form, the (002) planes of the H-bonded sheets constituted the main active slip system. In a separate study Lin and Argon [5] also presented an interesting analysis of the crystal slip thermal activation.

Ito et al. [6] investigated the effects of the PA6 α and γ crystalline forms on deformation behavior. The α PA6 crystals were obtained from solution or melt under normal crystallization conditions. The α phase was converted into the γ form by iodine treatment. WAXS and SAXS techniques were used for structural characterization, and DMA was used to study the mechanical properties. The general conclusion was that the γ form was more ductile than the α form. However, the authors did not elucidate the potential influence on ductility of the profound chemical changes of the γ PA6 phase studied.

The mechanical behavior and structural evolution on uniaxial and biaxial drawing above the glass-transition temperature of PA6 films was studied in detail by Penel-Pierron *et al* [7] by means of WAXS, infrared spectroscopy (FT-IR), and DSC. The authors observed a higher ductility of PA6 in what they called the mesomorphic β form compared to samples in the γ and α forms. Under uniaxial drawing, a greater part of the β phase was shown to undergo strain-induced transition into α PA6, with the latter being more pronounced above 120°C. The γ phase, which was thermally stable up to 200°C, also transformed into α PA6. A structural explanation for the improved ability of PA6 for biaxial orientation at temperatures below 120°C was presented. It was related to the β-to-α phase reorganization at higher temperatures accompanied by a collapse of the van der Waals interactions between the sheets, which led to sample splitting under normal stress conditions.

This chapter contains a report on the mutual relationship between the crystalline structure and the mechanical behavior in oriented or isotropic PA6 samples containing different amounts of α and γ polymorphs. The main goal of this study was twofold: (i) to investigate the influence of the starting structure (*i.e.*, degree of crystallinity, content of α and γ polymorphs, and orientation) on the mechanical properties of the samples, *e.g.*, E modulus, yield stress σ_y, strain at yield, stress at break (σ_{br}), strain at break; and (ii) to elucidate the influence of strain on the crystalline structure after sample failure with changes in the crystalline phase taken into consideration.

For this purpose, synchrotron WAXS and SAXS patterns were obtained before and after mechanical failure of various PA6 samples and processed to extract information related to the crystallinity, d-spacings, long spacings, and phase transitions. An attempt was made to associate the WAXS and SAXS structural data with the mechanical properties of the samples.

4.2. Experimental Details

Two types of PA6 samples were prepared and studied [8]. The first one, designated as PA6 film, was obtained by the compression molding of as-supplied granules; it was preliminarily dried for 5 h at 90°C. The starting material was pressed at 250°C, and a pressure of 6 tons was applied for 5 min, which was followed by isothermal crystallization for 1 h at three different temperatures: 120, 160, and 200°C. The 200–250 mm thick films so prepared were cooled to room temperature at a rate of about 20°C/min.

The second sample, designated as PA6 oriented cable (OC), was prepared in the extruder line at a set temperature of 250°C (Chapter 1). The oriented PA6 OCs were annealed with free ends at 120, 160, or 200°C in an oven. Each annealing temperature was reached at a heating rate of 10°C/min. After 1 h of annealing at the respective temperature, the heating was switched off, and the sample was cooled at about 10°C/min until it returned to room temperature.

WAXS and SAXS measurements were performed in Setups 1 and 2 (Fig. 2.6) with PA6 samples before and after their mechanical failure applying the conditions and the data treatment procedures as previously described in Chapter 1.

4.3. Results

4.3.1. Mechanical Data

Figure 4.1 shows the stress–strain curves of differently annealed isotropic PA6 films [Fig. 4.1 (a)] and oriented cables [Fig. 4.1(b)]. All data extracted from these curves are presented in Table I.

Isotropic PA6 samples displayed an augmentation (from 40 to 50 MPa) of σ_y as the temperature of annealing increased, accompanied by a statistically significant growth in *E*. At the same time, the strain dropped (Table 4.I).

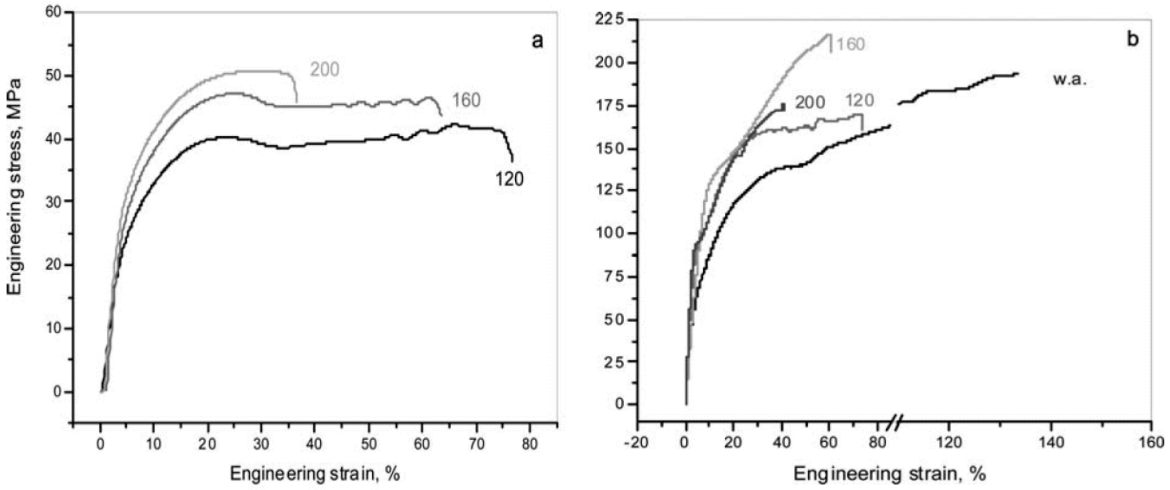

Figure 4.1 Stress–strain curves of various PA6 samples: (a) isotropic films annealed for 1 h at 120, 160, or 200°C and (b) oriented PA6 cables without annealing (w.a.) and annealed at 120, 160, and 200°C for 1 h. The curves represented were selected to best fit the averaged data in Table 4.1 Reprinted from [8].

The oriented PA6 samples demonstrated different stress–strain curves on annealing [Fig. 4.1(b), Table 4.1]. All samples showed two yield points, with the first being in the range between 66 MPa (cable without annealing) and 105 MPa (1 h at 160°C) and the second yield point being between 123 MPa (cable without annealing) and 180 MPa (1 h at 200°C).

Table 4.1 Mechanical properties of isotropic and oriented PA6 samples after various annealing procedures [8]

Sample	**Ann. Temp,** ºC (for 1 h)	**E** (GPa)	σ_y, (MPa)[a]	**Yield Strain** (%)	**Max. stress** (MPa)	**Max. strain** (%)	σ_{br}, (MPa)	ε_{br} (%)
Isotropic PA6	120	0.73 ± 0.02	42 ± 2	24 ± 2	44 ± 3	66 ± 18	17 ± 8	81 ± 18
Isotropic PA6	160	1,01 ± 0.04	47 ± 2	24 ± 3	47 ± 4	24 ± 3	30 ± 14	70 ± 18
Isotropic PA6	200	1.03 ± 0.04	51 ± 2	28 ± 3	51 ± 2	28 ± 5	41 ± 12	37 ± 6
Oriented PA6	- (w.a.)	0.99 ± 0.04	66 ± 2 123 ± 2	42 ±14	201 ± 17	149 ± 26	193 ± 16	150 ± 68
Oriented PA6	120	1.78 ± 0.12	88 ± 1 157 ± 2	36 ± 3	169 ± 19	72 ± 20	169 ± 19	74 + 20
Oriented PA6	160	3.18 ± 0.14	105 ± 2 170 ± 3	28 ± 5	223 ± 14	62 ± 13	223 ± 16	64 + 14
Oriented PA6	200	3.78 ± 0.17	103 ± 3 180 ± 2	25 ± 3	185 ± 9	47 ± 9	185 ± 9	48 ± 10

[a] Oriented cables displayed two yield points

After the second yield point, strain hardening occurred; this was better observable in the sample without annealing. This same sample showed the biggest strain at break (ε_{br}). As with the isotropic films, an increase in the annealing temperature led to a significant drop in the strain values, whereby the sample annealed at 200°C showed almost brittle failure. At the same time, E displayed an increase of more than three times and attained its maximum of 3.8 GPa for the sample heated at 200°C (Table 4.1)

4.3.2. 1D WAXS Measurement

1D WAXS patterns were obtained for isotropic (Fig. 4.2) and oriented (Fig. 4.3) PA6 samples initially annealed for 1 h at different temperatures in the 100–200°C range before and after tensile testing. After the curves were fitted as indicated earlier [9], data on the α and γ crystal fractions, as well as of the total CIs, were obtained (Table 4.2). In isotropic PA6 samples, the α form was the predominant one, and annealing in the 120–200°C range did not significantly change the relation between the two polymorphs. The respective CI values remained between 44 and 45%. Stretching until mechanical failure of these samples led to an increase in α CI, which was better expressed for the sample annealed at 120°C (by 10%). The γ crystalline fraction before and after sample failure remained unchanged or dropped slightly at the lowest annealing temperature.

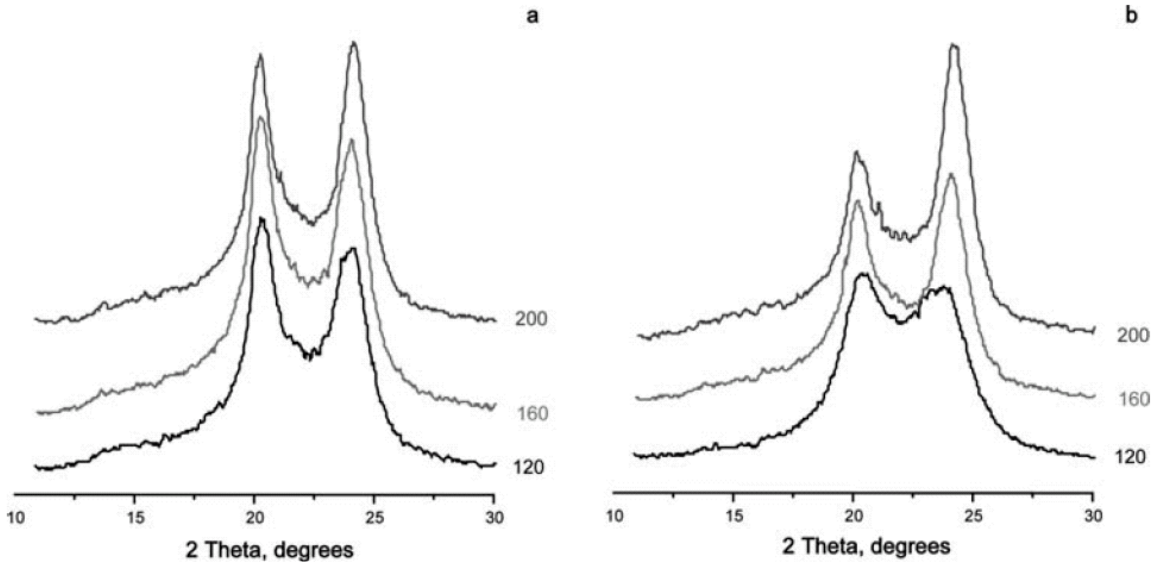

Figure 4.2 1D WAXS curves of isotropic PA6 films with annealing for1 h at different temperatures (a) before and (b) after tensile shear testing [8].

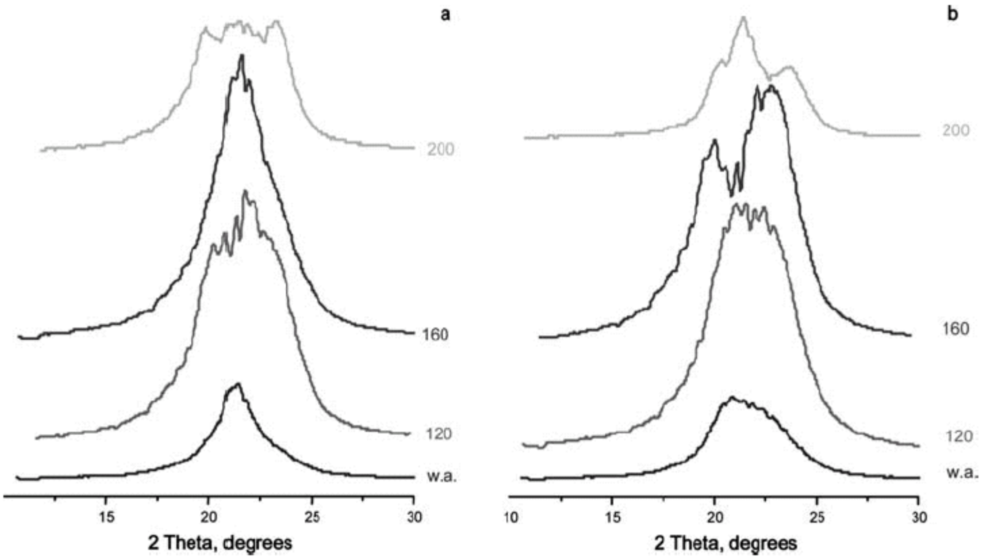

Figure 4.3 1D WAXS curves of oriented PA6 cables without annealing (w.a.) and with annealing for 1 h at different temperatures (a) before and (b) after tensile testing [8].

Figure 4.3 (a) and Table 4.2 confirm the finding in the previous chapter that oriented PA6 cables obtained by cold drawing to a high DR resulted in a crystalline structure containing more γ crystalline form than α crystalline form (33 vs 12%, respectively). Annealing of such cable in the 120–160°C range decreased the γ phase content 2–5 times, whereas the α type crystallinity grew at a similar rate. After 1 h at 200°C, this trend inversed with a slight decrease in the α phase content. When an external tensile stress was applied to the oriented cable without annealing, this led to additional transformation of the γ form to the α form. As shown in Table 4.2, the γ PA6 fraction decreased from 33 to 16%, whereas the α phase content grew from 12 to 32%. A similar trend was registered with the oriented PA6 samples annealed at 120 and 160°C. Stressing the sample annealed at 200°C caused the inverse transition: the γ CI value on the tensile tested sample was more than 10% higher than before the tensile test. At the same time, α CI decreased by 6%.

Table 4.2.Crystallinity data of the variously annealed isotropic and oriented PA6 samples [8]

Sample/ Ann. Temp. ºC (1 hour)	α_{200}, %	**$\alpha_{002}/\alpha_{202}$ %**	**αCI %**	γ_{001}, (%)	γ_{200} **(%)**	**γCI %**	**CI_{Total} or ECI**	**α/γ content**
PA6 isotropic 120ºC	17 (20)	21 (28)	38 (48)	4 (2)	2 (2)	6 (4)	44 (52)	6.3 (12)
PA6 isotropic 160ºC	17 (16)	22.(25)	39 (41)	4 (5)	2 (2)	6 (7)	45 (48)	6.5 (6.0)
PA6 isotropic 200ºC	14 (12)	23 (29)	37 (41)	4 (3)	2 (4)	7 (7)	44 (48)	5.3 (5.8)
PA6 oriented (w.a.)	5 (15)	7 (17)	12 (32)	24(8)	9 (8)	33(16)	45 (48)	0.4 (2.0)
PA6 oriented 120ºC	17 (18)	13 (27)	30 (44)	2 (7)	17(2)	20 (9)	50 (53)	1.5 (4.9)
PA6 oriented 160ºC	17 (11)	25 (30)	42 (40)	4 (5)	2 (1)	6 (6)	48 (46)	7.0 (6.7)
PA6 oriented 200ºC	16 (11)	20 (19)	36 (30)	4(16)	10 (9)	14(25)	50 (55)	2.6 (1.2)

Notes: The numbers in parenthesis are the respective values after mechanical failure of the corresponding sample. For the isotropic samples, CI_{Total} is the total crystallinity index representing the sum of the amounts of the α and γ polymorphs. In the oriented samples, ECI accounted for the intensity of the equatorial PA6 reflections without the meridional 020 reflections. (w.a. = without annealing)

4.3.3. 2D SAXS and 2D WAXS of isotropic PA6

Figure 4.4 shows the 2D SAXS patterns of differently annealed isotropic PA6 films before [Fig. 4.4 (a–c)] and after [Fig. 4.4 (d–f)] the mechanical tests. Figure 4.4 (g–i) also shows the 2D WAXS patterns of the respective samples after mechanical failure. As expected, the SAXS patterns of the samples before mechanical testing were non-oriented and of circular symmetry. They showed an almost homogeneous distribution of scattered intensity in the azimuthal angular region between -1.5 and 1.5 rad (Fig. 4.5, solid symbols).

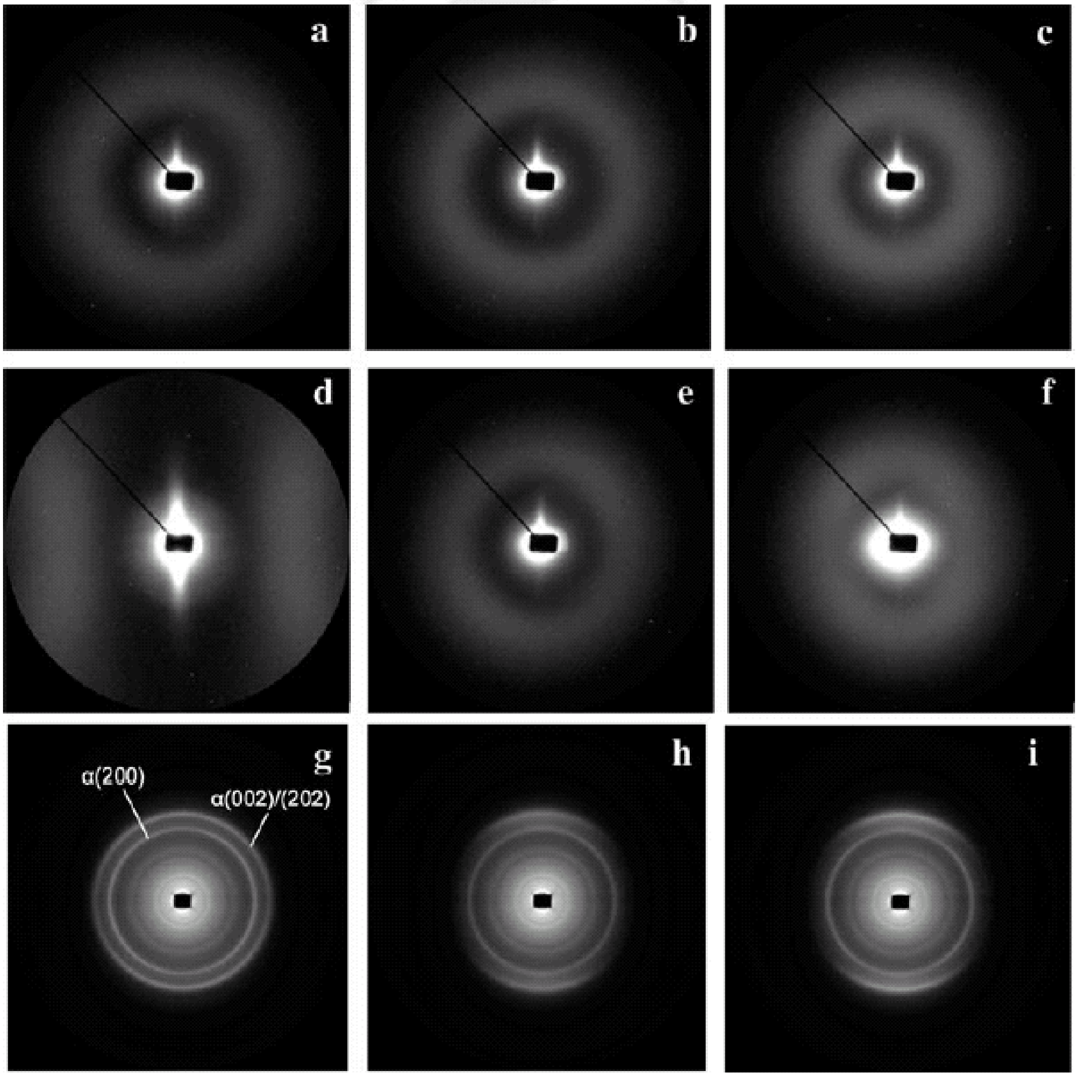

Figure 4.4 2D SAXS patterns of PA6 isotropic films annealed for 1 h at (a) 120, (b) 160, and (c) 200°C before tensile testing. (d–f) SAXS patterns of the same samples after testing; (g–i) 2D WAXS patterns of samples d–f [8].

Stretching to mechanical failure had a different effect on the orientation of the SAXS patterns, depending on the temperature of annealing. The sample annealed at 120°C, which attained the highest ε_{br} [Fig. 4.1 (a)], displayed an oriented SAXS pattern of fiber symmetry [Fig. 4.4 (d)]. Its azimuthal scan (Fig. 4.5, 120°C, open symbols) was a typical example of a four-point scattering diagram with a bimodal distribution of scattered intensity. There was a strong orientation in the direction of the applied stress. Interestingly enough, in the 2D WAXS pattern of this same sample [Fig.

4.4 (g)], the two Debye rings had apparent isotropic intensity distribution. Azimuthal scans in the above angular region showed an almost isotropic internal ring (α200) and some weak orientation in the external α(002)/(202) ring coinciding with the stretching direction [Fig. 4.6 (a)].

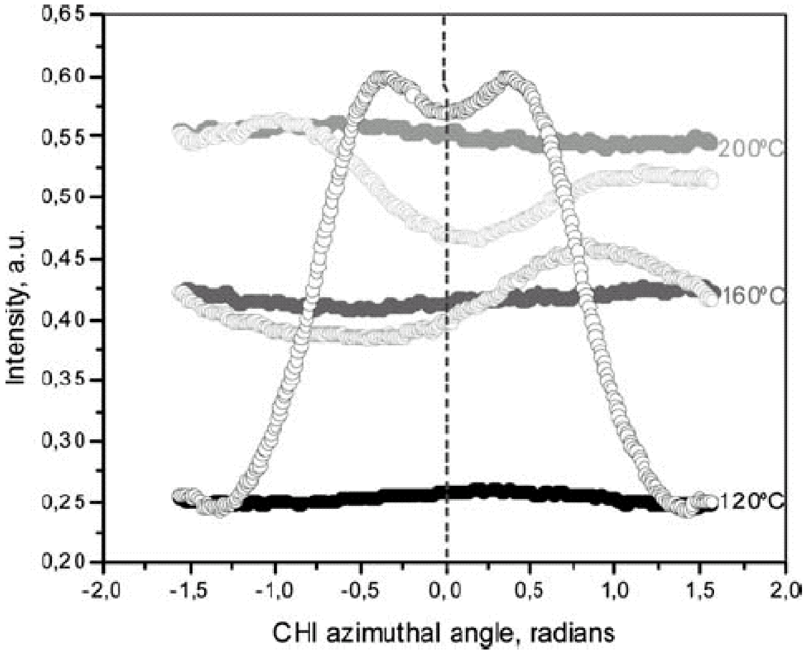

Figure 4.5 Azimuthal scans in the -1.5 – 1.5 rad azimuthal angle (CHI) region of the 2D SAXS patterns of differently annealed isotropic PA6 films before (solid symbols) and after (open symbols) mechanical failure [8].

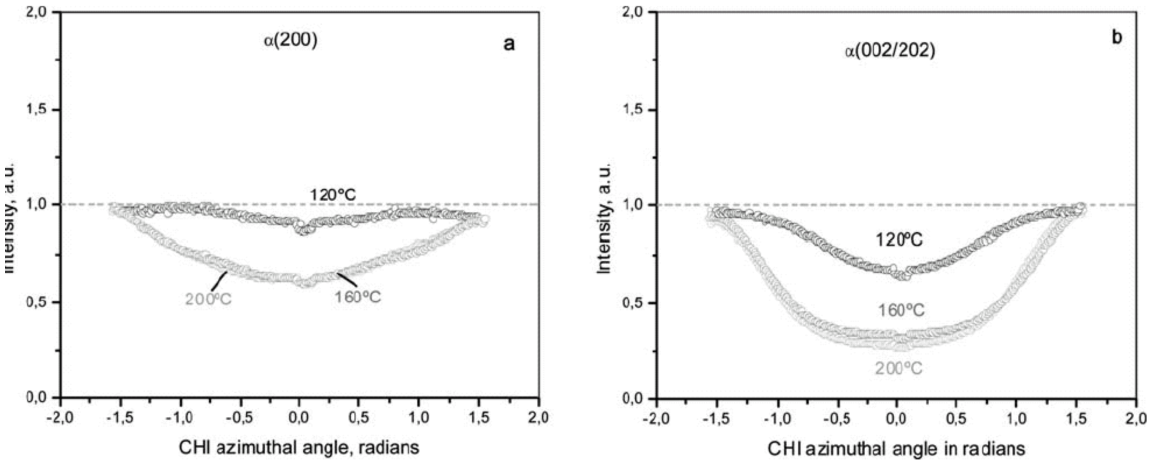

Figure 4.6 Azimuthal scans in the -1.5 – 1.5 rad azimuthal angle (CHI) region of 2D WAXS patterns of differently annealed isotropic PA6 films after mechanical failure for the (a) inner α(200) reflection and (b) outer α(002/202) reflection [8].

Annealing at 160°C caused the stretching of this sample to result in a much weaker orientation of the 2D SAXS pattern [Fig. 4.4 (e)] compared to that of the previous sample. The difference of the azimuthal distribution of the scattered intensity between the initial unstressed and the broken samples was quite small (Fig. 4.5). At the same time, the anisotropy of the α(002)/(202) WAXS refection [Fig. 4.6 (b)] was significantly stronger than the broken sample annealed at 120°C, which indicated a higher deformation of the crystalline phase. Similar effects were observed with the 2D SAXS and WAXS patterns of the sample annealed at 200°C and stretched to break [Fig. 4.4 (f,i)].

As shown in the corresponding azimuthal scans in Figure 4.6, the anisotropy of the two WAXS reflections were basically the same as those of the sample annealed at 160°C. The SAXS pattern after break of the film annealed at 200°C was slightly more anisotropic than that of the previous sample (Fig. 4.5)

Table 4.3 shows the evolution of the long spacing estimates of the isotropic PA6 samples as a function of the initial annealing temperature and stretching during the mechanical test.

Table 4.3 Long spacing estimates for differently annealed isotropic and oriented PA6 samples before and after the tensile stress test [8]

	Annealing of 1h at	***L* estimates$^{a)}$ Å**		**L_c Å**		**L_a Å**	
		Before	**After**	**Before**	**After**	**Before**	**After**
Isotropic PA6 films	120ºC	90-92	$71^{b)}$	67	-	25	-
	160ºC	91-94	97-98	68	63	26	34
	200ºC	101-105	103-107	67	64	36	41
Oriented PA6 cable$^{b)}$	w.a.	68	$-^{c)}$	-			
	100ºC	67	$-^{c)}$	-			
	120ºC	66	70	-			
	160ºC	69	73	-			
	200ºC	88	82	-			

Notes: The l_c and l_a were calculated from the respective linear CF;

[a] For the isotropic samples, L estimates include L_B, L_c^m and L_c^M values;

[b] For the oriented samples, the L_B values were obtained only after Lorentz correction and subtraction of the liquid scattering, I_b (See Equation 2.2)

[c] These samples did not show coherent SAXS scattering.

In the non-deformed samples, annealing at 200°C resulted in a clear growth of the L values. The latter was due to an increase in l_a to 36 Å with the respective values at 120 and 160°C being 25 and 26 Å. At the same time, the l_c values remained unchanged (67–68 Å). Mechanical failure of the samples annealed at 160 and 200°C resulted in a slight decrease of l_c, whereas the l_a values increased so that the resulting long spacings were slightly larger than those before the test. Only the isotropic sample annealed at 120°C, which after stretching showed an oriented 2D SAXS pattern, displayed a decrease in *L* of almost 20 Å.

4.3.4. 2D SAXS and 2D WAXS of oriented PA6

Table 4.3 also displays the long spacing values of all oriented cables before and after stretching. The L_B values of the oriented cables annealed up to 160°C before mechanical testing remained relatively constant in the same range of 67–69 Å. The cable annealed at 200°C, however, displayed a larger L_B of 88 Å. The stretching of all cables parallel to their fiber axis until failure resulted in slightly larger long spacings, with the exception of the cable annealed at 200°C, which showed a smaller *L*. All of the oriented 2D SAXS patterns were very similar to those shown in Figure 4.7 obtained with a cable annealed for 1 h at 160°C before [Fig. 4.7 (a)] and after [Fig. 4.7 (b)] tensile testing. All cables showed typical two-point scattering diagrams with a streak in the central region.

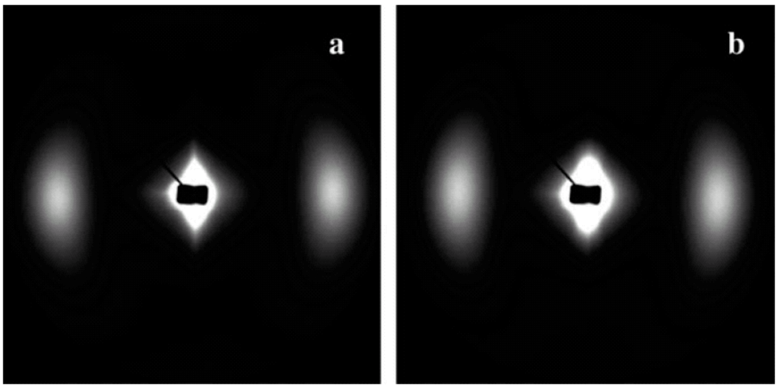

Figure 4.7 Typical 2D SAXS patterns of oriented PA6 cables (a) before and (b) after tensile testing. Before testing, the sample was annealed for 1 h at 160°C [8].

The 2D WAXS patterns of differently annealed PA6 cables taken before and after tensile testing are presented in Figure 4.8. Here, the aforementioned increase in the α form content that occurred as a result of annealing was best noticed in the sample heated for 1 h at 200°C before the tensile test [Fig.

4.8 (d)], whereas the cable without annealing showed the most pronounced growth of the α form content as a result of the tensile test [Fig. 4.8 (e)]. As shown by the differences in the diffracted intensity, the cable without annealing [Fig. 4.8 (e)] and that annealed at 120°C (f) suffered serious damage in their crystalline structures caused by stretching. This damage was more evident than that in the cables annealed at 160 and 200°C [Fig. 4.8 (g, h)]. Also, the (020) meridional point-like reflections of the γ PA6 were observable regardless of the fact that the content of this polymorph strongly decreased as a result of both annealing and stretching (Table 4.2).

The (020) reflections were used to calculate the b axis of the γ phase in all cables (Table 4.4). The rest of the d-spacings shown in Table 4.4 were extracted from the corresponding 1D WAXS patterns as a function of the annealing temperature and stretching. These data are analyzed in the next section.

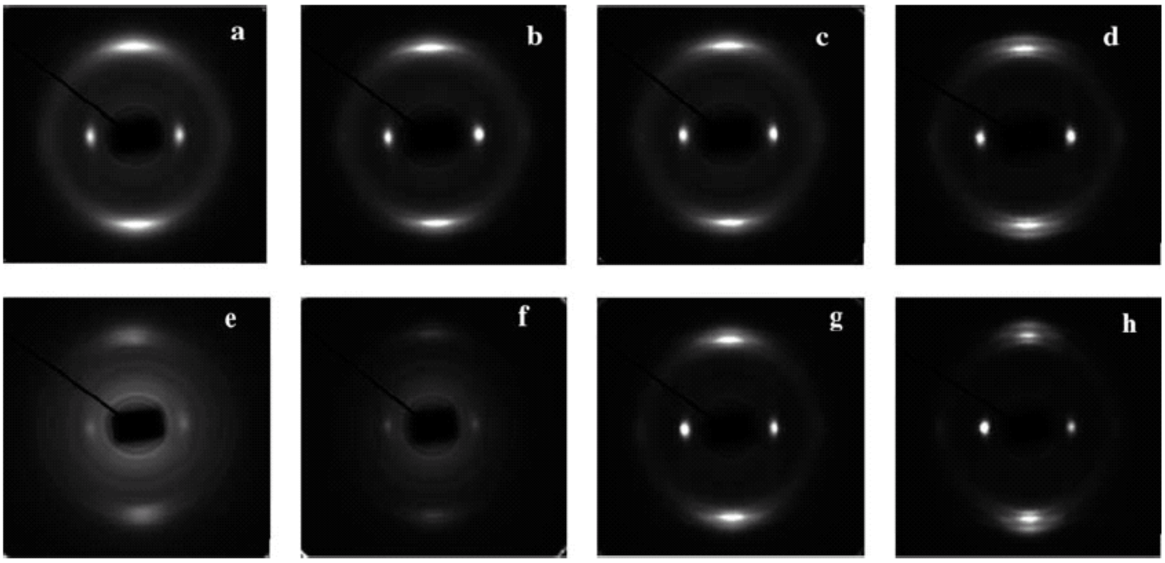

Figure 4.8 2D WAXS patterns variously annealed PA6 oriented cables before tensile testing: (a) without annealing, (b) annealing at 120°C, (c) annealing at 160°C, and (d) annealing at 200°C. (e–h) WAXS patterns of the same samples after tensile testing [8].

Table 4.4 Unit cell vectors and the corresponding d-spacings obtained from the 1D WAXS patterns of isotropic and oriented PA6 Samples as a function of their initial annealing before and after the tensile test that resulted in sample failure [8]

Annealing of 1 h	**$d_{\alpha 200}$**		**$d_{\alpha 002/202}$**		**$d_{\gamma 200}$**		**$d_{\gamma 001}$**		**$d_{\gamma 020}$**	
	Before	**After**	**Before**	**After**	**Before**	**After**	**Before**	**After**	**Before**	**After**
PA6 isotropic film										
At 120ºC	8.499	8.465	7.216	7.314	7.675	7.808	3.990	4.008	—	—
At 160ºC	8.522	8.566	7.197	7.187	7.682	7.649	4.011	4.002	—	—
At 200ºC	8.558	8.554	7.165	7.138	7.640	7.671	4.100	4.054	—	—
PA6 oriented cables										
Without annealing	8.610	8.453	7.467	7.544	7.800	7.828	4.080	4.105	16.858	15.300
At 120ºC	8.342	8.418	7.438	7.633	7.928	7.826	4.074	4.038	15.880	15.300
At 160ºC	8.522	8.566	7.197	7.187	7.682	7.649	4.011	4.002	16.028	14.640
At 200ºC	8.558	8.554	7.165	7.138	7.640	7.671	4.100	4.054	16.028	14.400

The **b** vector of the γ form was obtained from the meridional (020) reflection (Fig. 4.8).

4.4 Discussion

4.4.1. Isotropic PA6 films

Analyzing the stress–strain curves in Figure 4.1 (a) and the numeric data in Table 4.1, it becomes evident that the higher the annealing temperature was, the higher the E and σ_y values were, with the ε_{br} decreasing from 80 to about 40%. At the same time, X-ray analysis showed that annealing did not significantly change the crystalline structure of the isotropic PA6 films. As shown in Table 4.2, α PA6 was the preferable crystalline form, independent of the annealing temperature. The α form content varied in the range 37–39%, whereas the γ form content was 7%. The data in Table 4.3 demonstrates that annealing changed neither L's, nor the respective thicknesses of the crystalline and amorphous domains of the isotropic PA6. Only annealing close to the Brill transition point (190–200°C) resulted in an increase in L of about 10 Å, which was mainly due to the increase in l_a whereas l_c remained the same.

Regardless of the fact that all the characteristics of the crystalline structure (degree of crystallinity, polymorph type, and lamellar and amorphous domain thicknesses) did not change significantly under annealing, the tested PA6 isotropic samples displayed different tensile behaviors. It is known that the changes in E and σ_y values can be related to the crystalline phase [10]. The PA6 plasticity in particular was found to be governed by the crystal slip parallel to the H - bonded sheets, that is, parallel to the (002) crystalline plane in the α form and to the (200) crystalline plane in the γ form, without breakage of the H bonds [4,5,7] Therefore, σ_y of PA6 was controlled, on the crystallographic level, by the inter-sheet distance of the two crystalline forms, which corresponded to the d-spacings of the above planes. As shown in Table 4.4, the inter-sheet distance of the α type crystallite remained lower than that of the γ type within the entire annealing temperature range. Moreover, the increase in the annealing temperatures led to a decrease in the d(002) of the α form from 7,216 to 7.165 Å. Although the contribution of the γ form is very small (only 6–7% from the total CI), the d-spacing of the (200) plane in this polymorph also decreased from 7.675 to 7.640 Å. As a result, the critical resolved shear stress of the main sleep planes in both PA6 polymorphs became bigger at higher annealing temperatures and thus contributed to the σ_y growth.

Considering the 2D SAXS patterns in conjunction with the respective 2D WAXS images of the samples after tensile testing [Figs. 4.4 (d–f) and 4.4 (g, i), respectively] allowed a deeper insight into the relation between the structure and the mechanical properties of PA6 isotropic films. The α form content and total CI of all samples after break increased by 2– 10%; this was more notable in the sample annealed at 120°C (Table 4.2). When considered that the γ type crystallinity was almost constant, this increase could not be due to a phase transition but was probably a result of stress-induced crystallization of amorphous material into α PA6, which was better expressed with the sample annealed at 120°C. The same sample displayed, after break, a high anisotropy of the SAXS pattern along the DR and a significant decrease in L_B [Fig. 4.4 (d), Fig. 4.5 (120°C), and Table 4.3]. At the same time, in its WAXS pattern, the two Debye rings corresponding to the α(200) and α(002/202) reflections were entirely isotropic [Fig. 4.4 (g)]. Evidently, annealing at 120°C resulted in a quite ductile PA6 film with an amorphous phase susceptible to crystallization. Stretching increased the α form/γ form proportion almost twice (Tab. 4.2), mainly at the expense of strain-induced crystallization. The amorphous regions were those that bore the stress, whereby a microfibrilar structure was formed with such an alignment of the crystalline domains that led to a decrease in the L values [11]. As shown in Figure 4.4 (g), these crystalline domains deformed very slightly, without a change in the almost isotropic distribution of the scattered intensity along the (α200) or α(002/202) reflection (Fig. 4.6).

Unlike the PA6 film annealed at 120°C, the samples treated at 160 and 200°C had SAXS patterns after stretching that were much more isotropic [Fig. 4.4 (e, f) and Fig. 4.5], but the WAXS images showed more orientation along DR, especially of the outer α(002/202) reflection. As also shown in the respective 1D WAXS patterns in Figure 4.2, the sample annealed at 200°C suffered the strongest changes in its crystalline structure after break. It can be concluded that after annealing at 160 and 200°C, the external stress applied led to the deformation of the crystalline phase rather than to the deformation of the amorphous phase. It seems that annealing at elevated temperatures provoked a certain hardening of the amorphous domains that could not be accounted for by SAXS and WAXS but affected the deformability of the isotropic PA6. The existence of a harder (also called rigid) amorphous phase in the PA6 fibers was proven by solid state ^{13}C NMR and ^{1}H NMR [12-14]. Again, in the PA6 fibers, the presence of an oriented fraction in the amorphous phase has been discussed [15, 16]. There have been no reports so far relating the changes in the mechanical properties of isotropic PA6 (e.g., E, stress, and strain values) to alterations in its amorphous structure on annealing, as suggested in this study.

4.4.2. Oriented PA6 cables

The stress–strain curves of all PA6 cables [Fig. 4.1 (b)] were characterized by double yield, with the two σ_y values increasing linearly with the annealing temperature (Table 4.1). Another observation was a drop in the ductility as the annealing temperature increased. The biggest ε_{br} and concomitant strain hardening was displayed by the sample without annealing, whereas the PA6 cables annealed above 160°C exhibited an almost brittle failure. As to the *E* values, they were also affected by annealing: the higher the temperature, the bigger the *E*.

The explanation of the tensile behavior of the annealed PA6 cables was related to the alterations in their respective crystalline structure. As shown in Table 4.2, the preferable crystalline modification for non-annealed cable was the γ form. On annealing, the γ-to-α form transition started; this was better expressed above 120°C. The α polymorph became the predominant crystalline form for cables annealed between 120 and 200°C. Table 4.2 also shows that ECI increased slightly (by 3–5%); this indicated that some formation of α form crystals out of the amorphous material also occurred. The SAXS results showed that the γ-to-α phase transition and the additional crystallization did not result in alterations of L_B when the annealing temperature was up to 160°C (Table 4.3). Annealing in the 160–200°C range, however, caused a growth in the L_B values of approximately 20 Å. It was not possible to determine the discrete contribution of the two thicknesses (l_c and l_a) to the said growth because the linear CF was not applicable for samples with fibber symmetry. Because CI after annealing did not change significantly, the bigger L_B after annealing at 200°C could hardly be related to l_c growth due to lamellar thickening. Moreover, as shown in Table 4.4, the d-spacings of all planes decreased, which meant that the thermal expansion should also be excluded as a possible reason for the increase in L_B. It could be supposed, therefore, that some structural changes in the amorphous domains occurred during annealing at 200°C and the subsequent cooling to 30°C, which contributed to the L_B change.

One can consider that the aforementioned γ-to-α form transition occurring on annealing was the main reason for the increase in *E* and σ_y. The γ PA6 polymorph was shown to be more ductile, whereas the α polymorph was characterized by a bigger tensile strength [6,7]. Because with the increase of the annealing temperature the α form became predominant, it was expected that PA6 cables annealed at higher temperatures would display bigger σ_y values, as was really the case. From the point of view of crystal slip-governed plasticity, this behavior could be related to the decrease in the inter-sheet distance in the two crystalline forms when annealed. As shown in Table 4.4, the d-spacing of the (002)/(202) crystalline plane, which corresponded to the inter-sheet distance of the α form, remained smaller than that of the respective plane (200) in the γ form for each annealing temperature. In addition, the said distance decreased from 7.467 to 7.165 Å for the α form and from 7.800 to 7.640 Å for the γ form when the annealing temperature was increased to 200°C. Annealing, therefore, as in the case of the PA6 isotropic films, increased the critical resolved shear stress of the main slip planes in both the α and γ polymorphs of oriented PA6 cable, which thus led to higher σ_y and E values.

With regard to the appearance of two yield points, this could not be unambiguously related to the crystal slips occurring in the respective γ type and α type crystallites. There will have always been a contribution by the amorphous phase, provided that the tensile tests were made at room temperature, that is, below the T_g of the material. The PA6 isotropic films, however, were also tested at room temperature, and both α and γ polymorphs were also present. Nevertheless, the respective stress–strain curves showed different behaviors. The observed double yield is more likely related to the appearance of the oriented fraction in the amorphous phase rather than to the presence of two polymorphs. The presence of such an oriented fraction was proven in oriented PA6 fibers [16]. One may suppose that the cold drawing used for the preparation of the PA6 cables in our case also may have generated an inhomogeneous amorphous phase that could have had an impact on yielding.

The effect of stretching on the structure of the PA6 oriented samples was related to a clear, stress-induced γ-to-α transition. Interestingly, the latter depended on the annealing temperature. The stretching of the cables with no annealing or with 1 h of annealing at 120°C resulted in a very accentuated phase transition, whereas with annealing at 160°C, this trend became weaker and even inverted when annealing at 200°C was applied (Table 4.2, Fig. 4.8). One may suppose that the amorphous phase had an important influence on the phase transitions in the crystalline domains. When it was more flexible, as in the case of cables without annealing or with 1 h of annealing at 120°C, the stress-induced crystalline modifications were more intense. On the contrary, when there was a hardening of the amorphous phase at higher annealing temperatures, this impeded the crystalline phase transitions. Most probably, this effect had to do with the effectiveness of the transfer of the external stress to the crystalline domains.

4.5 Conclusions

The PA6 isotropic films obtained by the compression molding of granules were predominantly in the α crystalline form, whereas the γ form was the preferred form for PA6 cables obtained by extrusion and consequent cold-drawing. The annealing applied did not significantly change the crystalline structure of isotropic films but caused a γ-to-α form transition in the oriented cables. Both isotropic and oriented PA6 showed a growth in the E and σ_y values with increasing annealing temperature. This behavior was explained, on a crystallographic level, by a decrease in the d-spacing of the main crystal slip planes of the two polymorphs after annealing. The external stress applied led to additional γ-to-α form transitions in both the isotropic and oriented PA6 samples, whereby the higher the annealing temperature was, the weaker the inclination to the stress-induced transition it caused. This effect was attributed to the possibility of the formation of a hard fraction (PA6 films) or an oriented fraction (PA6 cables) in the amorphous phase.

4.6. References

1. Aharoni SM, n-Nylons, Their Synthesis, Structure and Properties, John Wiley & Sons: New York, 1997, p. 316-317.
2. Galeski A, Argon AS, and Cohen RE, *Macromolecules* 24:3945 (1991).
3. Galeski A, Argon AS, and Cohen RE, *Macromolecules* 24:3953 (1991).
4. Lin L, Argon AS, *Macromolecules* 25:4011 (1992).
5. Lin L, and Argon AS, *Macromolecules* 27:6903 (1994).
6. Ito M, Mizuochi K, and Kanamato T, *Polymer* 39:4593 (1998).
7. Penel-Pierron L, Seguela R, Lefebvre J-M, Miri V, Defecher C, Jutigny M, Pabiot,. J *Polym. Sci. Part B: Polym Phys* 39:1224 (2001).
8. Dencheva N, Denchev Z, Oliveira MJ, Funari SS, *J Appl Polym Sci* 103:2242 (2007)
9. Samon JM, Schultz JM, and Hsiao BS, *Polymer* 41:2169 (2000).

10. Schrauwen BAG, v. Breemen LCA, Spoelstra AB, Govaert LE, Peters GWM, and Meijer HE, *Macromolecules* 37:8618 (2004).

11. Stribeck N, Extraction, representation and interpretation of nanoscale domain structure information from small-angle scattering patterns, *Conference on X-ray Investigations of Polymer Structures (XIPS 2001)*, 5-8 December, 2001 Bielsko Biala, Poland

12. Schreiber R, Veeman WS, Gabrie1lse W, and Arnauts J, *Macromolecules* 32:4647 (1999).

13. Litvinov VM, and Penning J P, *Macromol Chem Phys* 205:1721 (2004).

14. Buda A, Demco DE, Bertmer MB, Blu1mich B, Litvinov VM, and Penning JP, *J Phys Chem* 107:5357 (2003).

15. Murthy NS, Minor H, Bednarczyk C, and Krimm S, *Macromolecules* 26:1712 (1993).

16. Murthy NS, Bray RG, Correale ST, and Moore RAF, *Polymer* 36:3863 (1995).

CHAPTER 5

CRYSTALLINE STRUCTURE OF POLYAMIDE 12 AS REVEALED BY SOLID STATE NMR AND SYNCHROTRON X - RAY STUDIES

In this chapter the study on the crystalline structure of PA12 by solid-state ^{13}C NMR as well as by synchrotron WAXS and SAXS will be reported. Isotropic and oriented PA12 showed different NMR spectra ascribed to γ and γ' crystalline modifications, respectively. On the basis of the position of the first diffraction peak, the isotropic γ form and the oriented γ' form were shown to be with hexagonal crystalline lattice at room temperature. When heated, the two PA12 polymorphs demonstrated different behaviors. Above 140°C the isotropic γ PA12 partially transformed into α modification. No such transition was observed with the oriented γ' PA12 phase even after annealing at temperatures close to melting. A γ'–γ transition was observed here only after isotropization by melting. Various structural parameters were extracted from the WAXS and SAXS patterns and analyzed as a function of temperature and orientation: the degree of crystallinity, the d-spacings, L_B, l_c, l_a and x_{cl} values.

5.1. Introduction

Crystalline structure and polymorphism of polyamides obtained by ring-opening polymerization have been studied by many researchers [1–14]. It is generally accepted that these polymers possess layer-like structure formed by hydrogen-bonded sheets. As pointed out in the previous chapter, two basic crystalline modifications designated as α and γ forms were established for the first time in PA6, and subsequently shown to exist in other polyamides with even number of carbons. The α crystalline form was originally proposed by Holmes et al., introducing the concept of a crystalline structure consisting of sheets made of hydrogen-bonded, fully extended, anti-parallel polymer chains [1]. In a more recent study, Arimoto et al [2] described for the first time that the γ crystalline form of PA6 is composed of pleated sheets of parallel chains joined by hydrogen bonds. To enable hydrogen bond formation in this crystalline form, amide linkages should twist by approximately 60° out of the plane of the molecular sheets, which explains the smaller unit cell [2,3] and the less-expressed hydrogen bonding [4] in the γ crystal as compared with those of the α crystal.

Similarly to PA6, polyamide PA12 may also crystallize in α and γ crystalline modifications, the more stable one being the γ form [5]. Depending on the crystallization conditions, four PA12 polymorphs designated as α, α', γ, and γ' were reported. The α polymorph can be obtained under the following conditions: crystallization from the melt at a pressure above 500 MPa [6], precipitation from phenol–ethanol solution [7], or by drawing [8] close to the melting point. It is generally accepted that the PA12 α form is monoclinic with two clearly defined WAXS reflections having d-spacings at about 0.37 and 0.44 nm, respectively [9]. The α' polymorph of PA12 has been observed near melting [9] also showing a WAXS pattern with two crystalline reflections located, however, closer to each other as compared with those of the α PA12.

The main crystalline form obtained by melt crystallization of PA12 at atmospheric pressure is the γ form, whereas the polymorph obtained by cryogenic quenching from the melt and subsequent crystallization at 60°C is denoted as γ' modification [10]. The γ and γ' phases of PA12 have similar WAXS patterns. A hexagonal lattice has been assigned to both, characterized by only one strong reflection corresponding to a d-spacing of about 0.42 nm [9]. Deviations from the hexagonal unit cell were also reported, leading to suppositions of pseudo-hexagonal [11] or monoclinic [12] crystalline lattice.

As regards the transitions between the four PA12 polymorphs, it was reported that thermal treatment under pressure gives rise to a γ'- to - α form transition, whereas the same treatment does not change the γ crystalline form [6,13]. The γ' structure can be transformed into α form also by annealing above 110°C at atmospheric pressure [13]. In their early WAXS study, Northolt et al. [14] investigated the effect of drawing on the structure of PA12. Two samples were studied drawn 4.5 and 7 times. The difference in the 2D WAXS patterns was attributed to two different forms. Hiramatsu et al [13] reported later that drawing above 50 and 70 °C could result in γ–γ' or α–γ' transitions, respectively. Ishikawa et al [8] observed a partial γ- to - α form transition occurring while drawing at temperatures near the melting point.

It may be concluded that the crystalline structure of PA12 is very sensitive to the crystallization conditions and the mechanical treatment. The experimental data on PA12 polymorphism available up to now are scarce and not very well outlined. Direct comparison of structural data obtained by different researchers does not seem to be straightforward because of the variations in sample material (different PA12 polymers), incomparable thermal histories, and different sample preparation and characterization.

In this chapter a report is made on the crystalline structure and phase transitions in PA12 samples based on the same polymer grade, as a function of their thermal history and orientation. To shed more light on PA12 polymorphism, a combination of solid-state ^{13}C NMR and synchrotron WAXS and SAXS techniques was used, which has not been communicated with PA12 samples as yet.

5.2. Experimental details

Three different PA12 samples were investigated [15]. The first sample designated as 'PA12 granules' was as supplied granules with no initial mechanical or heat treatment. The second sample was called oriented cable, and was prepared by melting the granules in a melt flow index apparatus, followed by drawing of the resulting cables until undergoing neck formation at a temperature of about 100°C. Some oriented PA12 cables were annealed with free ends at 120, 130, 140, and 165°C in a hot stage and designated as 'annealed oriented cables'. Each of these annealing temperatures was reached at a heating rate of 10deg/min. After 30 min annealing at the respective temperature, the heating was switched off to allow the sample to return to room temperature.

5.3. Results

5.3.1. Solid-state NMR studies

MAS/CP-DD ^{13}C NMR spectra of PA12 granules and the PA12 oriented cable were obtained and analyzed. Figure 5.1 shows the extended aliphatic region of the PA12 granules (a) and the PA12 oriented cable (b). The peaks of the carbonyl group C-atoms appear at about 170 ppm and are not shown in Figure 5.1 (a,b). To better resolve the overlapping signals in the aliphatic region, peak fitting was performed. The corresponding data, for example, chemical shifts, full widths at half maximum, and intensities are summarized in Table 5.1. The table also contains chemical shift data for non-oriented α, γ, and γ' crystalline forms of PA12 as obtained by Mathias and Johnson [16].

Comparing the reference data with those of the PA12 granules, the peak at 30.4 ppm in the spectrum of the PA12 granules can be attributed to the carbons of the methylene groups in gauche conformation; at 33.1 ppm, to the all-trans methylenes; at 36.5 ppm, to the C-atom located next to the carbonyl group (C_α); and at 39.9 ppm, to the one next to the amide N-atom (C_N) [Fig. 5.1 (a), Table 5.1]. The resonance at 172.9 ppm belongs to the carbonyl C-atom. The signal of the carbon in β-position with respect to the carbonyl group, C_β , appearing as unresolved shoulder, after peak fitting, is shown to be centered at 26.9 ppm.

.

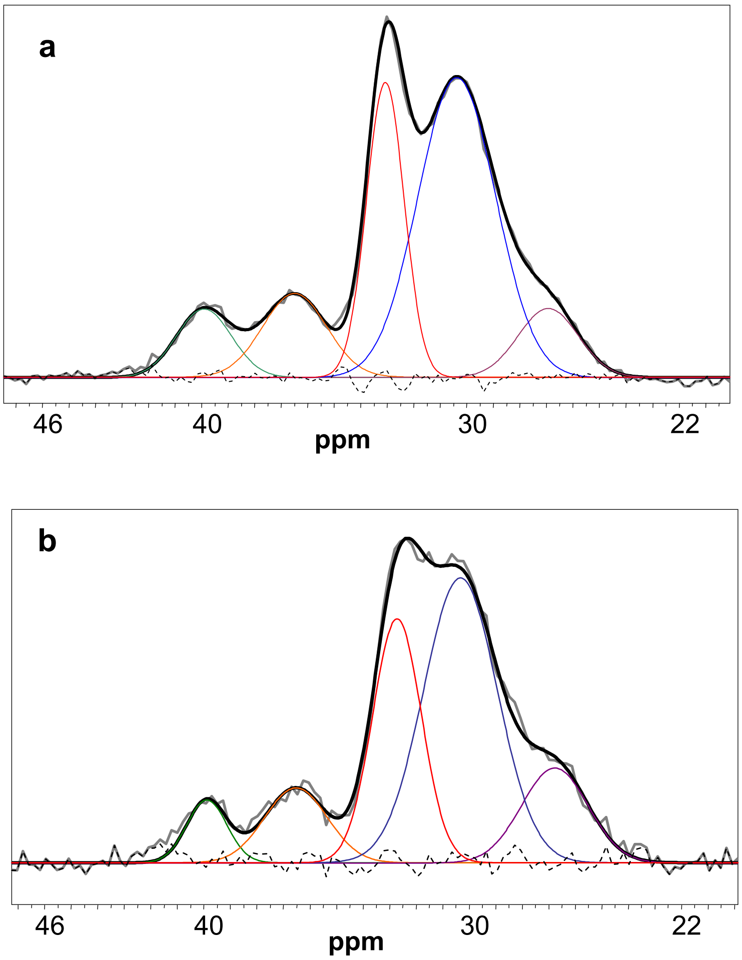

Figure 5.1 MAS/CP-DD 13C spectra of PA12 samples at 20°C (gray lines) showing the aliphatic carbon region of (a) PA12 granules and (b) PA12 oriented cable. Simulated individual peaks (thin solid lines), composite spectra (thick solid lines), and residues (dashed lines) are also displayed. (Reprinted from [15])

The spectrum of the PA12 oriented cable [Fig. 5.1 (b), Table 5.1] is similar to that of the granules containing the same carbon resonances with similar shifts. However, the signal of the carbonyl C-atom is shifted downfield with 0.5 ppm with respect to that of PA12 granules, and the peak of all-trans methylenes is shifted upfield with about 0.4 ppm (Table 5.1). Furthermore, the intensity ratio of the all-trans to gauche methylenes is different: in the isotropic sample [Fig. 5.1 (a)], this ratio is 1:1, whereas upon orientation [Fig. 5.1(b)] it changes to 0.85:1.00 (Table 5.1).

Table 5.1 Chemical Shifts for Each Indicated Aliphatic Carbon Obtained by Fitting of the MAS/CP-DD 13C Spectra of PA12 Granules and PA12 Oriented Cable. Experimentally Measured Chemical Shifts for the C=O Carbons Are Also Shown [15]

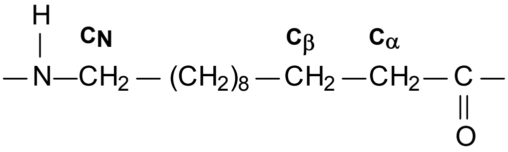

$$-\overset{\overset{H}{|}}{N}-\overset{C_N}{CH_2}-(CH_2)_8-\overset{C_\beta}{CH_2}-\overset{C_\alpha}{CH_2}-\underset{\underset{O}{\|}}{C}-$$

Sample	**Chemical shifts of carbons, ppm; (FWHM, Hz; Intensity, a. u.)**					
	C_β	**CH_2 – gauche**	**CH_2--all trans**	**C_α**	**C_N**	**C=O**
α-PA12[a]	27.3	30.9	34.2	38.9	43.0	172.9
γ-PA12[a]	~ 28	30.3	33.6	37.3	39.8	173.1
γ´-PA12[a]	~ 27	30.8	33.1	37.0	40.3	173.6
PA12 granules	26.9 (201; 5.7)[b]	30.4 (260; 24.7)	33.1 (126; 24.3)	36.5 (214; 6.9)	39.9 (185; 5.6)	172.9
PA12 Oriented cable	26.8 (222; 6.3)	30.3 (248; 24.0)	32.7 (164; 20.6)	36.5 (210; 6.3)	39.9 (134; 5.3)	173.4

Notes:

a) Data from ref.18.

b) Values in parentheses indicate full width at half maximum (FWHM) in Hertz and intensity in arbitrary units.

From the reference data in Table 5.1 it may be seen that the biggest differences between α and the two γ forms are in the chemical shifts of C_N and C_α signals. In the α PA12 form, they are shifted downfield with almost 3 ppm. Since this shift is by far above the accuracy of NMR peak positions, the C_N and C_α chemical shifts can be used to prove the presence of α form. The spectra of the PA12 granules and the PA12 oriented cable do not display any resonance lines above 40 ppm and they also display no peaks around 38.9–39.0 ppm. This finding rules out the presence of α form in both PA12 granules and PA12 oriented cable at room temperature. However, to prove which of the γ forms corresponds better to their structure is not so straightforward. Analyzing the chemical shifts and intensities in Table 5.1 and using the approach of Mathias and Johnson [16], the crystalline form of PA12 granules was designated as γ isotropic, and that of the PA12 cables as γ’ oriented. More details are presented in the Discussion part of this chapter.

5.3.2. WAXS studies

Figure 5.2 shows the 2D WAXS patterns of PA12 granules (a) and of a PA12 oriented cable annealed for 30 min at 160 °C (b).

The first pattern is isotropic. A heating ramp in the 30–175°C range does not change apparently the number of rings in the image and their intensity. The pattern in Figure 5.2 (b) proves the strong orientation in the PA12 drawn sample, the draw direction being vertical. Heating and cooling cycles in the 30–175°C range (*i.e.* before melting) change this pattern only slightly, mostly the intensities of the arc- and point-like reflections. Melting with isotropization at 200°C, followed by cooling and irradiating at 30°C, result in an isotropic pattern similar to that in Figure 5.2 (a).

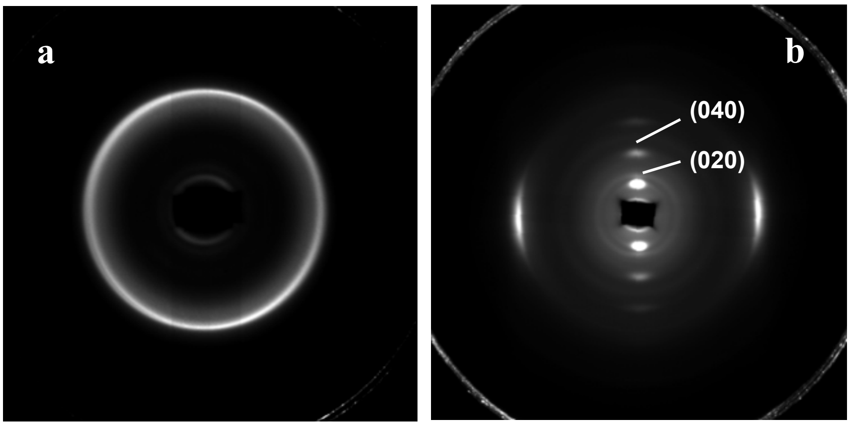

Figure 5.2 2D WAXS patterns of: (a) PA12 isotropic granules at 160°C; (b) oriented PA12 cable annealed for 30 min at 160°C, image taken at 30°C. The draw direction in (b) is vertical and “b” axis is the chain axis [15].

Figure 5.3 shows the 1D WAXS curves of PA12 granules during in-beam heating. The pattern at 30°C contains a crystalline peak at about 2θ =21.2° corresponding to a d-spacing of 0.410 nm.

The study of Ramesh [9] reports a value of 0.42 nm assigned to the γ crystalline form. As the temperature increases to 175°C, the angular position of this peak shifts slightly to the smaller 2θ values and its width and form change. Above 100°C, a shoulder in the lower 2θ region appears, becoming better expressed with the increase in temperature. This effect is in good agreement with other studies on PA12 [9,10] which have reported the appearance of crystalline material in α form coexisting with the γ crystals at elevated temperatures. Figure 5.3 also shows that melting of the sample at 200°C and cooling down to 30°C restores the initial γ crystalline structure and no α form is detectable anymore.

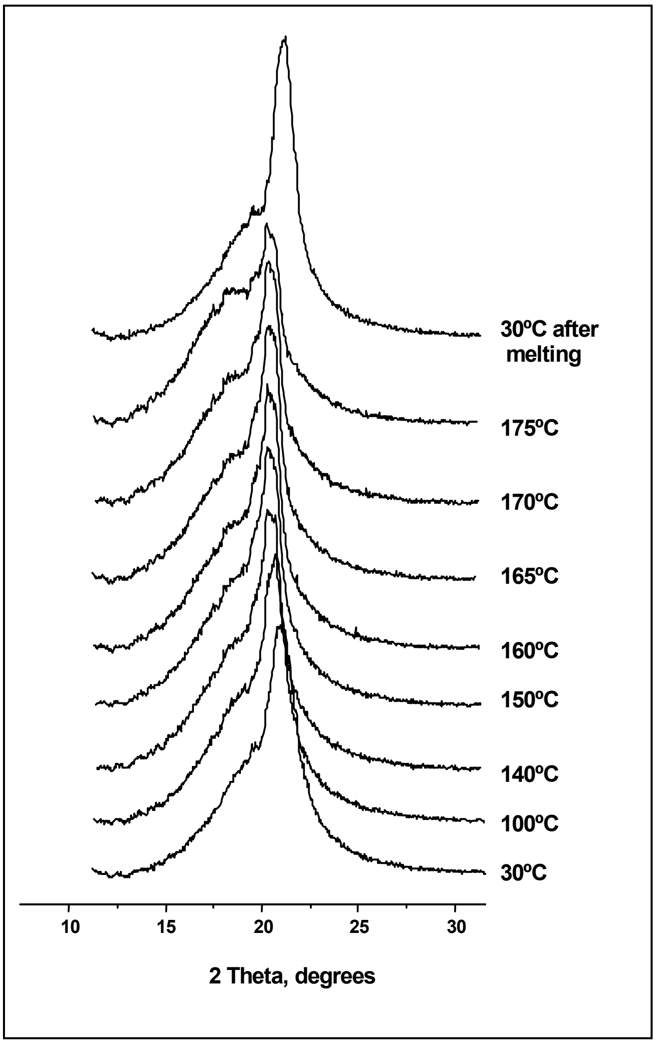

Figure 5.3 1D WAXS profiles of PA12 granules obtained after keeping the sample for 30 s at the respective temperatures. The curves are shifted along the y axis [15].

Figure 5.4 shows the WAXS profiles of PA12 oriented cable obtained at various temperatures while heating in the 30–170°C range. Two more patterns obtained at 30°C after fast cooling, before and after melting, respectively, are also included for comparison. A crystalline peak at 2θ = 20.9° (d = 0.414 nm), slightly dependent on the temperature, is observed as in the previous case, indicating again the presence of γ type crystalline structure. However, this sample behaves differently when heated. As the temperature increases, no additional crystalline peaks appear in the curves of Figure 5.4, and the present one becomes narrower and more symmetric. This is an indication that heating of PA12 oriented cable results only in a more perfect crystalline phase, with no phase transition taking place. Rapid cooling down to 30°C after heating at 170°C (*i.e.* before melting) does not lead to changes in the crystalline form, whereas cooling to 30°C after melting (i.e. isotropization) results in a WAXS pattern similar to that of the PA12 granules at 30°C in Figure 5.3.

The different response of isotropic and oriented PA12 samples to elevated temperatures seen from the comparison between Figures 5.3 and 5.4 evidences one more time the differences in their γ type crystalline structure and justifies their different designation as γ isotropic and γ' oriented.

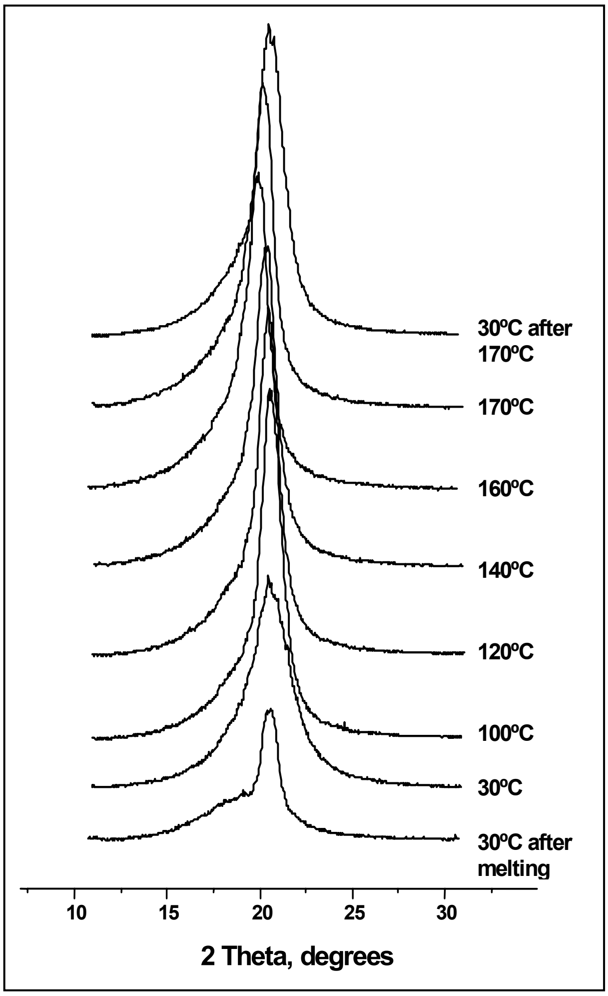

Figure 5.4 1D WAXS profiles of PA12 oriented cables obtained after keeping the sample for 30 s at the respective temperatures. The curves are shifted along the y-axis. [15]

Figure 5.5 shows oriented PA12 samples annealed for 30 min at various temperatures, irradiated after cooling to 30°C. These patterns are similar to those of the in-beam heated PA12 oriented cable. Therefore, it may be concluded that the different behavior of the PA12 isotropic and oriented samples is really inherent and is not related to the duration of the heat treatment. To extract more information from the WAXS patterns, fittings of all the curves in Figures 5.3 - 5.5 were performed. Figure 5.6 visualizes how these fits were made in each particular case. The fitting of the patterns of PA12 granules in Figure 5.3, obtained between 100 and 175°C, was made using Gaussian curves for α and γ crystalline modifications. Best fitting coefficients were obtained with five Gaussians - one to fit the amorphous halo and two for each crystalline form *i.e.*, monoclinic α and non-hexagonal γ phases.

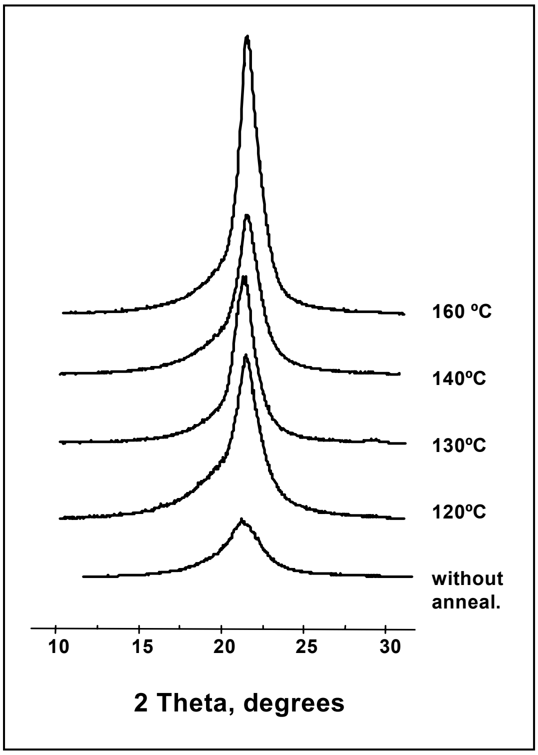

Figure 5.5 1D WAXS profiles of PA12 oriented cables annealed for 30 min in a hot stage at the indicated temperatures. The 1D WAXS images were obtained at 30°C. The curves are shifted along the y-axis [15].

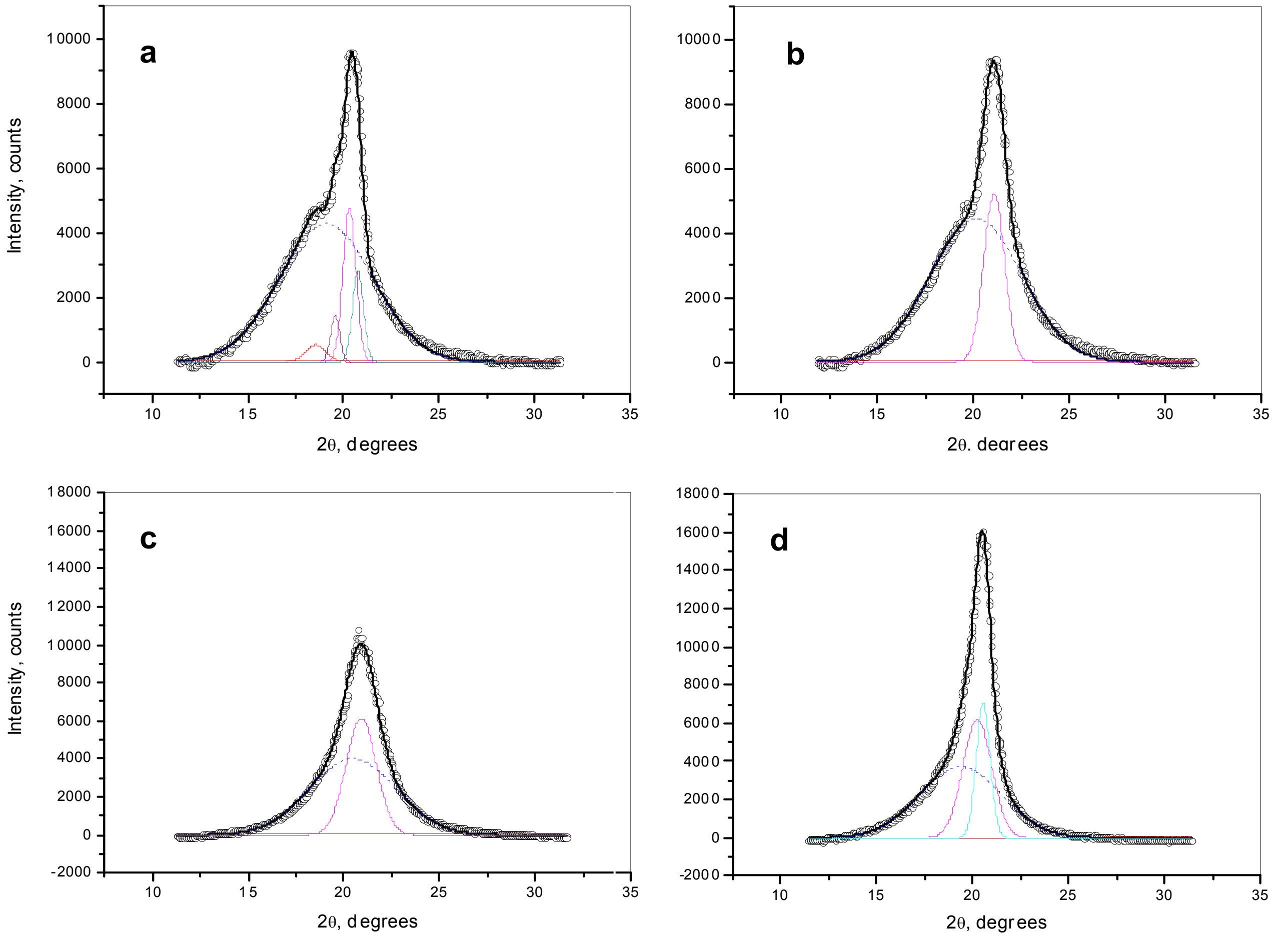

Figure 5.6 Selected 1D WAXS patterns of isotropic and oriented PA12 samples and their fitting with Gaussian peaks: (a) PA12 granules at 160°C; (b) initial PA12 granules at 30°C; (c) initial PA12 oriented cable at 30°C; (d) PA12 oriented cable at 160°C. (Crystalline peaks are given by solid lines and the amorphous halo by dashed lines. The latter was obtained by fitting the WAXS pattern of molten PA12 [15].

In increasing order of their 2θ-position, these four crystalline peaks can be ascribed to α(200), γ(001), γ(200), and α(002) planes [Fig.5.6 (a)], considering the b-axis as the chain axis.

Fitting of the WAXS profile of PA12 granules at 30°C was tried with one or two crystalline peaks positioned close to each other and corresponding to γ(001) and γ(200) planes. In both cases the same fitting coefficients were obtained and the hypothesis of hexagonal γ phase was assumed for the PA12 granules at room temperature [9]. Visualization of this fit is shown in Figure 5.6 (b). The same relates to the pattern of the PA12 granules obtained at 30°C after melting at 200°C (Fig. 5.3).

Figure 5.6 (c) shows the fitting of the initial oriented PA12 sample at 30°C. One or two crystalline peaks were used corresponding to (001) and (200) crystalline planes of the oriented γ' form. Since the same fitting coefficients were obtained in both cases, a hexagonal lattice was supposed, as with the PA12 granules at 30°C. However, as seen from Figure 5.6 (c,b), the shape of the initial oriented and isotropic patterns is different: in the oriented sample the maxima of the crystalline peak and of the amorphous halo almost coincide, which is not the case in isotropic PA12.

At elevated temperatures (100–170°C) better fits were obtained with two crystalline peaks for the oriented γ' form, meaning that the latter becomes non-hexagonal under these conditions [Fig. 5.6 (d)]. Elimination of sample orientation by melting produces, at 30°C, WAXS curves similar to those in Figure 5.6 (b) that is typical of the isotropic γ lattice. Apparently, the different structure and behavior of the γ and γ' phases have to do with the sample orientation.

Peak fitting of all WAXS curves gave a more quantitative insight into the structural changes in both isotropic and oriented PA12 samples. Tables 5.2 and 5.3 display the temperature dependences of the total crystallinity index, α and γ crystallinities, and the d-spacing values for PA12 granules and PA12 oriented cable, respectively.

5.3.3. SAXS measurements

Figure 5.7 shows the SAXS images of selected representative PA12 samples. The non-oriented ones [e.g., the initial granules at 30°C in Fig. 5.7(a) and the PA12 cable after melting at 200°C [Fig. 5.7 (e)] show patterns of circular symmetry, thus verifying the absence of orientation demonstrated by the 2D WAXS traces. The oriented samples [Fig. 5.7 (b–d)] reveal two-point scattering diagrams with the draw direction being horizontal.

Table 5.2 Temperature Dependence of the Total Crystallinity Index $\mathrm{CI_{total}}$, **α** CI, **γ** CI, and d-Spacings in PA12 Granules Heated in the X-Ray Beam at a Heating Rate of 20°C/min [15].

Temperature (ºC)	**Crystallinity Index (%)**			**d-Spacings, (Å)**			
	αCI	**γCI**	**$\mathrm{CI_{Total}}^{a}$**	**αd_{200}**	**αd_{002}**	**γd_{001}**	**γd_{200}**
30	–	21.1	21.1	–	–	–	4.103
100	12.6	13.7	26.3	4.594	4.105	4.324	4.202
140	10.5	14.2	24.7	4.623	4.167	4.402	4.233
150	7.6	15.8	23.4	4.597	4.142	4.394	4.236
160	9.1	13.6	22.7	4.613	4.158	4.400	4.251
165	8.0	14.9	22.9	4.651	4.163	4.412	4.252
170	10.6	9.5	20.1	4.650	4.183	4.406	4.278
175	9.8	5.8	15.6	4.682	4.186	4.367	4.269
30 after 200	–	24.0	24.0	–	–	–	4.088

Notes: WAXS patterns are taken 30 s after reaching the respective temperature. The **b**-axis is the chain axis.
[a] $\mathrm{CI_{tota}}$ = αCI + γCI.

Table 5.3 Temperature Dependence of the **γ**' Type Equatorial Crystallinity Index (ECI) and d-Spacings in PA12 Oriented Cable Heated in the X-Ray Beam at a Heating Rate of 20°C/min

	Crystallinity Index (%)		**d-Spacings (Å)**			
Temperature (ºC)	**α ECI**	**γ' ECI**	**γ' (d_{001})**	**γ' (d_{200})**	**γ'-(d_{040})^{a} (heating)**	**γ'-(d_{040})^{a} (cooling)**
30	–	37.8	–	4.135	7.470	7.845
60	–	47.4	–	4.091	–	7.828
80	–	47.5	–	4.113	–	7.824
100	–	48.7	4.140	4.134	–	7.691
120	–	53.0	4.187	4.165	7.512	–
140	–	52.1	4.244	4.188	7.492	–
160	–	48.4	4.272	4.204	7.489	–
170	–	47.6	4.287	4.206	7.613	7.613
30 after 170	–	45.0	4.079	4.029	–	–
30 after 200	–	27.8	–	4.111	–	–

Notes: WAXS patterns are taken 30 s after reaching the respective temperatures. The **b**-axis is the chain axis.
[a] The d_{040} values of oriented γ'- PA12 were determined from the meridional slices of the corresponding 2D WAXS patterns taken during heating or cooling between 30–170°C

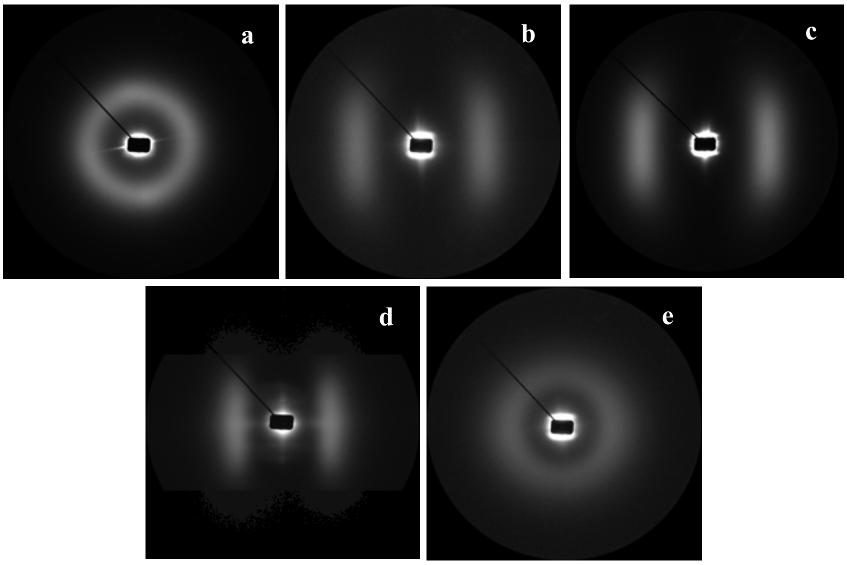

Figure 5.7 Selected 2D SAXS patterns of PA12: (a) PA12 granules at 160°C; (b) oriented cable heated in-beam at 160°C; (c) oriented cable at 30°C after heating at 160°C; (d) oriented cable annealed for 30 min at 160°C, image taken at 30°C; (e) sample (c) after isotropization at 200°C, image taken at 30°C. (The draw direction in oriented samples is horizontal.) [15]

All SAXS images were sliced along the equator to produce the corresponding raw SAXS curves used to determine the Bragg's long spacings L_B. For PA12 granules, the linear CFs were calculated in the 30–200°C range (Fig. 5.8).

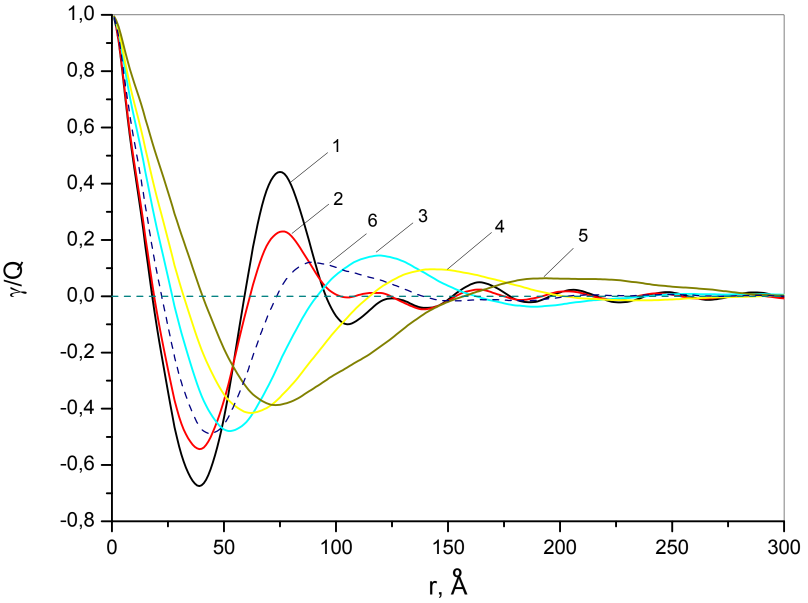

Figure 5.8 Linear correlation function (CF) curves calculated from the SAXS patterns of PA12 granules: 1 – starting sample at 30°C; 2 – at 100°C; 3 – at 160°C; 4 – at 170°C; 5 – at 175°C; 6 – CF at 30°C after melting at 200°C. [15]

For the oriented PA12, CFs were calculated only for the isotropized sample obtained by quenching after melting. It is known that the calculation of x_{cl} requires the solution of a quadratic equation [17]. On the basis of its two solution ($x_1 > x_2 ; x_1 + x_2 = 1$), two thicknesses can be calculated. To determine which one corresponds to l_a and which to l_c , one has to use additional information, for example, the degree of crystallinity, CI as determined by WAXS. If x_1 > CI > x_2 , then $x_1 = x_{cl}$ and this value is used for the l_c calculation. The reason is that the crystallinity within the stacks cannot be lower than the overall. For the PA12 granules, however, $x_1 > x_2 > CI$ throughout the entire temperature interval between 30 and 175°C. Having in mind the relatively low CI (about 21%), it was assumed that $x_2 = x_{cl}$, which led to the x_{cl} , l_a , and l_c values summarized in Table 5.4.

5.4. Discussion

5.4.1 Crystalline structure of isotropic PA12

As mentioned earlier, there is no α form in the isotropic PA12 sample at 30°C, and so the sample should be related to one of the γ polymorphs. According to a previous report [16], in γ PA12 form the signal of all-trans methylenes is downfield shifted with 0.5 ppm with respect to that of γ' PA12. Moreover, the C=O resonance of the γ polymorph appears in stronger fields (also with about 0.5 ppm). From Table 5.1 one can see this same trend for the two samples under investigation, the chemical shifts of the PA12 granules corresponding to γ type PA12 phase.

Further information about the structure of this sample is given by the 1D WAXS data (Fig. 5.3, Table 5.2) showing that the initial granules at 30°C contain γ form with hexagonal lattice. At elevated temperatures, the hexagonal PA12 γ form transforms into pseudo-hexagonal one, whose two crystalline peaks are close to each other with similar d-spacings (Table 5.2). Heating the granules also leads to the appearance of PA12 in α form coexisting with the γ phase. The evolution of the total CI [Table 5.2, Fig. 5.9 (a)] demonstrates a small increase of about 5% at 100°C as compared with that at 30°C. In the 100–165°C range, slight fluctuations of 2–3% are registered, being in the limits of the experimental error. Hence, between 100 and 165°C the total crystallinity can be considered constant. Therefore, the appearance of α form upon heating of PA12 granules can be attributed to a γ-α transition rather than to additional crystallization of amorphous material.

Table 5.4 Structural Parameters Extracted by Analysis of the Linear PA12 Samples with Various Thermal and Mechanical Pre-histories [15]

Temp. (ºC)	L_B^a, **Å**	L_B^b, **Å**	L_c^m, **Å**	L_c^M, **Å**	l_c, **Å**	l_a, **Å**	x_{cl}
PA12 granules (in-beam heating)							
30	88	78	78	75	31	44	0.419
100	99	83	80	77	34	43	0.447
140	118	103	89	92	37	55	0.406
150	129	109	95	102	39	63	0.371
160	145	127	105	119	41	78	0.344
165	156	133	112	128	42	86	0.324
170	187	152	124	142	45	97	0.325
175	–	208	146	193	58	135	0.302
30 after 200	128	103	88	89	43	46	0.493
PA12 oriented cable (in-beam heating)							
30	141	–[c]	–	–	–	–	–
60	98	–	–	–	–	–	–
100	98	–	–	–	–	–	–
120	99	–	–	–	–	–	–
140	102	–	–	–	–	–	–
160	108	–	–	–	–	–	–
170	121	–	–	–	–	–	–
30 after 170	110	–	–	–	–	–	–
30 after 200	140	119	106	108	46	62	0.425
PA12 annealed oriented cable[d]							
120	100	–[c]	–	–	–	–	–
130	97	–	–	–	–	–	–
140	111	–	–	–	–	–	–
150	114	–	–	–	–	–	–
165	124	–	–	–	–	–	–

[a] The L_B values are obtained from the raw SAXS patterns.

[b] The L_B values are obtained after Lorentz correction and elimination of the liquid scattering.

[c] Linear CF analysis inapplicable in oriented samples (see the text).

[d] PA12 cable annealed in hot stage for 30 min at the indicated temperature; SAXS curve obtained at 30°C.

Between 100 and 165°C, the said γ - to - α form transition is accompanied by an increase in the long spacing L_c^M as calculated by CF analysis [Fig. 5.9 (b), Table 5.4] — from 77 to 128 Ǻ. This is a result of the growth of both l_c and l_a, the latter being much faster. The increase in *L* in PA12 granules during heating can be related to processes of reorganization, including melting and re-crystallization of secondary lamellae, keeping the CI values without significant changes between 100 and 165°C [Fig. 5.9 (a)]. Other reason for the observed increase of *L* can be related to the phase transition from γ - to - α form mentioned earlier.

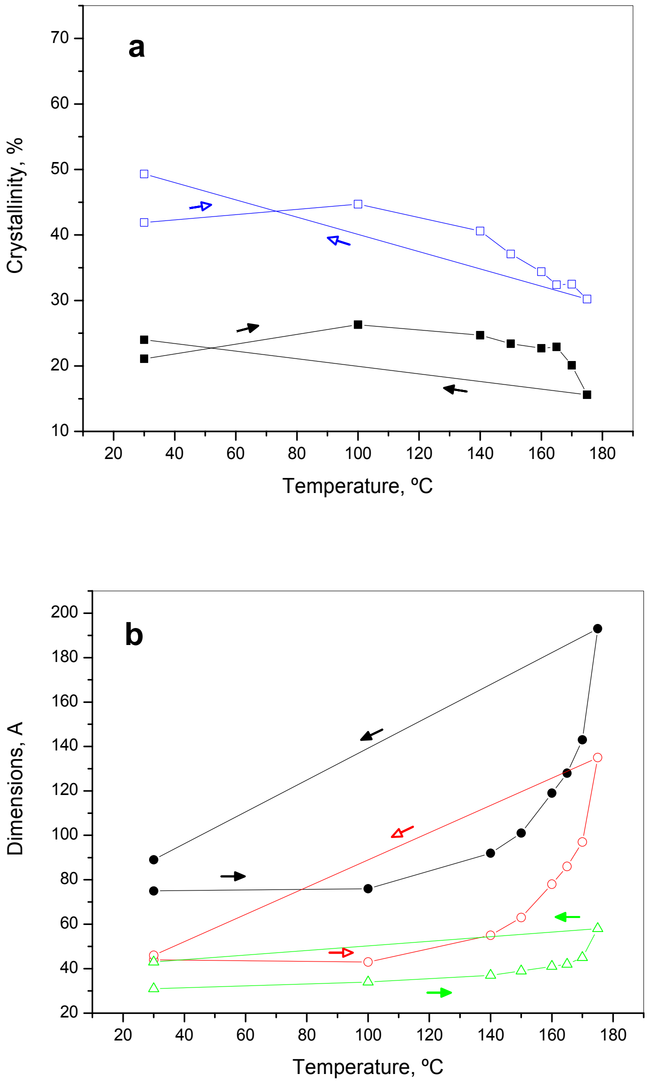

Figure 5.9 Temperature dependence of some structural parameters of PA12-granules: (a) -■- total crystallinity index *CI* (WAXS); -□- linear crystallinity within the stack x_{cl} (SAXS) (b) -●- *CF* long spacing L_c^M ; –△- average thickness of the crystalline phase, l_c ; -○- average thickness of the amorphous phase l_a (SAXS) [15].

Further temperature increase results in the rapid growth of L and l_a values probably due to the sample melting, which is confirmed by the drop of the CI values in this range. Cooling down to room temperature after melting of the PA12 granules leads to a total recovery of the hexagonal γ crystalline structure and disappearance of the α phase (Fig. 5.3), as well as to CI values slightly higher than the initial ones [Fig. 5.9 (a)]. As far as L values are concerned [Fig. 5.9 (b)], they do not recover completely mainly because of an l_c growth with about 12 Å, whereas the l_a values, after quenching, remain the same as those of the initial sample. Apparently, the l_c growth while heating is not only related to thermal expansion evidenced from the increase of the d-spacings (Table 5.2) but also to some lamellar thickening. Judging from the higher values of x_{cl} after quenching, a more perfect crystalline structure should be supposed for the molten and cooled PA12 granules as compared with that for the initial sample.

5.4.2. Crystalline structure of oriented PA12

Comparing the all-trans CH_2 and C=O resonances of PA12 granules to those of the oriented cable and to the reference data in Table 5.1, a γ' structure was attributed to the oriented PA12 sample. Along with the said differences in the peak positions of the two samples studied, the signal ratio of all-trans/gauche methylenes was found to be different, too. In the oriented PA12 sample [Fig. 5.1 (b), Table 5.1], the gauche-CH_2 signal is stronger than that of all-trans methylenes, which is another feature of the γ' PA12 polymorph [16]. Since the intensities of the rest of the signals of the two samples are almost identical, it can be concluded that the aforementioned variation cannot be related to the different degrees of crystallinity, but to a different structure.

It has to be mentioned that the PA12 structure known as γ' form is isotropic and was obtained by consecutive melting, quenching by liquid nitrogen, and annealing at 60°C [10]. The PA12 sample in this study to which γ' structure is attributed, obtained by drawing at 100°C, is highly oriented. To enable distinction from the known isotropic γ' form, we designated the crystalline structure of oriented PA12 sample as γ' oriented. Fitting of the 1D WAXS data in Figure 5.6(c) shows that, at room temperature, the oriented γ' form is also hexagonal. However, it demonstrates quite a different behavior upon heating, as compared with that of the isotropic γ phase. As seen from Figure 5.4, no appearance of α PA12 is observed within the whole temperature interval up to melting. The hexagonal lattice persists up to 100°C, changing (above this temperature) into pseudo-hexagonal one with two crystalline peaks (Table 5.3) being closer to each other than in the pseudo-hexagonal isotropic γ PA12 (Table 5.2).

Raising the temperature between 30 and 140°C results in a substantial increase of *ECI* from 38 to 53% [Table 5.3, Fig. 5.10 (a)]. At the same time, L_B drops with almost 43 Å during the initial heat increase from 30 to 60°C [Fig. 5.10 (c), Table 5.4]. A possible reason for this effect can be the decrease of the d-spacings (γ'-(200) crystalline planes) in the said temperature interval. On the other hand, it can be supposed that drawing of PA12 at 100°C gives rise to orientation and alignment in the amorphous regions. Thus, slight heating to 60°C results in rapid crystallization, producing smaller and less perfect crystallites embedded into the oriented amorphous domains, which causes ECI to go up and L_B to decrease. This process continues up to 140°C with slight increase of L_B [Fig. 5.10 (c)] and d-spacings (Table 5.3).

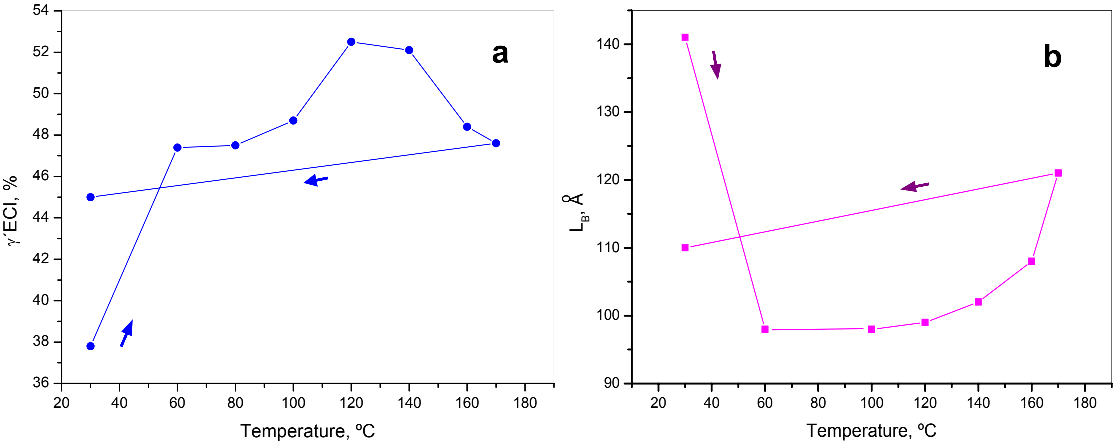

Figure 5.10 Temperature dependence of structural parameters in oriented PA12: (a) ECI; (b) Bragg's long spacings [15].

Further heating above 140°C results in a decrease of ECI and significant increase of the long spacing values. Irrespective of the fact that in this oriented sample there are no data for l_a and l_c, this effect is apparently attributable to the incipient fusion of these newly formed imperfect γ' crystallites. Rapid cooling after 170°C (i.e. before isotropization) does not change the pseudo-hexagonal γ' crystalline form (Fig. 5.4, Table 5.3) and maintains the ECI values registered at 170°C [Fig. 5.10 (a)]. The d-spacings of γ'-(001) and γ'- (200) crystalline planes decrease by 2.5% as compared with those at initial 30°C. A notable exception is the interplanar distance of γ'(040) crystalline plane, which after quenching becomes about 5% larger than its initial value (Table 5.3). Such an expansion of the crystalline lattice in the direction of the polymer chains was also observed with the d-spacing of (020) crystalline plane of oriented PA6 at quenching before melting (See Section 3.4.3). Quenching after melting of the oriented PA12 cable at 200°C gives rise to sample isotropization, resulting in turn in a clear γ'–γ transition. The shape of the 1D WAXS pattern at 30°C after melting (Fig. 5.4) is similar to that of the PA12 granules (Fig. 5.3). As seen from Tables 5.2 and 5.3, the crystalline phase thus formed is identical to the hexagonal γ form of the PA12 granules.

5.4.3. The Effect of Annealing on the Crystalline Structure of Oriented PA12

The corresponding 1D WAXS patterns (Fig. 5.5) show that the PA12 cables keep their γ' hexagonal crystalline form that is annealing at the said temperatures does not change the crystalline form. As seen from Figure 5.11 (a), annealing leads to an increase in ECI, whereby the higher the annealing temperature, the larger the growth of crystallinity index. The duration of heat treatment also influences the crystallinity index, longer annealing times leading to larger ECI increase.

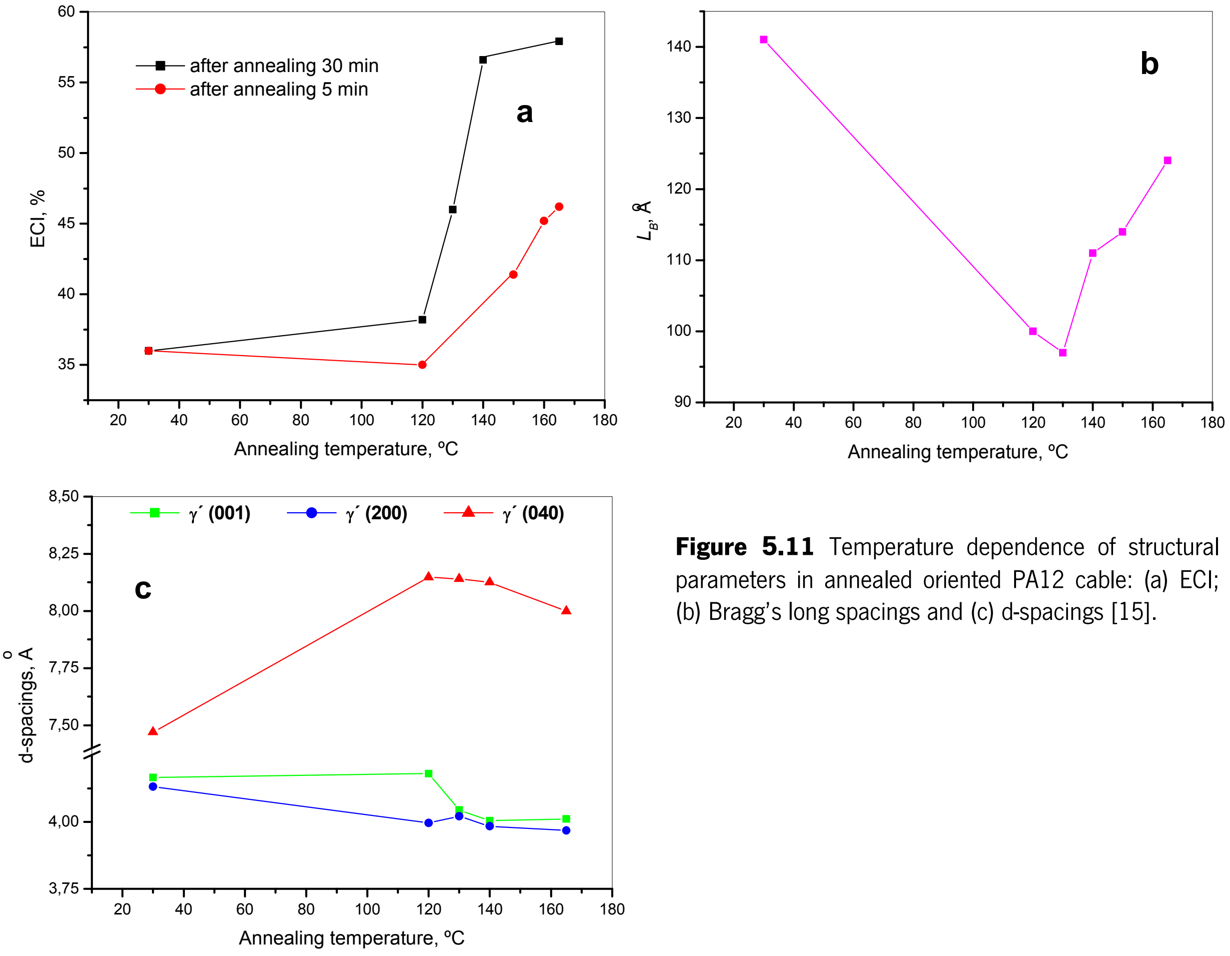

Figure 5.11 Temperature dependence of structural parameters in annealed oriented PA12 cable: (a) ECI; (b) Bragg's long spacings and (c) d-spacings [15].

The effect of annealing on the L_B values is quite interesting [Fig. 5.11 (b)]. Generally, annealing of polyamides leads to an increase in L_B as observed in PA6 in Chapter 3. In the PA12 oriented sample, however, annealing at 120–130°C leads to a notable decrease in L_B with almost 40 Å, as compared with the values of the sample without annealing at 30°C. Having in mind the visible contraction of the PA12 cables annealed at 120 and 130°C with free ends, the decrease of the long spacings here can be related with relaxation of the amorphous regions. As seen from Figure 5.11 (a), crystallization of amorphous material into less perfect crystallites could also be an additional reason. Annealing at higher temperatures (between 130 and 165°C) is accompanied by an increase in L_B and ECI.

As regards the d-spacings, annealing does not cause significant changes of d_{001} and d_{200} [Fig. 5.11 (c)]. The d-spacing of the sample at 30°C without annealing is similar to those observed by Rhee and White in oriented PA12 [18], while those of the samples that underwent some annealing are close to the values obtained by Owen and Kollross [19]. Unlike these researchers, in all of the studies in this thesis related to the (0k0) d-spacings of oriented PA12 (Table 5.3) and annealed oriented PA12 [Fig. 5.11 (c)], the (040) reflection was studied for calculating the (0k0) d-spacing. The latter was selected after studying the temperature dependence of the d-spacings of (020), (040), (060), and (0100) meridional reflections. The d-spacing of (040) reflection showed the lowest oscillations with temperature.

The structure of oriented PA12 after annealing at 120°C is worth mentioning. At this temperature, the difference between the d-spacings of the γ'(001) and γ'(200) crystalline planes is the biggest, that is here the deviation from the hexagonal lattice is best expressed. Also, after annealing at 120°C, the γ'(040) d-spacing shows its highest value.

5.5 Conclusions

The isotropic PA12 sample reveals γ type crystalline structure that is hexagonal at room temperature. With the increase in temperature, it becomes pseudo-hexagonal and partially transforms into α crystalline form. This process is reversible – after rapid cooling, the hexagonal γ form is completely restored. Orientation by cold drawing at about 100°C results in a different crystalline modification denoted as γ' oriented. The oriented γ' form is also hexagonal at 30°C; however, high temperatures do not cause any phase transitions in it, but only an increase of the degree of crystallinity. Even prolonged annealing (30 min) at temperatures close to the melting point does not change the PA12 γ' oriented form. Rapid cooling to 30°C from temperatures below melting does not modify the structure of this polymorph. A γ'–γ transition is only possible after isotropization (melting) of oriented PA12).

5.6. References:

1. Holmes DR, Bunn CW, and Smith DJ, J *Polym Sci* 17:159 (1955).
2. Arimoto H, Ishibashi M, Hirai M, Chatani Y, *J Polym Sci Polym Chem* 3:317 (1965).
3. Fornes TD, and Paul DR, *Polymer* 44:3945 (2003).
4. Samon J M, Schultz JM, and Hsiao BS, *Polymer* 41:2169 (2000).
5. Aleman C, and Casanovas J, *Colloid Polym Sci* 282:535 (2004).
6. Hiramatsu N, Hashida S, and Hirakawa S, *Jpn J Appl Phys* 21:651 (1982).
7. Ishikawa T, Nagai S, and Kasai N, *J Polym Sci Part B: Polym Phys Ed* 18:291 (1980).
8. Ishikawa T, Nagai S, and Kasai N, *Die Makromol Chem* 182:977 (1981).
9. Ramesh C, *Macromolecules* 32:5704 (1999).
10. Li L, Koch M, and de Jeu WH, *Macromolecules* 36:1626 (2003).
11. Cojazzi G, Fichera A, Garbuglio C, Malta V, Zanneti R, *Makromol Chem* 168:289 (1973).
12. Inoue K, and Hoshino S, *J Polym Sci Part B: Polym Phys Ed* 11:1077 (1973).
13. Hiramatsu N, Haraguchi K, and Hirakawa S, *J Appl Phys* 22:335 (1983).
14. Northolt MG, Tabor BJ, van Aartsen JJ, *J Polym Sci Part A-2: Polym Phys* 10:191 (1972).
15. Dencheva N, Nunes T, Oliveira MJ, and Denchev Z, *J Polym Sci Part B: Polym Phys* 43:3720 (2005).
16. Mathias LJ and Johnson CG, *Macromolecules* 24:6114 (1991).

17. Santa Cruz C, Stribeck N, Zachmann HG, and Baltá-Calleja FJ, *Macromolecules* 24:5980 (1991).

18. Rhee S, and White JL., *J Polym Sci Part B: Polym Phys* 40:1189 (2002).

19. Owen AJ, and Kollross P, *Polym Commun* 24:303 (1983).

CHAPTER 6

RELATIONSHIP BETWEEN CRYSTALLINE STRUCTURE AND MECHANICAL BEHAVIOR IN ISOTROPIC AND ORIENTED POLYAMIDE 12

This chapter reveals studies on the relationship between the crystalline structure and the mechanical behavior of differently processed and annealed PA12 samples. The approach is the same as in Chapter 4 with PA6 samples. Thus, PA12 isotropic films and OC were prepared by compression molding or by consecutive extrusion and cold-drawing. These samples were isothermally annealed in the 80 - 160°C range and then subjected to tensile tests at room temperature. A combination of solid state carbon 13 NMR and synchrotron WAXS and SAXS methods was used to obtain reliable structural data from these samples, before and after a tensile test (TT). These data were then related to the mechanical properties of the respective PA12 samples. Deformation models were suggested for the different PA12 samples explaining the experimental results.

6.1. Introduction

The commercial PA12 is generally obtained by hydrolytic polycondensation in 260-300°C range and is characterized by very low monomer content in melt equilibrium [1]. Much smaller market volume is related to the activated anionic ring-opening polymerization PA12. The properties of PA12 represent a valuable combination of the typical nylon and polyolefin properties, *e.g.* low moisture absorption and density accompanied by chemical resistance similar to that of PA6 with lower sensitivity to stress cracking [2]. PA12 shows excellent impact strengths and high E modulus values. All this makes PA12 an important engineering plastic with multiplicity of applications in technical engineering, especially in automotive and electrical industries [1,3]. Therefore, studying the relationship between the PA12 structure and its mechanical properties is of both practical and academic interest. The data obtained will be further used to understand and to control the mechanical properties of MFCs with a HDPE matrix reinforced by PA12 microfibrils.

The few studies available up to now that relate the structure or the properties of PA12 to the conditions of its orientation and/or annealing were mentioned in the introductory section of Chapter 5. Own results presented in the same chapter displayed some differences in the polymorphic transitions occurring in the isotropic γ-form and in the oriented γ´ form. Upon heating above 140°C, the isotropic γ-polymorph partially changed into α PA12 that only existed at high temperature and rapidly changed back into γ form when cooled. No such γ-to - α transformation was observed with the oriented γ PA12 phase even after annealing at temperatures close to melting. A γ'- to - γ transition was observed here after isotropization by melting [4].

No studies have been published so far on the relationship between the mechanical properties of PA12 and its crystalline structure considering the respective polymorphic transitions and also the changes in the amorphous phase. This will be the main goal of the present chapter. The influence of the starting structure upon the tensile properties of the PA12 samples will be studied. Then, the influence of strain upon the crystalline structure after sample failure considering the changes in the crystalline phase will be elucidated. As characterization techniques synchrotron WAXS and SAXS techniques will be used complemented with solid state ^{13}C NMR spectroscopy.

6.2. Experimental details

Two types of PA12 samples were prepared and studied. The first one, designated as "isotropic film", was obtained by the compression molding of as-supplied granules preliminarily dried for 5 h at 90°C. The starting material was pressed at 250°C, and a pressure of 6 tons was applied for 5 min, which was followed by isothermal crystallization for 1 h at three different temperatures: 120, 140, or 160°C. An additional sample was prepared with 3 h of isothermal crystallization at 120°C. In all cases 200–250 μm thick films were prepared cooling to room temperature at a rate of about 20°C/min after completing the annealing. The second sample, designated as "oriented cable" (OC), was prepared in the extruder line at a set temperature of 230°C (Chapter 2). The oriented PA12 OCs where annealed with free ends at 80, 100, 120, and 160°C in an oven. After 1 h of annealing at the respective temperature, the heating was switched off, and the sample was cooled at about 10°C/min until it returned to room temperature. Major sample contraction was observed in each annealing temperature with all PA12 cables.

WAXS and SAXS measurements were performed in Setups 1 and 2 (Fig. 2.6) with PA12 samples before and after their mechanical failure applying the conditions and the data treatment procedures as previously described in Chapter 2. Solid state NMR and tensile tests were preformed in the standard way (Chapter 2).

6.3. Results

6.3.1. Mechanical data

Figure 6.1 shows the stress–strain curves of differently annealed isotropic PA12 films [Fig. 6.1 (a)] and oriented cables [Fig. 6.1(b)]. All data extracted from these curves are presented in Table 6.1.

.

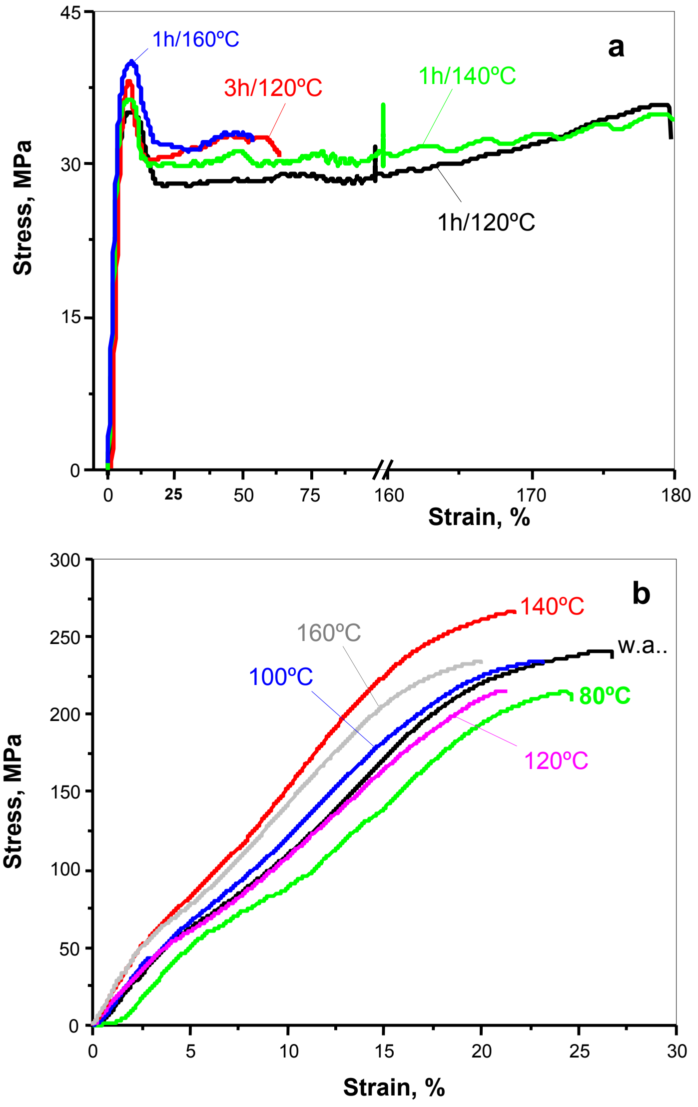

Figure 6.1 Stress–strain curves of various PA12 samples: (a) isotropic films annealed for 1 h at 120, 140, or 160°C, and for 3 h at 120°C; (b) oriented PA12 cables without annealing (w.a.) and annealed at 80, 100, 120, and 140°C for 1 h. The curves represented were selected to best fit the averaged data in Table 6.1

As seen from Fig. 6.1 (a), all isotropic PA12 samples display clear yield points at low strains (between 7 and 9%) and cold flow regions – a behavior typical of necking. The samples annealed at 120/1h and 140°C failed at strains of ca. 200%, whereas the other two films broke at ε_{br} values of 50-60%. From Table 6.1 it can be seen that the isotropic PA12 samples displayed a slight augmentation of the E

modulus (from 830-890 MPa to 1030 MPa). This effect was achieved by increasing either annealing temperature T_a in the 120 - 160°C range, or the time duration of the treatment – from 1 to 3 h at 120°C. The σ_y values of all isotropic samples were between 32 and 36 MPa, the highest value corresponding to the highest annealing temperature of 160°C. It can be concluded that annealing results in a stronger PA12 film.

Fig. 6.1 (b) shows that all oriented PA12 cables are characterized by two yield points. As seen from the data in Table 6.1, the first yields appear at low strains (3-5%) with σ_y values between 45 and 59 MPa. At strains of 16-21% one can recognize in all OCs, a second yield point with σ_y values in the 207-254 MPa. Statistically significant increase of the *E* modulus values determined as explained in Chapter 2 was reached only at annealing temperatures of 140° and 160°C; at lower temperatures the mechanical behavior of the annealed OCs is similar to that of the OC without annealing.

Table 6.1 Tensile properties of isotropic and oriented PA12 samples after various annealing (OC = oriented cable).

Sample/ Annealing	E **(GPa)**	σ_y **MPa**[a]	**Yield Strain %**	**Max. Stress MPa**	**Strain at Max. Stress, %**	σ_{br} **MPa**	ε_{br} **%**
PA12 film 120°C/1h	0.83 ± 0.07	32 ± 3	8.1 ± 0.5	33 ± 10	188 ± 16	33 ± 8	189 ±20
PA12 film 120°C/3h	1.01 ± 0.10	34 ± 5	6.9 ± 0.1	35 ± 6	7 ± 2	27 ± 6	63 ± 5
PA12 film 140°C/1h	0.89 ± 0.07	32 ± 1	8.3 ± 0.6	34 ± 6	200 ± 11	35 ± 9	203± 13
PA12 film 160°C/1h	1.03 ± 0.06	36 ± 1	8.7 ± 0.5	36 ± 3	9 ± 1	28 ± 7	54 ± 6
PA12 OC, w.a.	1.63 ± 0.08	56 ± 1 220 ±2.0	4.2 ± 0.4 18.7 ± 1.0	241± 10	26 ± 3	235 ± 7	27 ± 3
PA12 OC 80°C/1h	1.23 ± 0.16	53 ± 1 207 ± 2	4.9 ± 0.3 21.3 ± 1.4	215± 6	24 ± 2	209 ± 7	25 ± 2
PA12 OC 100°C/1h	1.67 ± 0.07	45 ± 1 227 ± 2	2.9 ± 0.2 18.5 ± 1.1	234 ± 3	23 ± 2	233 ± 10	23 ± 3
PA12 OC 120°C/1h	1.46 ± 0.10	50 ± 2 213 ± 2	3.6 ± 0.2 19.6 ± 1.5	216 ± 8	21 ± 2	214 ± 9	21 ± 2
PA12 OC 140°C/1h	2.19 ± 0.12	59 ± 2 254 ± 3	2.9 ± 0.1 16.5 ± 0.9	266 ±10	21 ± 3	265 ± 10	22 ± 2
PA12 OC 160°C/1h	2.24 ± 0.15	58 ± 1 230 ± 3	2.8 ± 0.2 16.5 ± 0.8	234 ± 8	20 ± 1	233 ± 11	20 ± 1

Note: [a] Oriented cables displayed two yield points; w.a. = without annealing

6.3.2. Solid state ^{13}C NMR data

In the previous chapter, the spectra of PA12 granules and PA12 cable obtained by melting the same granules in a melt flow index apparatus followed by stretching at ca.100°C, did not reveal any resonance lines above 40 ppm and also no peaks around 38.9–39.0 ppm. On this basis, the presence of α polymorph in both samples was ruled out. For the mechanical experiments in this chapter isotropic films were prepared by hot pressing and OCs – using the extruder line with several stretching devices (Chapter 2). The MAS/CP-DD ^{13}C NMR spectra of a PA12 isotropic film annealed for 1 h at 160°C and of the new OC with the same thermal prehistory obtained before and after the mechanical failure of the samples were visibly different from those previously mentioned. Having in mind also the prolonged annealing of the samples at elevated temperatures, it was decided to analyze the new NMR data by peak-fitting supposing the presence of both α and γ-PA12 polymorphs. This supposition was based on the previous works reporting on γ- to α-form transition upon cold drawing [5] or pressing [6]. The crystallinity data obtained by fitting the NMR curves were then correlated with the X-ray scattering results (See Section 6.3.3).

Fitting of the NMR spectra is possible having in mind the four types of carbons found in the repeat unit of both α- and γPA12 (Table 6.2). In each polymorph, its eight CH_2 methylenes (type c carbons) co-exist in all-trans and in gauche (skewed) conformations, the resonances of these structures being in the 30.3-34.3 ppm range. The methylene type b carbon, being the most electron-shielded, appears in stronger fields of ca. 27 ppm. As expected, the carbon located next to the $C{=}O$ and that next to the NH group (type a and d, respectively) produce resonance lines in weaker fields (up to 43 ppm) [7].

Figures 6.2 and 6.3 represent the fittings of the extended methylene carbon regions of an isotropic PA12 sample annealed for 1h at 160°C and an OC with the same thermal history before (a) and after (b) tensile test. The respective chemical shifts obtained after the peak fitting for all types of carbons are presented in Table 6.2. They are very close to those found previously by other authors shown in the first column of the same table [7].

Fitting the NMR spectra allows the calculation of the α/γ polymorph ratio, which was done in the following way. The areas of all-cis and all-trans methylene carbon γ-PA12 peaks were summed and divided by 8 obtaining in such a way the integral intensity corresponding to one γ-carbon. This value was then used to divide the integral intensity of the d-type carbon of the α-PA12. One has to mention that it is possible to calculate the α/γ ratio relating the intensity of any NMR signal of a carbon belonging to α-PA12 with that of any carbon of the γ-phase. In all cases very similar values were obtained. The signal of the α-PA12 d–carbon was used because of two reasons. This signal appears above 40 ppm where there are no γ-form signals whatsoever so the presence of it undoubtedly proves the α form. Below 40 ppm superposition is possible between α- and γ form signals. The second reason was the better agreement with the WAXS data.

Table 6.2 Solid state ^{13}C NMR analysis of PA12 isotropic and oriented samples annealed for 1 h at 160°C before and after tensile test (aliphatic **C** region)

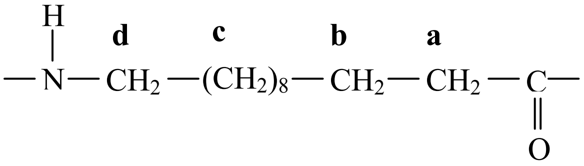

$$-\overset{\overset{\displaystyle H}{|}}{N}-\underset{d}{CH_2}-\underset{c}{(CH_2)_8}-\underset{b}{CH_2}-\underset{a}{CH_2}-\underset{\underset{\displaystyle O}{\|}}{C}-$$

NMR resonances	**Samples**				
	PA12 from [7]	**PA12 film**	**PA12 film, after TT**	**PA12 OC**	**PA12 OC, after TT**
	Chemical shifts, ppm				
b γ form (γ' form)	~28 (~27)	26.5[a]	25.1	26.4[a]	25.3
b (α form)	27.3		26.7		26.7
c gauche γ form	30.3	29.9	29.7	29.7	30.0
c gauche γ'-form)	30.8				
c gauche (α form)	30.9	31.6	31.4	31.6	31.4
c trans (γ form)	33.6	32.8	32.5	32.8	32.8
c trans (γ' form)	33.1				
c trans (α form)	34.2	34.4	34.2	34.6	34.5
a (γ form)	37.3	36.3	36.5	36.5	36.6
a (γ' form)	37.0				
a (α form)	38.9	37.4	-[b]	-[b]	-[b]
d (γ form)	39.8	39.8	40.2	39.5	39.9
d (γ' form)	40.3				
d (α form)	43.0	42.2	42.7	42.1	42.8
a / γ content	**-**	**0.19**	**0.27**	**0.24**	**0.52**

Notes:

[a] The resonances of the corresponding nucleus of α and γ form cannot be separated.

[b] Fitting does not suggest a resonance peak in this region in oriented samples.

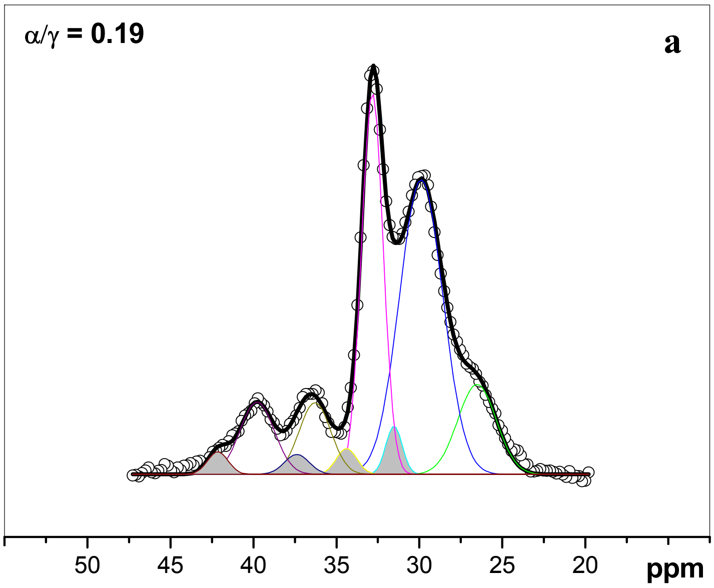

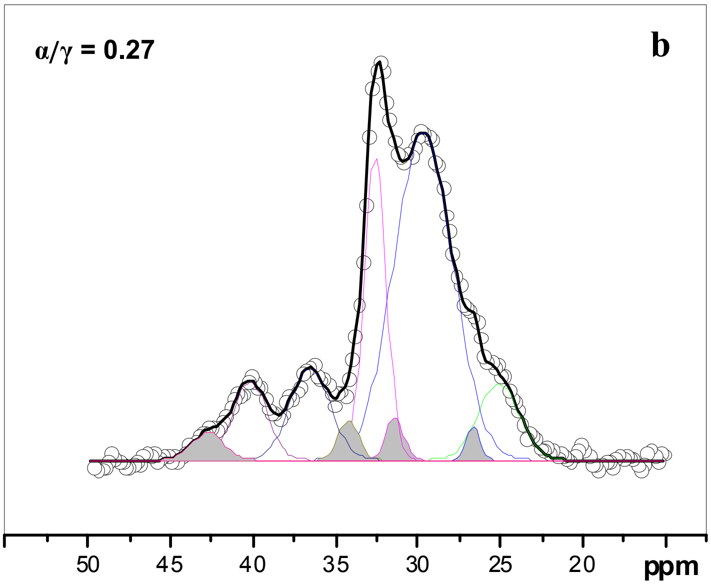

Figure 6.2 MAS/CP-DD ^{13}C spectra at 20°C of isotropic PA12 film annealed for 1h at 160°C in the aliphatic C-atom region: (a) before and (b) after tensile test. The resolved resonance lines of the α-PA12 are shaded. The chemical shifts of all resonance lines are given in Table 6.2

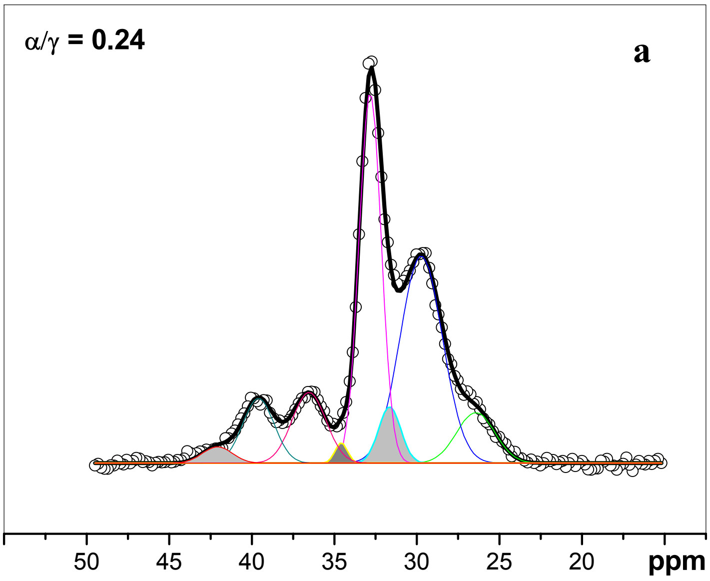

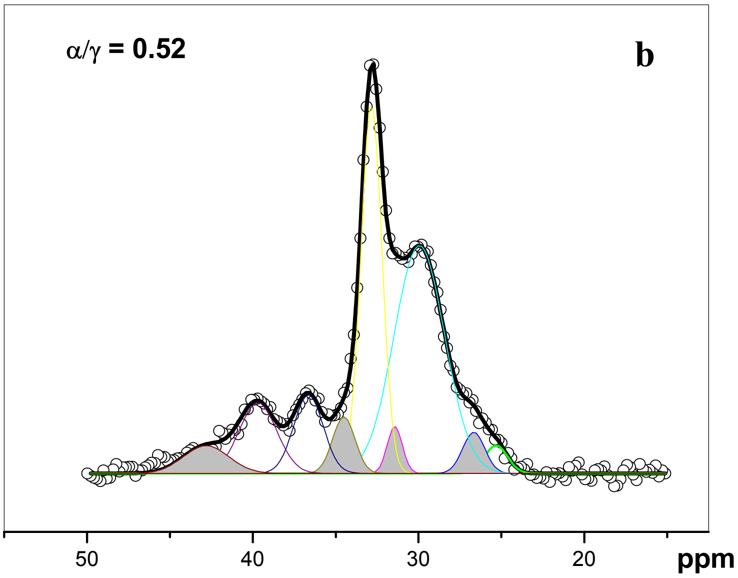

Figure 6.3 MAS/CP-DD 13C spectra at 20°C of PA12 OC obtained by extrusion/cold drawing and annealed for 1h at 160°C in the aliphatic C-atom region: (a) before and (b) after tensile test. The resolved resonance lines of the α-PA12 are shaded. The chemical shifts of all lines are given in Table 6.2

6.3.3. 1D WAXS measurements

As seen from the comparison between the literature and the chemical shift data presented in Table 6.2, in isotropic PA12 films and PA12 OCs a clear distinction is possible between the α- and γ-PA12 phases. As to the γ-PA12, it was shown in Chapter 5 that the isotropic and oriented γ-polymorphs have different behaviour when heated, related to the different thermal changes in the shapes of the 1D WAXS patterns on Figures 5.3 and 5.4. That is why the respective crystalline phases were denoted differently – as γ-isotropic and γ'-oriented. In this chapter, analogously, when referring to oriented PA12 samples, one will have in mind the γ'-oriented PA12 phase; the isotropic PA12 films will be considered then as containing γ type isotropic phase only.

Figure 6.4 shows the fitted 1D WAXS patterns of the same isotropic and oriented PA12 samples studied by solid state NMR. All fits were made with 5 Gaussians – two for the monoclinic α-polymorph, two for the pseudo-hexagonal γ-type isotropic polymorph and one broad peak for the amorphous halo.

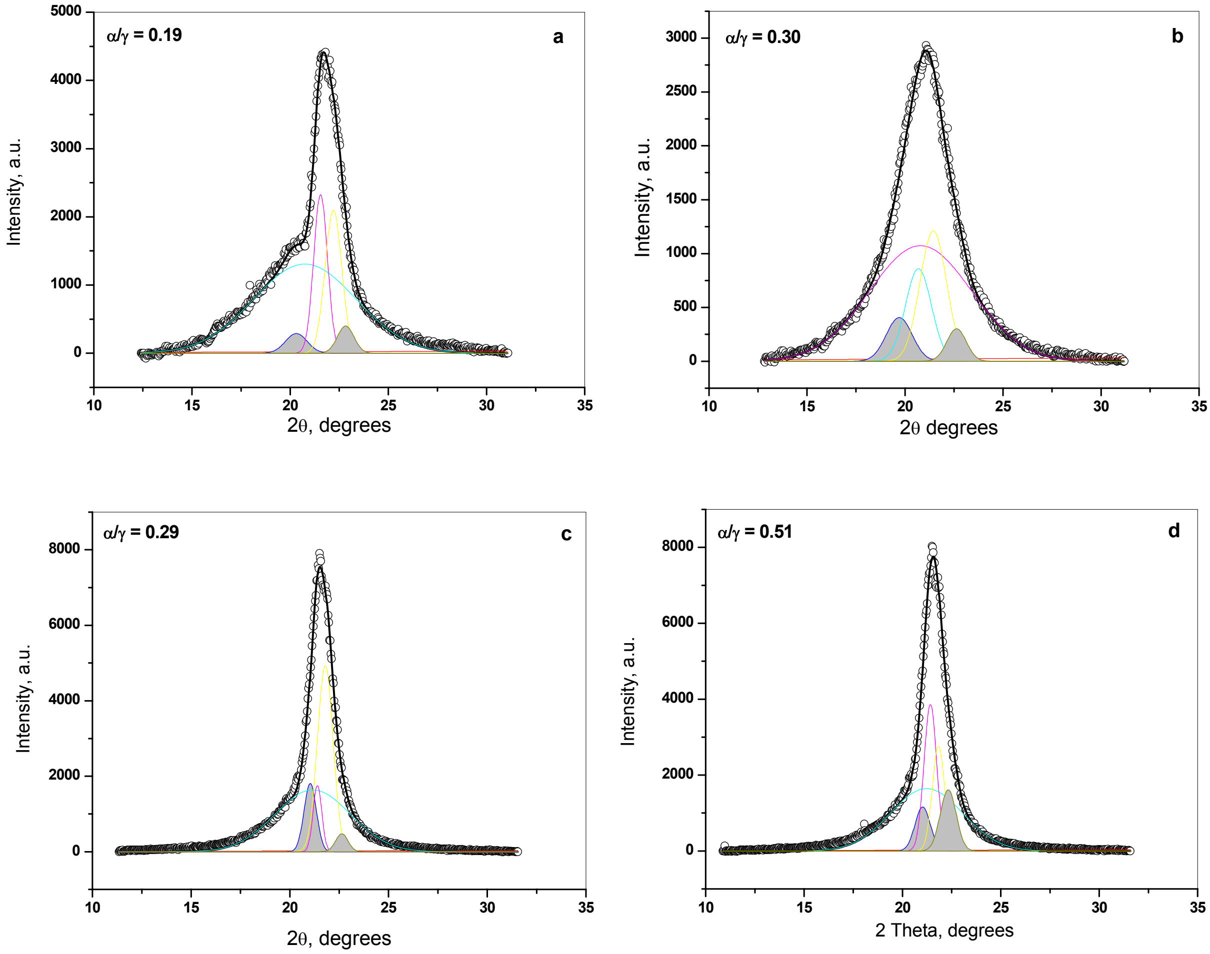

Figure 6.4 1D WAXS patterns of PA12 samples annealed for 1 h at 160°C and their fitting with Gaussian peaks: PA12 film before (a) (and after (b) TT; PA12 OC before (c) (and after TT (d). The peaks of the αPA12 are shaded. The amorphous halo was modeled by one Gaussian.

Comparing the shape of the patterns confirms the conclusion of the previous chapter that isotropic and oriented PA12 have different crystalline structures: the centers of the amorphous halos in the isotropic sample (Fig. 6.4 (a)) do not coincide with the main crystalline peaks as in PA12 with orientation (Fig. 6.4 b-d). Contrary to the oriented PA12 samples studied in Chapter 5, the OCs obtained in the extruder line, before and after the tensile test, contain significant amounts of the α-polymorph, larger than those found in the PA12 films. From the shapes of the 1D WAXS patterns of the oriented samples it is not straightforward whether or not they should be fitted with crystalline peaks for the α-phase. This becomes evident only on the basis of the NMR results shown in Table 6.2. It is worth noting that the α/γ ratios obtained from the WAXS patterns of the isotropic and oriented PA12 samples annealed at 160°C before and after TT almost coincide with those obtained with the same samples by fitting their NMR patterns. Therefore, the procedure of fitting of these particular WAXS curves was extended to all 1D WAXS patterns. The structural data obtained in such a way are presented in Table 6.3.

Table 6.3 Temperature dependence of the crystallinity indices CI_{total} or ECI, **α**-CI, **γ**-CI, and the **α/γ** polymorph ratio before and after tensile test resulting in sample failure (w.a. = without annealing).

Sample/ Annealing temperature, °C	**Before tensile test**				**After tensile test**			
	CI_α %	**CI_γ %**	**CI_{Total} or ECI**	**α/γ content**	**CI_α %**	**CI_γ %**	**CI_{Total} or ECI**	**α/γ content**
PA12 Isotropic Films								
120/1h	4.1	26.9	31.0	0.18	12.3	26.1	38.4	0.47
120/3h	6.6	27.0	33.6	0.24	9.2	27.5	36.7	0.33
140/1h	7.5	26.0	33.5	0.29	10.1	28.3	38.4	0.36
160/1h	6.0	31.3	37.3	0.19	9.1	30.2	39.3	0.30
PA12 Oriented Cables								
w.a.	8.4	33.4	41.8	0.25	-	-	-	-[a]
80/1h	9.4	31.9	41.3	0.29	14.9	28.3	43.1	0.53
100/1h	12.8	38.0	50.8	0.34	19.4	32.9	52.3	0.59
120/1h	14.5	36.6	51.1	0.39	20.9	32.4	53.3	0.65
140/1h	13.3	39.3	52.6	0.34	18.2	32.9	51.1	0.55
160/1h	11.5	37.8	49.3	0.30	17.6	33.9	51.6	0.52

[a] No data available.

As seen from Table 6.3 annealing of isotropic PA12 samples results in a small increase of CI, better expressed for the γ-crystals. Stretching during the tensile test resulted, as a rule, in stress-induced crystallization of amorphous material predominantly in α-form. With the PA12 OCs, when increasing the annealing temperature in the 80-140°C range, a significant increase in ECI of ca. 11% was produced. The small drop in ECI at 160°C, which is 15 degrees below T_m of PA12 should be attributed to some melting/recrystallization processes. The tensile test with the differently annealed OCs resulted in a general γ-to α-transition maintaining almost the same ECI values as before tensile testing.

6.3.4. 2D WAXS measurements

The crystallinity indices in Table 6.3 and the most of the d-spacings data in Table 6.4 were obtained on the basis of the 1D WAXS patterns. The latter, however, account only for the equatorial WAXS reflections. It is known from previous studies that the oriented γ-PA12 displays also meridional point-like reflections. Therefore, 2D WAXS patterns were obtained with Setup 2 (Chapter 2) from which the $d_{\gamma 020}$ were determined for some PA12 samples, before and after the tensile test. Selected 2D WAXS patterns are shown in Fig. 6.5.

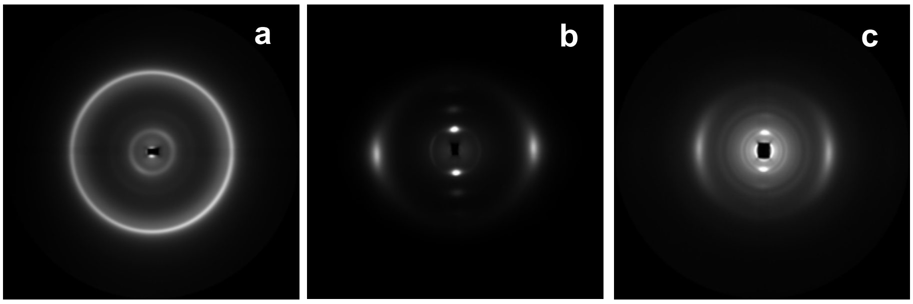

Figure 6.5 2D WAXS patterns of: (a) PA12 film annealed for 1h at 160°C; (b) oriented PA12 cable, without annealing; (c) sample (a) after the tensile test. All patterns are obtained at 30°C. The draw direction in (b) and (c) is vertical and **b** axis is the chain axis

The first pattern in Fig. 6.5 is isotropic. The equatorial cut of its external ring produces the pattern in Fig. 6.4 (a). The internal ring is related with $d_{\gamma 020}$ and is also quite isotropic. The pattern in Figure 6.5 (b) proves the strong orientation in the PA12 OCs, the DD being vertical. Drawing the PA12 films to sample failure transforms the isotropic pattern in Fig. 6.5 (a) into the well-oriented pattern in Fig. 6.5 (c) indicating that the external force is transferred to the crystallites. The 2D WAXS patterns of PA12 OCs upon drawing do not change their symmetry, only the scattering intensity decreases most probably due to smaller sample cross-section.

Increasing the annealing temperature of PA12 films in the 120 -160°C region leads to a decrease of $d_{\alpha 200}$, $d_{\gamma 001}$ and of $d_{\gamma 020}$ values while the rest of the d-spacings remain constant (Table 6.4). Drawing the films to sample failure results, generally, in a well-expressed growth of all d-pacing obtained from the equatorial reflections, whereas the $d_{\gamma 020}$ values drop. With the oriented PA12 samples, a clear trend toward diminution of $d_{\alpha 200}$ and $d_{\gamma 020}$ as a function of the annealing temperature was registered, the rest of the d-spacings remaining constant. The application of external force changes only the $d_{\gamma 020}$ values best revealed in the OC without annealing.

6.3.5 2D SAXS measurements

The evolution of the 2D SAXS patterns in isotropic and oriented PA12 samples as a function of the annealing temperature before and after tensile test is given in Figure 6.6. All PA12 initial films display isotropic patterns similar to that in Fig. 6.6 (a). After the tensile test, the films annealed for 1 h at 120 and 140°C produce clear four-point scattering diagrams of fiber structure (Figure 6.6 b), whereas the PA12 films with 3 h at 120°C and 1 h at 160C show only a central streak perpendicular to DD and no evidence of coherent scattering at larger s-values (Fig. 6.6 c).

The OCs have a completely different nanostructure (Fig. 6.6 d - f). The as-drawn cable and that annealed at 80°C show only a more or less symmetric central streak (Fig. 6.6 d) both before and after tensile test. Annealing in the 100-160°C interval results in the appearance of coherent scattering typical of a lamellar structure (pattern e), whose form does not change after the mechanical test (pattern f).

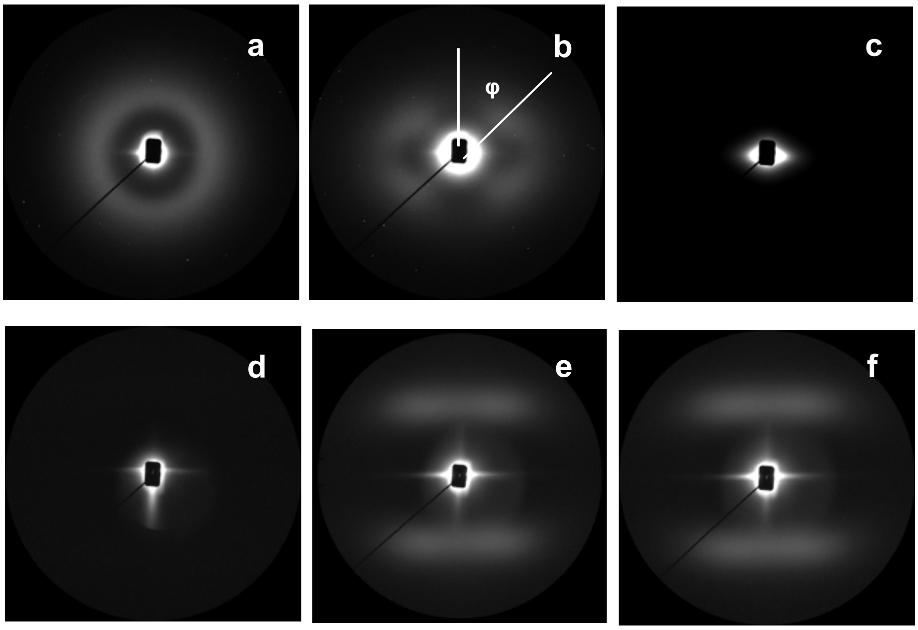

Figure 6.6 2D SAXS patterns of: selected isotropic films (a – c) and OCs (d - f) with various annealing before and after TT: (a) isotropic film, 1h at 140°C; (b) sample (a) after TT; (c) film 1 h at 160°C, after TT; (d) OC without annealing; (e) OC 1h at 160°C; (f) sample (e) after TT. All patterns are obtained at 30°C. The draw direction in oriented patterns is vertical.

Table 6.4 Unit Cell Vectors and the Corresponding d-Spacings Obtained from the 1D and 2D WAXS Patterns of Isotropic and Oriented PA12 Samples as a Function of Their Initial Annealing Before and After the Tensile Test that Resulted in Sample Failure.

Annealing, ºC	**$d_{\alpha200}$**		**$d_{\alpha002}$**		**$d_{\gamma200}$**		**$d_{\gamma001}$**		**$d_{\gamma020}$**	
	Before	**After**	**Before**	**After**	**Before**	**After**	**Before**	**After**	**Before**	**After**
PA12 isotropic film										
At 120/1h	4.28	4.36	3.82	3.90	4.02	4.14	3.96	4.02	14.00[a]	13.68
At 120/3h	4.25	4.36	3.82	3.86	4.02	4.12	3.92	4.02	-	-
At 140/1h	4.22	4.32	3.83	3.86	4.04	4.14	3.91	4.00	-	-
At 160/1h	4.21	4.38	3.79	3.82	4.01	4.18	3.90	4.03	13.34	12.99
PA12 orient. cables										
Without annealing	4.26	-	3.83	-	4.09	-	3.98	-	13.98	13.02
At 80/1h	4.22	4.20	3.84	3.88	4.07	4.07	3.96	3.99	-	-
At 100/1h	4.28	4.26	3.89	3.91	4.09	4.08	4.00	3.99	-	-
At 120/1h	4.15	4.13	3.89	3.90	4.04	4.04	3.98	3.96	-	-
At 140/1h	4.14	4.13	3.89	3.92	4.09	4.09	3.97	4.01	-	-
At 160/1h	4.11	4.11	3.82	3.87	4.03	4.03	3.96	3.96	13.50	13.12

[a] The **b** vector of the γ form for some samples was obtained from the meridional (020) reflection of the respective 2D WAXS patterns.

More structural information can be extracted from the above 2D patterns after their integration. Integrating in radial direction provides quantitative information about the L_B values and sample's scattering power, while the angular integration shows the intensity distribution in a given azimuthal angular range. Figures 6.7 and 6.8 display these data for PA12 films and OC before and after tensile testing as a function of the annealing temperature.

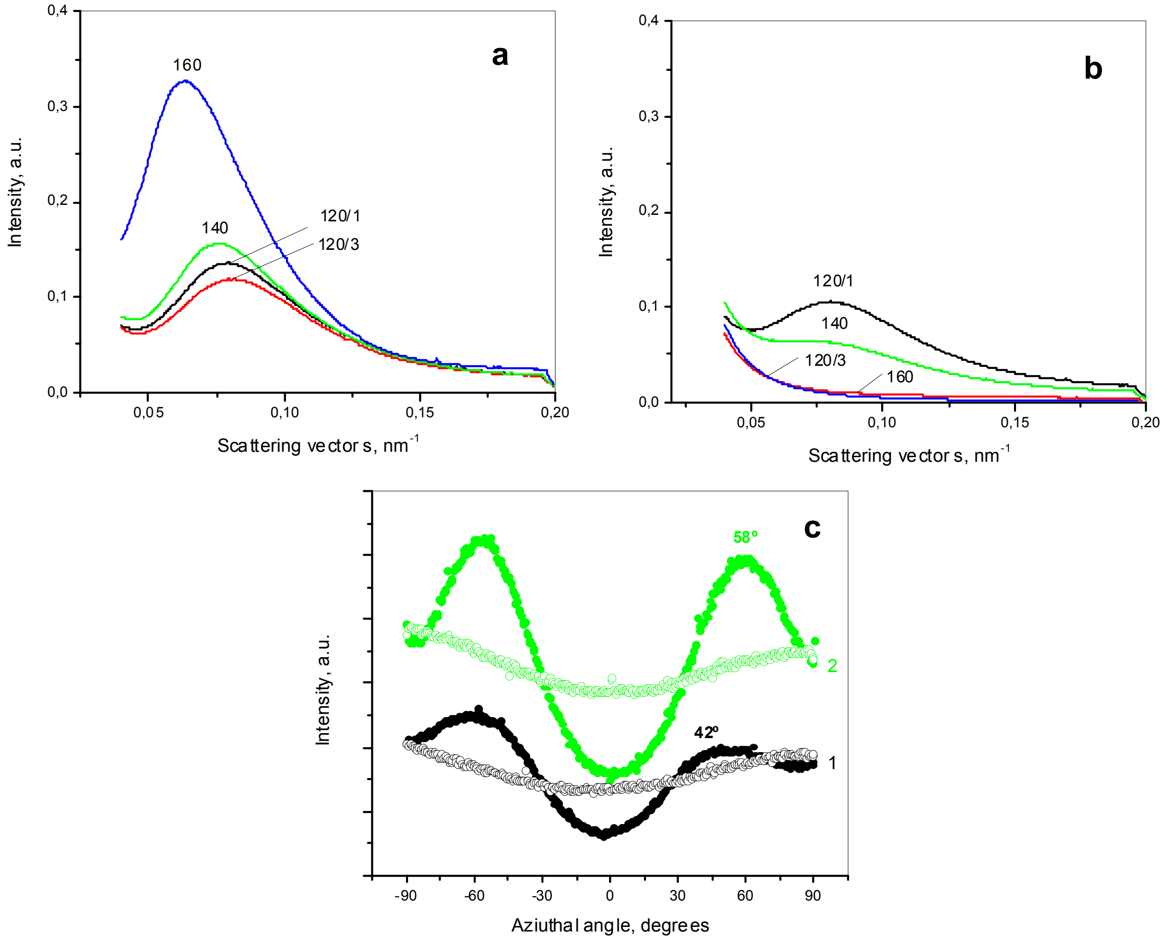

Figure 6.7 Integration of 2D SAXS patterns of initially isotropic PA12 films: (a) Raw 1D SAXS profiles as a function of the annealing temperature and duration, before TT; (b) same as (a), after TT; (c) azimuthal scans in the -90 – +90° range for a sample with: 1 - 1h at 120°C and 2 - 1 h at 140°C. Open symbols – before TT, solid symbols – after TT.

Analyzing the 1D SAXS profiles before and after tensile test presented in Figs. 6.7 and 6.8 shows that increasing the annealing temperature above 100°C results in a gradual increase of all L_B values (Table 6.5) and of the scattering power, especially at 160°C. Stretching to mechanical failure in PA12 films (Fig. 6.7.(b)) leads, in general, to significantly lower scattering intensities and lower L_B values (1h/120 and

1h/140°C) or to the complete disappearance of coherent scattering (3h/120, 1h/160°C). As seen from Fig. 6.7 (c), with the former two samples, the external load resulted in clear bimodal distribution of the scattered intensity with peaks at azimuthal angles φ = 45 and 60°, φ being the angle between DD and the normal to the lamellae surface (Fig. 6.6). Similar trends were revealed with the OCs. (Fig. 6.8 a, b), with the notable exception of the sample with 1h at 140ªC that after tensile test displayed higher scattering strength as compared to that of the initial OC. The azimuthal scans of all OC patterns before and after tensile test revealed curves very similar to those in Fig. 6.8 (c) indicating a four-point scattering diagram with φ = 30°.

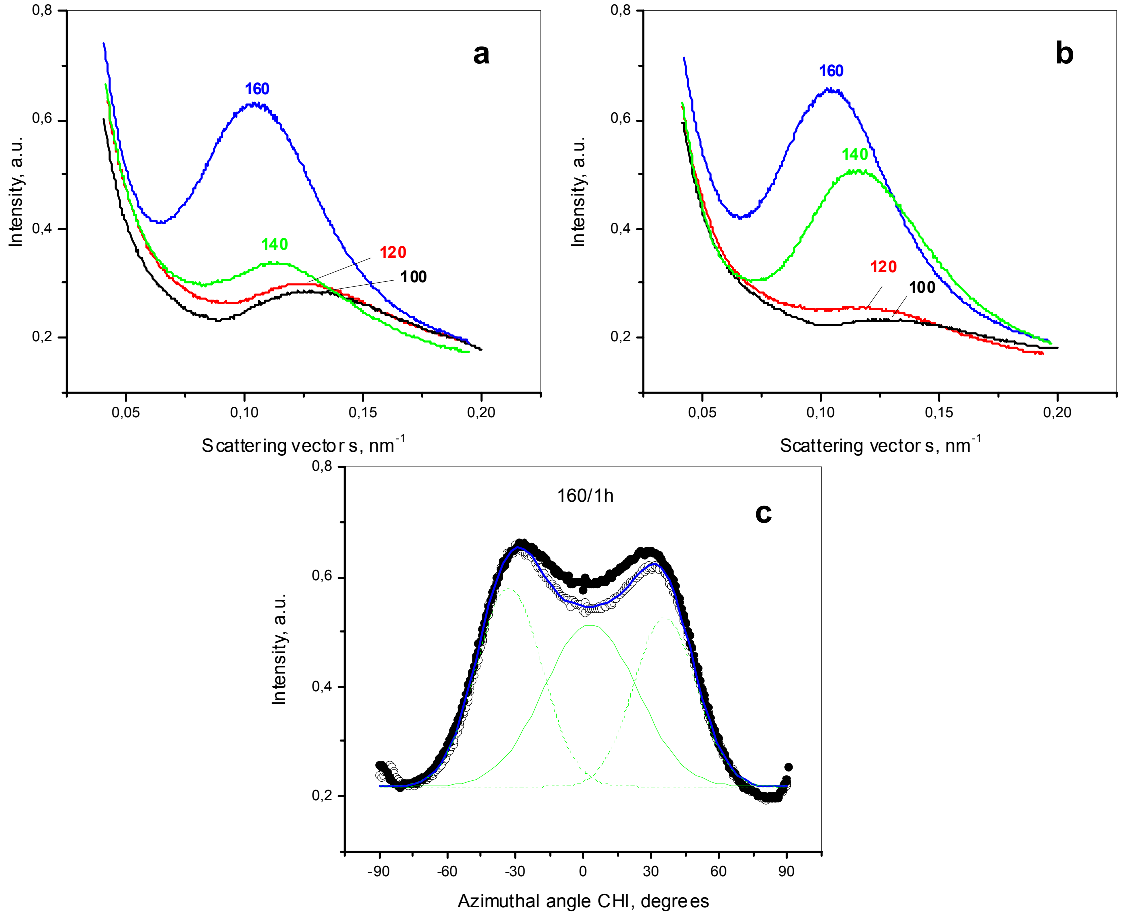

Figure 6.8 Integration of 2D SAXS patterns of PA12 OCs: (a) Raw 1D SAXS profiles as a function of the annealing temperature and duration, before TT; (b) same as (a), after TT; (c) azimuthal scans in the -90 +90° angle range for a sample with 1h at 160°C; open symbols – before TT, solid symbols – after TT. The fit is made with the sample before TT.

Table 6.5 summarizes the L_B values of all samples studied. They will be discussed in the next section.

Table 6.5 Long Spacing Estimates for Differently Annealed Isotropic and Oriented P12 Samples Before and After the Tensile Stress Test

Annealing at, ºC		L_B estimates[a], Å	
		Before	After
Isotropic PA12	120/1h	126	122-[b]
	120/3h	128	
	140/1h	130	124
	160/1h	160	-
Oriented PA12 cables	w.a.	-[b]	-[b]
	80/1h	-[b]	--[b]
	100/1h	77	78
	120/1h	78	78
	140/1h	84	85
	160/1h	96	96

Notes:

[a] The L_B values are determined form the raw SAXS profiles obtained after radial integration of the respective 2D images;

[b] No coherent SAXS scattering.

6.4. Discussion

6.4.1. PA12 Isotropic films

Analyzing the stress–strain curves in Figure 6.1 (a) and the numeric data in Table 6.1, it becomes evident that the annealed isotropic PA12 samples studied can be divided into two groups. Within each group the mechanical properties can be considered very similar. Thus, annealing for 1h at 120°C and 140°C results in ε_{br} values in the 190 - 200% range, σ_y being of ca. 32 MPa and the E values – below 900 MPa. With the other two films annealed for 3h at 120°C and 1h at 160°C respectively, the ultimate strain drops to 50-60%. At the same time, E goes above 1.0 GPa and σ_y also grows to ca. 35 MPa.

Relating the above mechanical behavior to the degree of crystallinity and the polymorph type (Table 6.3.) before tensile test is not clear-cut. On the one hand, increasing T_a from 120 to 160°C results in a 6% growth of CI_{total}, the largest difference being between 140 and 160°C. On the other hand, the α/γ content has its maximum at 140°C and goes back to the initial values of *ca*. 0.20 at 160°C. None of these changes can be linked directly to the mechanical performance of the respective samples. At the same time, however, Table 6.4 shows that increasing T_a and its time duration can lead to a slight but observable decrease of $d_{\alpha 200}$, $d_{\gamma 001}$ and $d_{\gamma 020}$ values. In the case of $d_{\alpha 200}$ and $d_{\gamma 001}$ this would mean a drop of the H - bond lengths within the α-PA12 and γ-PA12 sheets respectively. In the case of $d_{\gamma 020}$, one deals with a well-expressed shrinkage of the γ-type unit cell along the chain axis. Both effects are related to a denser packing of the macromolecules in the crystalline domains, which is a probable explanation of the increase of σ_y as the T_a grows.

All initially isotropic PA12 films after tensile test showed 2D WAXS patterns with fiber symmetry similar to that in Fig. 6.5 (c) indicating strong orientation of the crystallites along DD. Most all d-spacings increase after tensile test (Table 6.4) suggesting a stress-induced unit cell expansion. Only the $d_{\gamma 020}$ displays some decrease. The same effect was observed in oriented PA6, too (Chapter 4). At this point this experimental fact is not well understood.

The 2D and 1D SAXS data provide additional help in trying to understand the structure-properties relationship in isotropic PA12 films before tensile test. Figs. 6.6 (a) and 6.7 (c) show that the PA12 films are isotropic with an almost uniform distribution of the scattered intensity along the circular 2D SAXS pattern. As a result of annealing, the scattering strength increases – gradually between 120 and 140°C and with an abrupt jump between 140 and 160°C (Fig. 6.7 (a)). Exactly in the same way the respective L_B values grow (Table 6.5). Having in mind the CI_{total} values at the latter two temperatures (33.5 and 37.3%), the significant increase of L_B with 30 Å could hardly be attributed to lamellar thickening only, i.e., to changes exclusively in the crystalline domains. Considering also the mechanical data, a more logical explanation would be the supposition that annealing for 1h at T_a> 140°C or for 3h at 120°C results in the formation of certain amounts of rigid amorphous phase that cannot be detected by WAXS, whose density, however, is very similar to that of the crystalline domains and is registered by SAXS.

The structural data after tensile test in this chapter support the supposition of amorphous phase hardening above certain T_a. As already mentioned, the samples annealed for 1h at 120 and 140°C have similar ε_{br} of ca. 190 and 200%, as compared to the 50-60% of the samples with 3h at 120 and 1h at 160°C. This observation can be explained by the well-known concept that deformation of semicrystalline polymers takes place by unfolding of the flexible macromolecules found in the disordered domains between the stiff ordered crystalline regions. Apparently, more flexible amorphous domains would correspond to higher ε_{br} values and *vice versa*.

A logical consequence of the above concept is that a part of the external force applied during tensile test would be transferred to the crystalline domains thus enabling stress-induced structural changes. Comparing the α/γ content before and after tensile test (Table 6.3) suggests that the strongest γ- to α-transition as a result of the tensile test is registered after 1 h at 120°C and the lowest – after 1h at 160°C. This leads to the unexpected conclusion that more flexible disordered domains would transfer to the adjacent crystalline domains a bigger part of the external force applied upon stretching. The evolution of σ_{br} as a function of T_a (Table 6.1) would explain this apparent paradox. Due to strain hardening, the films annealed for 1h at 120 and 140°C have reached higher σ_{br} values that have intensified the stress-induced γ- to α-polymorph transition.

More evidence of the appearance of rigid amorphous phase as a result of annealing is found in the SAXS data in Figures 6.6 and 6.7. After the tensile test, the PA12 films annealed for 1h at 120 and 1h at 140°C reveal four-point patterns similar to that in Fig. 6.6 (b). The structure that gives rise to such patterns is still being debated. According to some authors, the lamellar surface can tilt because of the progressive shear between the crystalline stems within the lamellae [8-10]. In this model, a two- or a four-point pattern is obtained depending on whether this surface is perpendicular or tilted away from the chain axis (in this case coinciding with DD), respectively. In a second group of models [11,12], a four-point pattern is obtained when the lamellae are arranged in a lattice that resembles a checkerboard, and a two-point pattern is obtained when the lamellae are arranged in columns and the positions of the lamellae in the neighboring columns are not correlated. A recent extensive SAXS study on the deformation behavior of some thermoplastic polymers combines the above two models. Thus, samples subjected to high deformations (250 - 500%) and thereafter unloaded consist of parallel crystalline lamellae tilted with respect to DD. Under stress, however, there occurs a disruption of the tilted lamellae into smaller pieces. These fragments form a macrolattice with hexagonal order. When the elongation is increased beyond 250%, the lattice is transformed into an ensemble of microfibrils with little correlation in lateral direction giving rise to a two-point (lobe type) pattern [13].

To explain the four-point patterns in the films annealed at 120°C/1h and 140°C/1h after the tensile test, the presence of flexible amorphous phase was supposed. The simplified scheme in Fig. 6.9 visualizes the application of the tilted lamellae deformation model with these samples. Underneath the cartoons of the respective lamellar structures, the scattering patterns produced by them are given.

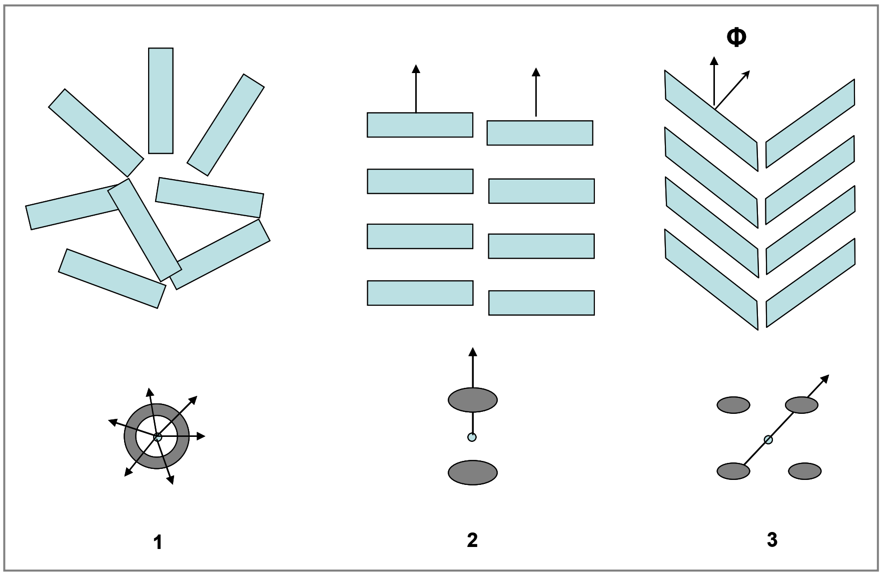

Figure 6.9 Simplified scheme of the stress-induced changes in isotropic PA12 films with flexible amorphous phase. The shaded rectangles represent the crystalline domains of the lamellae. 1 – Random distribution of lamellae in the starting films resulting in spherical SAXS patterns; 2 – Oriented lamellar stacks before TT resulting in two-point scattering patterns; 3 – Tilting of the lamellar stacks after TT producing four-point patterns

Straining the isotropic PA12 films with flexible amorphous phase during the tensile test causes the arrangement of the random lamellae (1) into lamellar stacks oriented perpendicularly to DD (2). The latter is present while the sample is still under stress in the testing machine. Depending on the force applied, various increases in the L_B values will be registered. After sample failure, rupture of the tie molecules between the crystalline domains occurs. The release of the external force allows for the said lamellar tilt to take place. From the azimuthal scans in Fig. 6.7 (c) It was found out that the lamellar tilts are at ca. 45 (1h/120°) and 60° (1h/140°C). This is accompanied by a measurable decrease of L_B which is expectable in the case of relaxation. Figure 6.7 (b) shows also that the tensile test of the latter PA12 films results in a loss of scattering power, most probably due to a lesser density of the scattering domains.

After the tensile test of the harder PA12 films (3h/120°C and 1h/160°C), a complete loss of coherent SAXS scattering is observed (Figs. 6.6 c, 6.7 b). The reason for this effect cannot be the disappearance of the denser domains since the CI_{total} of the stretched samples increases as compared to that in the respective samples before the tensile test. Most probably, as a result of stretching along the chain axis, the L_B values become too large to be registered by a sample-to-detector distance of 2.7-2.8 meters. Evidently no relaxation with L_B decrease could occur after stress release. This fact indirectly supports the hypothesis that harder amorphous phase is produced at higher T_a or longer annealing times in PA12 films.

6.4.2. Oriented PA12 cables

The stress–strain curves of all PA12 cables [Fig. 6.1 (b), Table 6.1] were characterized by double yield, The two σ_y values change with T_a reaching the highest values after annealing at 140°C but it is difficult to trace any proportionality between these two parameters. All PA12 cables display similar ductility. As expected, the biggest ε_{br} was displayed by the OC without annealing, and the smallest – by the OC annealed at 160°C. The E values were also affected by the annealing: In principle, the higher the T_a was, the bigger E values were obtained.

Comparing the mechanical data of the OCs in Table 6.1 to the structural data extracted from the crystalline phase in Table 6.3 shows that the highest ultimate stress values of 266 MPa was obtained with the OC annealed at 140°C, which has the highest ECI of ca. 53% containing at the same time the highest percentage of γ-polymorph – close to 40%. Any decrease of ECI led to diminution of the ultimate stress values. Annealing temperature of 160°C seems to be higher than the optimum causing some loss of crystallinity directly reflecting in lower stress values (Tables 6.1., 6.3) Annealing the OCs in the 80-160°C leads to a general decrease of the $d_{\alpha 200}$ and $d_{\gamma 020}$ values indicating a denser packing of the macromolecules. As expected, all 2D WAXS patterns display a strong orientation along the DD (Fig. 6.5). This observation was confirmed by the 2D SAXS patterns in Figure 6.6. Some coherent scattering of lamellar structures was revealed only after annealing of the OCs at T_a >100°C. As in the previous section, increasing the annealing temperature increases the scattering power of the OC before tensile test (Figure 6.8 a). The jump in the scattered intensities between 1h at 140 and 160°C was again attributed to the formation of rigid amorphous phase not detectable by WAXS.

All curves obtained by azimuthal integration of the 2D SAXS patterns of OCs annealed above 100°C are similar to that in Fig. 6.8 (c), which exemplifies the sample annealed at 160°C. These curves are different from those of the soft PA12 films after the tensile test (Fig. 6.7 c). The latter can be fitted with two Gaussians without any peak centered at 0° thus indicating a “pure” four-point pattern attributable to the presence of tilted lamellae (Fig. 6.9). The curves of the OCs in Fig. 6.8 (c) need to be fitted with three Gaussians, the middle one being at 0° in respect to the chain axis direction. This finding supports the coexistence of two- and four-point patterns in the oriented PA12 samples. As mentioned above, such patterns are typical of oriented semicrystalline fibers under stress whose scattering elements are arranged in a macrolattice. Figure 6.10 gives a schematic representation of the various structures and the respective SAXS patterns in PA12 OCs.

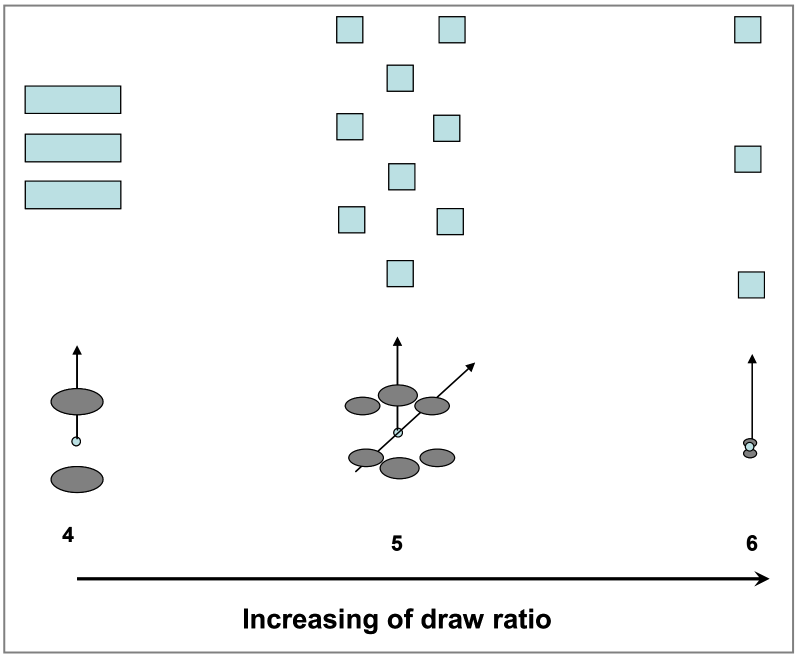

Figure 6.10 Simplified scheme of the stress-induced changes in PA12 OCs. The shaded rectangles represent the crystalline domains of the lamellae. 4 –Oriented lamellar stacks formed at lower DR resulting in two-point scattering patterns; 5 – Co-existence of two- and four-point patterns at medium DR arranging the scattering elements in macrolattice; 6 - loss of lateral correlation and formation of fibrils with very large L_B .

Thus, the initial OC without annealing as obtained in the extruder line is characterized by a nanostructure composed of laterally uncorrelated fibers with very large long spacings impossible to register with the maximum sample-to-detector distance of 2800 mm of Setup 1. The scattering pattern is supposed to be of two-point type with its lobes being hidden behind the beamstop (cartoon 6 in Fig. 6.10). Annealing the OCs with free ends at a $T_a \geq 80^{a}$C results in relaxation whose macroscopic effect is the strong cable contraction observed with all OCs upon heating and drop in L_B being sufficient to reveal coherent SAXS scattering with Setup 1. Moreover, the significant increase in ECI registered in samples annealed at $T_a \geq$ 100°C (Table 6.3) may be related to the formation of some new crystalline domains of α-type appearing between the lamellae and leading to macrolattice formation similar to Fig. 6.10, cartoon 5. As a result, the L_B values drop significantly making possible their registration. The scattering type also changes displaying coexistence of two- and four-point patterns. As seen from Table

6.5, increasing the T_a to 140 and especially to 160°C starts a trend toward L_B growth. Based on the ECI data (Table 6.3), this effect can be explained with lamellar thickening (up to 140°C) or with incipient fusion of some elements of the macrolatttice (at 160°C), apparently from the α-PA12 polymorph.

With the PA12 OCs one does not observe pure two-point patterns corresponding to structure 4 in Fig. 6.10. The reason is that such a structure is expected at relatively low deformations. The preparation of OCs includes cold drawing to high DR causing irreversible disruption of the crystalline lamellae to form fibrillar structure. However, undisrupted oriented lamellar stacks giving two-point patterns have been undoubtedly registered at low deformation rates (ca 50%) with a number of thermoplastic neat polymers and segmented copolymers [13].

All OCs display ε_{br} values between 20 and 30%. Straining during the mechanical test leads to a well-pronounced γ- to α-form transition (Table 6.3). As seen from Fig. 6.8 b, the tensile test results in a decrease of the scattering power with T_a of 100 and 120°C as compared to the respective values before tensile test (Fig. 6.8 a). With the samples annealed for 1h at 140^{a}C and 160°C there is an increase of the scattered intensity, much stronger in the former case. These results can be explained with the formation of additional amounts of rigid amorphous phase. As seen from Table 6.5, there are no changes in L_B after tensile test, *i.e.* relaxation does not occur upon sample failure in any of the OCs. This finding indicates that the amorphous phase is hard enough to prevent any significant shrinkage of the microfibrils even at the lowest annealing temperature. This is in good agreement with the fact that the d-spacings of all OCs before and after tensile test do not change significantly (Table 6.4). The notable exception is the $d_{\gamma 020}$ value dropping strongly upon sample failure, the reason for which is not well understood at this point.

6.5 Conclusions

The PA12 isotropic films obtained by the compression molding and the PA12 oriented cables obtained by consecutive extrusion and cold drawing contained predominantly the γ-crystalline form with some amounts of PA12 α-modification, the fraction of the latter being larger in the oriented samples. The combination of Carbon 13 solid state NMR with WAXS and SAXS from synchrotron was very useful for obtaining of reliable structural information about the polymorph transitions in PA12. Thus, the annealing applied caused an additional γ-to-α form transition expressed in an increase of the α/γ content. Both isotropic and oriented PA12 samples showed a growth in the E and σ_y values, as well as a decrease in ε_{br} values as the annealing temperatures increased. This behavior was explained, on a crystallographic level, by a denser packing of the macromolecules in the crystalline domains. All structural data obtained allowed the supposition of formation of rigid amorphous phase in the annealed samples. The external stress applied during the tensile test led to additional stress-induced γ-to α-form transitions in all PA12 samples accompanied by changes of the respective nanostructures.

6.6. References

1. Ulf H, and Rohde-Liebenau W, Nylon 12 in: *Polymer Data Handbook*, ed by Mark JE, Oxford University Press, New York, 1999, pp. 225-229.
2. Apgar GB and Koskoski MJ, Nylon 12 in: *High Performance Polymers: Their Origin and Development*, ed by Seymour RB and Kirshenbaum CS. Elsevier Science Publishing, New York,1986, pp. 55-65
3. Kohan MI, *Nylon Plastics Handbook,* Hanser Publishers, Munich (Hanser/Gardner Publications, Cincinnati), 1995.
4. Dencheva N, Nunes T, Oliveira MJ, and Denchev Z, *J Polym Sci Part B: Polym Phys* 43:3720 (2005).
5. Ishikawa T, Nagai S, and Kasai N, *Die Makromol Chem* 182:977 (1981).
6. Hiramatsu N, Hashida S, and Hirakawa S, *Jpn J Appl Phys* 21:651 (1982).
7. Mathias LJ and Johnson CG, *Macromolecules* 24:6114 (1991)
8. Pope DP, and Keller A, *J Polym Sci Polym Phys Ed* 13:533 (1975).
9. Matyi RJ, and Crist B Jr, *J Polym Sci Polym Phys Ed* 16:1329 (1978).
10. Gerasimov V I, Genin Ya V, Kitaigorodsky A I, Tsvankin D Ya, *Kolloid Z Z Polym* 250 :518 (1972).
11. Statton WO, *J Polym Sci* 16:143 (1959).
12. Wilke W, and Bratrich M, *J Appl Cryst* 24:645 (1991).
13. Stribeck N, Fakirov S, Apostolov AA, Denchev Z, and Gehrke R, *Macromol Chem Phys,* 204:1000 (2003)

CHAPTER 7

STRUCTURE DEVELOPMENT IN POLYAMIDE 6 REINFORCED COMPOSITES

This chapter presents studies on the morphology and the fine structure of polyamide 6 reinforced MFCs and their precursors. The methods of SEM and X-ray scattering were used to the purpose. The evolution of the structure was followed during the various processing stages and as a function of the blend composition. In Table 2.2, column 1 (Chapter 2) the compositions of all PA6 blends was presented. As indicated there, four types of composites were prepared: unidirectional ply lamina (UDP), cross-ply composites (CPC), composites from middle-length, randomly oriented bristles (MRB) and from non-oriented material (NOM). The objective was to investigate the effect of the length, diameter and alignment of the reinforcing fibrils on the structure and properties of the respective composite. The NOM sample, which does not contain fibrous reinforcement, was included as a reference. The presence of nanofibrils in the final MFCs was undoubtedly confirmed and conclusions were drawn about how processing and blend composition influence the orientation and the dimensions of these nanofibrils.

7.1. SEM investigations

Figure 7.1 displays selected SEM images of PA6-containing materials at different stages of the MFC processing: after the extruder die (column 1), after the first haul-off unit (column 2) and of the final MFC in the form of unidirectional ply (column 3). To be able to observe the reinforcing fibrils, specimens were cut out of the MFC plate in a direction perpendicular to the fibril axis. These specimens were then fractured as indicated in the experimental part. The sample shown in Figure 6 c that corresponds to the MFC containing the maximum amount of PA6, was impossible to fracture under these conditions. The observation of microfibrils by SEM was only possible after selective dissolution the HDPE matrix in hot toluene for 5 hours. One should mention that, due the removal of the matrix, the reinforcing fibrils lost its original alignment in the composite.-

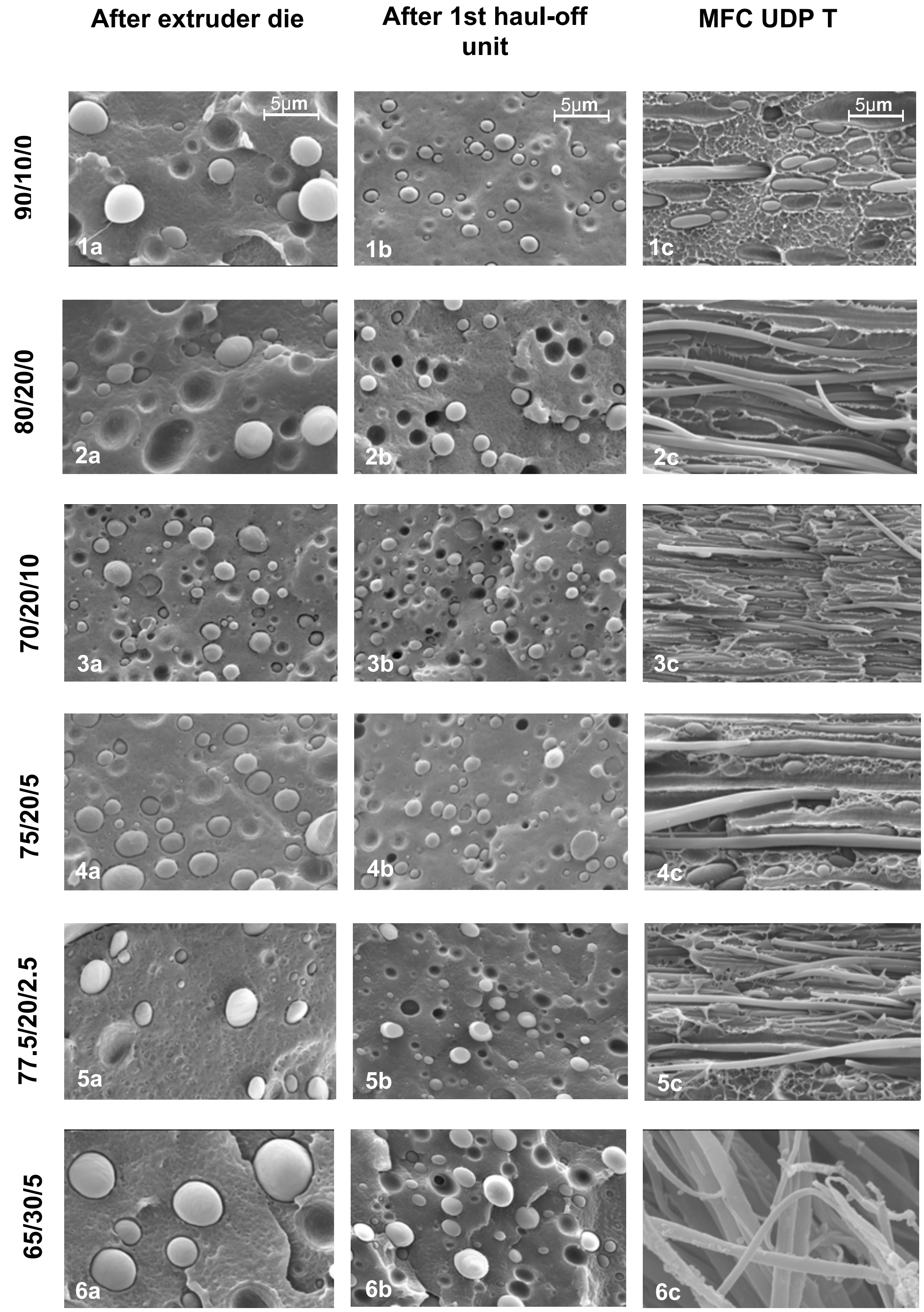

Figure 7.1 SEM images of various HDPE/PA6/YP materials after cryogenic fracture at the various stages of the MFCs preparation (compositions given in wt. %): non-oriented blend right after the extruder die (1-6 (a)); slightly oriented blends after the first haul-off unit (1-6 (b)); UDP composites fractured along the fibrils axis (1-5 (c)); UDP composite 65/30/5 after selective extraction of the HDPE matrix (6 (c)).

As it can be seen in Figure 7.1, immediately after the extruder die, the PA6 phase is well dispersed in small globular domains with diameters in the 2-4 μm range. In the presence of the Yparex compatibilizer (images 3-5 a), the diameter of the globules become smaller (from 0.5 to 2.5 μm), whereby the higher the compatibilizer concentration, the smaller the size and narrower the distribution are. It is evident from the pictures that the compatibilizer contributes for a better dispersion of the PA6 phase within the HDPE matrix. The system with 30% of PA6 (image 6 a) is an exception as the diameters of the PA6 droplets reached the biggest value – ca. 5 μm. This may be due to an unfavourable combination of a high PA6 concentration with low compatibilizer concentrations that prevented a good mixing in this system.

As expected, after the first haul-off unit (samples 1-6 b), the diameter of the polyamide globules decreases. This decrease is larger in the blends without compatibilizer, most probably because the PA6 phase, being less linked to the matrix, could attain higher orientation.

The SEM images of the final MFCs (1-6 c) deserve special attention because the SEM method undoubtedly confirms that: (i) the PA6 reinforcing phase has well-expressed fibrillar morphology and (ii) the average diameter of these fibrils are in the upper nanometer – lower micrometer range, *e.g.*, from 0.6 to 1.5 μm (samples without compatibilizer) and from 0.5 – 1.0 μm (compatibilized samples). Therefore, depending on the compatibilizer content, the resulting composites can be considered as either nanostructured (NPC) or microfibrilar (MFC). Further on we will accept the second abbreviation indicating when necessary the real fibre diameter.

Figure 7.2 displays the influence of the length and alignment of the reinforcing phase on the morphology of two representative examples of MFCs – without (80/20/0) and with 10% compatibilizer (70/20/10). While the UDPs show all the long fibrils laying nearly parallel to the fracture plane (Fig. 7.2, images 1a and 1b), as it would be expected in the case of the CPCs, the fibrils are aligned in two perpendicular directions (the fibrils with perpendicular orientation to the fracture plane show a circular cross-section).

Images 3a and 3b correspond to the composites produced from randomly oriented middle-length bristles. Here a great variety of fibril cross-section shapes can be seen: rectangular, spherical or oval, depending on the angle between the fibril and the fracture plane. In the NOM samples, however, oval-shaped entities instead of fibrils are only observed, which indicates that after the first haul-off unit the orientation of the PA6 component is either absent or very low. It is also interesting to observe in the images of Figure 7.2 the improvement in the adhesion between the PA6 and the HDPE in the presence of compatibilizer. This effect is particularly clear when one compares images 1a and 1b. In the absence of YP compatibilizer (first image) the fibrils are completely detached from the matrix while in the specimen with compatibilizer (second image) they are well imbibed, evidencing a good adhesion.

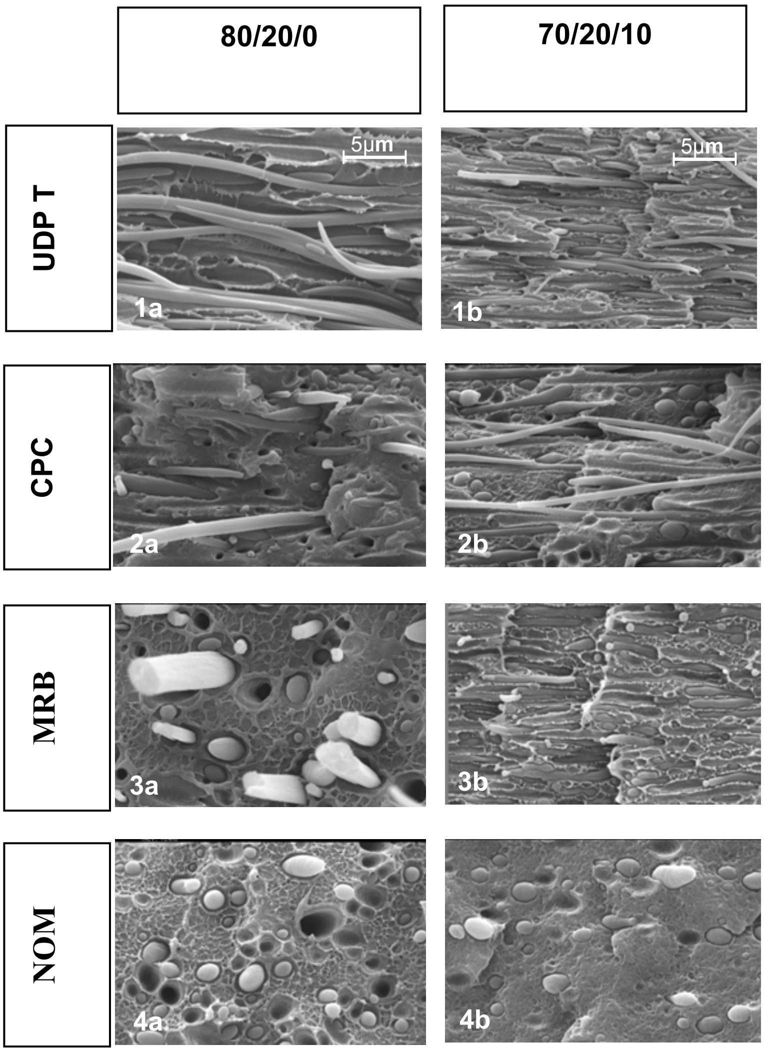

Figure 7.2 SEM images (after cryogenic fracture) of various MFCs made from two HDPE/PA6/YP blends [1-4 (a): 80/20/0 wt.%; 1-4 (b): 70/20/10 wt.%]: UDP T - unidirectional ply fractured parallel to the fibril direction; CPC - cross-ply composite; MRB – composite from middle-length PA6 bristles with random orientation; NOM – obtained from non–oriented granules of the two blends.

None of the images of MFCs in Figure 7.1 permits to measure directly the fibrils lengths. Indirectly, the average lengths and aspect ratios of the reinforcing PA6 fibrils could be evaluated in the following way. It can be seen that in the micrographs at the extruder die, *i.e.*, in the absence of orientation, the PA6 entities are globular (Figure 7.1, images 1a-6a). After measuring the diameters of theses globules, the average volume of the spherical PA6 entities is calculated. Furthermore, the diameters of the fibrils in the final MFCs are measured and averaged. Supposing that the fibrils' geometry is cylindrical and that they are produced by deforming the respective PA6 spheres without the formation of voids, *i.e.*, the volume of the PA6 spheres at the extruder die and of the MFC fibril are the same, it is possible to determine the average length of the fibrils. The aspect ratio then will be given by the relation between this length and the cross-section of the fibril calculated on the basis of the fibril diameter (Images 1c-6c). Thus, in non-compatibilized PA6-reinforced MFCs the length of the reinforcing fibrils can reach 120 μm, whereas the maximum length in the presence of compatibilizer is *ca.* 40 μm. This would give aspect ratios of 80-200 and 40-80, respectively.

The next SEM study was performed for a better understanding of the influence of the Yparex compatibilizer on the composite morphology. As confirmed by several studies (Chapter 1, [66, 67]), the Yparex reacts chemically with the PA6 component. The copolymer formed acts like a bridge between the pure HDPE and PA6 thus strengthening the interface. It was interesting to check how the pure fibrils (*i.e.*, after selective removal of the HDPE matrix) will look like in MFCs prepared without Yparex (Figure 7.3, image 1a) and with 10 and 5% of it (2a, 3a). Apparently, in the absence of compatibilizer the HDPE matrix is easier to dissolve and remove, that is why the remaining fibrils are smooth. In the presence of 10% Yparex, after the same time of extraction, the fibrils are still covered by many globular fragments, most probably originating from the HDPE isotropic matrix. Increasing the PA6 content and decreasing the percentage of Yparex gives again smooth fibrils, similar to those when no compatibilizer is applied (image 3 a). Therefore, the fibrils roughness in Figure 7.3 could be related with the HDPE-PA6 copolymer formation at the interface resulting in better adhesion at the fibril-matrix interface

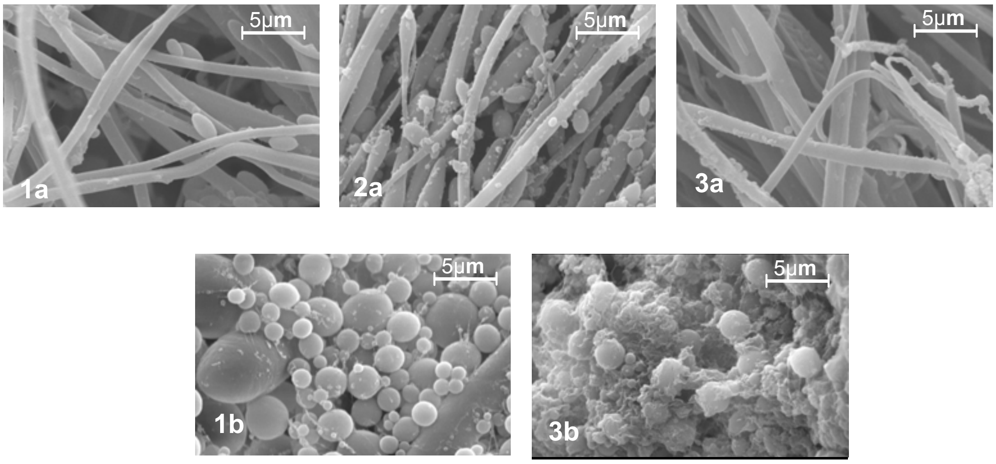

Figure 7.3 SEM images of various HDPE/PA6/YP samples (after extraction of the matrix) with the following compositions (wt. %): 1 - 80/20/0; 2 - 70/20/10; 3 - 65/30/5; (a) – final MFCs; (b)– non-oriented blends after the die exit.

The images 1b and 3b allow drawing the following conclusions: (i) after the die exit the reinforcing phase is indeed globular (ii) under identical extraction conditions, the removal of the HDPE matrix is much more difficult when the compatibilizer is present than when it is absent; (iii) in the compatibilized material the linkage at the PA6/HDPE interface appears to be stronger in the globules than in the final composite.

Discussing the MFCs in Figure 7.3 it is worth noting that the fibril thickness in images 1-3 (a) is quite similar, irrespective of the sample composition. The question arises if the fibrils observed are of pure PA6 or also include at their interface physically (image 1a) or chemically (2a, 3a) bonded, oriented HDPE. This question can be elucidated by X-ray scattering experiments.

7.2. X-Ray analyses – WAXS and SAXS

To study further the structure of the PA6 reinforced MFCs and their precursors, WAXS and SAXS measurements were performed as explained in the Experimental part. Figure 7.4 displays some representative 2D WAXS patterns of oriented cables obtained after the second haul-off unit before the selective isotropization of the HDPE component.

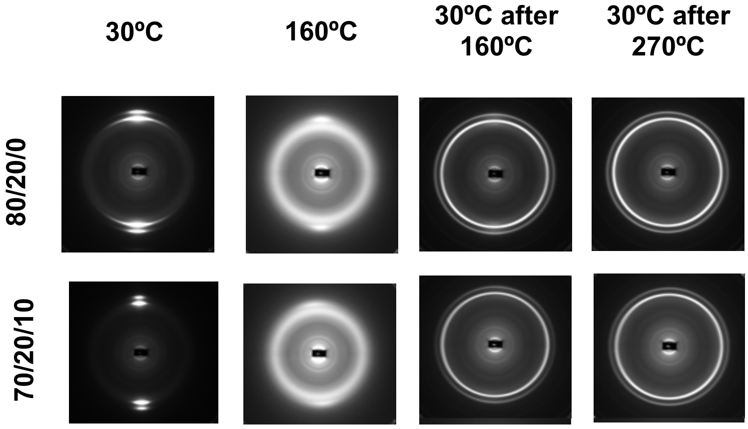

Figure 7.4 2D WAXS patterns of HDPE/PA6/YP oriented cables taken at various temperatures. DD is horizontal.

Visual inspection of the above WAXS patterns is enough to draw some initial conclusions about the structure development during the transformation of the oriented precursors into composites. At 30°C, both oriented samples are characterized by high orientation along the horizontal DD. The two reflections of HDPE ([110] – internal; [200] - external) are almost superimposed with those of the PA6 component. Comparing the arc reflections of the HDPE phase in the non-compatibilized 80/20/0 oriented blend with the respective point-like reflections in the compatibilized one, it can be concluded that in the latter case the HDPE component is better oriented. Heating the two blends at 160°C models the temperature profile of the isotropization stage. The two images at this temperature show a clear amorphous halo of the molten and isotropized HDPE. The reflections observed perpendicular to DD indicate that the PA6 component retains its orientation. Moreover, it can be seen that in the absence of compatibilizer the PA6 phase reaches higher levels of orientation, which is in good agreement with the SEM data. Undoubtedly, the PA6 phase is in α-crystalline form, since there are no meridional reflections (parallel to DD), typical of the oriented γPA6 polymorph (Table 3.3, Chapter 3).

The two WAXS images obtained at 30°C after heating to 160°C model the structure of the MFC. The circular reflections (Debye rings) of HDPE matrix are superimposed on the oriented reflections of the PA6 component.

As expected, isotropic Debye rings for the two components are only obtained at 270°C, *i.e.*, after the melting of the PA6 component, too.

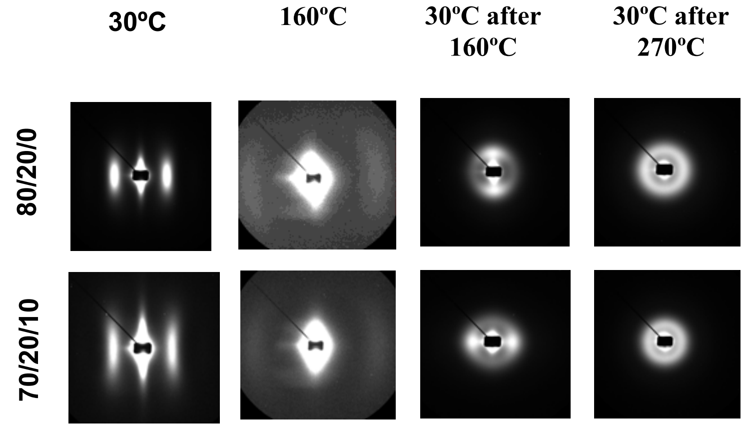

Figure 7.5 2D SAXS patterns of HDPE/PA6/YP oriented cables taken at various temperatures. DD is horizontal.

Additional important information about the structure development during the MFC preparation may be obtained from the SAXS patterns of the same representative HDPE/PA6/YP oriented cables (Figure 7.5). The characteristic SAXS images at 30°C confirm the fiber symmetry of the two OCs suggesting some differences in the lamellar structure of the oriented HDPE component. The PA6 component can be visualized only at 160°C after melting the matrix. At this temperature both images show low-intensity SAXS reflections oriented parallel to DD. Cooling the two samples down to 30°C reveals a significant difference between the non-compatibilized and compatibilized samples. In the first case, the recrystallized HDPE lamellae change their initial orientation and become perpendicular to DD, whereas in the second case the HDPE lamellae maintain the same direction - parallel to DD. It can be concluded that the presence of compatibilizer in the OCs impedes the reorientation of the HDPE phase when it crystallizes epitaxially upon the oriented PA6 fibrils.

The two patterns obtained after heating the blends above the melting point of PA6 with subsequent crystallization are isotropic.

Similar WAXS and SAXS measurements were performed with the respective 80/20/0 and 70/20/10 UDP composites (Figures 7.6 and 7.7).

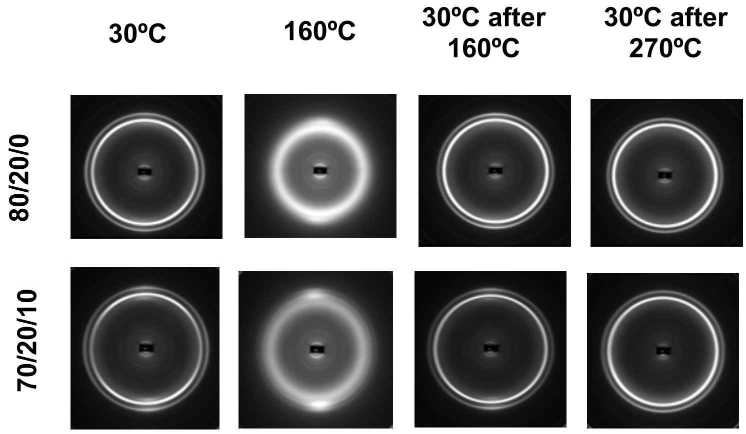

Figure 7.6 2D WAXS patterns of HDPE/PA6/YP microfibrilar composites taken at various temperatures. DD is horizontal.

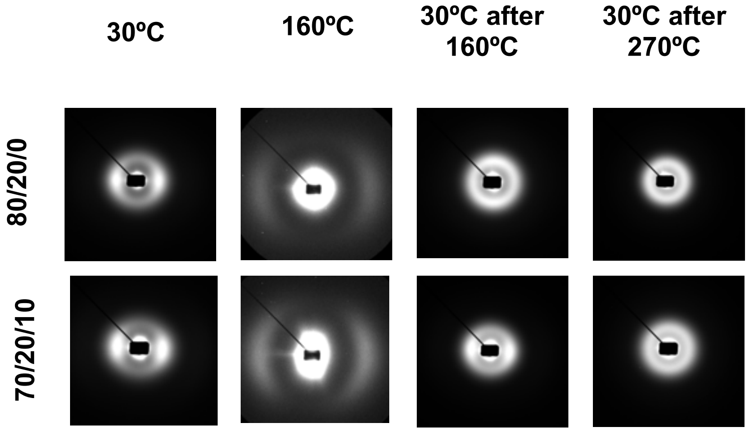

Figure 7.7 2D SAXS patterns of HDPE/PA6/YP microfibrilar composites taken at various temperatures. DD is horizontal.

As expected, the WAXS patterns of the two starting MFCs at 30°C (Figure 7.6) seem to be very similar to those of the respective oriented cables obtained at 30°C after heating at 160°C (Figure 7.4). Nevertheless, one has to keep in mind that the model isotropization was done in the sample chamber of the WAXS synchrotron setup with one single oriented cable by heating it up to 160°C and then cooling it down to 30°C. The isotropization occurring during the MFC preparation takes place by hot pressing the oriented cables under a pressure of 20 bars, with both the heating and the cooling rates being very distinct from those used in the synchrotron experiment. However, the said differences do not seem to influence the crystalline structure as revealed by WAXS.

The SAXS patterns presented in Figure 7.7 show~~s~~ the presence of oriented reflections (L_B >200 Å), which cannot be attributed to the PA6 phase, whose typical values are in the range of 60-80 Å (Chapter 3). Due to the big differences in the contrast of the two blend components in the patterns, the oriented PA6 phase can only be seen after the melting of the matrix. Figure 7.7 clearly shows the presence of oriented PA6 at 160°C. Therefore, the oriented reflections in the starting MFCs at 30°C belong to HDPE matrix material crystallized upon the oriented PA6 fibrils. Consequently, the reinforcing fibrils have a layered structure: a core of oriented PA6 and a shell of oriented HDPE. This finding is in good agreement with the SEM results.

Another observation is that the direction of orientation of the HDPE shell can vary. The SAXS images of the MFCs at 30°C that are supposed to be similar to those at 30°C after heating to 160°C, in fact, show some differences. The matrix reorientation registered in the non-compatibilized OC (Figure 7.5) is not observed in the respective starting MFC (Figure 7.7). However, if this MFC is further heated to 160°C in the X-ray beam, the matrix recrystallizes again with reorientation (Figure 7.7). Apparently, the application of pressure in the real processing conditions does not allow for reorientation of the HDPE matrix in the shell.

To understand better the influence of the processing conditions on the structure of the MFC and from there – on its mechanical properties, one has to analyze thoroughly the differences in the WAXS and SAXS patterns of various MFC compositions obtained under various conditions. This will be made in Chapter 9.

CHAPTER 8

MECHANICAL PROPERTIES OF PA6 REINFORCED *IN SITU* COMPOSITES

This chapter considers some of the most important mechanical properties of the HDPE/PA6/YP MFCs prepared in this research program, as a function of the composition of the precursors, length, diameters and arrangement of the PA6 reinforcing fibrils. It will be shown how by controlling these parameters by means of the processing conditions, various composites could be prepared with tailored mechanical properties on the basis of the same blend components and using the same processing techniques.

8.1. Introduction

As demonstrated in the literature survey in Chapter 1, microfibrilar composites (MFCs) are a special type of composite materials combining the easier processability of the conventional polymer composites with the nanosized, high aspect ratio reinforcements based on liquid crystalline polymers and carbon nanotubes. The MFCs are created *in-situ* following three basic processing steps: (i) blending, (ii) fibrillation by cold drawing and (iii) isotropization of the matrix component by its selective melting. It is during this stage of matrix isotropization that the oriented precursors are transformed into a composite. This could be done in two different ways, depending on the precursor's geometry [1-3]. The continuous oriented cables (OCs) in the form of woven or non-woven precursors can be processed by compression molding. When precursors in the form of non-oriented mixture (NOM) or middle-length randomly oriented bristles (MRB) are used, one can use either compression molding or injection molding. In the latter case, the precursors are reprocessed at a temperature below the T_m of the dispersed reinforcement phase.

It is important to note that the mechanical properties of the MFCs can depend on the way the isotropization was achieved. In the study of MFCs based on PA6 matrix reinforced by PET fibrils it was found out, that the compression molding route, in contrast to injection molding, allows staying accurately within the required temperature processing window that preserves the fibrilar morphology of PET during the isotropization stage [4]. In addition, compression molding permits the preparation of MFCs from oriented precursors in the form of unidirectional ply (UDP) laminae or laminates with different plate geometries. The use of woven precursors is also possible, i.e., there is a variety of possible morphologies of the reinforcing fibrils in the resulting composite. Conversely, injection molding can only use NOM or MRB precursors to get matrices reinforced by either isotropic entities or short, randomly oriented micro- or nanofibrils.

With all these ideas in mind, compression molding was selected as the method for matrix isotropization in HDPE/PA6/YP MFCs. The processing parameters (temperatures and times) were chosen to match the conditions under which the PA6 reinforcing phase reaches the best mechanical properties (see Chapters 2 and 3), not causing degradation of the lower-melting HDPE matrix. The constitution and the preparation of the composites were already described in Chapter 2. Blend compositions were prepared with the percentages of PA6, HDPE and YP as shown in Table 8.1.

Table 8.1 Composition of the HDPE/PA6/YP MFCs

HDPE/PA6/YP composite designation	**MFC type**	**HDPE** wt.%	**PA6** wt.%	**YP** wt.%
90/10/0	UDP, CPC, MRB, NOM	90.0	10.0	0
80/20/0	UDP, CPC, MRB, NOM	80.0	20.0	0
70/20/10	UDP, CPC, MRB, NOM	70.0	20.0	10.0
75/20/5	UDP, CPC, MRB, NOM	75.0	20.0	5.0
77.5/20/2.5	UDP, CPC, MRB, NOM	77.5	20.0	2.5
65/30/5	UDP, CPC, MRB, NOM	65.0	30.0	5.0

Note: UDP – MFC lamina obtained from continuous oriented cables arranged in the form of unidirectional ply;
CPC - MFC laminate obtained from cross-ply arranged oriented cables;
MRB – MFC obtained from middle-length randomly distributed bristles;
NOM – Composite obtained from non-oriented mixture.

Thus, six HDPE/PA6/YP MFCs were obtained in the form of either UDP or CPC, or MRB and subjected to mechanical tests. Compression molded non-oriented granules of the mixtures obtained after the extruder die (NOM) were also produced from each blend for comparison.

Usually the mechanical characterization of the MFCs is done by tensile tests [5] or flexural tests [6] for determining the Young's modulus, E; the tensile strength σ, the ultimate strain ε, or the deflection at break, δ.

As generally agreed [7], composite materials can be divided into two large groups: homogeneous and heterogeneous. The MRB and NOM composites, prepared in this research project, contain relatively modest proportions of nanosized PA spheres, rods or fibrils, well distributed within the HDPE matrix and randomly aligned (Chapter 1, Figure 1.3, C and D). At a macroscopic scale, these systems are expected to behave isotropically. Differently, the MFCs obtained from woven precursors (Chapter 1, Figure 1.3, B) are fully anisotropic, i.e., their properties vary according to the direction from a point. The UDP MFCs (Chapter 1, Figure 1.3, A) have three mutually perpendicular planes of symmetry defined by axes corresponding to extreme values of the properties. This specific type of anisotropic system is termed orthotropic. Laminates are obtained by bonding together uniaxial laminas which are superimposed with variable orientations of the reinforcement. The CPC MFCs obtained in this work will be considered laminates prepared by compression molding of two plies of oriented cables arranged perpendicularly.

Thus, UDP MFC laminas were used for tensile tests while impact strength and three-point flexural tests were performed with CPC MFC laminates. MRB and NOM composites were also prepared and studied using all mechanical tests to evaluate the influence of the fiber length and the laminate arrangement. The composite properties were compared with those of the HDPE matrix and/or the oriented PA6.

8.2. Tensile properties

8.2.1. HDPE/PA6/YP UDP

Since the UDP lamina represents the basic building block in long fiber reinforced composites [7] it was characterized by tensile testing. Test samples were cut out along the longitudinal axis of orientation, denoted with index 1. Samples were also taken in transverse direction, indexed with 2. Figure 8.1 shows typical stress-strain curves of UDP MFCs in the longitudinal direction.

The 90/10/0 composition containing 10 wt% PA6 displays a ductile behavior similar to the HDPE matrix. In both curves there exist clear yielding and necking, even though the strain at break of the composite (about 100%) is much smaller than the HDPE (about 800%). The other stress-strain curves have the typical brittle shape of composite materials: with strain at break not exceeding 30-40%, and ultimate tensile stress considerably higher than the matrix.

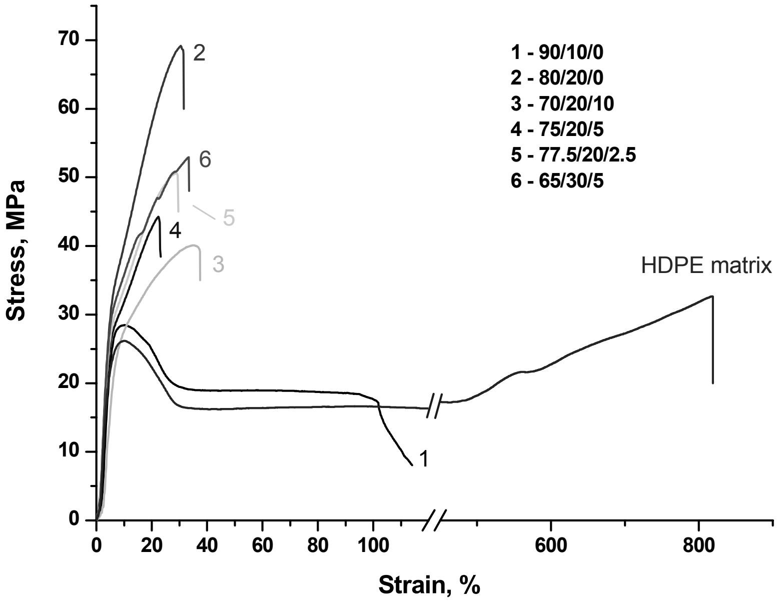

Figure 8.1 Representative stress-strain curves of HDPE/PA6/YP UDP MFCs. For comparison, the curve corresponding to the HDPE matrix is also shown.

8.2.1.1. Young's modulus

Based on the stress-strain curves of each series, the longitudinal Young's modulus E_1 was determined as the secant modulus at 1% strain and the data are summarized in Table 8.2. The same table presents also data on the longitudinal tensile strength $\sigma_{1\max}$ defined as the maximum stress the material can withstand, and on the longitudinal yield stress, σ_{1y}. For specimens without pronounced yielding, $\sigma_{1y} \equiv \sigma_{1\max}$. All MFC compositions show improved moduli as compared to the HDPE. The improvement is in the 11 - 33% range, the biggest being for composites without compatibilizer and the smallest for the composition with 10% of Yparex.

The yield stress and the tensile strength of all composites grow significantly - from 26 MPa for HDPE to approximately 60 MPa for 80/20/0 MFC composition. Again, the MFC with the biggest concentration of compatibilizer showed the smallest enhancement of the tensile properties. Similar influence of the compatibilizer has been observed in conventional (isotropic) HDPE/PA6 blends in the presence of MAH-g-PP copolymer [8].

Table 8.2 Longitudinal Tensile Properties of HDPE/PA6/YP UDP MFCs with various compositions

Composition HDPE/PA6/YP wt. %	**Vol. fract. of PA6, V_f**	E_1 MPa	ΔE_1 %	$\sigma_{1\max}$ MPa	$\Delta\sigma_{1\max}$ %	σ_{1y} MPa
100/0/0	-	827 ± 47	0	26 ± 1	0	26 ± 1
90/10/0	0.084	940 ± 21	13.7	27 ± 1	3.8	27 ± 1
80/20/0	0.171	1095± 52	32.4	57 ± 4	119.2	57 ± 4
70/20/10	0.171	920 ± 7	11.2	37 ± 2	42.3	37 ± 2
75/20/5	0.171	961 ± 19	16.2	45 ± 3	73.1	45 ± 3
77.5/20/2.5	0.171	1030 ± 19	24.5	45 ± 3	73.1	45 ± 4
65/30/5	0.261	1098 ± 48	32.8	52 ± 8	100.0	51 ± 9
0/100/0 oriented		1830 ± 31	-	230 ± 7	-	208± 7

Notes: E_1 was determined as secant modulus at 1% strain;
$\Delta E_1 = (E_{1HDPE} - E_1)/E_{1HDPE}$, %; $\Delta\sigma_1 = (\sigma_{1HDPE} - \sigma_1)/\sigma_{1HDPE}$, %

The explanation given by these authors is related to the low molecular weight of this compatibilizer, which produces adhesion between the two polymer phases but also acts as a mechanically weak boundary phase between them. Having in mind the character of the chemical reaction between Yparex (MAH-g-PE) and PA6 (Chapter 1, Figure 1.9), furthermore, it can be supposed that degradation in the PA6 phase takes place during the melt blending and mostly during the selective isotropization, thus contributing to the lowering of the tensile properties.

8.2.1.2. Prediction of the tensile properties

The micromechanics suggests that both the Young's modulus E_1 and the tensile strength $\sigma_{1\max}$ of the unidirectional lamina should follow the rule of the mixtures that can be used to predict the tensile properties of long fiber reinforced composites. Thus, the theoretical Young´s moduli and tensile strengths of all HDPE/PA6/YP compositions were calculated taking into account the corresponding values of the HDPE, of the oriented PA6 and the volume fraction of the PA6 fibers, as previously described in Chapter 2 (Eq. 2.8 and 2.10). The data are summarized in Table 8.3 and plotted in Fig. 8.2 and Fig. 8.3.

Table 8.3 Longitudinal tensile properties of HDPE/PA6/YP UDP MFCs compared to the theoretical values

Composition HDPE/PA6/YP wt. %	**Vol. fract. of PA6, V_f**	E_1 MPa	E_1* MPa	ΔE_1 %	$\sigma_{1\max}$ MPa	$\sigma_{1\max}$* MPa	$\Delta\sigma_{1\max}$ %
100/0/0	-	827 ± 47	-	0	26 ± 1	-	0
90/10/0	0.084	940 ± 21	911	3.2	27 ± 1	19	42.1
80/20/0	0.171	1095± 52	999	9.6	57 ± 4	39	46.2
70/20/10	0.171	920 ± 7	998	-7.8	37 ± 2	39	-5.1
75/20/5	0.171	961 ± 19	998	-3.7	45 ± 3	39	15.4
77.5/20/2.5	0.171	1030 ± 19	998	3.2	45 ± 3	39	15.4
65/30/5	0.261	1098 ± 48	1089	0.8	52 ± 8	60	-13.3
0/100/0 oriented	-	1830 ± 31	-	-	230 ± 7	-	-

Note: E_1* and $\sigma_{1\max}$ * are the theoretical values predicted using the rule of the mixtures;
$\Delta E_1 = (E_1 - E_1{*}) / E_1{*},\%$ and $\Delta\sigma = (\sigma_{1\max} - \sigma_{1\max}{*}) / \sigma_{1\max}{*},\%$.

Comparing the predicted and experimental values in Table 8.3 it can be concluded that the rule of the mixtures describes well all HDPE/PA6/YP UDP MFCs studied. Figure 8.2 shows that the experimental E_1 values are close and sometimes higher than the predicted ones, the lower the amount of compatibilizer, the bigger the difference. For example, the 80/20/0 system shows the largest positive deviation with ΔE_1 of *ca.* 10% while the experimental E_1 of the 70/20/10 composition is even smaller that the calculated one with a negative deviation of *ca.* 8%.

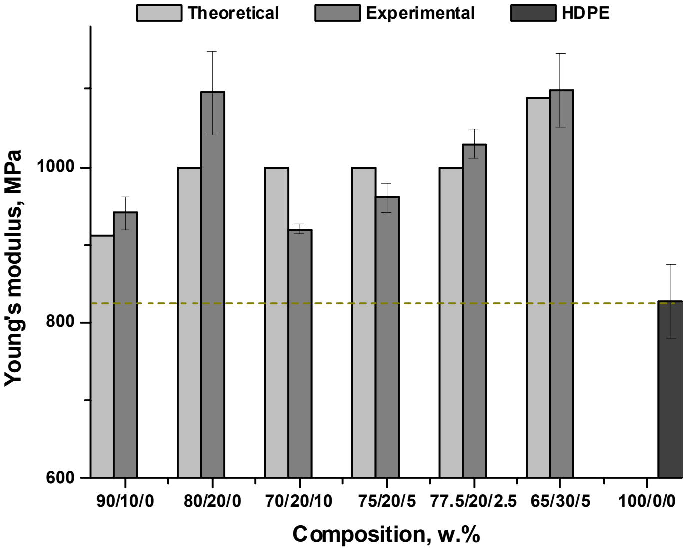

Figure 8.2 Longitudinal Young's moduli E_1 of HDPE/PA6/YP UDP MFCs compared to those predicted from rule of the mixtures and to the HDPE matrix.

Analysing the data on the tensile strength (Table 8.3., Figure 8.3.) one can conclude that the rule of the mixture can be also used for predicting of the tensile strength of the HDPE/PA6/YP MFCs, as the real values are closed or even higher than the theoretical. Again, the non-compatibilized MFCs display the biggest positive deviation in the range of 42-46%.

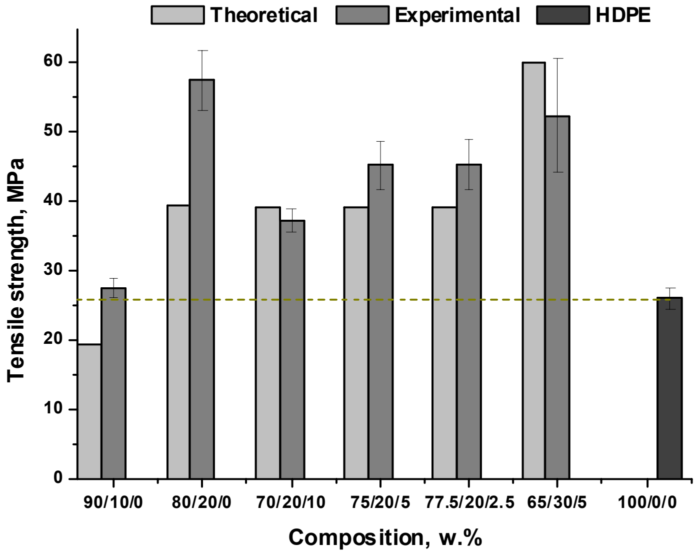

Figure 8.3 Longitudinal tensile strength, $\sigma_{1\max}$, of HDPE/PA6/YP UDP MFCs compared to those predicted from rule of the mixtures and to the HDPE matrix

Two conclusions may be drawn so far. First, in the HDPE/PA6/YP MFCs the compatibilizer should be used with caution. Strictly speaking, to improve the tensile properties, it would be better not to use any. However, since HDPE and PA6 are immiscible, small amounts of compatibilizer are necessary to impart adhesion between the two components as well as to obtain stable and uniform oriented precursors. Second, the tensile characteristics of most MFCs in the form of unidirectional ply laminae are higher than the calculated. The simplest possible explanation could be that the reinforcing PA6 fibrils in the composite have a much smaller diameter and are stiffer and stronger than the PA6 oriented cables, which were used to calculate the theoretical values of E and σ. This was due to the fact that the tensile properties of the PA6 reinforcing fibrils could not be measured directly as they do not exist as a separate material but are formed *in situ* during the composite preparation. Based on the SEM studies on the morphology development in HDPE/PA6/YP precursors and composites, it can be inferred that in non-compatibilized MFCs the length of the reinforcing fibrils can reach 120 μm, whereas the maximum length in the presence of compatibilizer is *ca.* 40 μm. This corresponds to aspect ratios of 80-200 and 40-80, respectively. This data are in good agreement with the tensile behavior – the higher aspect ratio of the reinforcing fibrils leads to better tensile performance. One should bear in mind, however, that the diameter visible by SEM could not be the real diameter of the PA6 fibrils, i.e. there may be a core of PA6 and a shell of HDPE material. This was confirmed by the X – ray analysis presented in the next chapter.

Let us consider now the tensile properties of the HDPE/PA6/YP UDP MFCs in the transverse direction. As it has been referred to by Powell [7], the tensile characteristics of the unidirectional lamina in the transverse direction do not follow the rule of the mixtures. For the E_2 modulus the correlation between simple models and experimental data is not accurate. Except at high volume fraction of fibers, E_2 is usually regarded as having a value similar to that of the matrix. The transverse strength $\sigma_{2\max}$ is considered to be only a function of about 1/3 of the matrix strength. Furthermore, the values of $\sigma_{1\max}$ and $\sigma_{2\max}$ can differ by one order of magnitude, often much more [7].

Table 8.4 shows some tensile properties of HDPE/PA6/YP UDP MFCs in the transverse direction.

Table 8.4 Transversal Tensile Properties of HDPE/PA6/YP UDP MFCs with various compositions.

Composition HDPE/PA6/YP wt. %	Vol. fract. of PA6, V_f	E_2 MPa	E_2* MPa	ΔE_2 %	$\sigma_{2\max}$ MPa	$\Delta\sigma_{2\max}$ %
100/0/0	-	851 ± 32	-	0	27.0 ± 0.4	0
90/10/0	0.084	962 ± 65	867	11.0	25.1 ± 1.0	181.7
80/20/0	0.171	630 ± 77	913	-31.0	12.6 ± 0.5	41.4
70/20/10	0.171	840 ± 27	913	-8.0	21.4 ± 0.3	140.2
75/20/5	0.171	870 ± 15	913	-4.7	17.0 ± 1.3	90.8
77.5/20/2.5	0.171	855 ± 24	913	-6.4	21.2 ± 1.2	137.9
65/30/5	0.261	323 ± 20	965	-66.5	3.7 ± 0.4	-58.5

Notes: E_2 was determined as secant modulus at 1% strain; E_2 * is the theoretical value calculated according to Eq. 2.9, Chapter 2; $\Delta E_2 = (E_2 - E_2^*)/E_2^*$,%; $\sigma_{2\max}^* = 0.33 * \sigma_{p\max}$ = 8.91 MPa, wherein $\sigma_{p\max}$ is the tensile strength of HDPE in transverse direction; $\Delta\sigma_{2\max} = (\sigma_{2\max} - \sigma_{2\max}^*)/\sigma_{2\max}^*$,%

Most of the Young´s moduli are lower than the prediction being, close to that of HDPE. The 90/10/0 composition is the only that shows a positive deviation from the theoretical value. As regards to the transversal tensile strength, it is significantly higher than the expected value that is 1/3 of the matrix. The positive deviations vary from 46% for 80/20/0 sample to 180% for 90/10/0 composition. An exception to this trend is the 65/30/5 MFC with very low experimental E_2 and $\sigma_{2\max}$ values.

It is to be noted that the 90/10/0 laminae display satisfactory tensile properties also in the transversal direction showing a Young modulus with *ca.* 11% higher than E_2^* and experimental tensile strength 180% higher than $\sigma_{2\max}^*$. The fact that in transversal direction there are also deviations from the values expected by the theory of the long fiber-reinforced composites suggests that the respective explanations should be related to the unique structure and morphology of the MFCs.

8.2.2. Isotropic HDPE/PA6/YP composites - MRB and NOM

MRB Composites

In order to evaluate the influence of the fiber alignment upon the tensile properties, composites with middle length randomly distributed bristles (MRB) were produced by chopping HDPE/PA6/YP oriented precursors to 20-40 mm length and subsequent compression molding at temperature below the melting point of PA6. However, as explained in the previous section, the length of the PA6 fibrils could reach up to 120 μm. Therefore it can be expected that both UDP and MRB composites will not differ in respect to the length of the reinforcing fibrils but only in their alignment – parallel in UDP and random in the MRB. In the latter case one should expect similar tensile characteristics in all directions from a point.

Table 8.5 Longitudinal and Transversal Tensile Properties of HDPE/PA6/YP MRB MFCs

HDPE/PA6/YP wt. %	Vol. fract. of PA6, V_f	E_1 MPa	E_2 MPa	$\sigma_{1\max}$ MPa	$\sigma_{2\max}$ MPa
100/0/0	-	827 ± 47	851 ± 32	26 ± 1	27 ± 1
90/10/0	0.084	899± 43	926 ± 46	24.±.1	23 ± 1
80/20/0	0.171	903 ±54	904 ± 47	24 ± 6	22 ± 3
70/20/10	0.171	854 ± 25	891 ± 7	25 ± 1	25 ± 1
75/20/5	0.171	898 ± 70	889 ± 65	29 ± 4	25 ± 1
77.5/20/2.5	0.171	886 ± 34	960 ± 36	31 ± 5	24 ± 3
65/30/5	0.261	744 ± 50	722 ± 31	16 ± 2	12 ± 1
0/100/0 oriented	-	1830± 31	-	230 ± 7	-

As seen in Table 8.5, the Young´s moduli and strengths in longitudinal and transverse directions are close to one another. Most of the compositions show some improvement in the tensile characteristics as compared to HDPE. The E and σ values, however, remain clearly below those of the UDP lamina in the longitudinal direction. This confirms that the alignment of the fibrils is of major importance for the tensile properties.

NOM Composites

Composites prepared from non-oriented mixtures (NOM) were tensile tested to evaluate how the absence of orientation in the PA6 reinforcing phase influences the properties. The precursors for these composites are HDPE/PA6/YP granulates obtained by extrusion and compression molded far below the melting point of the PA6 phase. This means that the NOM composite is not a conventional HDPE/PA/YP blend obtained by melting of all components. It could rather be considered a HDPE matrix reinforced by microspheres of PA6, analogously to the glass spheres reinforced composites. In addition, NOM composites are not MFCs, since the reinforcing phase is not fibrilar.

Some tensile characteristics of the NOM composites studied in the longitudinal and transverse directions are shown in Table 8.6.

Table 8.6 Longitudinal and Transversal Tensile Properties of various HDPE/PA6/YP NOM composites

HDPE/PA6/YP NOM wt. %	**Vol. fract. of PA6, V_f**	E_1 **MPa**	E_2 **MPa**	$\sigma_{1\max}$ **MPa**	$\sigma_{2\max}$ **MPa**
100/0/0	-	827± 47	851 ± 32	26 ± 1	27 ± 1
90/10/0	0.084	906 ± 53	906 ±35	24 ± 1	25 ± 1
80/20/0	0.171	871± 47	869 ± 52	22 ± 1	21 ± 3
70/20/10	0.171	973 ± 45	1028 ± 4	29 ± 1	31 ± 1
75/20/5	0.171	923 ± 10	986 ± 33	22 ± 2	21 ± 2
77.5/20/2.5	0.171	884 ± 75	893 ± 46	22 ± 1	22 ± 2
65/30/5	0.261	772 ± 59	712 ± 43	11 ± 1	9 ± 1
0/100/0 **isotropic**	-	1110 ±40	1080±35	51 ± 2	50±1

The following two observations are worth discussing. The 70/20/10 system displays considerable improvement of both Young's modulus and tensile strength. This is contrary to what was observed in the respective UDP where the PA6 phase was fibrilar with parallel alignment. At this point, a supposition can be made that when the PA6 is isotropic a better compatibilization can be achieved thus improving the adhesion at the HDPE/PA6 interface. Another observation is that the 90/10/0 system also displays enhanced modulus. This was not the case with the conventional HDPE/PA6 blends [8], where a minimum of 20% of PA6 was necessary to reach some improvement of the tensile properties. This difference can be attributed to the specific processing conditions of the NOM composites. Apparently, the PA6 component undergoes annealing that leads to higher crystallinity and increase of the α-PA6 polymorph content, therefore resulting in higher modulus values of the reinforcements. These effects were observed with isotropic and oriented PA6 annealed at 160°C, as it was already detailed in the Chapters 3 and 4.

8.2.3 HDPE/PA6/YP UDP, MRB and NOM – A Comparison

The longitudinal Young´s moduli of the materials discussed so far as a function of their HDPE/PA6/YP composition are compared in Figure 8.4. Most all of composites display Young´s moduli higher than HDPE, the only exception being the 65/30/5 system, where only the UDP lamina shows improved tensile stiffness.

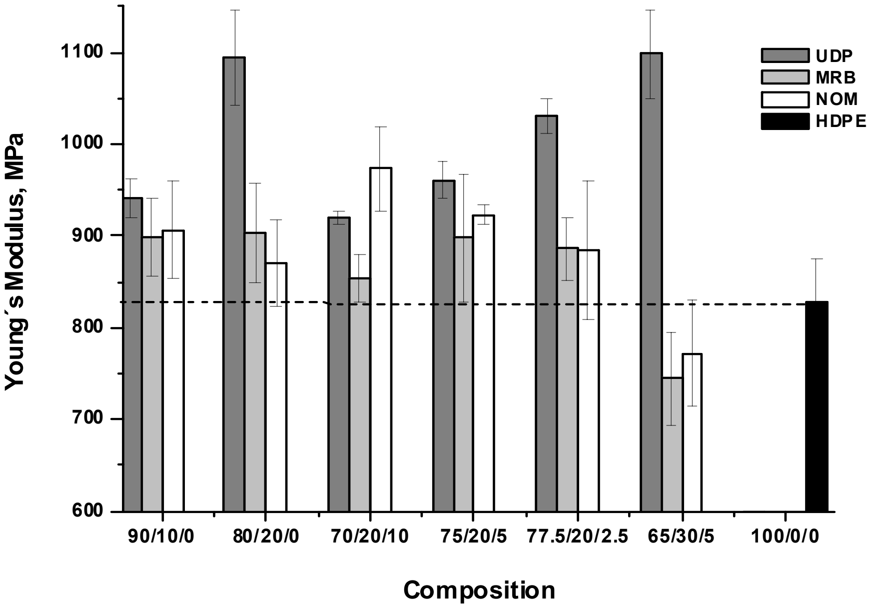

Figure 8.4 Longitudinal Young' s moduli E_1 of HDPE/PA6/YP UDP, MRB and NOM composites and the HDPE matrix.

In the case of the 90/10/0 composites there is no statistically significant difference between the moduli of UDP, MRB and NOM, i.e., the type of PA6 reinforcement (fibrilar or isotropic) and the alignment of the fibrils do not influence the stiffness.

Considering the compositions with 20% PA6, one can assess the influence of these two parameters, as well as that of the compatibilizer. Clear enhancement in the modulus exists only where the reinforcements are aligned fibrils – in the UDP laminae. Within this series, high moduli are observed either without or at low YP concentrations. When the reinforcing component is isotropic (NOM), the trend is inversed. In this case, the higher compatibilizer concentration favors the stiffness. Apparently, the compatibilizer acts better as such when the PA6 reinforcement is isotropic. This is in good agreement with what was observed in the SEM morphological study of various precursors after selective dissolution of the HDPE. The matrix was removed much easier in the oriented precursors leaving smoother fibrils (see Figure 7.3, Chapter 7).

As far as the tensile strength values are concerned (Figure 8.5), a clear increase of the $\sigma_{1\max}$ data is observed only in the UDP MFCs. The compatibilizer concentration influences the strength in the same way as the stiffness. The systems without compatibilizer show an improvement of the $\sigma_{1\max}$ above 100%.

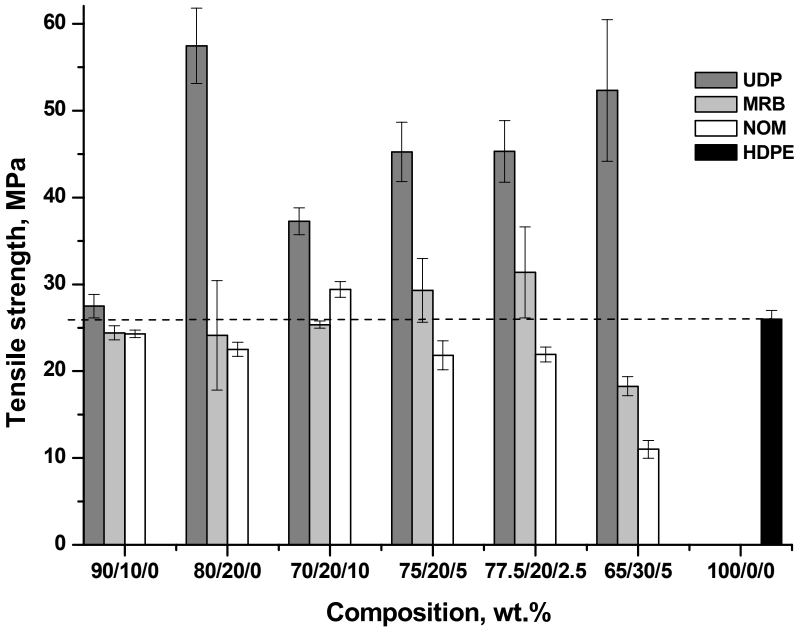

Figure 8.5 Longitudinal tensile strength $\sigma_{1\max}$ of HDPE/PA6/YP UDP, MRB and NOM composites and the HDPE matrix

In the isotropic MRB and NOM composites, the strength data are close or even worse than that of the he matrix. Apparently, to get *in situ* MFCs of higher strength and stiffness one should consider the preparation of laminates with several UDPs.

8.3. Flexural tests in plates

Polymer materials are applied in plates or shell-like products. These parts must be strong and stiff not only in tensile mode but principally in flexural mode in order to perform as designed. The behavior of plates in flexure can be assessed by the flexural stiffness, which is a measure of the resistance to bending. In order to evaluate this property, three-point support flexural tests were performed with HDPE/PA6/YP MFCs according to [9]. Details about this bending test and its data handling were given in Chapter 2. It should be mentioned that the authors who devised this test [9] worked with circular test specimens. In this study rectangular plates were used instead. Simulations with the ABAQUS software were performed at two forces (1 kN and 100 N) to assess the deviation introduced by the different geometries with respect to the theoretical test geometry. It was concluded that using rectangular plates instead of overhanging circular plates has negligible effect on the results. The output of this simulations is presented in Figure 8.6.

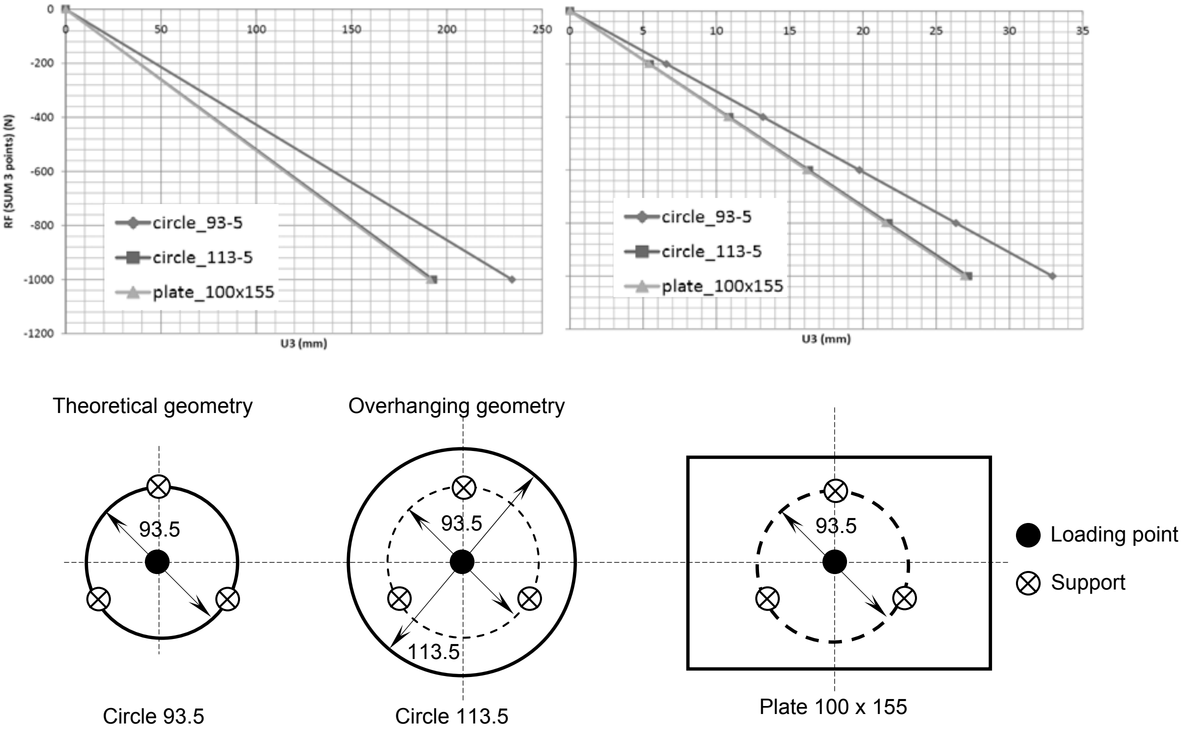

Figure 8.6 Simulation results obtained with the ABAQUS software with two circular and one rectangular test specimens subjected to three-point-support flexural tests.

Hence, rectangular cross-ply laminates (CPC) were made from all HDPE/PA6/YP compositions. To enable comparison, tests with isotropic composites (MRB and NOM) as well as with HDPE matrix were also made. The design of the laminates is shown in Figure 8.7.

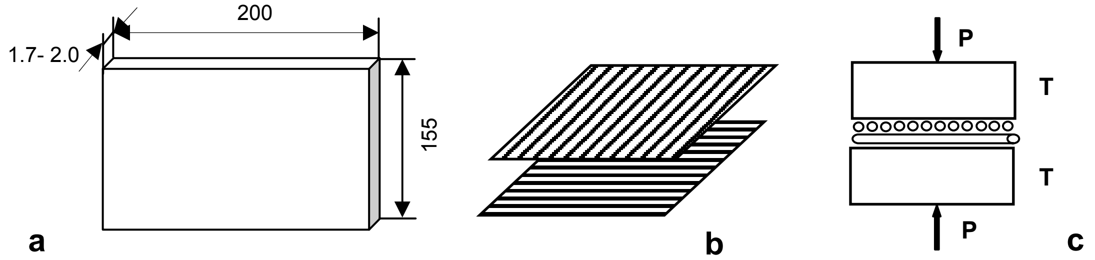

Figure 8.7 The cross-ply laminates in this work:
(a) – dimensions of the plates, mm;
(b) – two plies of oriented precursors, perpendicularly aligned;
(c) – compression molding at temperature, T, and pressure, P;
(d) – the resulting laminate plates used for flexural and impact resistance tests.

The plates were cut into two test pieces (100 mm x155 mm) that were subjected afterwards to the flexural test. From the load vs. displacement experimental curves the slopes at 1 mm displacement, S_p, were determined and the flexural stiffness, C_R was estimated according to equation 2.12 in Chapter 2. The improvement factor, IF, was calculated as the ratio between the difference in the flexural stiffness of the laminate and of the HDPE, with respect to the HDPE, in percentage. The data for HDPE/PA6/YP CPC MFCs are summarized in Table 8.7 and Figure 8.8.

All CPC composites show an improvement of the flexural performance of the order of 70%, with stiffness in the range between 2.3 – 2.6 GPa, well above the HDPE matrix value of 1.5 GPa. Thus, the improvement factor varies between 55% for 70/20/10 system to 78% for 80/20/0 composition. As in the case of the tensile tests, the bigger the concentration of YP, the smaller the improvement of the flexural stiffness. Above 5% the addition of the compatibilizer Yparex has a diluting effect that causes a reduction of the flexural performance. It can be also noted that a substantial enhancement of the flexural performance can be achieved with only 10% of PA6.

The 80/20/0 system deserves special attention. In the form of CPC laminate it shows a 78% increase of C_R. As mentioned before, the same system as UDP lamina had the best performance in tension, with improvements in the Young's modulus and tensile strength of 10 and 46%, respectively. The trend is the same with the other HDPE/PA6/YP compositions. This shows the clear advantages of the MFC composites when used as laminates working in bending.

Table: 8.7. Three-point Support Flexural Test of HDPE/PA6/YP CPC MFCs

Composition HDPE/PA6/YP wt.%	**Slope** S_p N/mm	**Average thickness** h mm	**Flexural stiffness** C_R GPa	**Improvement factor** IF %
100/0/0	11.361	2.002	1.478 ± 0.057	0
90/10/0	11.844	1.705	2.493 ± 0.148	68.7
80/20/0	17.262	1.893	2.624 ± 0.245	77.6
70/20/10	11.366	1.730	2.294 ± 0.224	55.2
75/20/5	12.868	1.736	2.564 ± 0.146	73.4
77.5/20/2.5	13.543	1.758	2.595 ± 0.109	75.6
65/30/5	14.621	1.823	2.516 ± 0.191	70.3

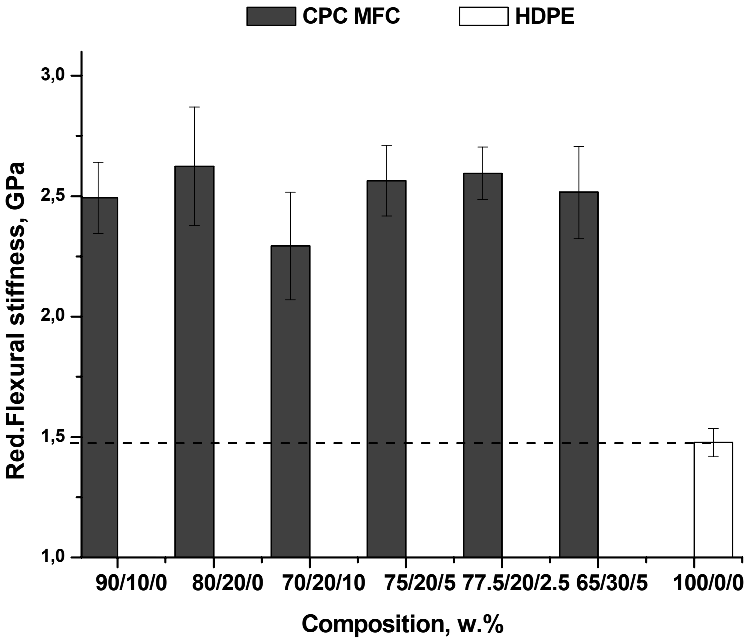

Figure 8.8 Reduced flexural stiffness C_R of HDPE/PA6/YP CPC MFCs

MRB Laminate Composites

When the HDPE/PA6/YP MFC is prepared in the form of MRB all compositions display better flexural stiffness in comparison to the HDPE matrix value with an improvement, *IF,* in the range of 50-84% (Table 8.8, Figure 8.9). The 65/30/5 MRB MFC seems to benefit from the larger amount of randomly arranged short PA6 reinforcing fibrils leading to the best flexural performance of the laminate composites.

Table 8.8 Three-point Support Flexural Test of HDPE/PA6/YP MRB MFCs

Composition HDPE/PA6/YP wt.%	**Slope** S_p N/mm	**Average thickness** h mm	**Flexural stiffness** C_R GPa	**Improvement factor** IF %
100/0/0	11.361	2.002	1.478 ± 0.057	0
90/10/0	12.946	1.774	2.425 ± 0.182	64.1
80/20/0	15.524	1.916	2.302 ± 0.148	55.8
70/20/10	13.198	1.766	2.503 ± 0.051	69.3
75/20/5	13.370	1.845	2.216 ± 0.175	50.0
77.5/20/2.5	12.559	1.791	2.282 ± 0.085	54.4
65/30/5	16.800	1.862	2.723 ± 0.376	84.2

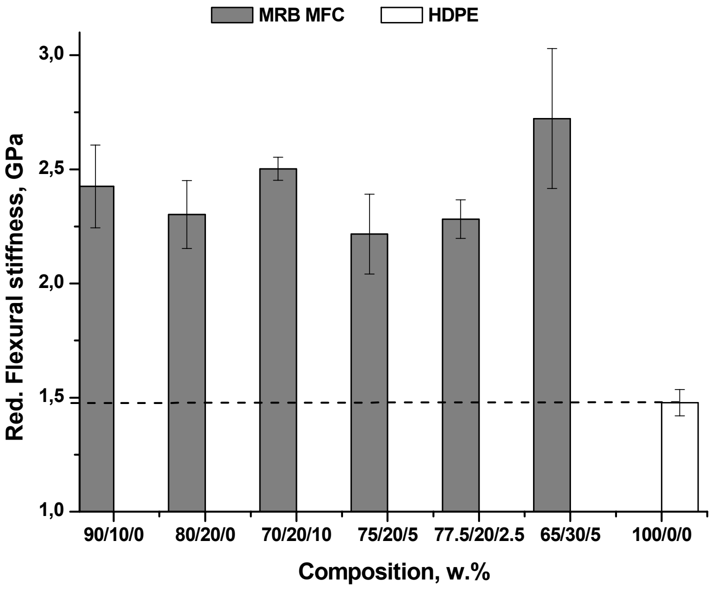

Figure 8.9 Flexural stiffness of HDPE/PA6/YP MRB MFCs.

Within the range of 20% reinforcing PA6 phase, the composition with 10% compatibilizer displays unusually good flexural characteristics.

NOM Laminate Composites

Table 8.9 and Figure 8.10 show that the HDPE/PA6/YP NOM composites with the reinforcing PA6 phase in the form of spherical entities also perform better than the neat matrix in the flexural test.

Table: 8.9. Three-point Support Flexural Test of HDPE/PA6/YP NOM Composites

Composition HDPE/PA6/YP wt.%	**Slope** S_p N/mm	**Average thickness** h mm	**Flexural stiffness** C_R GPa	**Improvement factor** IF %
100/0/0	11.361	2.002	1.478 ± 0.057	0
90/10/0	12.365	1.736	2.464 ± 0.110	66.8
80/20/0	11.448	1.740	2.267 ± 0.176	53.4
70/20/10	10.521	1.710	2.198 ± 0.098	48.7
75/20/5	11.042	1.719	2.271 ± 0.024	53.6
77.5/20/2.5	11.192	1.719	2.301 ± 0.072	55.7
65/30/5	18.919	2.017	2.408 ± 0.138	62.9

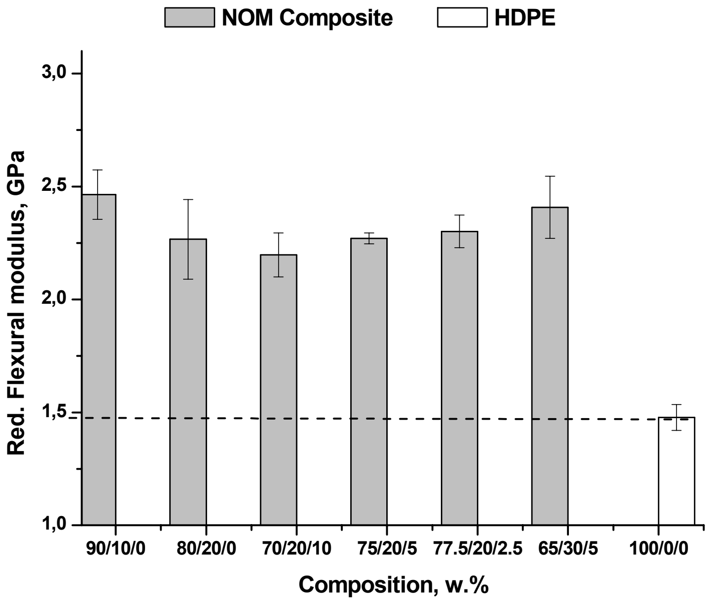

Figure 8.10 Flexural stiffness of HDPE/PA6/YP NOM composites.

There is no big difference between the compositions of the NOM in respect to the flexural stiffness values. Nevertheless, it is possible to notice the slightly lower average values of all NOM materials with 20% PA6 as compared to the NOM composites containing 10 and 30 % of the reinforcing phase.

Compared Laminate Performance

A comparison between all types of HDPE/PA6/YP composites concerning their flexural stiffness is plotted in Fig. 8.11.

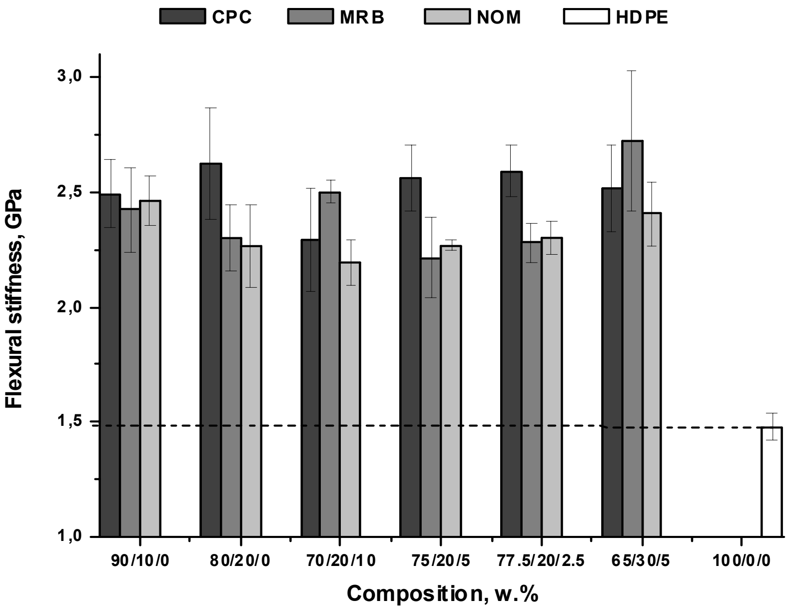

Figure 8.11 Comparative chart of the flexural stiffness of all HDPE/PA6/YP composites studied

Figure 8.11 shows that all HDPE/PA6/YP composites prepared as MFC laminates or NOM plates possess flexural moduli better than HDPE for all compositions studied. There is no statistically significant difference in the flexural stiffness data of CPC, MRB and NOM composites reinforced by 10 wt. % of PA6. This means that at low concentration of the reinforcing phase, it does not really matter if the reinforcement is isotropic or oriented. The alignment of the PA6 fibrils do not seem to be important for the flexural resistance of the 90/10/0 materials either. It should be pointed out that only 10% of PA6 is sufficient to impart a notable flexural stiffness to the HDPE matrix, the improvement being in the range of 60-70%. Higher improvement factors of 70 – 80% were observed in the CPC laminates containing 20% PA6, in the absence or at low concentration of the YP compatibilizer. The increase of the YP concentration up to 10% causes deterioration of the flexural behavior of the CPC composites.

The composition with 30% PA6 also leads to an improvement in the flexural properties comparable to that with 20% reinforcement.

8.4. Impact resistance tests of HDPE/PA6/YP laminates

Another property that is essential to the robustness of the plastic products is the ability to survive abuse in the form of impact. This ability is given by the material's impact resistance or toughness. Unfortunately, high stiffness and high toughness are often properties simultaneously not found in the same material. That is why one of the objectives of the mechanical studies on HDPE/PA6/YP composites was to analyze also their impact resistance as a function of the composition and reinforcement type.

Similarly to the flexural tests, cross-ply HDPE/PA6/YP laminates were used with the design as indicated in Fig. 8.7. For comparison, composites with MRB and NOM precursors were also prepared and tested using the instrumented falling weight equipment as already explained in Chapter 2.

Figure 8.12 depicts the way the peak and total energies were determined from the force/displacement impact curves. Two examples are given: (a) the 90/10/0 CPC and (b) – the HDPE.

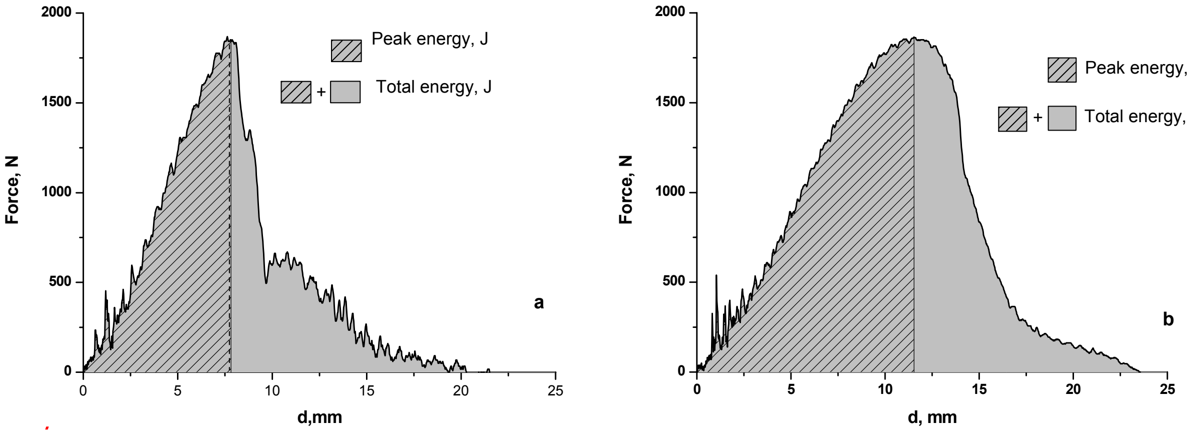

Figure 8.12 Examples showing the determination of peak and total energies in (a) – 90/10/0 CPC MFC; (b) – HDPE matrix

The peak energy represents the area under the curve between the origin and the initiation of the fracture, while the total energy was determined as the whole area below the curve between its origin and the end of the fracture. In Figure 8.13 the peak and total energies per thickness, J/mm, for all samples are represented as a function of composition.

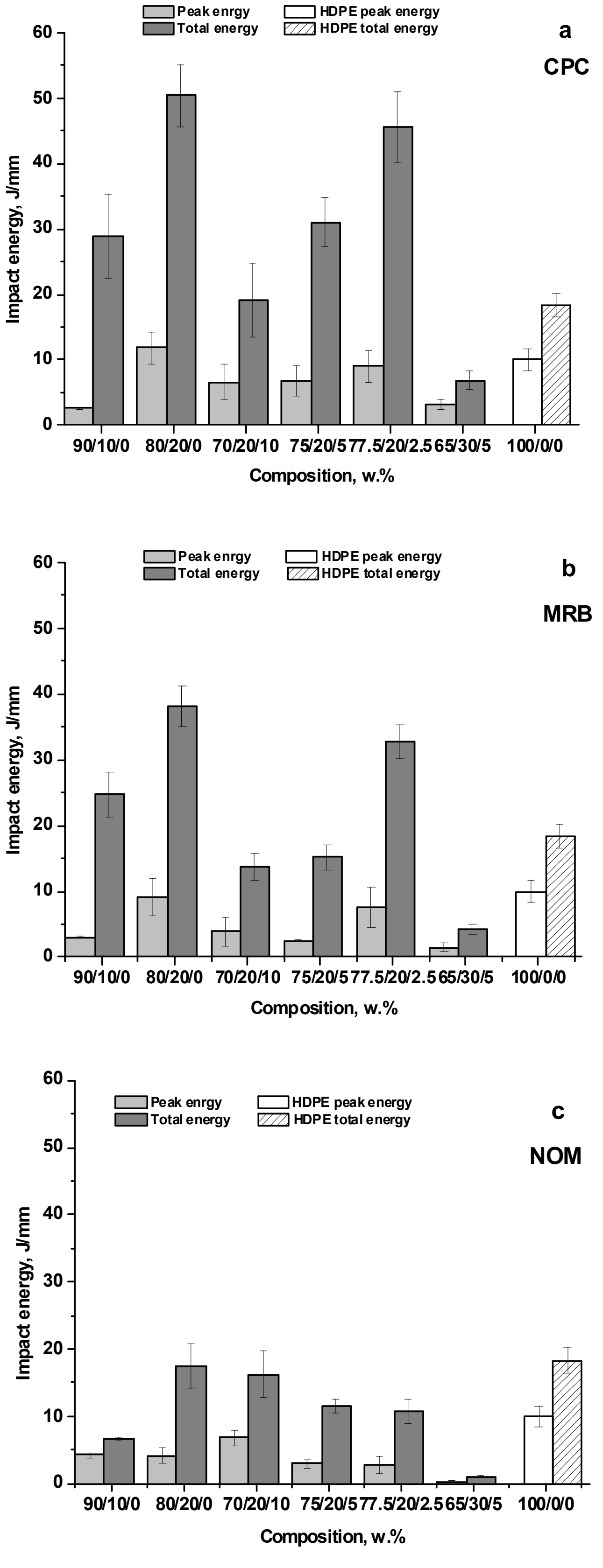

Figure 8.13 Impact energy /mm of HDPE/PA6/YP composites with various compositions and reinforcement: a – cross-ply laminate MFC (CPC); b – MFC with middle length randomly distributed bristles (MRB) ; c – Composite prepared by non-oriented mixture (NOM)

In the case of CPC MFC (Fig. 8.13 (a)) the peak impact energy is lower than that of the HDPE. The total impact energy, however, is much higher than of the matrix. This means that in the CPC composites the sample failure starts at lower energy levels, but the crack propagation requires more energy before the total failure.

It can be noted that the 80/20/0 and 77.5/20/2.5 CPC composites display a considerable increase of the total energy, while their peak energies are only slightly above that of the matrix. A negative deviation in respect to these two impact characteristics is the 65/30/5 composition. It seems that in CPC MFCs 20% of PA6 is the optimal concentration; increasing the PA6 phase to 30% has a negative effect and keeping it as low as 10% is not enough, having in mind the very low value of the peak energy. An analysis of the four compositions with 20% PA6 allows evaluating the influence of compatibilizer on the CPC impact resistance. As with the tensile properties, here the systems without or with minimum amount of YP perform the best. It is noteworthy that the total impact strength is quite sensitive to the YP content, decreasing quickly as YP increases.

The HDPE/PA6/YP MRB MFCs (Figure 8.13, b), have poorer impact performance. As a whole, the general trends observed with the CPCs in terms of PA6 and YP content remain the same. Again the 80/20/0 MRB composition shows the best impact behavior. Evidently, the random arrangement of the reinforced PA6 fibrils affects both the peak and total impact energies of the MRB MFCs. However, it is important to note that the peak energy decreases more abruptly, i.e., the sample failure starts at lower energies.

The reinforcing phase in the NOM composites is globular, which appears to explain their impact characteristics being lower than the HDPE matrix (Figure 8.13, c). Comparing the results in Figures 8.13 (a) and (c), one can conclude that in order to obtain HDPE/PA6/YP composites with good impact resistance, the reinforcing PA6 phase should be fibrilar, preferably with long fibrils as in the CPC laminates.

As already discussed, the PA6 and YP concentrations, as well as the fibril alignment, affect differently the peak and the total impact strengths. The next two graphs show the influence of these factors on each of these impact characteristics.

Only MFCs in the form of CPC laminates or MRB have peak impact energies comparable to that of the HDPE (Figure 8.14). Only the 80/20/0 CPC has a positive deviation from this trend with peak energy of 11.8 J/mm, i.e., slightly higher than HDPE (10 J/mm). Any addition of Yparex reduces the peak energy. Apparently, 20% PA6 is the best concentration within the whole range studied.

As regards the total impact strength (Figure 8.15), all compositions prepared as CPC, MRB or NOM have close or better performance than the matrix, leaving out of account the 65/30/5 system. The most impressive values are displayed the 80/20/0 and 77.7/20/2.5 MFCs in their CPC or MRB form.

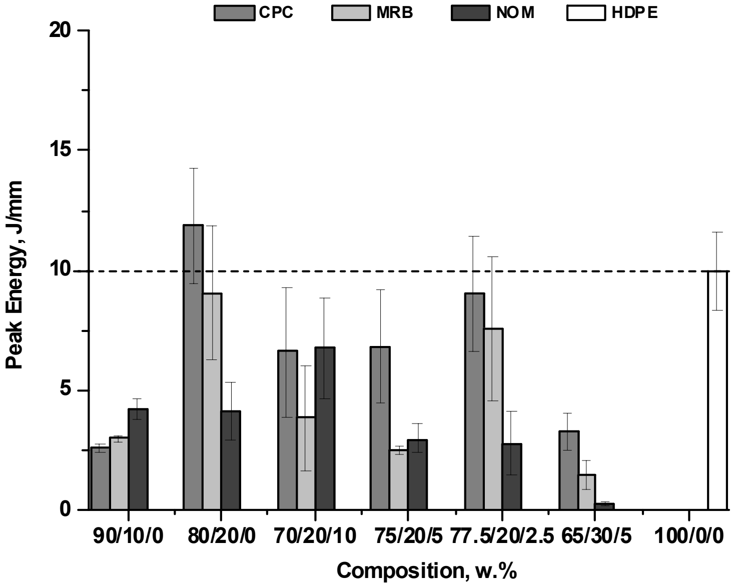

Figure 8.14 Peak energy per unit thickness of HDPE/PA6/YP composites with various compositions and reinforcement

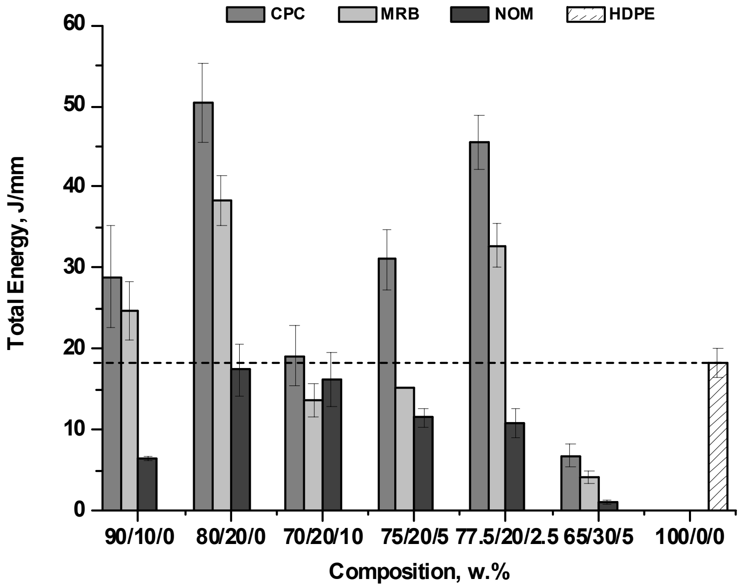

Figure 8.15 Total energy per unit thickness of HDPE/PA6/YP composites with various compositions and reinforcement

In the 75/20/5 system only the CPC MFC shows a clear improvement, while in the 70/20/10 system even CPC is already statistically equal to the pure matrix. With this composition, the three composite types display equal impact strengths, no matter if the reinforcing phase is isotropic or oriented, with aligned or randomly distributed fibers. The 65/30/5 system that contains the largest amount of PA6 displayed the worst values for both peak and total energies.

It seems to be interesting from both theoretical and applied point of view to outline the relation between the structure of the respective composite and its mechanical performance. An attempt to do this with the HDPE/PA6/YP composites will be made in the next chapter.

8.5. References

1. Monticciolo A, Cassagnau P, Michel A, *Polym Eng Sci* 38:1882 (1998).
2. Pesneau I, Ait-Kadi A, Bousmina M, Cassagnau P, Michel A, *ANTEC 99, New York*, 2661;May 2-6 (1999).
3. Evstatiev M, Fakirov S, Krasteva B, Friedrich K, Covas JA and Cunha AM, 2002, *Polym Eng Sci* 42:826 (2002).
4. Evstatiev M, Fakirov S, Bechtold G and Friedrich K, *Adv Polym Techn* 19: 249 (2000).
5. Fakirov S, Evstatiev M and Friedrich K, Nanostructured Polymer Composites from Polymer Blends: Morphology and Mechanical Properties, in: *Handbook of Thermoplastic Polyesters*, ed by Fakirov S, Wiley-VCH, Weinheim, pp. 1093-1132 (2002).
6. Friedrich K, Evstatiev M, Fakirov S, Evstatiev O, Ishii M Harras M, *Comp Sci Techn* 65:107 (2005).
7. Powell PC, *Engineering with Fiber-Polymer Laminates,* Chapman & Hall, London, UK, p. 23 (1994).
8. Palabiyik M, Bahadur S, *Wear* 246:149–158 (2000).
9. Nunes JP, Pouzada, AS, Bernardo CA, *Polym Testing* 21:27 (2002).